The Photoemission of Correlated Neutron-Proton Pairs from ^{12}C

by

Stephen Nicholas Dancer.

Presented as a Thesis for the Degree of Doctor of Philosophy

to the Department of Physics and Astronomy,

The University of Glasgow,

November 1987.

Great are the works of the LORD;

they are pondered by all who delight

in them.

Psalm 111:2

Abstract

The work presented in this thesis was undertaken between October 1983 and September 1987. It describes an experiment designed to study the $^{12}C(\gamma,pn)$ reaction at photon energies between 80 and 130 MeV. In this region the (γ,pn) exit channel is known to be an important contributor to the total photon absorption cross section. It provides a testing ground for the predictions of medium- to short-range correlation effects in nuclear matter.

The experimental system is able to determine completely the kinematics of the reaction. The 180 MeV microtron at Mainz University provides a 100% duty cycle primary electron beam which is then used to create bremsstrahlung photons at a 25 μm aluminium radiator. The photons are tagged by the recoil electrons which are momentum analysed by the tagging spectrometer. At 90° to the beam is centred a large solid angle E-ΔE_1-ΔE_2 scintillation telescope detector for the detection of protons. Neutrons are detected by an array of plastic scintillator time-of-flight detectors placed at angles between 52.5° and 127.5° inclusive. Enough kinematic variables are measured to enable the reconstruction of the recoil nucleus momentum and the excitation energy of the residual nucleus. A deuterated polythene target allows simultaneous evaluation of the cross sections for carbon and deuterium so that the quasideuteron models can be tested.

The precision of the system is sufficient to determine the shells from which the nucleons emerge through spectra of missing energy. The data have been separated into those with low missing energy, where both nucleons come from the 1p-shell ((1p1p)), and those with high missing energy, where it would be expected that one comes from each of the 1p- and 1s-shells ((1p1s)). The recoil nucleus momentum

distribution of both the (1p1p) and (1p1s) data show good agreement with the quasideuteron calculation of Gottfried using harmonic oscillator wavefunctions. A phase space calculation does not reproduce either dataset very well.

The $^{12}C(\gamma,pn)$ cross section from (1p1p) data is found to be 60–70% of that expected by the simple Levinger model. The effect could easily be explained be final state interactions. Indeed, there is a suggestion that some events undergo interactions sufficiently strong to place them in the (1p1s) missing energy region.

Some microscopic calculations which associate the absorption with meson exchange currents fail to provide cross sections of sufficient magnitude. Microscopic approaches are much in need of revision as the data require more detailed predictions.

Declaration

The data presented in thesis were obtained by the Nuclear Structure Research Group at the University of Glasgow, as a part of the collaboration with the Universities of Edinburgh and Mainz, West Germany, in which I undertook a principal rôle. The analysis and the interpretation of the data is entirely my own work. This thesis has been composed by myself.

Stephen N. Dancer

Acknowledgements

I would like to convey my sincerest thanks to Dr. Douglas MacGregor, my supervisor, for his encouragement, help and enthusiasm throughout the execution of this experiment and for his critical comments and discussions during the composition of this thesis.

My thanks are also due to Profs. H. Ehrenberg and B. Schoch, of the Institut für Kernphysik, the University of Mainz, who afforded me the use of the accelerator facilities. Prof. Schoch also helped in the running of the experiment.

I owe my thanks to Professor Bob Owens, the director of Kelvin Laboratory, for affording me the use of the Kelvin Laboratory facilities and for stimulating and valuable discussions concerning many aspects of the work. I am grateful to Dr. Cameron McGeorge whose critical comments and probing questions enabled me to avoid many pitfalls along the way. To him I am indebted as I am also to Drs. John Annand, Ian Anthony, Ian Crawford, Sam Hall, Jim Kellie, Messrs. Alan MacPherson, Stuart Springham and Peter Wallace without whom the experiment could not have taken place.

I would like to thank Messrs. Reinhart Beck and Guido Liesenfeld of the Institute in Mainz who, during the run, made themselves available in the event of any technical hitches. I am extremely grateful to Dr. Johannes Vogt for his invaluable assistance in setting up the electronics and for his help in the development of the analysis software.

My thanks to Messrs. Andy Sibbald and Arrick Wilkinson who showed much patience in dealing with my computing queries and problems; to the technical staff at the Kelvin Laboratory who constructed the detector frames and other essential items; and to Mrs. Eileen Taylor who, in large measure, helped in the preparation

of the diagrams.

My warm thanks to Messrs. Sean Doran, Gary Miller and Salah Salem who, in addition to those from Kelvin already mentioned, lightened days of heavy physics with irrepressible humour.

The Science and Engineering Research Council have provided financial support in the form of a SERC studentship. Professor I. S. Hughes, head of the Department of Physics and Astronomy at the University of Glasgow, has also provided funding for conferences and a summer school. To both parties I am extremely grateful.

Finally, and above all, I am deeply grateful to my wife, Susan, whose wisdom, love and prayerful support have been a constant source of encouragement and help. I am especially grateful for her willingness to bear the bulk of the mundane duties of life in order to free me for this work. The love of my parents, Celia and Elton, and my "in-laws", Bill and Ella as well as the kind wishes of many friends have been deeply appreciated.

Contents

Chapter 1

Introduction

1.1 Introductory Remarks

The work of this thesis comprises an investigation of the $^{12}C(\gamma,pn)$ reaction in the intermediate photon energy range 80–130 MeV. The range is referred to as intermediate since the region lies between the two large resonances observed in the total photon absorption cross section. Figure 1.1 shows the results of a total cross section measurement carried out on ^{9}Be at Mainz [1] at energies from threshold up to $\sim$ 350 MeV. The general features apparent in the figure are common to most nuclei. At low energies the excitation mode known as the giant dipole resonance occurs. In this region the absorption mechanism is a collective phenomenon in which the whole nucleus is excited to a collective oscillatory mode. The compound nucleus decays statistically mainly by the emission of neutrons. At energies above 150 MeV a second resonance occurs in which the main absorption mechanism is through pion photoproduction on single nucleons. In the intermediate region, between the resonances, the absorption mechanism is still controversial. The main competing reactions appear to be (γ,p), (γ,n) and (γ,pn).

An important feature possessed by real photons is the combination of high energy with relatively little momentum. In the intermediate energy region, this means that the energy must be shared between more than one particle in the final state. The existence of (γ,N) reactions demonstrates this fact where a nucleon and a residual nucleus part company. A direct knockout interpretation of a process such as (γ,N), which accounts for the anisotropic nucleon angular distributions and the high nucleon energies observed, runs, however, into difficulties as higher photon energies are used. For example, a nucleon ejected from ^{12}C at 90° by a 100 MeV photon has a momentum of $\sim$ 390 MeV/c. In the direct knockout picture the proton would need $\sim$ 400 MeV/c within the nucleus to balance momentum. The necessary momentum increases with both photon energy and emission angle. These momenta are far higher than the Fermi momentum of the ^{12}C nucleus

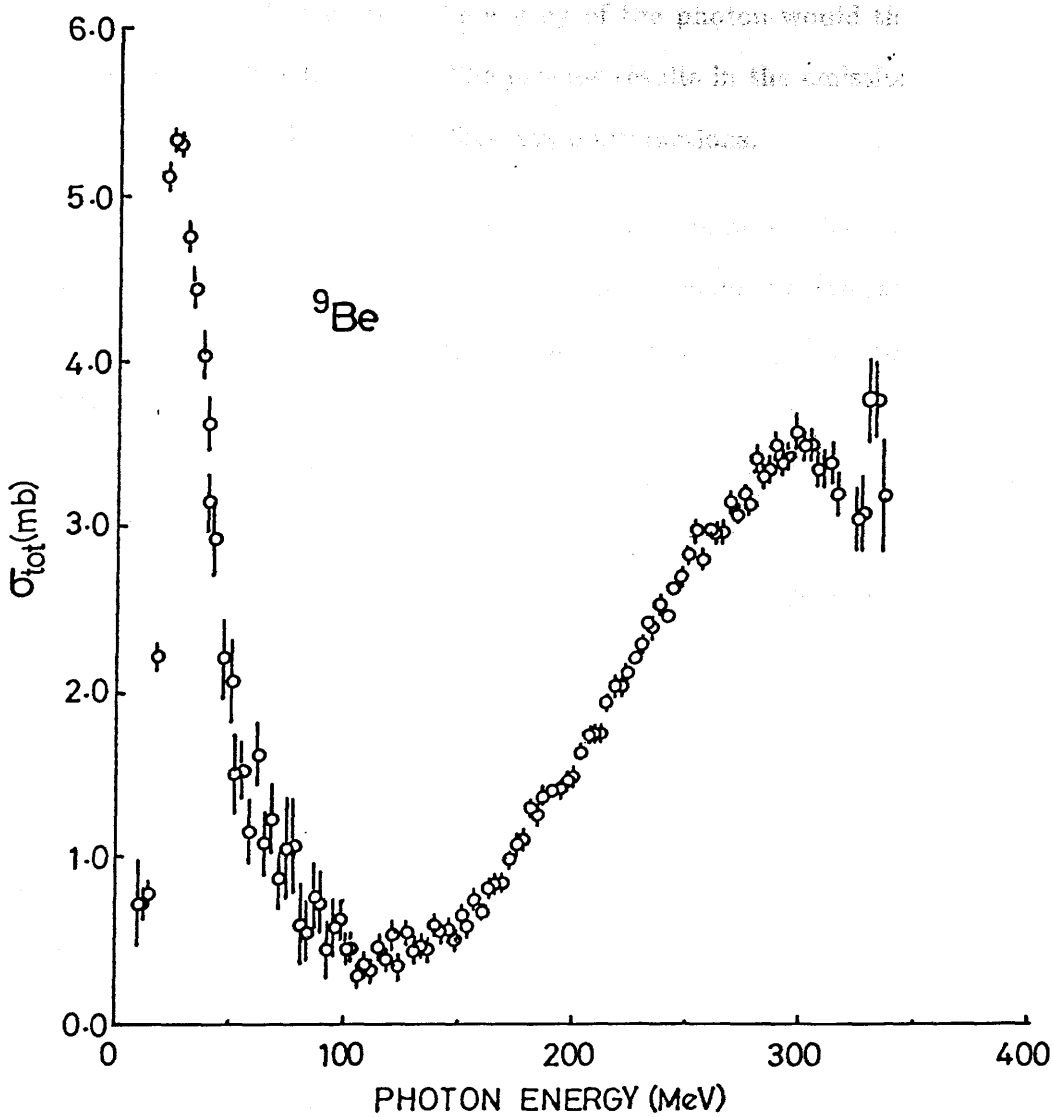

Figure 1.1: Total photonuclear absorption cross section in ^{9}Be[1].

which is $\sim$ 250 MeV/c. A nuclear independent particle model predicts that the probability of finding a nucleon with such a high momentum in the initial state is very small. The number of particles with enough momentum are enhanced if, in the model, nucleons are allowed to interact strongly with another nucleon at the time of photon absorption. The energy of the photon would then be shared mainly between the nucleon pair. The process results in the emission of a pair of correlated nucleons if there are no final state interactions.

The electromagnetic interaction (real or virtual photons) has several advantages as a probe of nuclear structure. The electromagnetic interaction is weak compared with the strong interaction between nucleons found within the nucleus so that it only weakly perturbs the system. Its weakness allows the photon to probe the entire nuclear volume, in contrast to hadronic probes which interact strongly and thus probe the nuclear surface only. In addition, the electromagnetic interaction with charge and current densities is well understood, and is governed by well established laws.

The photon is thus a good tool for investigating initial state short range correlations. These ideas have led to the development of two-nucleon models to describe them. The intuitive notion of quasideuterons inside the nucleus was first proposed by Levinger [2] in a model which related the two nucleon absorption cross section to the deuteron photodisintegration cross section in a simple way. Other authors developed the model and achieved considerable success in fitting the data. The comparable magnitudes of the (γ,p) and (γ,n) cross sections at intermediate energies have encouraged some authors [3] to apply Levinger's model to these reactions by assuming that the primary absorption mechanism is on two correlated nucleons. In this picture, one of the nucleons remains in a bound state while the other escapes. The model has met with success in explaining the general features of the data.

The technical difficulties involved in producing monochromatic photon beams have hindered the progress of experimenters. As a result much of the theory developed in the last 30 years remains to be examined in detail. Only recently, with the advent of 100% duty cycle machines and good photon tagging systems have multiple coincidence experiments been made practical. The ability to measure the photon energy enables the experimenter to completely determine the kinematics of the reaction. Such a possibility was sadly lacking in previous experiments but is crucial to an understanding of the (γ,pn) mechanism.

The rest of this chapter reviews in more detail the ideas outlined in this section. Chapter 2 describes the development of the present experimental system and its setup, while Chapter 3 outlines the techniques employed in analysing the data. The experimental results obtained and interpretations of them are presented in Chapters 4 and 5 respectively. Conclusions are drawn in Chapter 6.

1.2 Early Photonuclear Experiments

The earliest photonuclear experiments found the compound nucleus model successful in describing low-energy nuclear excitation processes. In this model the absorption of a photon is pictured as a two step process. In the first place the target nucleus forms an excited intermediate "compound" state which possesses a nuclear "temperature". In the second step the nucleus cools down, "boiling off" nucleons. Emission of protons is severely inhibited by the Coulomb barrier so that emitted particles are predominantly neutrons. In fact for ~18 MeV photons and a medium weight nucleus ($A \approx 100$) the ratio of the number of emitted protons to emitted neutrons is expected to be between 10^{-3} to 10^{-5}. The decay of the compound nucleus is a statistical process in which the angular distribution of the emitted particles is isotropic and their average energy is small. An early experiment [4] at this energy indicated that the ratio was between 20 and 1000 times

greater than expected by this model. Further evidence of such discrepancies was obtained from experiments performed at higher energies.

A photonuclear experiment was carried out by Walker [5] on carbon using 195 MeV endpoint bremsstrahlung photon radiation. Spectra of photoprotons of energy up to 124 MeV were measured at various angles. It was found that angular distributions of both 70 MeV and 90 MeV protons were strongly forward peaked. Spectra of T_p, the proton energy, showed a cross section proportional to $\sim T_p^{-5}$ which decreased up to an energy approximately half that of the peak bremsstrahlung energy. Thereafter the spectrum decreased more rapidly. (An example is shown in Figure 1.2.) A similar experiment by Levinthal and Silverman [6] using a higher energy beam showed the same forward asymmetry for 40 MeV protons (see Figure 1.3). However, they found that 10 MeV protons were almost isotropic. In addition, they made measurements with several targets of various atomic number and showed that the cross section was closely proportional to Z. Keck's measurements [7] verified those of [6] in a similar experiment which extended the measureable proton energy range to higher energies. The data revealed the "break" observed in Walker's data at approximately half the peak photon energy.

All three reports concluded that the compound nucleus model was inadequate on two grounds. Firstly, the number of high energy protons detected was larger than that predicted by the model and that, secondly, the marked anisotropy of the angular distributions of protons pointed to a direct interaction with a subunit rather than the whole of the nucleus. Levinthal and Silverman chose to compare the data with a "one nucleon" model in which the cross section was shown to be related to the momentum space wavefunction of the proton in the nucleus. They used the Chew-Goldberger momentum distribution [8] and, after folding in a bremsstrahlung distribution, obtained a shape for the proton energy spectrum which fitted the higher energy region quite well. Such a fit underestimated the

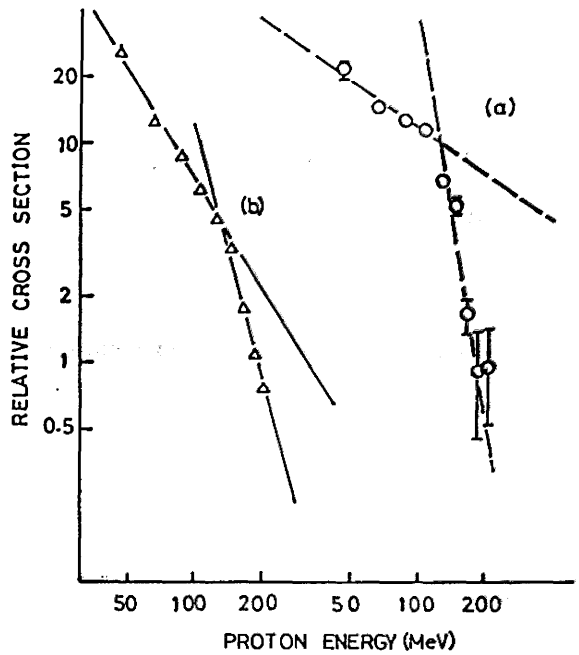

Figure 1.2: Proton energy distributions from carbon at $\theta_p = 60° \pm 15°$ with a 310 MeV endpoint bremsstrahlung beam [9]. (a) Using monoenergetic photons; (b) using raw bremsstrahlung photons.

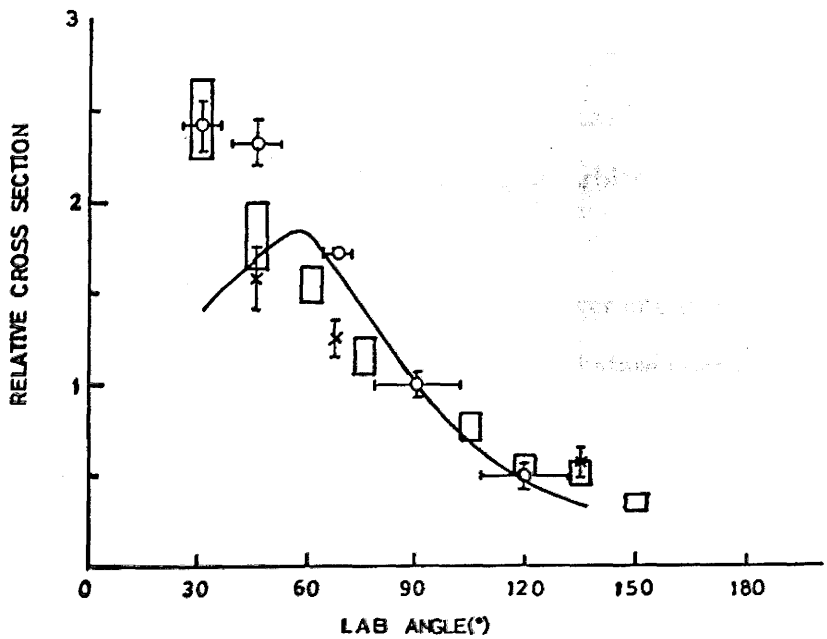

Figure 1.3: Angular distributions of photoprotons obtained by various authors from carbon and compared with the calculation of Levinger [2] . Crosses–ref. [6]; circles–ref. [7]; boxes–ref. [13].

cross section at lower energies since, as they concluded, the evaporation process is important in this region. The absolute values of the data and the calculation differed by a factor greater than two. The model, however, failed to explain the sharp breaks in the proton spectra observed. The fact that these occurred at half the bremsstrahlung endpoint energy suggested that the energy is shared by two nucleons.

The proton spectra observed thus far were dominated by the shape of the bremsstrahlung spectrum in such a way that nuclear effects were difficult to unravel. A new technique, which is described later, was devised by Weil and McDaniel [9] to select photons of particular energies from the bremsstrahlung spectrum by detecting the bremsstrahlung scattered electrons in coincidence with photoprotons. Both "monoenergetic" and raw beams were compared. Both spectra showed the characteristic break in the slope although the monoenergetic data showed a less steeply falling function below the break energy and a steeper function above. The angular distribution for 70 MeV protons obtained from the raw bremsstrahlung source was in agreement with those of other authors; that for monoenergetic data was found to be slightly less forward peaked. They analysed their data using a two nucleon model and, after correcting the calculated proton spectrum approximately for final state scattering and including an arbitrary normalisation factor, found reasonable agreement.

In conclusion they commented that the fit at lower energies was largely fortuitous due to the very approximate nature of the final state correction but that the fit at high proton energies showed the approximate correctness of the two-nucleon model.

1.3 The Development of Two-Nucleon Models.

Levinthal and Silverman were able to fit their data using a proton momentum

distribution which reaches $1/e$ of the peak value at $\sim$ 500 MeV/c. The width of the distribution is unrealistically large since the Fermi momentum for most light nuclei is much less than this. However, the approach did illustrate the need for high momentum components in the nuclear wave function. In 1951 Levinger [2] proposed a two nucleon model. He argued that since emitted protons have a high momentum in the final state as a result of relatively little input photon momentum, the "momentum mismatch" must be made up by a high momentum in the initial state. This occurs when the proton is being acted on by strong forces arising from the close proximity of another nucleon. If the distance between the nucleons is less than their average spacing in the nucleus then it is very likely that no other nucleons are involved. Configuration space relative nucleon-nucleon wavefunctions which have large short range components have correspondingly large high momentum components in momentum space. It follows that the two nucleon model is expected to become more important as high momentum components of the particle wavefunctions are probed. Levinger further argued that since the dipole term in the photonuclear interaction is dominant only neutron-proton pairs need be considered thus transforming the two-nucleon model into the quasi-deuteron model.

Factorising the nuclear wavefunction as

$$\Psi(1,\ldots,A) = e^{i\mathbf{k}'.\mathbf{r}'}\psi_k(r)\varphi(3,\ldots,A)$$

where $e^{i\mathbf{k}'.\mathbf{r}'}$ is the wavefunction of the motion of the centre of mass of the quasi-deuteron, $\psi_k(r)$ is the wavefunction describing the relative motion of the neutron-proton pair of separation r and relative wavenumber k, and $\varphi(3,\ldots,A)$ is the wavefunction of the residual $A-2$ nucleons, Levinger showed that for $kr \ll 1$ the deuteron wavefunction was proportional to that of the quasi-deuteron used by Heidemann [10]. After averaging over k using Fermi distributions for the nucleon momenta, normalising for the nuclear volume, and adding up all possible neutron-

proton pairs, the cross section was shown to be

$$\sigma_{QD} = 6.4 \frac{NZ}{A} \sigma_D \tag{1.1}$$

where σ_D is the deuterium cross section given by Schiff [11], and Marshall and Guth [12].

Levinger further calculated the expected proton energy spectra from a bremsstrahlung source and the angular distributions of monoenergetic protons. The results agreed qualitatively with the data of [5,6,7], showing the familiar break in the proton energy spectrum and the forward asymmetry of the angular distribution, although not quite so marked as in the data. Quantitative comparisons were difficult due to the wide difference in the experimental results. The error in the calculation was estimated to be a factor 3. Levinger's treatment omitted the effect of final state interactions, meson exchange effects and photomagnetic transitions. The first two would tend to make the angular distributions more isotropic and the third would slightly enhance the cross section at forward angles.

Further detailed measurements by Rosengren and Dudley [13], using 322 MeV bremsstrahlung, and by Feld *et al.* [14], using 325 MeV bremsstrahlung showed a cross section much more forward peaked than that predicted by Levinger's theory. It was pointed out by Rosengren and Dudley that the angular distributions for deuterium used by Levinger were not consistent with later experiments (see [15]) which showed an appreciable isotropic component underneath a distribution peaked at forward angles. Assuming an isotropic deuterium angular distribution and using it in Levinger's calculation provided a distribution which was in better agreement with their measurements.

Dedrick[113], taking up the two-nucleon cause, assumed that photon absorption took place on a pair of nucleons which were scattering off each other inside the nucleus. Although a deuteron wave function was not initially assumed for the initial state relative wavefunction of the pair, it was found that if all other relative states

were ignored except the triplet S state then the calculation simplified considerably and the relative wavefunction reduced to that of the deuteron. After accounting for the motion of the centre of mass of the pair, Dedrick found good agreement with the low energy photoproton data of Johansson [16].

In a more sophisticated treatment of two nucleon correlations, Gottfried [17] showed that the cross section for the emission of correlated neutron proton pairs could be factorised as

$$d\sigma = \frac{1}{(2\pi)^4} F(P) S_{fi} \delta(\varepsilon - \bar{\varepsilon}) d^3\mathbf{k}_1 d^3\mathbf{k}_2$$

where $\mathbf{k}_1$ and $\mathbf{k}_2$ are the momenta of the two nucleons, $F(P)$ is the probability density of finding two nucleons of zero separation and net momentum $P = |\mathbf{k}_1 + \mathbf{k}_2 - \omega|$ (ω is the photon momentum) in the Slater determinant of independent particle shell model wavefunctions. S_{fi} is the sum of the squares of the matrix elements for transitions evaluated in the frame where $\mathbf{k}_1 + \mathbf{k}_2 = 0$. In arriving at this expression four assumptions were made:

1. The photonuclear interaction is the sum of two-body operators. Justification for this was obtained from deuteron photodisintegration measurements which showed a maximum of the cross section at the same energy as that of the resonance of photomeson production. It was suggested that the dominant disintegration mechanism was by virtual pion production and reabsorption. Three-body effects are ignored since the probability of finding three nucleons close enough together can be neglected.

2. The excitation of the residual nucleus is small compared to the initial photon energy. At the time there was no experimental confirmation of the validity of this assumption. However, its inclusion enables a summation over the final states to be carried out.

3. During the absorption act the influence of the other nucleons can be ignored.

4. The form of the ground state Ψ_0 was assumed to give a two-body density matrix of the form,

$$\rho(\mathbf{r}_1, \mathbf{r}_2) = \rho_S(\mathbf{r}_1, \mathbf{r}_2)\, |g(|\mathbf{r}_1 - \mathbf{r}_2|)|^2$$

where $\rho_S(\mathbf{r}_1, \mathbf{r}_2)$ is the shell model two-body density matrix given by

$$\rho_S(\mathbf{r}_1, \mathbf{r}_2) = \int \Phi_S^* \Phi_S d^3\mathbf{r}_3 \ldots d^3\mathbf{r}_A$$

and Φ_S is the ground state shell model nuclear wavefunction. g is the modification of ρ_S which accounts for the residual interactions not included in the shell model potential. This form of ρ follows from the wavefunctions given by Jastrow [18] which are of the form

$$\Psi_0(1, \ldots, A) = \prod_{i>j=1} C_{ij} \Phi_S(1, \ldots, A)$$

where C_{ij} is of the form

$$C_{ij} = \sum_{ST} g_{ST}(|\mathbf{r}_i - \mathbf{r}_j|) \Lambda^S_{\sigma_{ij}} \Lambda^T_{\tau_{ij}}$$

where the sum is over the spin and isospin quantum numbers and the Λ's are the projection operators on to singlet and triplet states. Gottfried pointed out that there are other forms of Ψ_0 which justify this assumption.

The form factor $F(P)$ contains information about the centre of mass of the nucleon pair and since it is derived from the "long range" shell model wavefunctions information about the short range interactions cannot be deduced from it. The effects of short range correlations are contained in S_{fi} which is a function of the relative momentum $\mathbf{K}$ of the nucleons, the photon momentum ω_0 in the frame where $\mathbf{k}_1 + \mathbf{k}_2 = 0$, and the angle between them. A slight dependence of S_{fi} on $\mathbf{P}$ comes through the Doppler shift $\omega \longrightarrow \omega_0$ which is dependent on $\mathbf{P}$. However, S_{fi} is a much less rapidly varying function of $\mathbf{P}$ than F. Gottfried thus concluded that angular correlations would lead to more information about ρ_S than about g.

Following Levinger and Dedrick, Gottfried assumed that only the $^3S_1$ contribution was important and further assumed that g_{10} took the form,

$$|g_{10}(x)|^2 = \gamma^3 |\phi_0(x)|^2$$

for $x = |\mathbf{r}_i - \mathbf{r}_j| < 1$ fm, where γ is a constant and ϕ_0 is the deuteron wavefunction. The factor S_{fi} can then be written as

$$S_{fi} = 4\pi \frac{3\gamma^3}{[k_p E_p]_0} \left[\frac{d\sigma_D}{d\Omega_p}\right]_0$$

so that

$$\frac{d\sigma}{d\Omega_p} = \frac{3\gamma^3}{4\pi^3} F(P) \left[\frac{d\sigma_D}{d\Omega_p}\right]_0 \frac{k_p E_p}{[k_p E_p]_0} \delta(\varepsilon - \bar{\varepsilon}) dT_p d^3k_n \qquad (1.2)$$

where $[\ldots]_0$ denotes evaluation in the frame where $\mathbf{k}_1 + \mathbf{k}_2 = 0$. A certain amount of slack exists in the calculation since, for a given direction Ω_p, ω_0 and k_{p0} are dependent, whereas in the complex nucleus case they are independent because of the additional recoil nucleus energy. Thus $\left[\frac{d\sigma_D}{d\Omega_p}\right]_0$ could be evaluated at ω_0 or k_{p0}. Gottfried himself evaluated it at ω_0 since $\sigma_D(\omega_0)$ changes rapidly with ω_0.

Equation 1.2 illustrates the resemblance of the kinematics of the (γ,pn) process to those of deuteron photodisintegration. The factor $F(P)$ determines the shape of the angular distribution of the correlated neutrons when Ω_p and ω are fixed. It essentially smears out the fixed correlation obtained from a stationary deuteron. The angular distribution of protons (or, alternatively, neutrons) is also smeared out somewhat by $F(P)$ but is essentially governed by the deuteron angular distribution. When comparing Equations 1.1 and 1.2 it can be seen that the Levinger parameter, evaluated as 6.4 by Levinger himself, is intimately related to γ. This reflects the fact that the Levinger parameter is a measure of the probability that the nucleon is close to another nucleon in the nucleus compared to such a probability in the deuteron.

In conclusion angular correlations are expected but are dominated by $F(P)$. To see the effect of g on the cross section an experiment would have to be set up

which could detect correlated nucleons over a wide range of energies and angles to determine the momenta $\mathbf{k}_1$ and $\mathbf{k}_2$. With the photon energy known, it would then be possible to select events with a fixed $\mathbf{P}$ and $T_p + T_n$ and measure the angular distribution of protons. Such a distribution would, if the assumptions were correct, follow the shape of the deuterium cross section, modified by final state interactions.

The form of wavefunction with correlations suggested by Jastrow [18] and alluded to by Gottfried has been taken up by several authors to provide a microscopic description of the (γ,pn) and (γ,N) reactions. Weise and Huber [19] investigated the effects of short range nucleon-nucleon correlations, ignored by the shell model, by writing the wavefunction as

$$\Psi(1,\ldots,A) = \Psi_S(1,\ldots,A) \prod_{j>i=1}^{A} f(r_{ij})$$

where $\Psi_S(1,\ldots,A)$ is a Slater determinant of independent particle wavefunctions, f is the two-nucleon correlation function, and r_{ij} is the distance between the ith and jth nucleons. The function f has the property of tending to 0 as $r_{ij} \longrightarrow 0$ and tending to 1 as $r_{ij} \longrightarrow \infty$, as shown, for example, in Figure 1.4. A reasonable choice of f would ensure that the function would approach 1 at a value of r_{ij} which is less than the nuclear radius. Weise and Huber write the correlation function as $f(r) = 1 - g(r)$ where g represents the the deviations from shell model behaviour. The matrix element for the interaction expands into a sum consisting of a single particle (shell) model transition amplitude and a two particle transition amplitude. The latter takes the form

$$T_{fi} = -A(A-1)\left\{\langle\psi_f\,|\bar{g}(1,2)H_{int}(1) + H_{int}(1)g(1,2)|\,\psi_i\rangle\right\}$$

where A is the mass number of the nucleus, ψ_i and ψ_f are the total initial and final state wavefunctions, H_{int} is the one body electromagnetic interaction operator and $1 - \bar{g}$ is the final state correlation function.

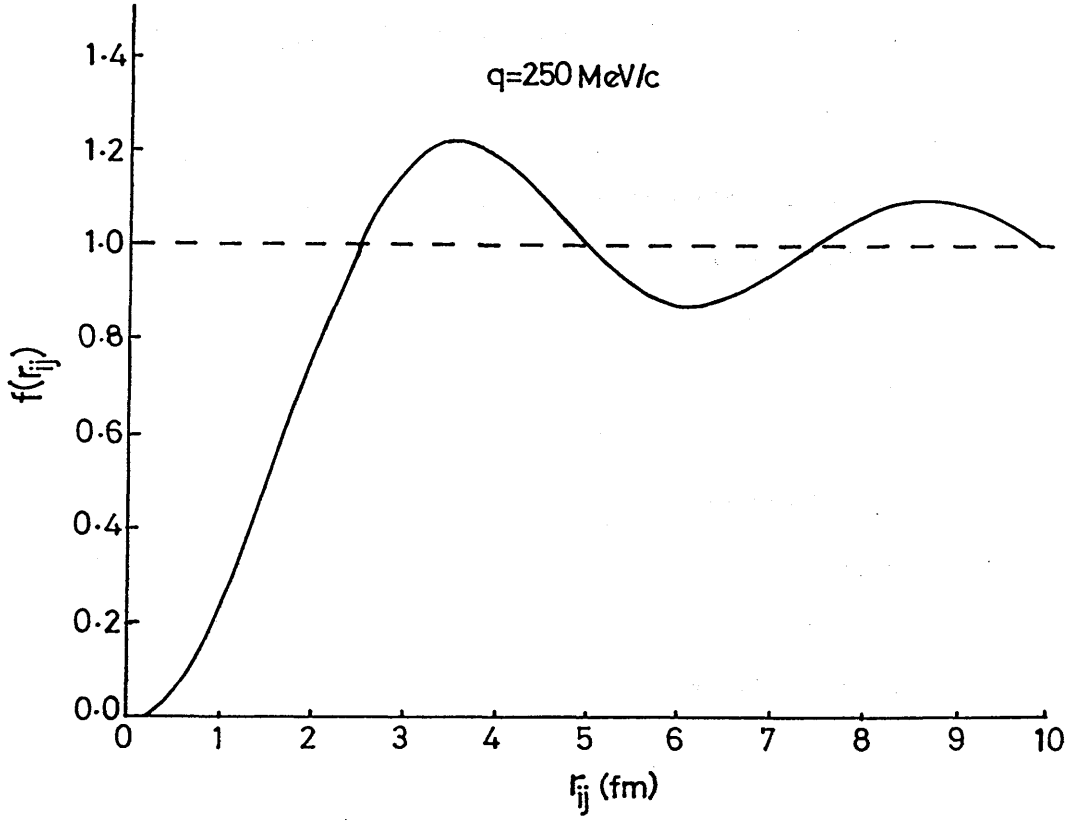

Figure 1.4: The correlation factor $1 - g(r)$ with $g(r) = j_0(qr)$ and $q = 250$ MeV/c used by Weise, Huber and Danos [19].

The initial state wave functions are calculated from a Woods-Saxon potential well which has the form

$$V(r) = \frac{V_0}{1 + e^{(r-R_0)/a_0}}$$

with parameters $V_0 = -50$ MeV, $R_0 = 3.2$ fm and $a_0 = 0.65$ fm. Optical model wavefunctions are used in the final state which account for the final state interactions. It is assumed in the calculation that $g = \bar{g}$ and that H_{int} and g commute. The correlation function $f(r)$ is simply the Fourier-Bessel transform

$$f(r) = \int w(q) j_0(qr) dq$$

of the spectrum of momenta $w(q)$ exchanged between the nucleons. j_0 is the zeroth order spherical Bessel function and is identically equal to $\frac{1}{4\pi} \int e^{iq.r} d\Omega_q$.

^{16}O(γ,pn) cross sections were calculated for nucleons in the various combinations of 1p- and 1s-shells using the form $w(q') = \delta(q') - \delta(q - q')$ which corresponds to the exchange of a definite momentum q. The most interesting results were presented as plots of σ_i/σ_{tot} versus q over the range from 0 to 600 MeV/c for various photon energies, where σ_{tot} is the total cross section for proton-neutron emission, σ_i is the cross section for proton neutron emission from a particular combination of initial shells of the nucleus, indicated by the subscript i. The contributions to the total cross section from (1p1s)- and (1s1p)-shells slowly increase with q but the shapes remain relatively unchanged as the photon energy increases. The (1p1p) contribution decreases sharply with q with slope becoming greater at higher energies. In contrast, the (1s1s) contribution increases with q and more so at higher energies. Such dependencies can be summarised in the form of missing energy spectra (Figure 1.5), where missing energy is defined as the difference between the total initial kinetic energy and the total final kinetic energy of the final state particles. For example, for 140 MeV photons and low exchange momenta emission of (1p1p)-pairs is dominant but at $q \sim 400$ MeV/c all possibilities ((1s1s), (1p1s), (1s1p) and (1p1p)) are equally likely.

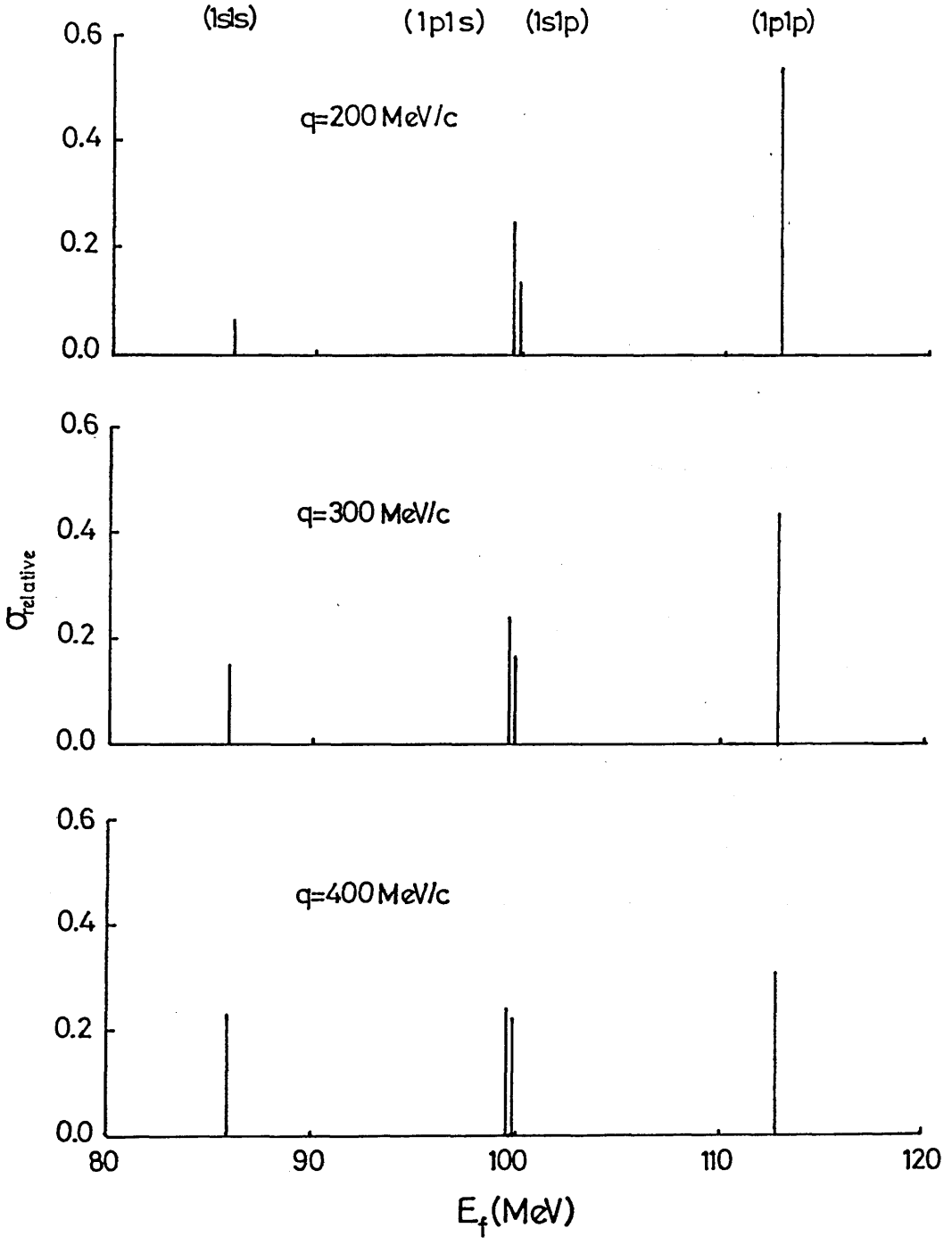

Figure 1.5: Missing energy (E_m) spectra, plotted as $E_f = \omega - E_m$, with $\omega = 140$ MeV and where E_f is the total final kinetic energy, shown for various values of q. The contributions from each 1p- and 1s-shell combination are shown separately.

The predictions of Gottfried and Weise and Huber could be tested by an experiment in which enough parameters were measured to completely determine the kinematics of the process. An experiment in which the sum of the final kinetic energies of the neutron-proton pair and **P** could be fixed, as suggested by Gottfried, is equivalent to fixing the missing energy region considered and fixing the rest frame of the quasi-deuteron. Such an experiment could compare in detail the deuteron cross section with that of a light nucleus to test the form of Equation 1.2 and would reveal the details of the nucleon correlations. The ability select a range of missing energy regions would also allow the predictions of Weise and Huber to be tested. The next section highlights the experimental developments towards this goal.

1.4 Correlated Nucleon Pairs from Bremsstrahlung

In order to clarify the relative importance of two-nucleon absorption relative to single particle absorption, programs of research into correlated nucleon emission were carried out initially by groups at M.I.T. [20,21,22,23] and Illinois [24,25]. Experiments were devised to look for neutron-proton coincidences.

The M.I.T. group, using 340 MeV bremsstrahlung, measured neutron-proton coincidences from oxygen, carbon and deuterium and showed that the angular distribution of neutrons correlated with protons of a fixed angle was narrow and centred around the neutron angle expected from deuterium photodisintegration. The widths of the distributions obtained are shown in Table 1.1. In a separate run, the ratio $\sigma_{nucleus}/\sigma_D$ was measured using a large solid angle neutron detector to detect all neutrons coincident with protons at various given proton angles. Restricting the measured proton energy range and assuming zero Q-value for the reaction, they estimated the photon energy sampled by the apparatus. The results

Nucleus	Neutron Distribution Width (°)
Deuterium	11
Lithium	30
Carbon	41
Oxygen	36
Aluminium	50
Copper	49

Table 1.1: The widths of the distributions of neutrons observed in coincidence with a proton at a fixed angle in the laboratory from ref. [22]. Bremsstrahlung from a 340 MeV electron beam was used.

were expressed as a ratio of the cross section per nucleon for oxygen and lithium compared to deuterium. According to Equation 1.1 this should give a value (with the approximation $NZ \approx \frac{1}{4}A^2$) for $\frac{1}{2}L$. The measured ratio for Li/D did not vary appreciably with angle, although the O/D ratio rose slightly at backward angles. Values of less than 1 were obtained with a lower value for oxygen than for lithium. These low values were explained by appealing to the different strengths of the final state interactions due to different nuclear volumes in each case.

Final state interactions were shown to have a marked effect on heavy nuclei. Extending the range of nuclei up to ^{207}Pb the Z-dependence of the cross section was measured. When normalised by the factor $\frac{NZ}{A}$, the ratio $\sigma_{nucleus}/\sigma_D$ was found to decrease monotonically with Z. On the assumption that the two nucleons left the nucleus back-to-back it was calculated [23] that the probability of escape of both nucleons from a given nucleus is given by

$$P(x) = \frac{3}{x^3}\left[2 - e^{-x}(x^2 + 2x + 2)\right]$$

where $x = 2R/\lambda$, $R = r_0 A^{\frac{1}{3}}$ and λ =the mean free path for absorption of the nucleons in the nucleus. Using $r_0 = 1.3$ fm and $\lambda = 3.6$ fm it was found that the corrected ratios were almost constant with Z with the Levinger parameter averaging out at a value of ~ 3.0.

Barton and Smith at Illinois carried out similar measurements on ^{7}Li and ^{4}He in which angular correlations were also observed. Values of the Levinger parameter for ^{7}Li and ^{4}He were found to be 4.1 ± 1.0 and 6.3 ± 1.0 respectively. The value for lithium was in agreement with that obtained by the M.I.T. group. Barton and Smith concluded that nearly all high energy photodisintegrations leading to the emission of a proton proceeded via a correlated neutron-proton pair. Final state interactions were estimated assuming all protons are produced as a result of photon absorption on a neutron-proton pair. In this framework the probability that one nucleon escapes is $(1 - \alpha)$, where α is the probability that a nucleon

strongly interacts on the way out of the nucleus. The probability that both escape is $(1-\alpha)^2$. Thus the ratio of (γ,pn) events to (γ,p) events gives $(1-\alpha)$. Values for α of 0.15 and 0.28 were obtained for helium and lithium respectively.

A few years later, the Glasgow group [26,27] measured angular correlations between protons and neutrons from photons in the 150–250 MeV range. Their data was analysed within Gottfried's framework. After folding in the bremsstrahlung spectrum they expressed their cross section as

$$\frac{d\sigma}{d\Omega_n} = F(P)L\frac{NZ}{A}\left(\frac{d\sigma}{d\Omega_n}\right)_d JB(E_\gamma)(1-\beta_D\cos\theta_D)d^3k_p d\varepsilon_n \qquad (1.3)$$

where $B(E_\gamma)$ is the photon spectrum, $(1-\beta_D\cos\theta_D)$ is the relativistic flux change due to the motion of the quasideuteron, and J is the Jacobian which transforms the deuterium cross section from the rest frame of the quasideuteron to the laboratory frame. $F(P)$ is the momentum distribution of the pair evaluated from harmonic oscillator shell model wavefunctions which are of the form

$$\text{1s-shell nucleons:}\quad \exp\left(-\frac{1}{2}r^2\gamma_0^2\right)$$

$$\text{1p-shell nucleons:}\quad \gamma_1 r\exp\left(-\frac{1}{2}r^2\gamma_1^2\right)$$

where γ_i $(i=0,1)$ is defined as $(M\omega_i/\hbar)^{\frac{1}{2}}$, where ω_i is the oscillator frequency. The resulting distribution for a 1p-shell proton and a 1p-shell neutron was calculated to be

$$F(P) = \left(3-\frac{P^2}{2\gamma_1^2}+\frac{P^4}{4\gamma_1^4}\right)e^{\frac{-P^2}{2\gamma_1^2}} \qquad (1.4)$$

The corresponding expression for a (1s1p) combination is

$$F(P) = \frac{\gamma_0^3\gamma_1^5}{k_{01}^{10}}P^2e^{\frac{-P^2}{2k_{01}^2}} \qquad (1.5)$$

where $k_{01}^2 = \frac{1}{2}(\gamma_0^2+\gamma_1^2)$. On integrating Equation 1.3 over the appropriate ranges of the experimental apparatus an angular distribution was obtained for comparison with the data. The Levinger parameter L was treated as a variable parameter and

used to normalise the theory with the data. The theoretical shape agreed with the data. After accounting for final state absorption as the nucleons leave the nucleus in the same manner as the M.I.T. group, an average value of 10.3 was obtained for L. The difference between this value and those obtained by the Illinois group was attributed to the different ways in which each group estimated the final state absorption. The wide discrepancy between M.I.T. and Glasgow values of L was explained by showing that the M.I.T. measurement was kinematically inefficient. Because M.I.T. assumed that both the separation energy of a neutron-proton pair and the excitation energy of the residual nucleus were zero, the estimated photon energy could have been as much as 70 MeV lower than in reality. When these effects were taken into account, Glasgow argued, the actual average photon energy required to satisfy the M.I.T. assumptions was greater than the peak energy provided by the beam. As a result, due to the bremsstrahlung spectrum shape the photon flux was actually smaller for a complex nucleus than for deuterium.

Cloud chamber experiments with photon energies up to the pion photoproduction threshold have been performed on ^{12}C by Taran [28] and Khodyachik *et al.* [29,30,31,32]. The tracks produced by charged particles enabled the experimenters to distinguish the various types of events. Khodyachik *et al* assumed that if a nucleon is removed from the 1s-shell the residual nucleus decays by the emission of an alpha particle or a proton. Such decays were separated out because of the identifiable tracks. Assuming that the ^{10}B nucleus was in its ground state, it was estimated that the energy of the initial photon could be reconstructed to within 5%.

The experiments of Taran [28] and Khodyachik *et al* [29] showed that in a large proportion of events, the neutron-proton pair carried away most of the initial energy. They compared the distribution of of the parameter t_{ij} defined as

$$t_{ij} = \left[T_i + T_j - \frac{(\mathbf{p}_i + \mathbf{p}_j)^2}{2\,(m_i + m_j)} \right] E_0^{-1} \tag{1.6}$$

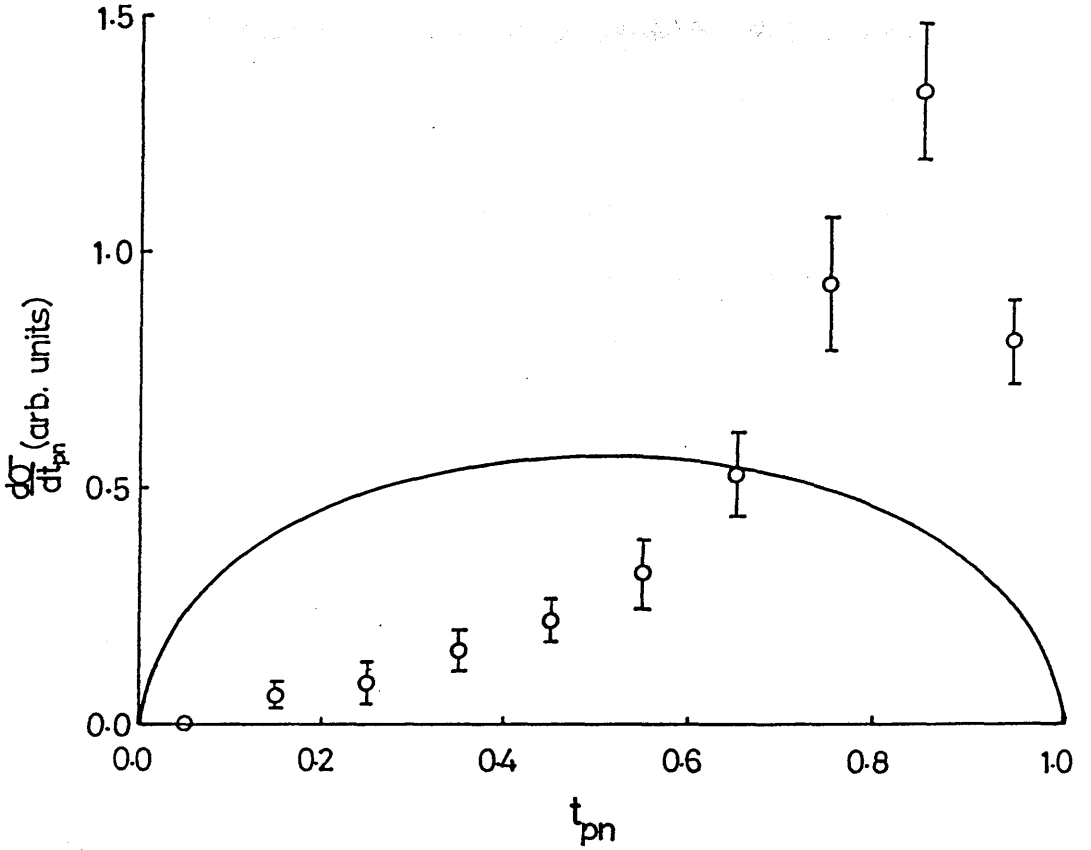

Figure 1.6: The distribution of relative energy. The data points, from ref. [29], were calculated event by event from Equation 1.6. The curve is the expected phase space distribution of Equation 1.7.

where T_i and $\mathbf{p}_i$ are the kinetic energy and momenta respectively of the emitted particle labelled i, m_i is its mass and E_0 is the sum of the kinetic energies of all the emitted particles. The distribution expected from the phase space is given by

$$\frac{d\sigma}{dt_{ij}} \propto \sqrt{t_{ij}(1-t_{ij})} \tag{1.7}$$

for three particles. The comparison is shown in Figure 1.6. The parameter t_{ij} represents the fraction of the total energy available which is carried off by the two particles in question. The t-distribution obtained for neutron-proton pairs was heavily weighted to high values of t, in contrast to the smooth phase space distribution, indicating a two-nucleon correlation in the initial state. Taran had illustrated this effect in a previous paper but with poorer statistics and showed in addition that at energies well above the Giant Dipole Resonance there was no correlation of each nucleon with the residual nucleus and that the relative energy distribution agreed with the phase space prediction.

Data obtained by Khodyachik *et al* showed that, in the centre of mass frame of the photon-nucleus system, the angular distributions of both nucleons became progressively more forward peaked with increasing photon energy, while the recoil ^{10}B became backward peaked showing an increasingly direct interaction with a correlated neutron proton pair. The quasideuteron momentum was deduced from the recoil nucleus momentum by assuming a direct interaction such that $\mathbf{P} = -\mathbf{P}_{recoil}$. In the laboratory frame the distribution of $\mathbf{P}$ was shown to be isotropic. In the photon-quasideuteron system at higher energies the angular distribution of protons followed the shape of the deuteron calculations of Partovi [33].

The absolute values of the cross sections presented, however, should be questioned since it was assumed by Khodyachik *et al* that the events excluded on the grounds of the decay characteristics of the residual ^{10}B arose from emission of 1s-nucleons. It is known [34] that excited states from $\sim$ 4.8 MeV upwards decay by the emission of an alpha particle so that many (1p1p) events would be excluded.

All the experiments discussed in this section verified that correlated neutron-proton pairs are emitted from nuclei when photons interact with them. The kinematics have been shown to be similar to those of deuterium but smeared out by the motion of the centre of mass of the pair in the nucleus. The reaction has been shown to become more direct with increasing photon energy and there is evidence that the cross sections are roughly proportional to that for deuterium. However, all experiments have relied on some assumption about the excitation of the residual nucleus and the separation energy of a neutron-proton pair since not enough experimental parameters were measured. The uncertainty in energy amounts to several tens of MeV. An uncertainty of this magnitude precludes the possibility of a detailed investigation of the quasideuteron effect. For example, correlations between nucleons within particular shells are impossible to quantify since the energy spacings of the shells are far less than the uncertainty. Determination of the photon energy would significantly improve matters since, if the kinematical variables of both nucleons are measured, the kinematics would be completely determined.

1.5 (γ,pn) Experiments with Tagged Photons

It is relatively straightforward to make a charged particle beam, such as an electron beam, monoenergetic. However, a monoenergetic source of photons, unlike other electromagnetic probes, is difficult to produce. There are three techniques which have been developed to produce "quasi"-monoenergetic photon beams:

1. Positron annihilation-in-flight. An electron beam is passed through a high Z converter creating a beam of positrons. These are momentum analysed and passed through a low Z material in which they annihilate with atomic electrons, producing two photons of equal energy in the centre of mass frame. In the laboratory frame one is observed as a high energy "hard" photon which goes on to interact with the target, and the other, low energy "soft" photon

is detected in coincidence with the reaction products to improve the energy resolution.

2. Laser backscattering. In this technique photons from a laser are collided with a high energy electron beam. The photons are Compton scattered into the direction of the electron beam due its centre of mass motion. Energy determination is improved by detecting the scattered electron in coincidence with the reaction products.

3. Bremsstrahlung radiation. A primary electron beam is passed through a material to produce bremsstrahlung photons. The photon energy is determined by measuring the scattered electron energy in coincidence with the reaction products.

All three methods are examples of the use of "tagged" photons in which some other particle involved in the photon production process is measured and which characterises the photon energy. The photon flux which can be used depends on the efficiency of the tagging detector used. The photon energy resolution depends on the energy resolution of the tagging detector. The last method is relatively easy and cheap, and is becoming the most widely employed method.

The method of tagging photons with the bremsstrahlung scattered electrons has been known for nearly thirty five years. The attempt of Weil and McDaniel [9] to measure single arm (γ,p) cross sections was hampered by the poor coincidence electronics available at the time. The fact that the accelerator had a very low duty cycle meant that to get a reasonable average photon intensity the instantaneous intensity of each beam pulse had to be very much higher. Such high intensities produced an unacceptably high random coincidence rate. As a result the photon intensity actually used was very low. They achieved a photon energy resolution of 60 MeV at 190 MeV . Cence and Moyer [35], in a similar experiment at higher

photon energies, achieved a resolution of 30 MeV at 245 MeV and a photon rate of $3 \times 10^5 s^{-1}$. However their proton production rate of two protons per hour was very poor.

Recent (γ,pn) experiments with tagged bremsstrahlung photons are scarce although new tagging systems are becoming available. Above the pion threshold the Bonn group [36] have investigated the ^{12}C nucleus with tagged photons in the 200–385 MeV energy range with 10 MeV resolution. They achieved a tagged photon rate of $\sim 3 \times 10^5$ s^{-1}. Protons were measured using a magnetic spectrometer which accepts protons with momenta between 100 and 800 MeV/c. Neutral and charged particles were detected on the opposite side in a system of E and ΔE scintillation counters. Single arm proton spectra measured over angles from 44°–130° showed a slowly decreasing cross section from threshold to the maximum proton energy with no outstanding features. (Endpoint peaks disappear above $E_\gamma \approx 100$ MeV [37].) However, spectra of protons which were coincident with pions showed that they contribute to the low energy part of the spectrum. Protons coincident with neutrons or protons in the scintillator arm are seen to contribute to the higher energy end of the spectrum.

Similar data were obtained by Homma *et al.* [38,39,40,41] for a range of nuclei from ^1H to ^{16}O. They measured proton spectra at 25° and 30° only, and over the photon energy range 180–420 MeV, extending to 580 MeV for ^{12}C. A magnetic spectrometer measured the proton momenta. An array of E-ΔE scintillators on the opposite side measured charged particles and neutrons as in the Bonn measurement. Unlike the Bonn group, they observed that the proton spectra had two broad but clear peaks (see Figure 1.7). The proton data in coincidence with a charged particle in the scintillator array drastically reduced the number of counts in the higher energy peak while only halving the lower energy one. After performing experiments on ^1H (to investigate the low peak) and on ^2H (to include

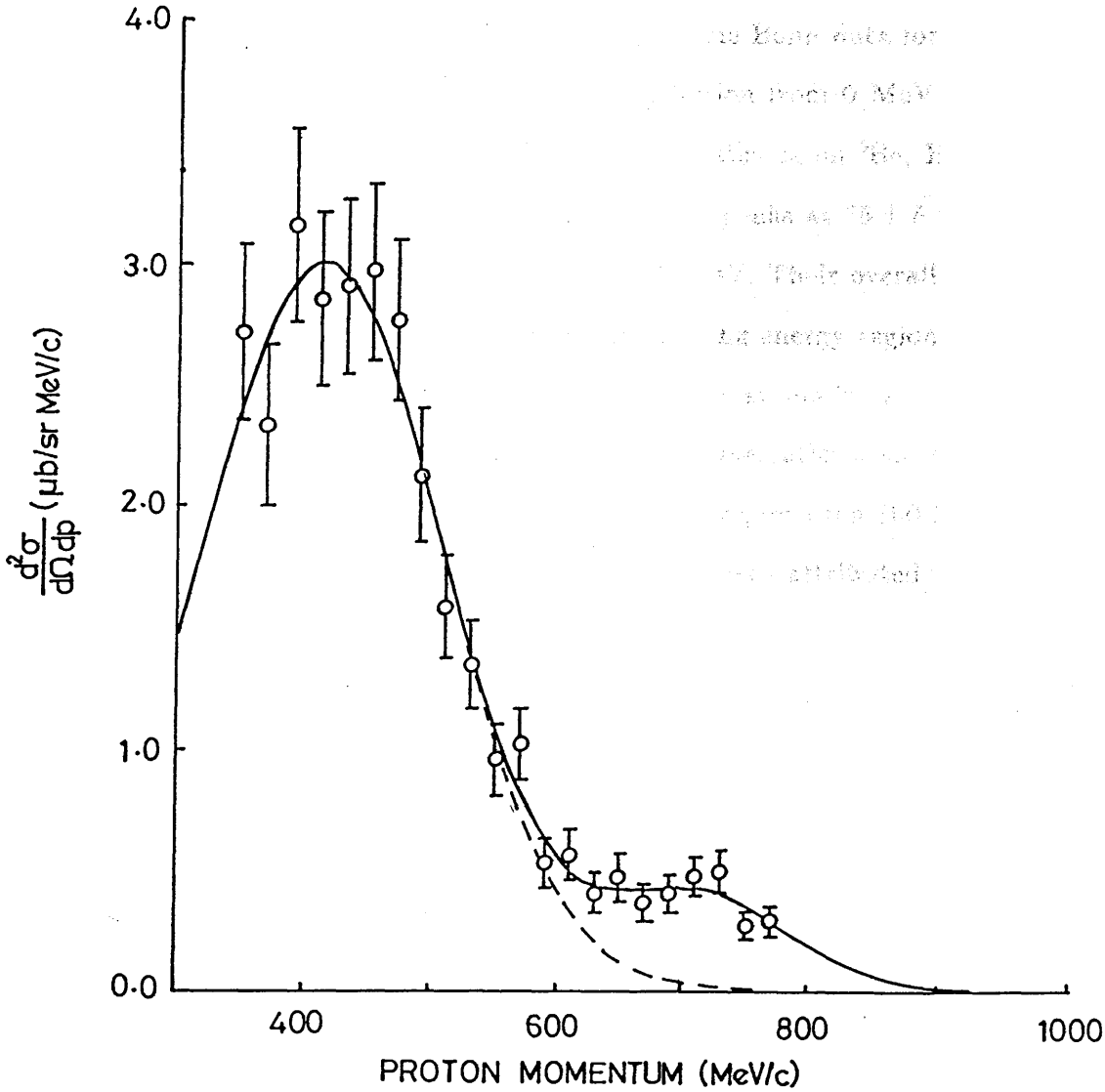

Figure 1.7: Momentum spectrum of protons at a laboratory angle of $25° \pm 5°$ in the reaction $\gamma + {}^{12}C \rightarrow p+$ anything. The data are from ref. [39]. The curves are fits to the data using two Gaussian distributions.

the higher peak) the peaks were interpreted as arising from pion production on quasi-free nucleons (low peak) and two nucleon emission from a quasi-free nucleon-nucleon pair (high peak).

Missing energy spectra for the (γ,pn) process, shown in Figure 1.8, have been produced by both the Bonn and Tokyo groups. The Bonn data for ^{12}C over the range E_γ =353–397 MeV shows a broad distribution from 0 MeV to 300 MeV missing energy with no structure. With better statistics on ^{9}Be, Homma *et al.* show that for $E_\gamma = 247 \pm 60$ MeV the distribution peaks at 35 ± 5 MeV missing energy with a tail in the distribution up to 150 MeV. Their overall energy resolution was $\sim$ 34 MeV. Selecting events in the missing energy region 0–100 MeV, they show that the neutron angular distribution for events in which $\theta_p = 30°$ is centred around the angle expected from deuterium kinematics with width of $\sim 50°$ FWHM . However, for events with missing energy greater than 100 MeV no such correlation is found. Such a loss in the correlation was attributed to final state interactions. The momentum distribution of the initial p-n pair for events with missing energy less than 100 MeV is fitted with a Monte Carlo calculation. The momentum of the pair is calculated from the sum of the momentum vectors of each nucleon. The choice of these vectors is weighted by the individual nucleon momentum distributions obtained from harmonic oscillator shell model momentum wavefunctions. A good fit is obtained using an oscillator parameter of 80 MeV/c.

Intermediate energy (γ,pn) data with tagged photons is just becoming available. The Sendai group [42] have irradiated ^{10}B with 63–103 MeV photons from their tagging system [43], detecting protons in four E-ΔE-ΔE scintillation counters and neutrons in liquid scintillator time-of-flight detectors. Charged particle veto counters were placed in front of the neutron detectors. Only a distribution of the opening angle between the p-n pairs for all the events in the 63–103 MeV photon energy range is presented. The spectrum shows a peak of width $70° \pm 10°$

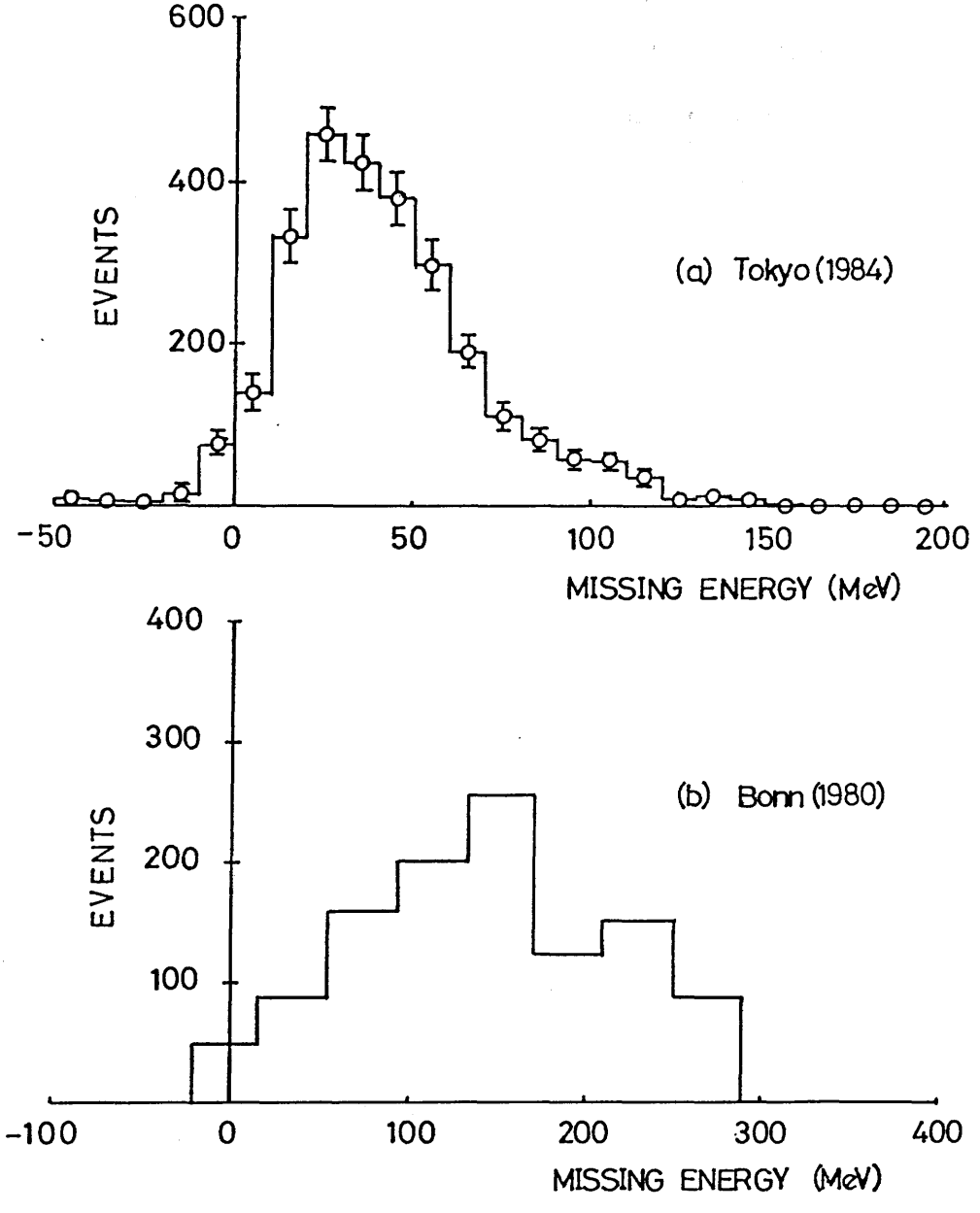

Figure 1.8: Missing energy spectra for the (γ,pn) reaction. (a) Data from ref. [40] taken at $\omega = 247 \pm 60$; (b) data from ref. [36] at ω = 353–391 MeV.

FWHM centred around 180°. Integrating over the distribution and dividing the result by a neutron transparency factor of 0.5 to account for neutron absorption, a cross section for the (γ,pn) was obtained. When compared with the ^{10}B(γ,p) cross section data collected simultaneously for protons in the missing energy range 20–50 MeV (where missing energy is defined as $E_m = E_\gamma - T_p - T_R$ and T_R is the recoil nucleus energy) the (γ,pn) cross section is shown to contribute nearly all of the (γ,p) cross section.

Although the Bonn and Tokyo data are taken at considerably higher energies than those relevant to this thesis, the experiments show the advantages of a system which fully determines the kinematics. Missing energy spectra have been shown but their use is limited in determining the original shells from which the nucleons came because of the poor overall energy resolution. Tokyo have illustrated the possibility of determining the momentum distribution of the initial proton neutron pair. A distribution for deuterium data would have been useful in assessing the pair momentum resolution. The data of the Sendai group, although determining the photon energy per event, are not greatly improved on previous measurements since they did not measure the neutron energy.

1.6 Other Related Experiments

In this section some attention is given to the related photon induced reactions (γ,p) and (γ,n). Often the (γ,p) reaction has been furnished with a theoretical treatment which "explains" the data. However, in some treatments, the success is not repeated when they are applied to other photonuclear reactions. As pointed out by Gari and Hebach [44], it is relatively easy to provide an explanation of one kind of photonuclear reaction on its own. It is more difficult to find a simultaneous understanding of several types of reaction. It would be expected that (γ,p) and (γ,n) reactions would require similar theoretical treatments to that of (γ,pn) and

that similar questions would arise. Attention is also given in this section to the pion induced reactions ($\pi^{\pm}$,NN) for which there is ample evidence of interactions with two nucleons, and which are similar in some respects to (γ,pn) reactions.

1.6.1 The (γ,N) Reactions

Due to experimental difficulties in working with photon sources and in creating the required fast electronic coincidence circuits, emphasis in the 1970's was placed on single arm (γ,p) and (γ,n) experiments. In (γ,p) particular attention was paid to the top end of proton spectra obtained from fixed E_γ data, where a simple interpretation suggests itself. Data from Matthews *et al.* [45] for various light nuclei reveal peaks in the proton spectra from 60 MeV photons which are interpreted as direct knockout of protons from particular shells, leaving the residual nucleus in its ground state or an excited state. Work by the Turin group [46,47,48] showed similar effects. When a simple shell model calculation is carried out assuming a plane wave for the outgoing nucleon wavefunction it turns out that the cross section may be written as

$$\frac{d\sigma}{d\Omega} = C|\phi(q)|^2 \tag{1.8}$$

where C is dependent solely on the reaction kinematics and $\phi(q)$ is the momentum space wavefunction of the bound proton. Consequently, cross section measurements should reveal valuable information regarding proton momentum distributions, and in particular, regarding the high momentum components of the wavefunction which were found necessary to explain the results of earlier experiments.

Considerable confusion has arisen since the (γ,p_0) calculation (where the subscript $_0$ indicates that the residual nucleus is left in its ground state) is sensitive to the initial and final state potentials used (viz. the results of [49,50,51,52,53,54]). In addition, Fink *et al.* [55] cast doubt on many final state wavefunction approxi-

mations concluding that violation of the orthogonality of the initial and final states could affect the resulting cross section by up to two orders of magnitude. Findlay *et al.* [56,57] using a consistent set of initial and final state wavefunctions from an Elton-Swift [58] potential show that the momentum distributions can be explained up to ~450 MeV/c. Extending the ^{16}O data [59,60] to 930 MeV/c missing momenta, the Glasgow-MIT group showed that the calculated distribution falls off faster than the data such that at 700 MeV/c the calculation is two orders of magnitude too low.

Shell model calculations fail, however, to explain (γ,n_0) reactions in any kinematic region since, in this picture, the photon can only couple to the magnetic moment of the neutron, thus predicting a very small cross section compared with (γ,p_0). The Mainz group [61,62,63,64] have made extensive measurements of the (γ,n_0) reaction in the 60–160 MeV photon energy range. The data show that the cross sections are comparable in magnitude with those for (γ,p_0) (Figure 1.9). Sené *et al.* [65,66] made a direct comparison of both reactions on ^7Li by measuring the recoil ^6He and ^6Li nuclei. They found their cross section ratio $\sigma(\gamma,n_0+n_2)/\sigma(\gamma,p_0)$ (where the subscript $_2$ indicates that the residual nucleus is left in its second excited state) to be between 1.5 and 2.0, or $\sim$ 1 per (γ,n) channel.

The failure of the shell model in explaining the (γ,n) reaction can be traced back to the shell model assumption that the particles move independently in an average potential. Levinger and Gottfried found it necessary to introduce the idea of strongly-interacting, non-independent nucleons in the nucleus since it was recognised that such effects exist and that the photon field would probe them. Weise and Huber [67,68] extended their treatment of (γ,pn) reactions to (γ,N) reactions, in which correlations are accounted for using the Jastrow formalism. The introduction of correlations automatically ensures the enhancement of the (γ,n) cross section since neutrons are then involved in the absorption process.

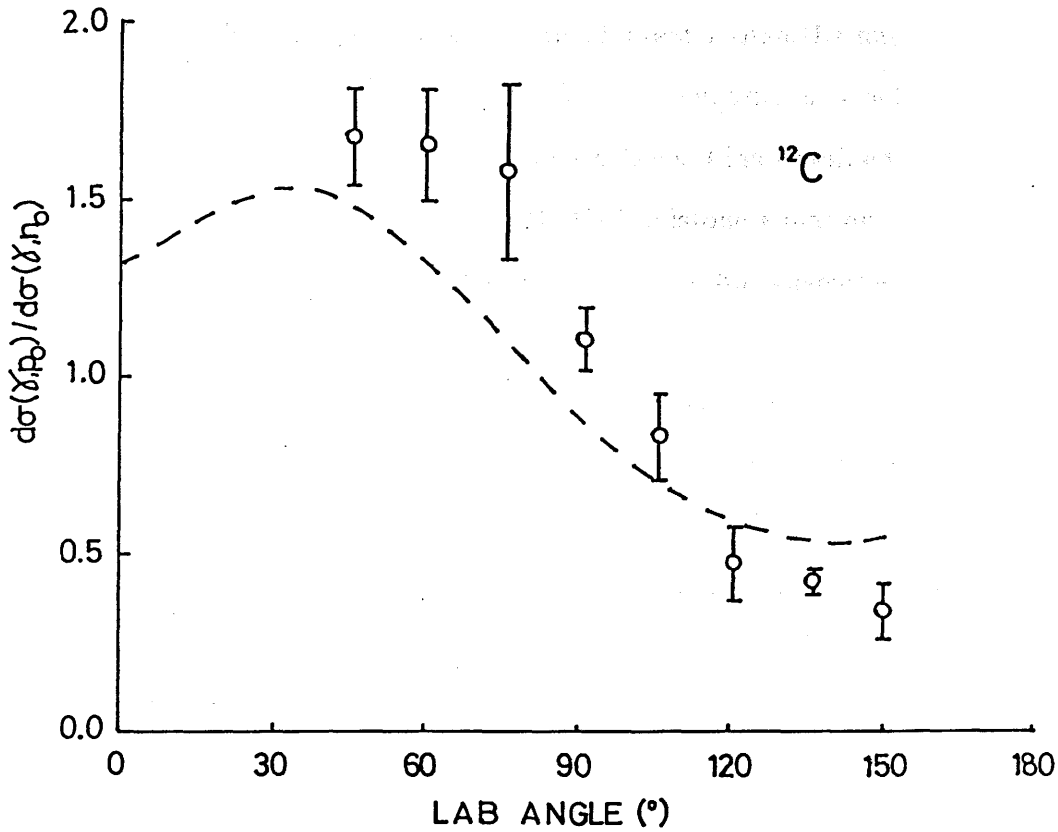

Figure 1.9: The ratio $\sigma(\gamma, p_0)/\sigma(\gamma, n_0)$ for ^{12}C [63] with a photon energy $\omega = 60$ MeV. The dashed curve is the MQD calculation of Schoch [3].

Weise and Huber found good agreement with both (γ,p_0) and (γ,n_0) measured cross sections with q = 250 MeV/c, although experimental data was scarce at the time, concluding that the contribution to the cross section from correlations was dominant.

The calculation was severely criticised by Fink *et al.* [55], pointing out that for q = 250 MeV/c, the function $1 - j_0(qr)$ had a healing distance (the distance at which the function becomes close to 1) much greater than the nuclear size and as such had little to do with short range effects. Even with q = 500 MeV/c the healing distance is comparable with the nuclear size. Fink obtained a more realistic correlation function by solving the Bethe-Goldstone equation. It contained momentum components between 400 and 1200 MeV/c but gave cross sections for (γ,n) which were at least an order of magnitude too small.

Schoch [3], in an attempt to explain ^{16}O(γ,p_0) and ^{16}O(γ,n_0) reactions, resurrected and modified the quasideuteron model. In his picture the reaction proceeds via a primary absorption on a neutron-proton pair followed by the emission of one particle. The other particle is reabsorbed into the same initial state. The cross section for (γ,p) (with a similar expresion for (γ,n)) is written as

$$\frac{d\sigma}{d\Omega}(\gamma,\mathrm{p}) = L\frac{Z_s N^2}{A}\left[\frac{d\sigma}{d\Omega}(k_\gamma,\theta_p)\right]_d P_s \left|\int d^3k_p \phi(k_p) F^{A-1}(q)\right|^2$$

where L is the Levinger parameter, Z_s is the number of protons in the active sub-shell, N is the number of neutrons in the nucleus, A is the atomic number of the nucleus and P_s is a phase space factor. $\left[\frac{d\sigma}{d\Omega}(k_\gamma,\theta_p)\right]_d$ is the centre of mass deuterium cross section , $\phi(k_p)$ is the momentum space wavefunction of the bound state proton calculated from an harmonic oscillator potential, and $F^{A-1}(q)$ is the elastic form factor of the residual nucleus taken from elastic electron scattering data [69]. After multiplying the result by a factor 0.4 to account for final state absorption, good qualitative agreement was found with the available data.

Sené, applying the calculation to the ^{7}Li nucleus found the correct angular and

photon energy dependence to within a factor two. The angular and photon energy dependence of the cross section ratios were also reproduced. It was concluded that photon absorption on two nucleons is probably dominant, considering the success of the MQD model in roughly fitting the (γ,p) and (γ,n) data.

Gari and Hebach [44] provide an explanation of the success of the quasideuteron models by including electromagnetic interactions with the charge currents arising from the exchange of mesons between the nucleons. The nuclear current density is determined through the charge conservation equation

$$\nabla.\mathbf{J}(\mathbf{r}) + \frac{i}{\hbar}[H, \rho(\mathbf{r})] = 0$$

where $\mathbf{J}(\mathbf{r})$ is the nuclear current operator, $\rho(\mathbf{r})$ is the nuclear charge density operator and H is the nuclear Hamiltonian. $\mathbf{J}(\mathbf{r})$ can be split into one-, two-, ... body operators. Thus the charge conservation equation can be separated into one and two body parts (neglecting higher order parts)

$$\nabla.\mathbf{J}_{[1]}(\mathbf{r}) + \frac{i}{\hbar}[T, \rho(\mathbf{r})] = 0$$

and

$$\nabla.\mathbf{J}_{[2]}(\mathbf{r}) + \frac{i}{\hbar}[V, \rho(\mathbf{r})] = 0$$

with $H = T + V$ where V is the nucleon-nucleon interaction and T is the nucleon kinetic energy operator. It is clear that the choice of the interaction V determines what the exchange currents are. Gari and Hebach found the electromagnetic interaction with these currents to dominate the cross section when a Yukawa type nucleon-nucleon interaction is used. The MQD model "works" essentially because all such contributions to the cross section, including the Δ degrees of freedom found at higher photon energies, are gathered together under the umbrella of the deuteron cross section.

The MQD model assumes that all primary absorption takes place on correlated neutron-proton pairs. The extent to which this is true is uncertain. Boffi *et al.*

[71] have suggested that measurements with polarised photons would go some way towards resolving the problem since quite different behaviour is expected for the direct knockout and quasideuteron mechanisms.

Consideration of the endpoint (γ,p_0) and (γ,n_0) reactions together have led to the conclusion that a nuclear model which ignores interactions between the nucleons in the initial nuclear state fails to explain all of the magnitude of the cross sections obtained. The (γ,n_0) cross section is particularly difficult to obtain theoretically. Only with the inclusion of some form of correlation, perhaps of the Jastrow type, or which involves the effect of interactions with exchanged mesons, can a more satisfactory agreement with the data be found.

1.6.2 The ($\pi^{\pm}$,NN) Reactions

Data from the absorption of charged pions in nuclei [72,73,74,75,76,77] provide further evidence of nucleon-nucleon correlations. As in the case of a photon, the pion provides a large amount of available energy, through its mass, in comparison to a small momentum, such that it shares its energy with two nucleons. Data on π^- absorption on ^{6}Li [74] show that ~70% of the absorption cross section proceeds by emission of two neutrons. The remaining 30% involves either absorption on clusters of nucleons or absorption via multistep processes (final state interactions). Both the (π^-,nn) and the (π^+,pp) reactions show fairly tight angular correlations about an opening angle of 180° between the emitted nucleons indicating correlations in the initial state. Experiments which completely determine the reaction kinematics have been able to examine the final states of the residual nucleus. The results from 1p-shell nuclei show that absorption on (1p1p) pairs is dominant with a little evidence of higher excitations.

A theoretical description of the data suffers from the fact that three strongly interacting particles are involved in the initial state. Such interactions of pion fields are poorly understood, in contrast to the electromagnetic interaction. Con-

sequently, it is difficult to disentangle the interaction of the pion with the nucleon pair from the interactions of the nucleons among themselves. Pion absorption measurements have, as a result, emphasised the interaction of pions with nuclear matter rather than the details of short range correlations in nuclei.

1.7 This Investigation

The present experiment is one of the first (γ,pn) experiments carried out using the tagged photon system developed at Mainz. This measurement, along with a similar experiment on ^{6}Li [78], marks the first of a series of investigations into short range nucleon-nucleon correlations. The objectives of the present experiment are twofold. Firstly, to establish a system which makes significant improvements upon previous attempts to measure photonuclear reactions and, in particular which exposes the photonuclear region between the Giant Dipole Resonance and the Δ-resonance to detailed investigation. The second aim is to make some preliminary investigations into the dynamics of the reaction.

Many of the problems which hindered or obstructed previous authors have been overcome or improved upon. The prohibitively low duty cycles encountered by others are eliminated in using the Mainzer Microtron (MAMI). The large number of passes through the MAMI end-magnets ensures excellent primary beam energy resolution. A purpose-built tagged photon spectrometer and detector measures the photon energy to within ± 0.3 MeV, with a large number of elements in the detector ensuring a high tagged photon rate. The detection apparatus allows complete determination of the kinematics of the (γ,pn) reaction, including the reconstruction of the recoil nucleus momentum as well as its excitation energy. The resolution of the nucleon detectors is sufficient, unlike previous measurements, to determine the shells (although not the subshells) from which the nucleons are ejected and to determine the recoil nucleus momentum to within 30 MeV/c. Detailed descriptions

of the apparatus are given in the next chapter.

From the data it will be possible to check the experimental results of previous authors. It will also be possible to specifically compare the momentum distribution of (1p1p) neutron-proton pairs with the calculations of Gottfried, and to make some qualitative deductions from the (1p1s) data obtained. The shape of the missing energy spectrum may make it possible to test the theory of Weise and Huber. Evaluations of the Levinger parameter L, which contains the effects of short range correlations, and its variation with nucleon angles and photon energies, will be presented.

Chapter 2

The Experimental System

2.1 Overview

The present experiment was carried out using the racetrack electron microtron situated at the Institut für Kernphysik, Universität Mainz, West Germany. The Mainzer Mikrotron (MAMI) [88,89] is a continuous beam facility which provided a 183.47 MeV energy beam for the current experiment. The complete system shown in Figures 2.1 and 2.2 was designed with a view to completely determining the kinematics of the (γ,pn) reaction under study.

The beam is transported from the accelerator hall through a thick concrete wall into the switchyard where the experiment is set up. A bremsstrahlung radiator intercepts the beam a few centimetres before the tagged photon spectrometer producing bremsstrahlung radiation which is collimated before reaching the target. The recoil electrons are momentum analysed by a magnetic spectrometer and detected by a scintillator array in its focal plane which yields photon energy information. The spectrometer system also serves to remove both electrons which do not radiate and the large number of electrons corresponding to the low energy region of the bremsstrahlung spectrum. These are transported to a Faraday cup $\sim$ 20 m downstream from the spectrometer. The collimated photon beam impinges on the target producing neutron-proton pairs through the (γ,pn) reaction. Protons are detected using a large solid-angle E-ΔE_1-ΔE_2 scintillator telescope [87] which covers an angular range from 50° to 130°. Neutrons are detected by an array of plastic scintillator blocks which cover an angular range of 52.5° to 127.5°. Each array produces analogue charge signals and digital timing signals which after processing by electronics are stored temporarily in CAMAC analogue-to-digital converters (ADCs) and time-to-digital converters (TDCs). A data aquisition computer reads the data and stores them on magnetic tape for later off-line analysis. The signals yield energy, position and particle identification information for each event. In total, up to 86 pieces of information in up to 176 bytes are stored per

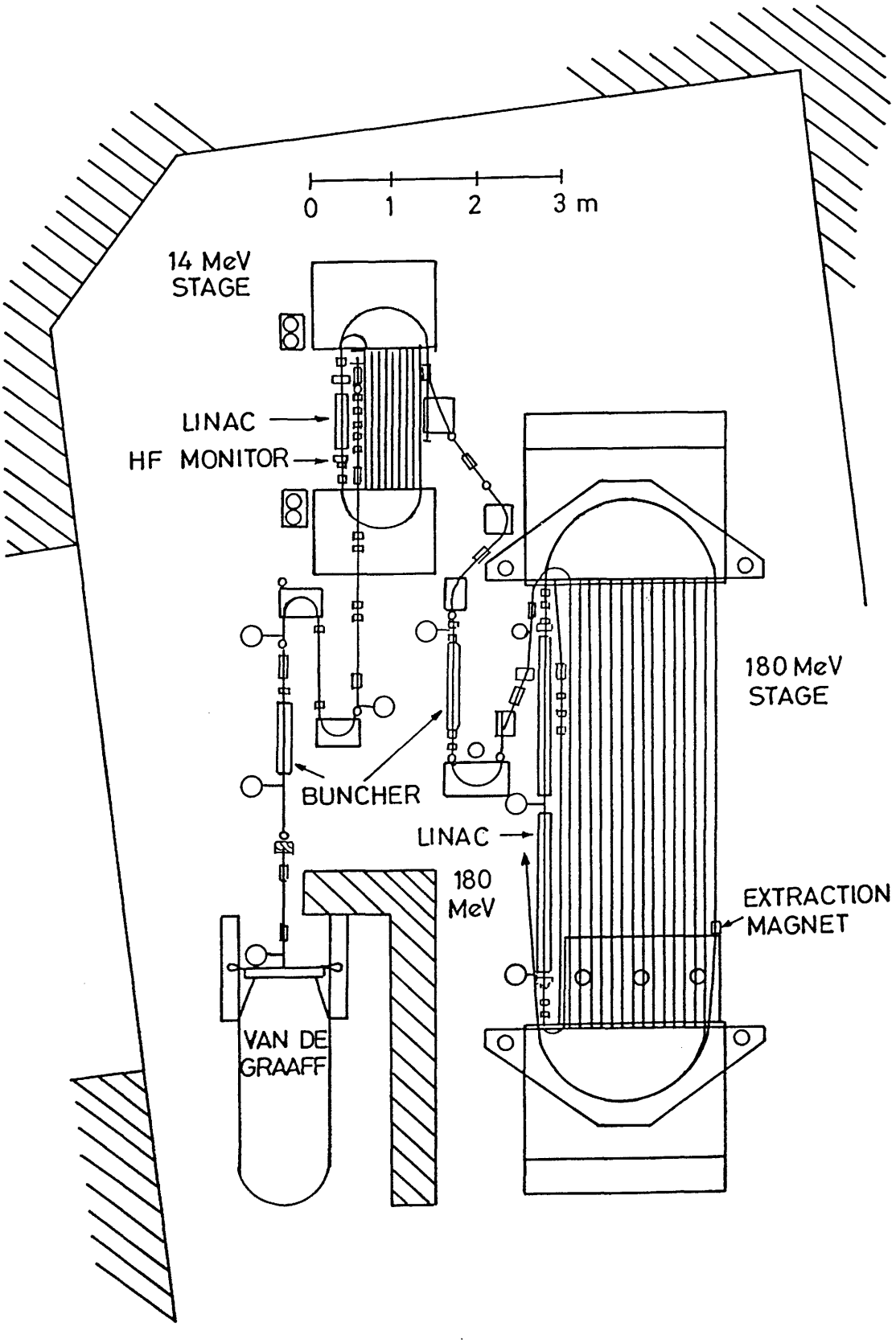

Figure 2.1: Scale diagram of MAMI accelerator layout.

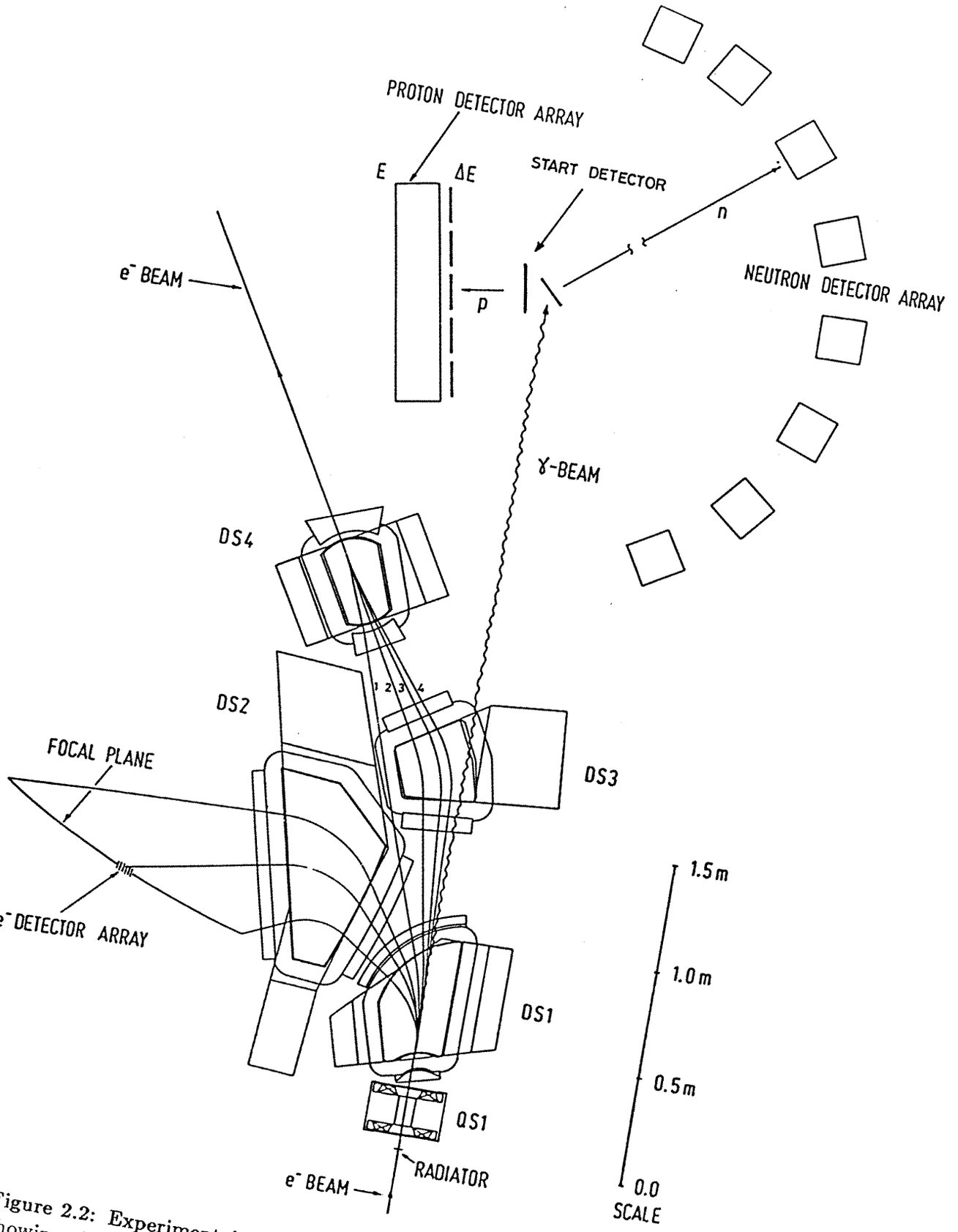

Figure 2.2: Experimental system downstream from the bremsstrahlung radiator showing the tagged photon spectrometer, and the neutron and proton detector arrays. The square detector position is not shown.

event.

2.2 The Accelerator

The use of continuous beam accelerators has proved to be essential in coincidence experiments using tagged photons. Previously, as discussed in Chapter 1, tagged photon experiments have been attempted with low duty cycle machines [9,35,36] which in normal operation produce a pulsed beam. Problems of pile-up in the detectors and a high random to real coincidence ratio proved to be a hinderance. However, a microtron avoids these problems as the instantaneous current is always low and the random to real coincidence ratio becomes manageable.

The principle of operation of a microtron is to recirculate electrons through a linac section many times, giving them a small increase in energy each time and extracting the beam at the required energy. The recirculation is achieved using two large end magnets each of which takes the beam through a 180° bend. In giving only a small amount of energy to the beam in this way the linac section can be operated continuously at low power, resulting in a 100% duty cycle.

A Van de Graaff preaccelerator injects a 2.1 MeV electron beam into the first stage of MAMI. The first stage is a small injector microtron in which the beam passes through the linac 20 times gaining 0.6 MeV per turn and finally emerging with 14 MeV. Between the Van de Graaff and the first stage is a buncher which adjusts the electrons' phase in line with the linac section of the microtron. The beam is transported $\sim$ 4 m by means of steering magnets through a further buncher to a second microtron which has up to 51 turns before extraction. The final beam is extracted using a moveable extraction magnet. It is housed in an evacuated extraction chamber into which the beam pipes on the "back straight" enter 2 m before entering the bending magnet. The extraction magnet can be placed over the pipe from which the beam is to be extracted and deflects the beam inwards

slightly such that it exits from the bending magnet at a slight angle. The beam does not reenter the linac but is transported by steering magnets away from the microtron. Quadrupoles focus the beam before it reaches the experimental area.

The design of MAMI is such that each loop of the beam in both microtron stages can be individually guided. The separation between each loop in both stages is sufficient for horizontal and vertical steering coils to be placed at both the beginning and the end of each "back straight". RF resonant cavities are situated before and after the linac in the "home straight" to monitor beam position and the phase of the beam microstructure when setting up the system. During the setting up procedure, the beam from the Van de Graaff is pulsed at a frequency of 10 kHz with a pulse length of 12 ns. This is sufficient for each beam pulse to pass through the entire accelerator before the next one is produced and for the RF cavities in both stages to resolve the signal from all the orbits between each pulse. The system is interfaced to an HP1000 microcomputer which optimises the RF power and phase and the steering coils automatically.

Although MAMI can produce up to 100 μA of current, limitations on the counting rate of the focal plane detector (FPD) restricts the beam to ~50 nA for tagged photon experiments. Because the beam passes many times through steering magnets the beam is extremely well momentum analysed. In this experiment the final beam was extracted from the 51st orbit giving an energy of 183.47 MeV $\pm$18 keV.

2.3 The Bremsstrahlung Radiator

The primary electron beam impinges on a bremsstrahlung radiator mounted in a radiator changer [81] 45 cm before the spectrometer dipole magnets. This consists of a wheel which rotates about an axis parallel to the electron beam line and vertically above it. There are sixteen positions in total of which nine

house radiators of various thicknesses and materials. An aluminium oxide screen is also mounted for beam position monitoring as well as a pair of crosswires for alignment purposes. A blank position is available to allow beam transport to other experiments when the tagged photon system is not in use. The wheel is driven by a stepping motor which provides 8000 angular positions. The required position can be selected remotely from the control room by entering the appropriate number of steps into the controller module. The wheel position is displayed by means of a counter, and an encoder checks that the number of steps requested has been executed correctly. If the wheel is rotated consistently in only one direction the position is reproducible to within one step. This corresponds to ± 0.15 mm at the beam line. The wheel can also be reset to a zero position by means of a 1mm pin hole in the wheel in conjunction with a red LED and photodiode detection system mounted in the wheel housing. This too is accurate to within one step.

An aluminium radiator was used and was available in thicknesses from 3 μm up to 100 μm. In a thin radiator there is less likelihood of multiple scattering of the electrons thus keeping the half-angle of the bremsstrahlung cone close to its intrinsic value. This is valuable in keeping the tagging efficiency high (see Section 2.9) but is at the expense of a low photon flux per unit primary beam flux. The effect can be compensated for by increasing the primary beam current. However, considerable background radiation is emitted from the Faraday cup which is only partially shielded by concrete. A reasonable compromise seemed to be to choose a 25 μm radiator which corresponds to 2.8×10^{-4} radiation lengths.

2.4 The Tagged Photon Spectrometer

After passing through the radiator the beam enters the tagged photon spectrometer system. The details of its design and performance are reported in [90]. However, a brief description is given here.

The necessary requirements of the magnet system are twofold. Firstly, as a spectrometer, it is required to momentum analyse recoil electrons which have produced bremsstrahlung radiation and hence to measure their energy. The energy of the corresponding photon can be simply determined through the expression $E_\gamma = E_0 - E_{recoil}$ where E_0 is the primary electron energy and E_{recoil} is the recoil electron energy. In this way the photon is said to be "tagged" by the electron. Its secondary requirement is to handle the non-radiative part of the beam, removing it from the experimental area to the beam dump. The spectrometer is installed as an integral part of the beam line, forming part of the beam handling system used by other accelerator users and so easily fulfils this latter requirement.

The magnet system designed to achieve the above requirements is shown in Figure 2.2. The spectrometer is arranged in a QDD configuration and has the following properties:

1. A momentum acceptance of $p_{max} : p_{min} = 2 : 1$.
2. An angular acceptance of 55 mrad for those electrons within this range.
3. Energy resolution of $\sim 10^{-3}$.
4. Compactness allowing the target to be reasonably near the bremsstrahlung radiator.

Focussing the quadrupole QS1 in the non-bend plane has the important effect of increasing the acceptance solid angle. The field strengths of DS1 and DS2 are always set in the same ratio and together analyse the bremsstrahlung scattered electrons. Different parts of the bremsstrahlung spectrum can be tagged by changing these field settings. For an electron beam of 183.47 MeV the 83.47–177.22 MeV photon energy range can be tagged in four spectrometer settings as shown in Table 2.1. Altering the energy range of detected electrons, however, alters the exit angle of the main beam from DS1 making removal of the main beam more complicated.

Trajectory	E_{recoil}^{max}	E_{recoil}^{min}	E_{γ}^{min}	E_{γ}^{max}
1	100	50	83.47	133.47
2	50	25	133.47	158.47
3	25	12.5	158.47	170.97
4	12.5	6.25	170.97	177.22

Table 2.1: Tagging spectrometer energy ranges for an incident electron beam energy of 183.47 MeV. All energies are in MeV.

The problem is solved by introducing DS3 and DS4. If the spectrometer is set for trajectories 2–4 (shown in Figure 2.2) the field in DS3 is adjusted in such a way that the main beam from DS1 is bent towards the centre of DS4 which has circular poles. In the setting for trajectory 1, the main beam does not pass through DS3 at all but travels directly from DS1 to DS4. On emerging from DS4 the beam is normal to the pole edge. Consequently a single output trajectory is allowed which simplifies beam dumping arrangements.

For the present experiment, trajectory 1 was used, tagging photons in the energy range 83.47–133.47 MeV.

2.5 The Focal Plane Detector

A focal plane detector (FPD) [90] has been designed to cover the full length of the spectrometer's 1.33 m long focal plane. The path of a recoil electron is bent by the spectrometer through an angle which depends on its momentum. Hence by measuring its position along the focal plane its energy can be measured. In order to achieve this 92 elements of 2 mm thick×17 mm wide×60 mm high NE Pilot-U plastic scintillator each coupled to a Hamamatsu R1450 photomultiplier have been arranged at ~14 mm intervals along the focal plane (see Figure 2.3). The angle of incidence of the electrons to the focal plane varies along its length as does the momentum bite per unit length. Ideally, it would be desirable to have elements which sampled the same momentum bite. However, for ease of manufacture the scintillator elements were made to a standard size. Although the angle and spacing of the scintillators varies along the focal plane, there is still a slight variation in momentum byte per element. The mean angle has been set at 37.35° so that as viewed by an incident electron each element overlaps the next by approximately 0.5 mm more than half its width. In this arrangement the path of every *bona fide* recoil electron must pass through two adjacent elements.

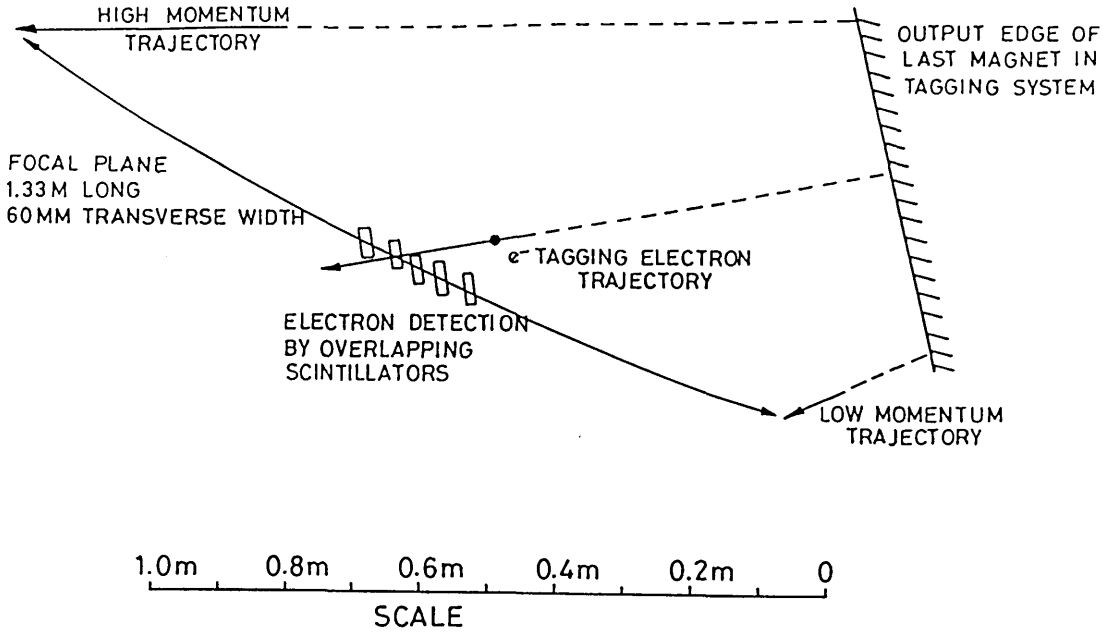

Figure 2.3: Focal plane geometry showing high and low momentum trajectories.

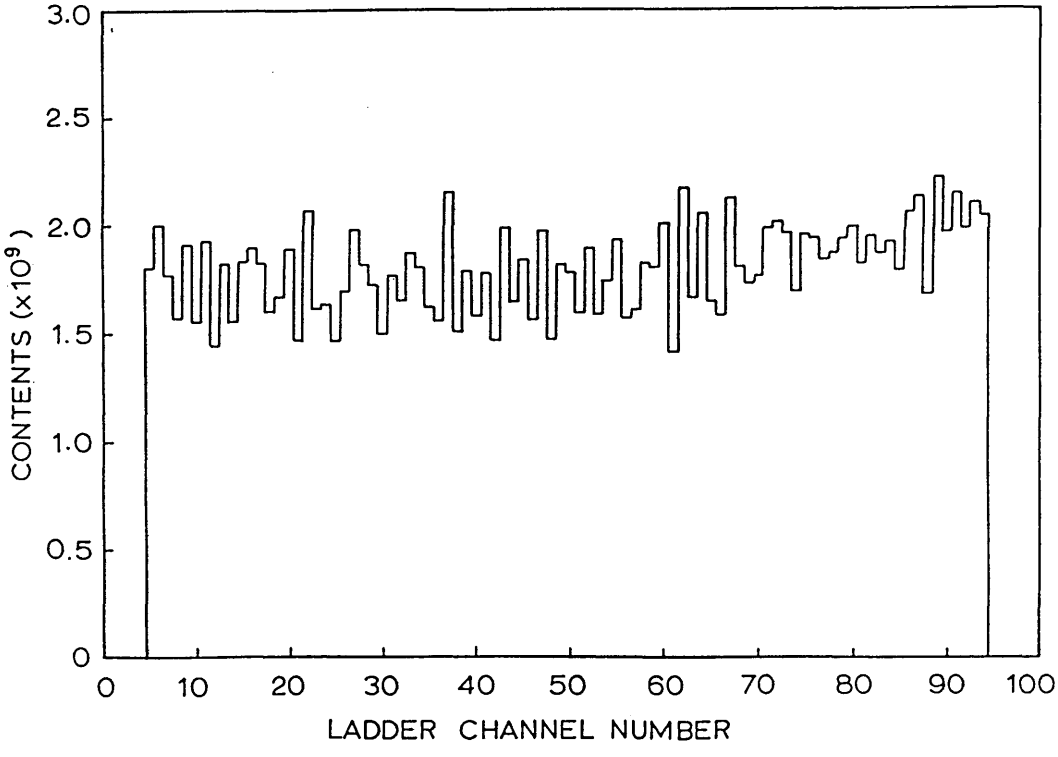

Figure 2.4: Count rate per ladder channel as explained in text. (The statistical error per channel is $\sim 0.0025\%$.)

Inaccuracies in the final positioning of the scintillators due to variations in the thickness of the wrapping materials produces random variations in the overlap. The effect is illustrated in Figure 2.4. The histogram shows the distribution of electrons as a function of channel detected from a ^{90}Sr source. The source was mounted in a motor driven carriage on the detector which scans the focal plane at a constant speed. The progressive variation with increasing channel number is the effect of the variation of spacing and angle. The marked variation from channel to channel over and above the general trend is an effect of the precision with which each scintillator element can be located in the focal plane.

2.6 The Photonuclear Targets

The targets were mounted in a target stand 3.79 m from the bremsstrahlung radiator. A collimator at the exit from DS3 ensured that the beam was ~4 cm in diameter at the target position. A frame consisting of two vertical aluminium struts fixed to a solid base held the targets in position. The frame could be manoeuvered vertically by a driver motor controlled from the control room. An automatic microswitch system ensured that the motor stopped at preset target positions. During the experiment the target was viewed by a closed-circuit television camera so that its position could be checked visually .

Deuterated polythene (CD_2) and pure carbon targets sufficiently large to intercept all of the photon beam (8.1×9.9 cm^2 and 10.0×16.1 cm^2 respectively) were mounted in the frame, one above the other. The deuterium in the CD_2 target provided a convenient online energy calibration of the proton detector. Most of the deuterium events are easily separated in later data analysis. The carbon target was included to show up any possible unexpected effects caused by the presence of deuterium. The CD_2 and carbon targets were 164.1 ± 0.6 mgcm^{-2} and 152.5 ± 0.8 mgcm^{-2} thick respectively. Below these a space was left for target-out

measurements.

2.7 The Proton Detector Array

A proton detector was designed with (γ,pn) measurements in mind. In order to maximise the count rate from such an experiment a large solid angle detector with large efficiency was required. However, in order to improve on previous measurements it was also necessary to design a detector with 2–3MeV energy resolution and less than 5° angular resolution. With these criteria in mind a E-ΔE_1-ΔE_2 plastic scintillator telescope detector was constructed. The configuration of three ranks of scintillator as illustrated in Figures 2.5 and 2.6 provides charged particle identification (through the Bethe–Bloch mass identification function [85]) and makes use of a time difference method to determine particle direction.

The rearmost rank consists of three blocks of NE110 plastic scintillator each of dimension 100 cm×11 cm×13.5 cm. These blocks are arranged in such a way that this rank has a detecting area of 100 cm×40.5 cm and a thickness of 11 cm. Directly on to each end of each block is coupled an EMI 9823B 130 mm photomultiplier tube. The gains of the photomultipliers are monitored online by use of a light emitting diode fitted to the scintillator, which is stabilised using feedback from a pin junction photodiode.

4.5 cm in front of this E detector is a rank of five 3 mm×20 cm×50 cm ΔE detectors also constructed using NE110. These are arranged vertically to form a detecting area of 50 cm×100 cm. A 52 mm EMI 9907B photomultiplier tube is coupled to each end of each strip by a twisted strip light guide which transports the light through a 90° bend to the tubes which sit horizontally above and below the E blocks. Finally, at 8 cm from the target is a thin ΔE detector of dimension 1 mm×25 cm×15 cm constructed from NE102A plastic scintillator. This is viewed by two EMI 9907B photomultipliers from the top and bottom. The light guides

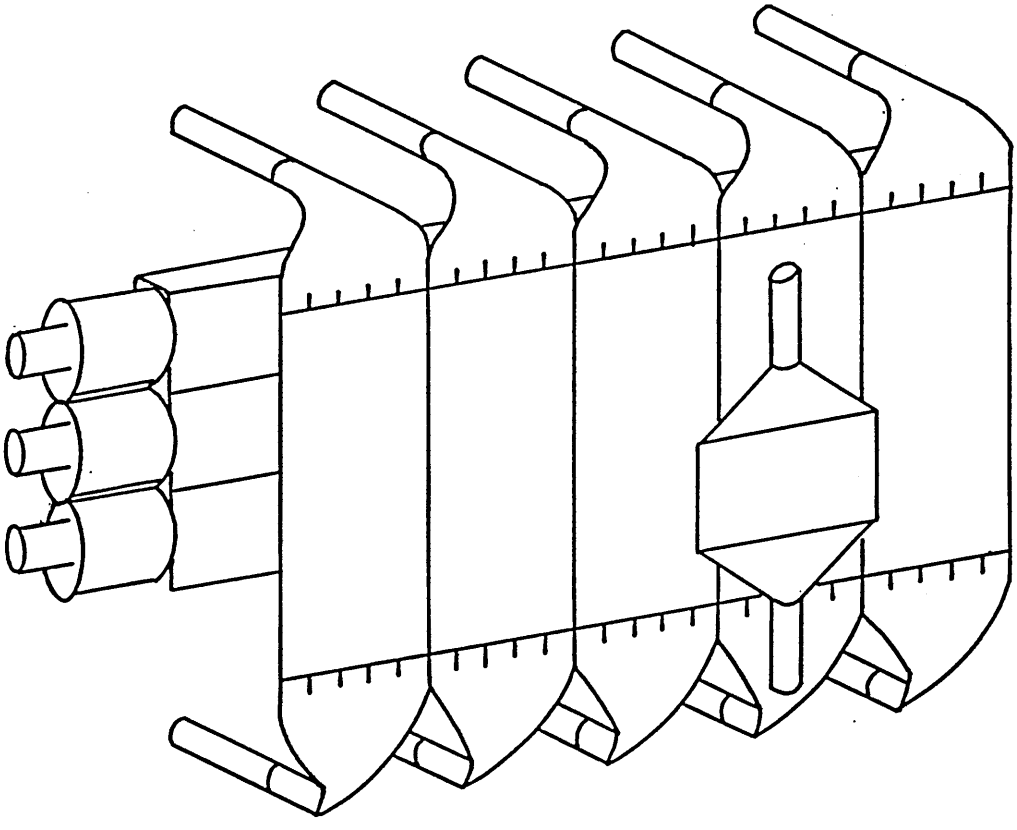

Figure 2.5: Expanded schematic diagram of proton detector.

transport the light from a 1 mm×250 mm area to a 1 mm× 50 mm area and hence to a small area on the photocathode.

NE110 was chosen for the rear and middle ranks as it has reasonably high light output (nominally 60% of that of anthracine), which results in good intrinsic energy loss resolution, and a long nominal attenuation length of 400 cm [91]. This indicates good light transmission properties which are essential for detectors of large dimension rendering the light collection less sensitive to the position of the detected particle in the scintillator. The thickness chosen is sufficient to stop protons of ~120 MeV incident perpendicular to the surface. Since the threshold for the (γ,pn) reaction in ^{12}C is 27.4 MeV this thickness is adequate for the 80–130MeV photon energy range. The small front detector was constructed from NE102A which has similar light output to NE110 and a shorter attenuation length of 250 cm. Each element of scintillator and its light guide were wrapped in aluminised mylar foil over the whole of the exposed surface area to improve light collection and further wrapped in three layers of thin black PVC for light proofing.

Owing to a restriction of space in the experimental area, the tubes on the rear rank have had to be coupled directly on to the scintillator resulting in the tube mating with only 64% of the scintillator area, assuming the photocathode is fully effective out to a radius of 55 cm. This results in the degradation of light collection especially for events close to the ends. Dow Corning Silastic 734 RTV adhesive, a silicone based compound, was used to give a firm but non-permanent join between tube and scintillator or tube and light-guide in all parts of the detector. The compound is slightly cloudy to look at but bench tests have shown that when compared with Dow Corning Optical Coupling Compound, a grease specially manufactured for this application, there is no observable difference in pulse height resolution.

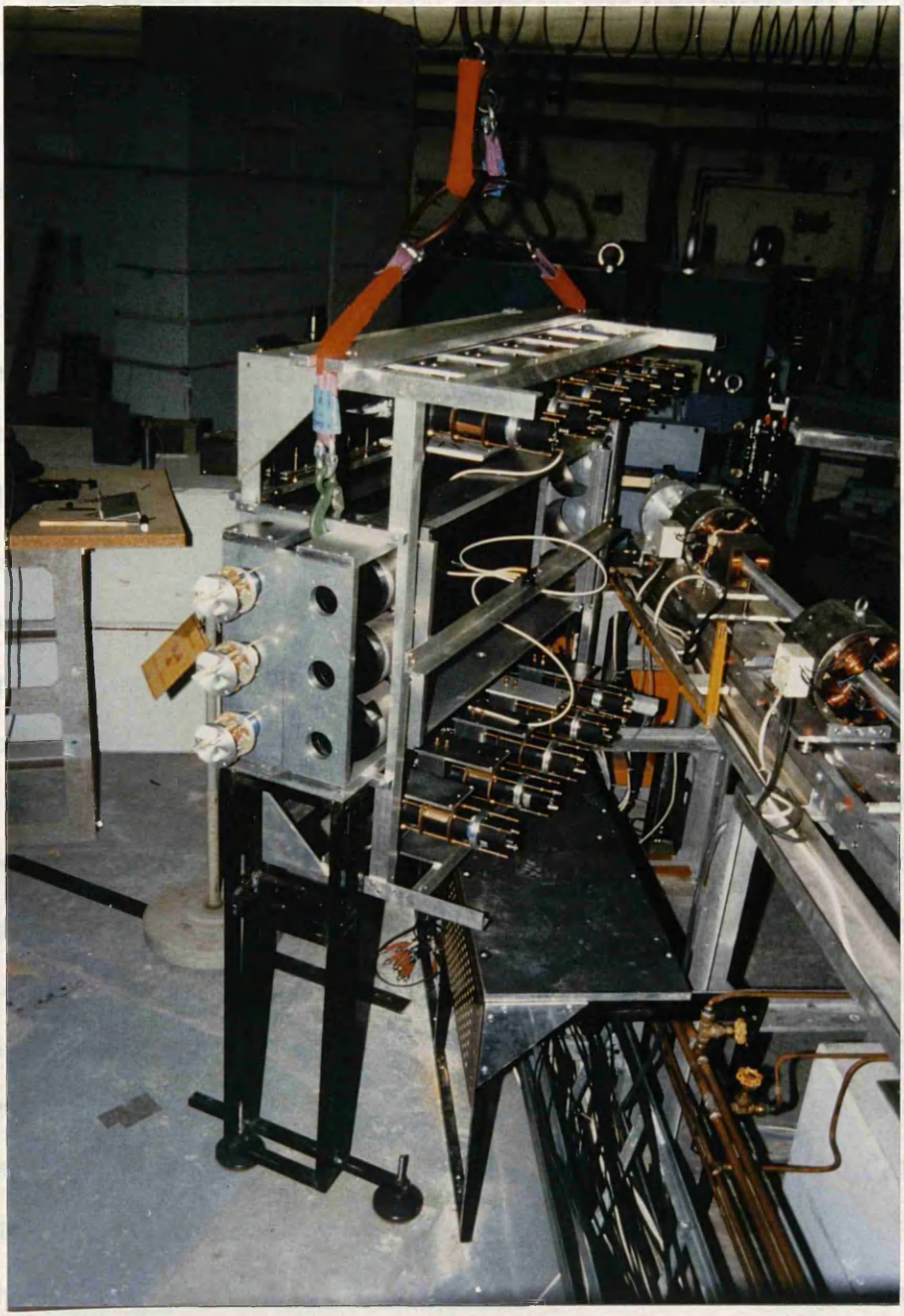

Figure 2.6: Photograph of the proton detector in position in front of the beamline. The ten ΔE photomultipliers are shown horizontally. The bases of three E photomultipliers are shown vertically. The photon tagging spectrometer can be seen in the background.

2.8 The Neutron Detector Array

An array of large plastic scintillator detectors was constructed for the detection of neutrons from the reaction. As well as energy determination from time of flight, the large size of the counters combined with the use of more than one photomultiplier tube (PMT) provides the additional feature of position sensitivity. Long detectors (Figure 2.7) viewed by two PMTs have been used and provide 1-dimensional position information. A square detector was also tested for the first time. Viewed from the corners by four PMTs, it provides 2-dimensional information.

The eight 1-dimensional detectors each of dimension 20 cm $\times$ 20 cm $\times$ 100 cm constructed from NE102 scintillator have been used. Each end is viewed by a Mullard 58AVP photomultiplier attached to the scintillator by means of a 20 cm long perspex lightguide which has constant 20 cm square cross section. The scintillator is wrapped in a layer of aluminised mylar foil to reduce light loss and a layer of black PVC for light proofing. Each detector is mounted vertically on a trolley which can be moved to the required position easily. Six of the detectors were placed on an arc centred on the target of radius 4.0 m and at scattering angles of 82.5°, 90.0°, 97.5°, 105.0°, 112.5°, and 127.5°. Due to a restriction of space the remaining two were placed on an arc of radius 3.8 m at angles of 67.5° and 75.0°. This configuration gives a total solid angle for these detectors of 101.9 msr. When mounted and in position the centres of the scintillators were within $\pm$2 cm of the height of the beam from the ground.

The square detector has been constructed for this and other similar experiments and is fully reported in [79]. It consists of two one metre square slabs of NE110 scintillator each 5 cm thick placed one behind the other. Each is wrapped in a layer of mylar and optically separated to improve light collection. 1 mm spacers are inserted between the slabs to prevent the foil being pressed too closely to the

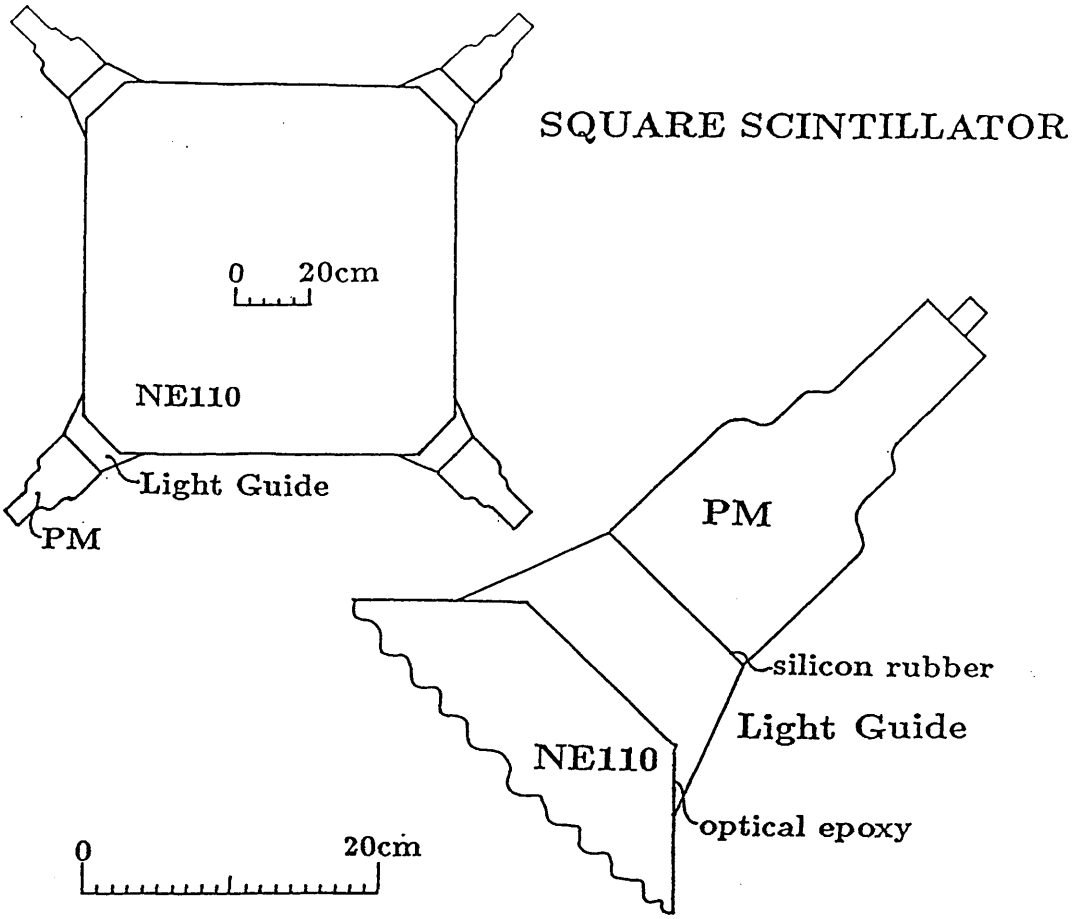

LONG DETECTOR

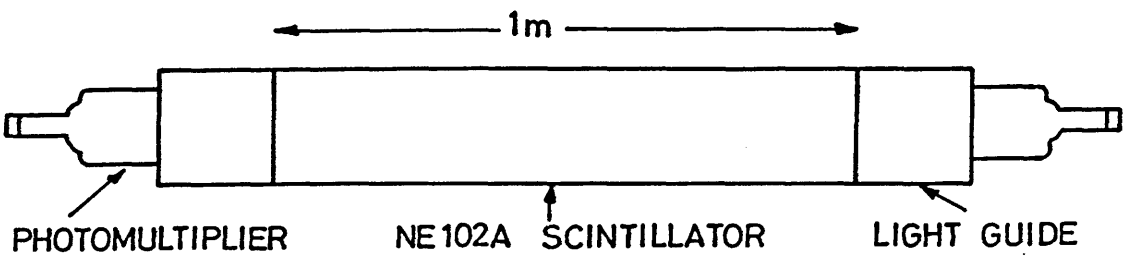

Figure 2.7: Schematic diagram of the square neutron detector and a long 1-dimensional detector.

scintillator and altering its total internal reflection characteristics. The corners of the detector are truncated to increase the light collection efficiency and each is viewed by an EMI 9823B PMT connected by a shaped acrylic lightguide. The optical joint is made by the same material as for the proton detector. The whole assembly is wrapped in 1.5 mm thick black neoprene sheet for lightproofing which also provides a degree of protection against mechanical shock. Its thickness has negligible effect on neutron detection.

2.9 The Photon Beam

After the photon beam passes though the exit window of the vacuum box in the spectrometer, it is collimated before reaching the target. The collimator consists of three parts: firstly, a lead precollimator with a tapered aperture which matches the bremsstrahlung cone originating at the radiator of half angle 4.46 mrad. This is followed by a small scrubbing magnet which removes any undesirable electron background. Such background is mopped up by a second lead collimator with an aperture large enough to allow the unhindered passage of the bremsstrahlung cone. In order to determine an absolute cross section in tagged photon experiments it is essential to know accurately the tagging efficiency of the system i.e. the percentage of the photons tagged by the spectrometer system which pass through the collimator and hit the target. To get maximum efficiency, the photon beam must pass through the centre of the collimator before hitting the target. To monitor the photon beam position, a black and white Polaroid Polaplan 4"×5" Land Film, Type 52, used in conjunction with a lead converter was regularly placed in front of the collimator throughout the experiment and exposed to a low intensity beam for a few seconds. The photograph thus indicated whether or not the electron beam incident on the radiator was correctly aligned and adjustments could be made if necessary. An example of a photograph is shown in Figure 2.8.

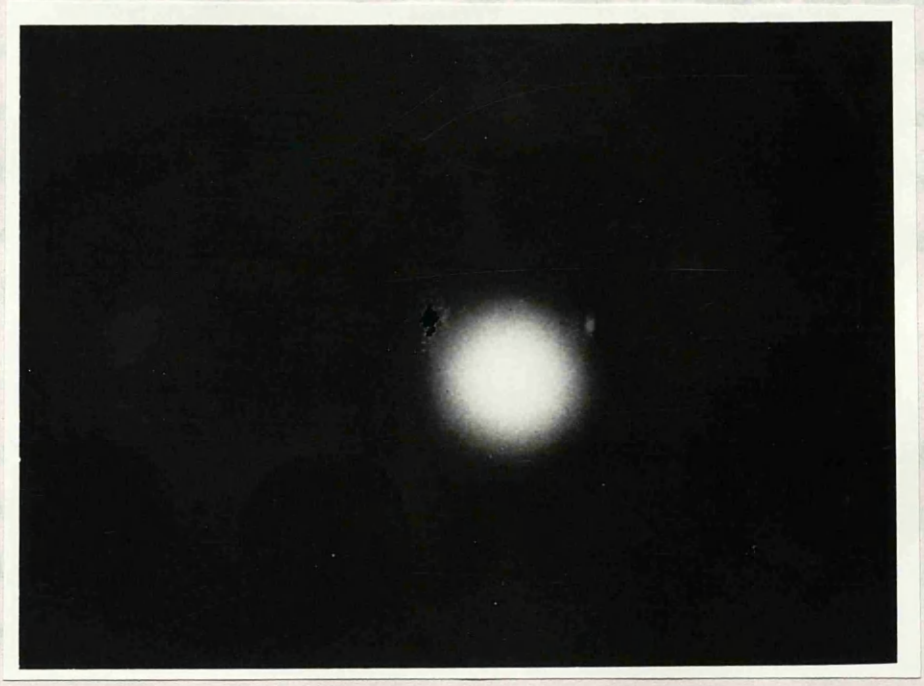

Figure 2.8: Photograph of the photon beam taken with a Polaroid film, as described in the text.

Having established that the beam direction was correct the tagging efficiency was measured. A cerium loaded barium glass scintillator detector was placed in a reduced intensity beam to provide the required X-triggers for the electronics (see Section 2.10.1 for a definition of "X-trigger"). At this low beam intensity the number of random coincidences between the detector and the ladder is negligible. The $15 \times 15 \times 50$ cm^3 block is large enough to absorb photons in the 80–130 MeV energy range with 100% efficiency. Both the number of X-triggers and the number of counts in the FPD were monitored by free running scalers. Runs were also made without a radiator to account for room background. A pulse generator provided output to a scaler to measure real time and so to provide a normalisation between the radiator-in and radiator-out runs. The tagging efficiency was then calculated from the expression

$$\epsilon = \frac{d_f X_f}{L_f - L_b \frac{t_f}{t_b}} \tag{2.1}$$

where d_f is a divide factor on the X-trigger scaler, X_f is the number of X-triggers recorded during the radiator-in run, L_f and L_b are the number of counts in the FPD during the radiator-in and radiator-out runs respectively, and t_f and t_b are the live times for the same runs.

2.10 Electronics

The electronics for the system are situated in a concrete bunker in the experimental area ~5 m from the experiment. The close proximity of the bunker to the experiment allows fairly short cables to be used, minimising the dispersion of the analogue signals as they travel from the detectors. The CAMAC interface in the bunker is connected by a serial link to a data aquisition computer in the control room several metres away. Each detector has a set of processing electronics and can be treated as an independent unit. The outputs from every unit are then processed together as a complete system.

2.10.1 Proton Detector

A simplified diagram of the electronics used for the proton detector is shown in Figure 2.9. A particle which loses energy in any part of the detector produces scintillations which are detected and converted into analogue charge signals by photomultipliers. Each raw signal is linearly fanned out, one output going to a constant fraction discriminator (CFD), another via a 250 ns delay to an ADC. Two signals are taken from the CFD one of which passes through a 250ns delay before stopping a TDC. These are known as the p-TDCs. The 250ns delays are necessary to allow the electronics to process, firstly, the proton detector ADC gates and, secondly, the start signal for the p-TDCs as explained later in Section 2.10.4. The other signal from the CFD, along with the corresponding signal from the other end of the detector element, is fed into a mean timer unit (MT). The output of the MT is produced at a time which corresponds to the average time of arrival of the input pulses plus a constant delay and hence independent of the interaction position of the particle in the detector. If there is only one input pulse there is no output.

In the case of the rear or middle rank of detectors, the MT outputs from that rank (up to three for the rear and up to five for the middle) are logically fanned together thus giving a signal indicating an acceptable event in that rank. A three-fold coincidence is then required of the output from all three ranks. A resultant signal here indicates an event which came from the target and fired all three parts.

In order not to submerge real proton signals in a sea of background atomic interactions, it is vital that an "electron reject" system is included in the circuitry. The raw analogue signals from the rear rank are linearly fanned together and similarly for the middle rank. The two signals are each fed through an attenuator and then fanned together before entering a leading edge discriminator. The input signal h_0 to the discriminator can be written in as $h_0 = ah_E + bh_{\Delta E}$ where h_E

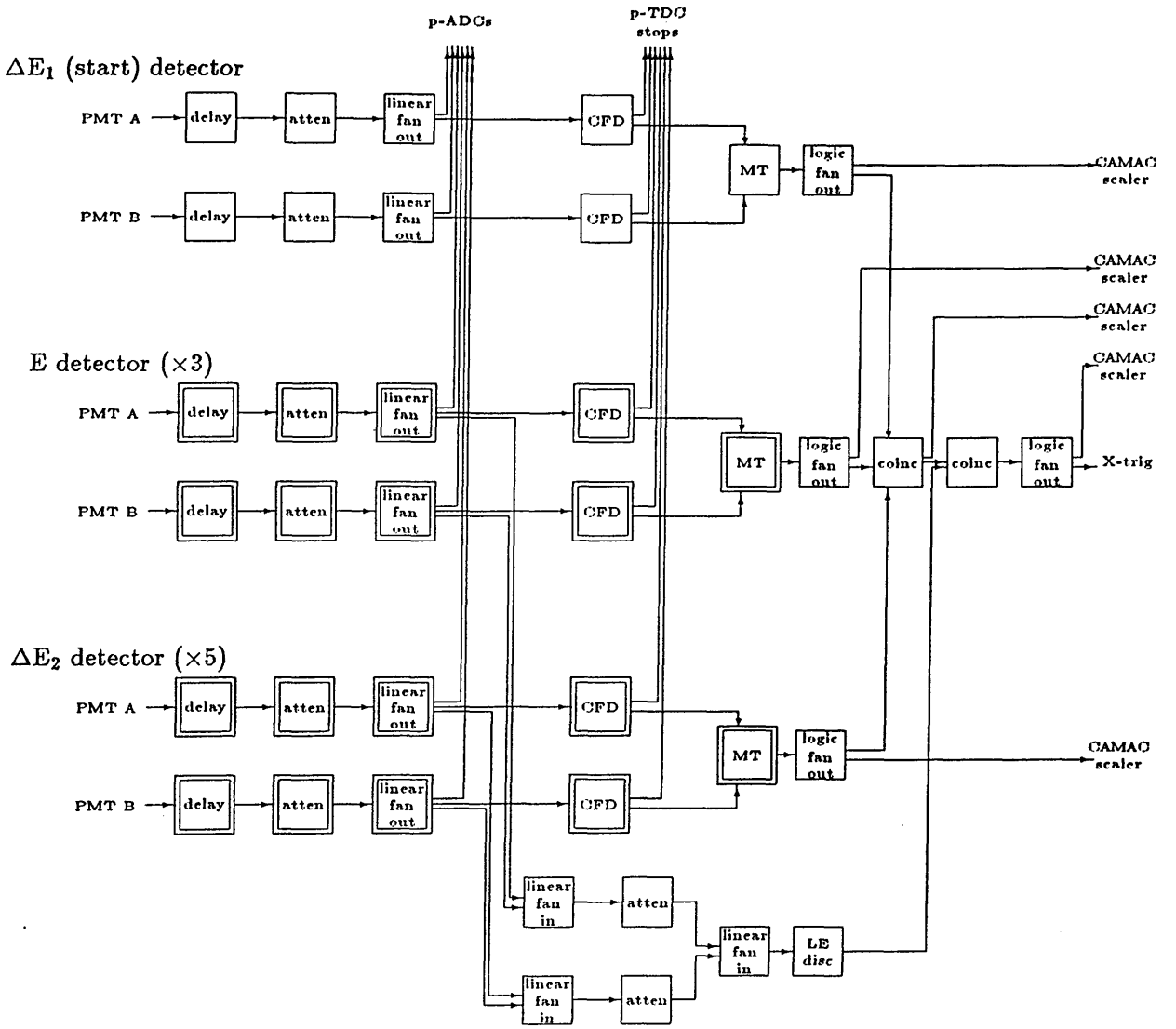

Figure 2.9: Block diagram of proton detector electronics. A double box signifies several identical units, as indicated. FIFO – fan-in fan-out; coinc – coincidence unit; atten – attenuator; LE disc – leading edge discriminator; CFD – constant fraction discriminator; MT – mean timer; PMT – photomultiplier; p-ADCs (p-TDCs) – ADCs (TDCs) associated with the proton detector.

is the summed input signal from the rear rank, $h_{\Delta E}$ is the summed input signal from the middle rank, and a and b are positive coefficients which indicate the level of attenuation on each signal. The effect of the attenuators can be seen from an h_E versus $h_{\Delta E}$ scatter plot (see, for example, Figure 3.12). For a preset h_0 (corresponding to a discrimination threshold) the above equation is a straight line with a negative gradient which depends on the level of attenuation. Consequently, electrons can be easily accepted or rejected by setting the electron reject discrimination threshold accordingly and the making an anti-coincidence with the overall detector output signal.

An event which successfully provides a signal from the final coincidence is said to have produced an "X-trigger". The X-trigger is used to enable the pattern recognition units (PUs) which receive signals from the FPD and is the first requirement in initiating a CAMAC read.

2.10.2 Focal Plane Detector

The FPD electronic system is required to produce only timing signals for recoil electrons. The analogue signals from the FPD photomultipliers are fed to six 16-channel circuit boards located beneath the scintillator array. The close proximity of the circuits to the array (<20cm of cables) preserves the rise time of the pulses which offsets the effect of the leading edge discrimination techniques employed. The discriminators use fast ECL circuitry which is carried through to the overlap coincidence logic for neighbouring detector elements. Thus 92 scintillator elements give rise to 91 output channels. The ECL pulses are converted to NIM pulses for compatability with the CAMAC data collection system. The channels are divided into six groups, one of 12 channels, four of 16, and one of 15. The output channels of each group are fed into a pattern recognition unit (PU) in the CAMAC crate. A strobe signal then holds the bit pattern for the CAMAC read. Each PU contains a fast coincidence circuit which makes an overlap between the OR of the input

channels and the X-trigger signal. The timing of the overlap signal is made to depend on the leading edge of the FPD signal and is then used to stop an e-TDC. This TDC has previously been started by the X-trigger itself, as mentioned later, and is used to identify real coincidences between the FPD and the proton detector.

2.10.3 Neutron Detectors

Figure 2.10 shows a block diagram of the neutron detector electronics. Both an ADC and a TDC (the n-TDCs) record information from each PMT on all of the neutron detectors. The processing of analogue signals is straightforward. A pulse from a PMT on one end of a 1-dimensional detector is linearly fanned out to provide two signals. One is sent via a 250 ns delay to an ADC and the other to a CFD. An output from the CFD provides a stop signal for the associated n-TDC. Another output is also taken from the CFD and a coincidence is made with the corresponding pulse from the other end. The output pulse or "neutron trigger" is first delayed and a coincidence is made with the X-trigger–FPD coincidence signal to provide a gating signal for the n-ADCs.

The square detector signals are processed similarly with a four-fold coincidence requirement instead of a two-fold requirement.

2.10.4 Signal Processing and Computer Interface

The ADCs, TDCs, PUs and scalers are housed in a CAMAC crate. The CAMAC controller is interfaced to a dedicated HP1000 microcomputer used in the first stage of data collection and data is transfered between them along a serial line. The HP1000 stores the data in a swinging buffer before sending them to an HP3000 mainframe which writes them on high density magnetic tape.

In order to generate an interrupt which initiates a read of the CAMAC modules the following two steps must occur :

- an X-trigger signal must be accepted from the proton detector

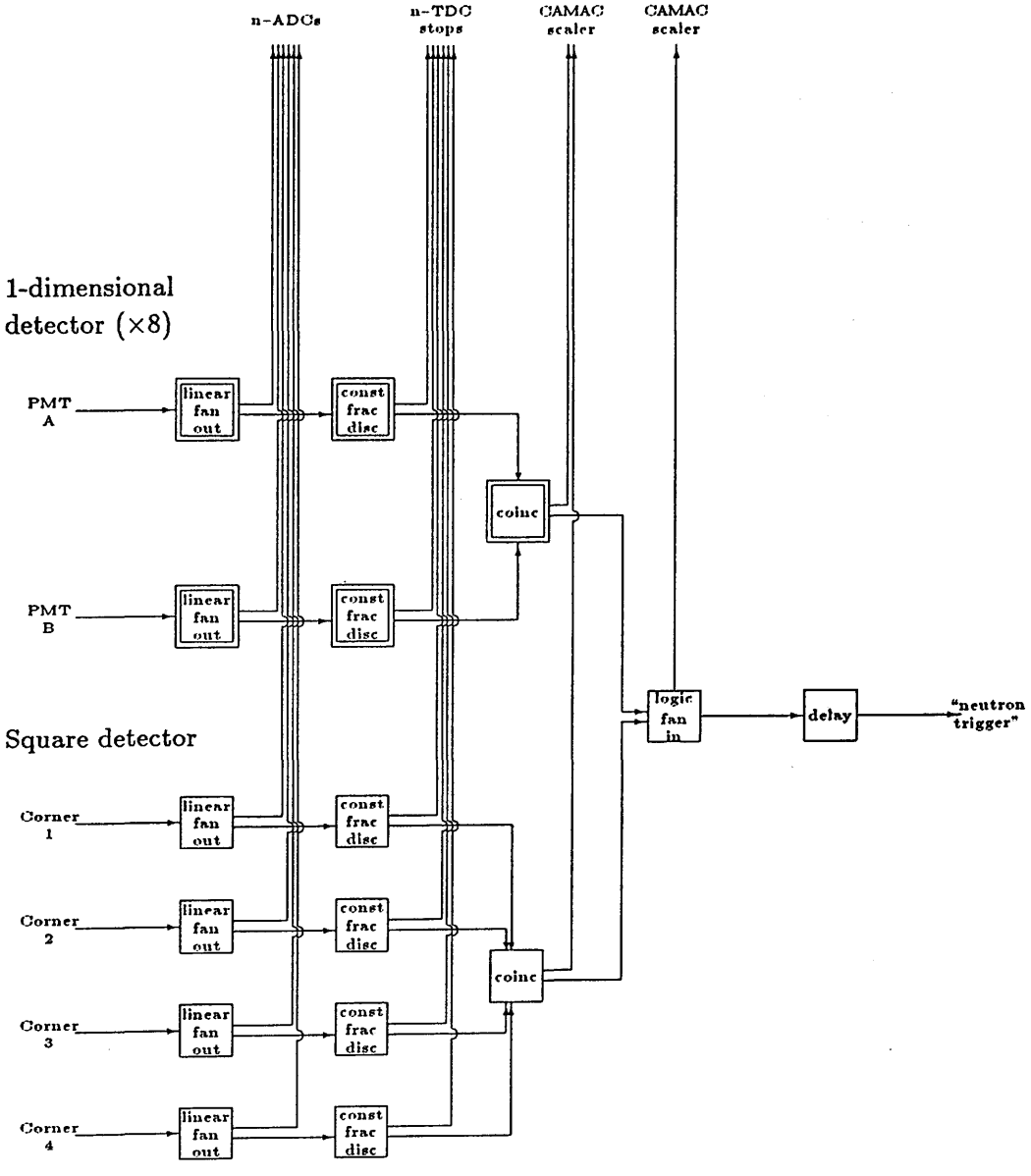

Figure 2.10: Block diagram of neutron detector electronics. A double box indicates several identical units. PMT – photomultiplier tube; coinc – coincidence unit; const frac disc – constant fraction discriminator; n-ADCs (n-TDCs) – ADCs (TDCs) associated with the neutron detectors.

- the FPD electronics, enabled by the X-trigger, must provide a signal indicating a recoil electron in the FPD

This coincidence signal is used to set a bit in the input register thereby informing the CAMAC controller that a read can take place. The controller then generates an interrupt for the HP1000

In order to prevent further X-triggers being accepted while the computer is receiving data, X-trigger input is controlled by a flip-flop (see Figure 2.11). When the computer is busy the flip-flop is set to 1 and when it is ready it is reset to 0. Its output is logically fanned in with the level from an enabling switch in the control room. The inverted signal is fed to a cable coincidence box along with the X-trigger. Hence the flip-flop and the control room switch both act as a gate for the X-trigger signal.

When an X-trigger signal is allowed through the gate it is then used to enable the ladder PUs. An OR output from each PU is fed to a seventh PU giving a pattern showing which group of ladder channels fired. The OR outputs are also fanned together. This signal (whose time is determined by the FPD) has several purposes:

- it sets the flip-flop disabling further x-triggers
- it starts the n-TDCs
- it makes a coincidence with the "neutron trigger" to provide a gate pulse for the neutron ADCs whose timing is determined by the "neutron trigger"
- it makes a further coincidence with the X-trigger to provide a pulse with timing determined by the X-trigger. This signal starts the e-TDCs and the p-TDCs as well as providing a gate pulse for the proton ADCs
- it stops the e-TDCs

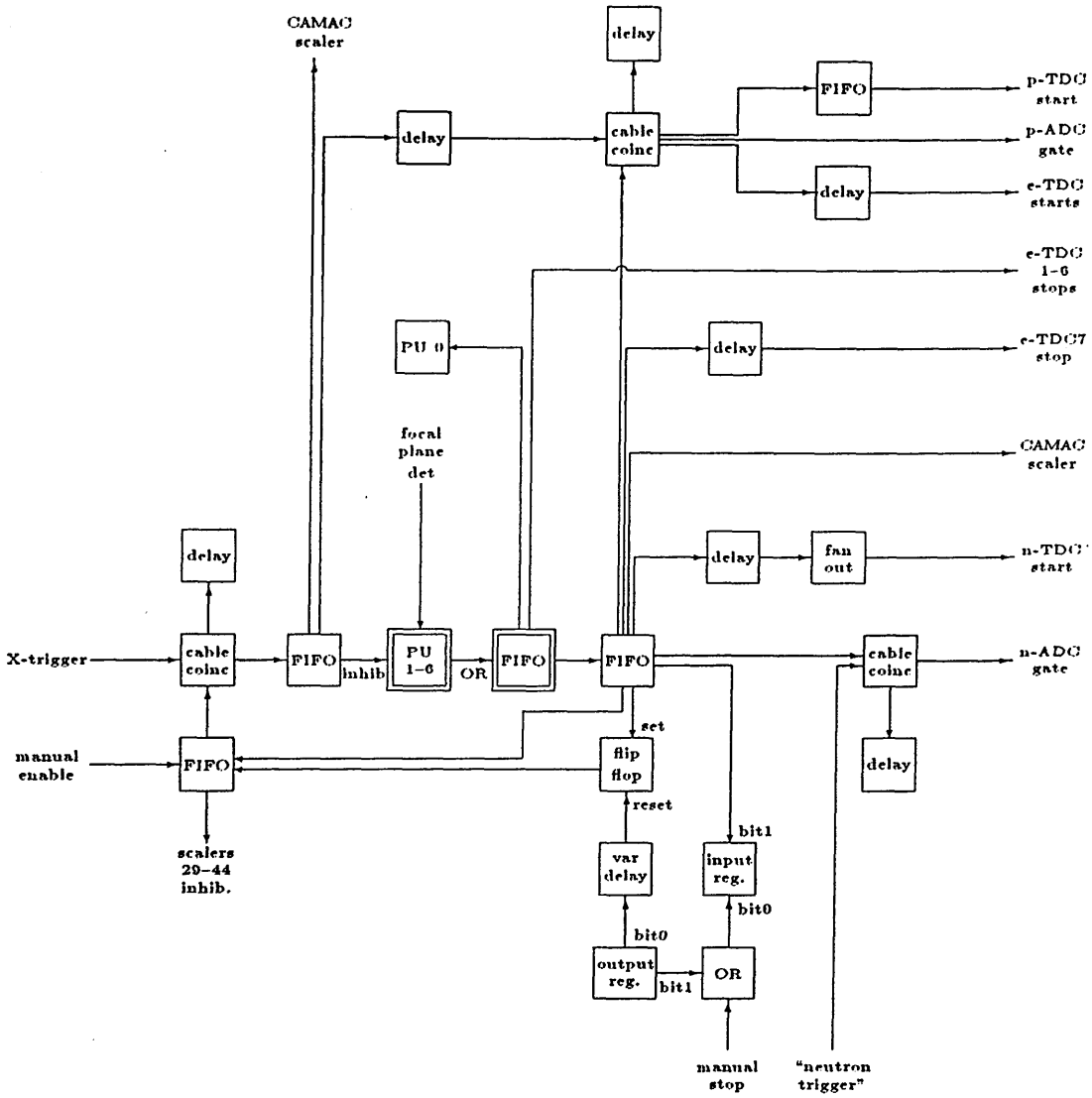

Figure 2.11: Block diagram of the processing electronics from the detectors to the HP1000 computer. Double boxes indicate six identical units. FIFO – fan-in fan-out unit; PU – bit pattern recognition unit; cable coinc – coincidence unit in which a length of cable is used to set the output pulse width; e-TDC – TDC started by the proton detector x-trigger and stopped by the FPD.

- it sets the input register generating an interrupt for the HP1000

After the interrupt has been received the controller is instructed to read the PUs, TDCs and ADCs sequentially. The HP1000 sorts the data, ignoring all datawords which are zero, and stores them in one half of a swinging buffer. When the computer is ready the controller is instructed to reset the output register which then resets the flip-flop. The system then awaits the next X-trigger. When the computer has filled up one side of the buffer the computer starts to fill the other half. Meanwhile, data in the first half are sent to the HP3000 to be written to magnetic tape.

Chapter 3

Data Analysis

3.1 Introduction

The data obtained from the experiment were analysed using the VAX 11/780 computer at the Kelvin Laboratory with programs developed at both the Institut für Kernphysik, Mainz and the Kelvin Laboratory. The steps involved in analysing the data can be categorised loosely under two headings:

Data reduction: that is, the process of reducing the size of the data set obtained from the experiment, removing all events which do not satisfy essential conditions such as background atomic electrons. The selections do not remove all random coincidences and so the process includes selection of corresponding data sets of randoms which must be subtracted in the final stages of the analysis.

Data evaluation: that is, evaluation of physical quantities, including the routine task of obtaining position and energy calibrations of the detectors and the evaluation of cross sections for comparisons with existing theories.

The following sections describe these processes in detail.

3.2 Data and Software

The data was written on to a magnetic tape at a rate of $\sim$ 80 events [1] per second. Up to 30 files each of $\sim$ 45 minutes duration and containing $\sim$ 200,000 events were stored per tape so that each file was small enough to transfer to disk if required. The total number of interrupts processed and the total number of X-triggers is shown in Table 3.1.

Data Format

Each file consists of a sequence of one kilobyte data records which are preceded

[1] An "event" is defined as all the information read from the CAMAC crate after an interrupt has been received by the HP1000.

	CD_2 Target	Target Out
# of X-triggers	5465857	351481
# of accepted X-triggers	5126421	350053
# of Interrupts	4988779	325068

Table 3.1: Some X-trigger statistics for the CD_2 target and the target out runs recorded over the whole experimental period.

by an identifier record and succeded by an end record. Information from an integer number of events are stored per data record in a sequence of two byte words. Each event can consist of up to 86 words with non-zero ADC contents written first, then non-zero TDC contents and finally non-zero PU contents. Every event is followed by a separation code since they are not necessarily of uniform length. A separation code also distinguishes PU words from ADC and TDC words. An ADC is distinguished from other ADCs and from TDCs by its CAMAC address contained in the five most significant bits of the dataword.

Program Package

The package of routines now in use derives from a simpler package written in Mainz. That basic package has been extended and improved at Kelvin Laboratory to accommodate the needs of increasingly complex experimental systems.

Its essential function is to translate the datawords for each event, extracting the charge and timing signals and storing them in arrays. From this raw information all kinematical quantities (such as neutron energy or proton direction) can be calculated for each event. The user can request that a particular quantity be evaluated for every event and a spectrum of values of that quantity accumulated, which can then be displayed for visual inspection or stored for later use. Two dimensional spectra can also be accumulated, where two quantities per event are evaluated and then displayed as a bi-dimensional scatter plot.

Any quantity (raw or processed) pertaining to a given event can be subjected to conditions. In the case of a single variable, a condition is defined by specifying a lower and an upper limit of that variable. A condition can be defined on a bi-dimensional plot by first accumulating the spectrum and then specifying the limiting points of a region using a cursor mechanism, which are then read in by the program when making the selection. Such conditions can be strung together using

the logical operators .AND., .OR. and .NOT.. If an event meets the conditions the relevant channels in the requested spectra are incremented. This feature is extremely valuable for examining a particular aspect of the experiment. The user can also request that all events which meet the specified conditions be written to an output file. If the raw data files are "edited" in this way, then much processing time is saved and less space is required on the storage medium.

3.3 Detector Calibrations

3.3.1 The Proton Detector

Position Calibration

The proton arm of the experiment provides x- and y-position information which is derived from the difference between the arrival times of the signals at the ends of the detector elements. Position calibration data were obtained straightforwardly using a 5 mm thick steel plate with 30 holes (6×5) of 2 cm diameter cut at regular intervals over its surface. During one experimental run the plate was placed in front of the proton detector. All except the highest energy protons were stopped by the plate except at angles where there was a hole. Electrons penetrated it more easily but were easily distinguishable from protons by their E-ΔE energy loss characteristics and were removed from the data set. The spectrum of time differences (Figure 3.1) shows the effect clearly where the peaks correspond to holes in the plate. The relationship between position and time difference is found to be linear over the whole length of the ΔE detectors. The E detectors are linear only in the central 80 cm with slight deviations towards the ends (see Figure 3.2). Allowing for the finite size of the holes in the steel mask, the measured position resolutions were ± 1.2 cm for the x-direction and ± 2.1 cm for the y-direction corresponding in the configuration of this experiment to angular resolutions of $\pm 1.35^\circ$ and $\pm 2.6^\circ$ in the polar and azimuthal angles respectively.

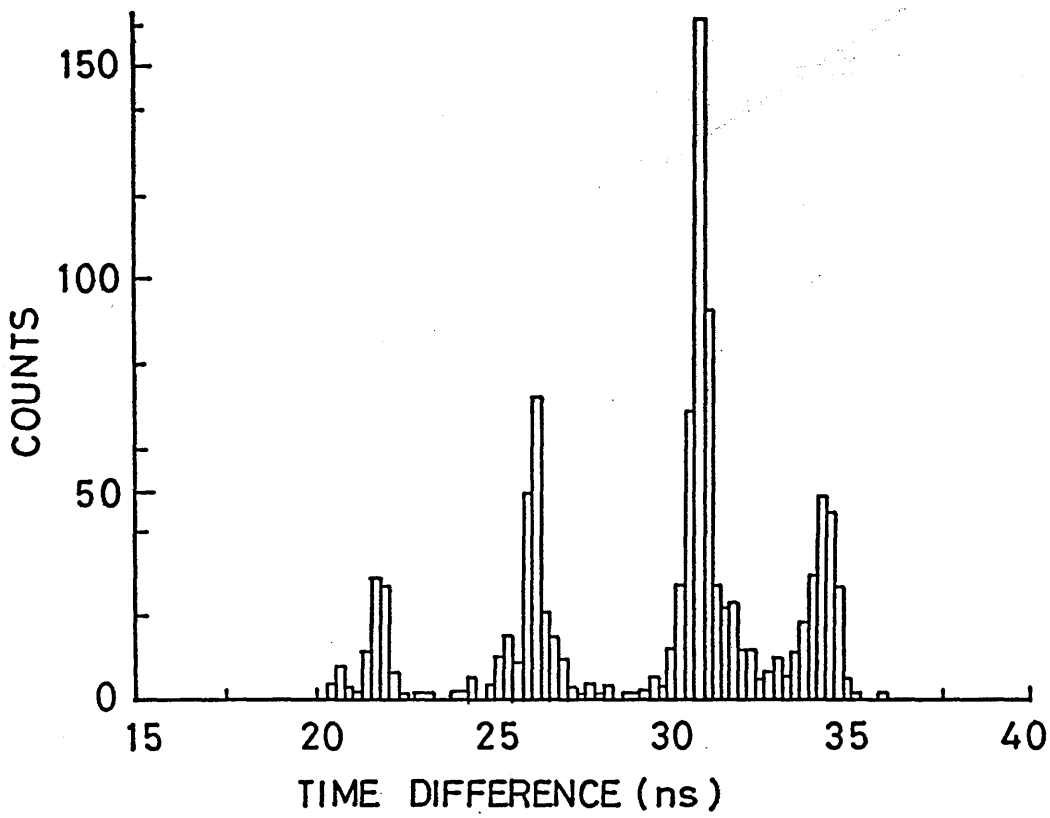

Figure 3.1: Time difference spectrum obtained from one E-scintillator using a perforated steel plate.

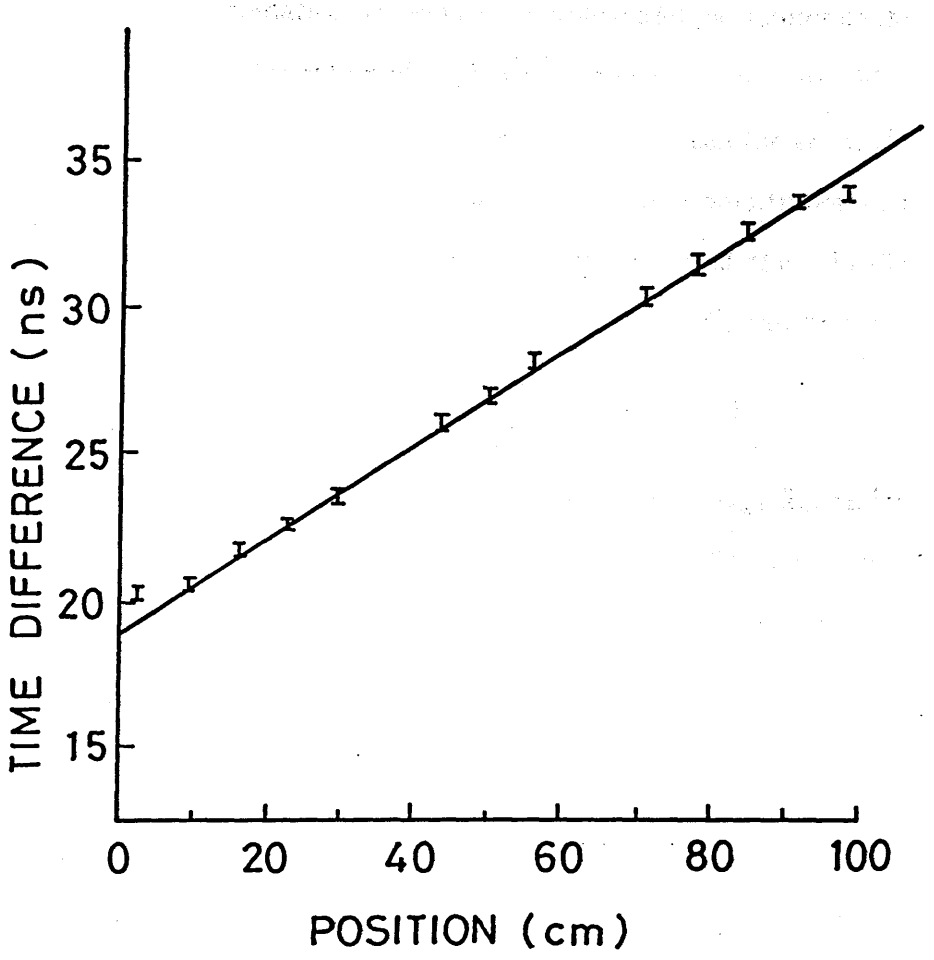

Figure 3.2: Hole position versus TDC time difference from calibration data.

Energy Calibration

Data from which the energy calibration of the rearmost detector elements could be established were obtained using protons from the D(γ,p)n reaction in the CD_2 target. The energies of these protons can be calculated from the tagged photon energy and either the measured proton angle or that of the associated neutron using two body kinematics. In order to establish and parameterise the calibration, the effect of light attenuation along the length of the scintillator blocks had to be separated from the expected non-linear relation between the emitted light and the proton energy. The output signal Q_i from the photomultiplier at one end of a scintillator block is proportional to the light output of the scintillator, but the constant of proportionality is position dependent. So Q_i can be written as

$$Q_i(x, T_p) = f_i(x)L(T_p) \quad (i = 1, 2)$$

where L is the light emitted as a function of proton energy T_p, and f_i is the light attenuation as a function of position in the element. Following Cierjacks *et al.* [84] it was assumed that the functions f_i are approximately exponential in character and so the output signals may be written

$$Q_1(x, T_p) = C_1 L(T_p) e^{-\mu x} \tag{3.1}$$

and

$$Q_2(x, T_p) = C_2 L(T_p) e^{-\mu(l-x)} \tag{3.2}$$

where x is the distance of the particle from end 1, l is the length of the scintillator and $\frac{1}{\mu}$ is the effective attenuation length. From Equations 3.1 and 3.2 the ratio of Q_1 and Q_2 is given by

$$k(x) = \frac{Q_2}{Q_1} = \frac{C_2}{C_1} e^{-\mu l} e^{2\mu x}$$

and so

$$\ln k(x) = 2\mu x - \ln\left(\frac{C_1}{C_2} e^{\mu l}\right)$$

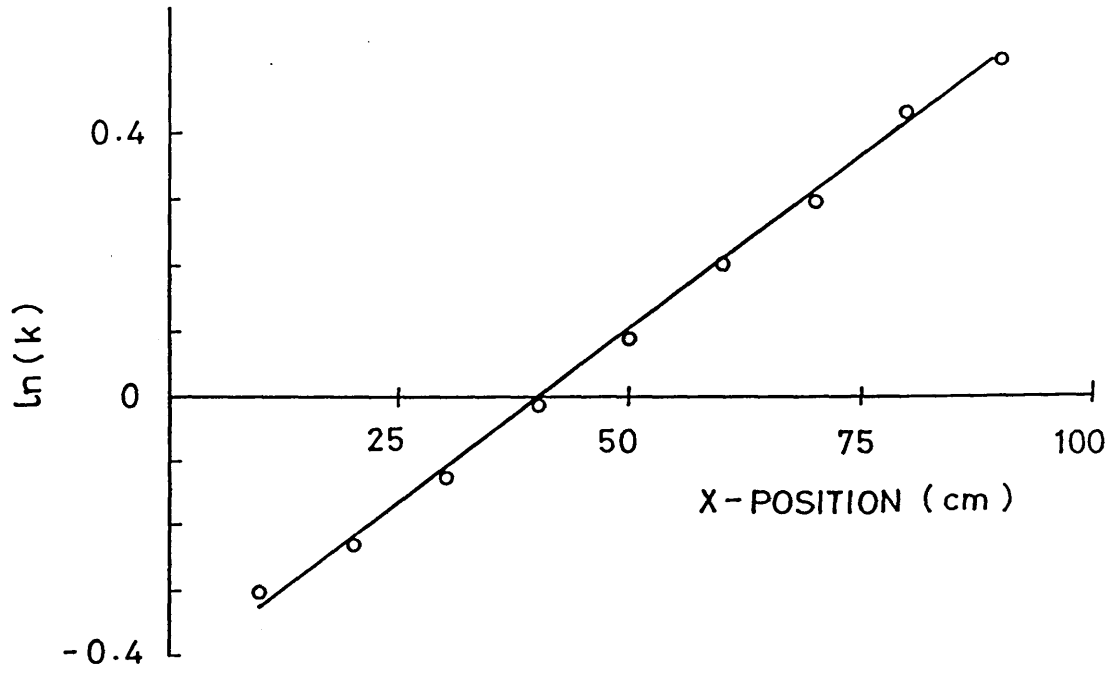

Figure 3.3: The logarithm of the ratio of pulse heights from each end of the middle element of the rear rank of the proton detector versus distance from end 1.

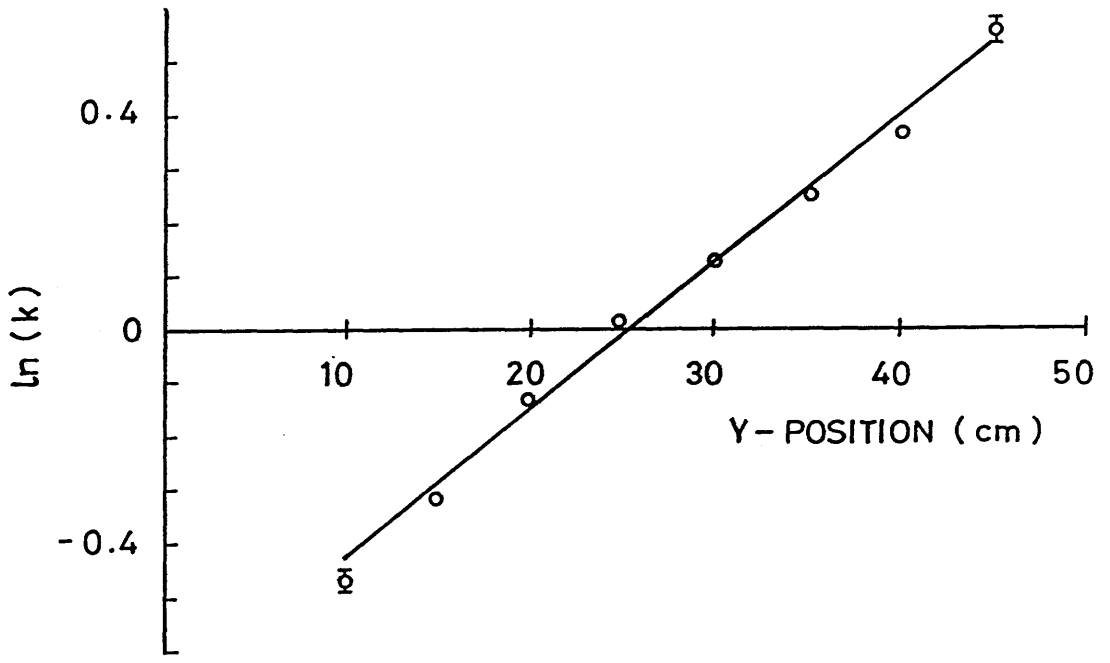

Figure 3.4: The ratio of pulse heights versus position as above for the middle element of the middle rank of ΔE strips.

In Figure 3.3 $\ln k$ is shown as a function of x for the central E-block of scintillator. This is found to be linear over the central 80% of the length and $\frac{1}{\mu}$ was determined to be 231.0±3.9 cm. The difference between this and the nominal value given above can be attributed to the finite geometry of the scintillator which gives rise to light loss and an increase in the average pathlength of a photon because of multiple reflections.

A convenient result of the exponential assumption is that the simple expression $\sqrt{Q_1 Q_2}$ is independent of x and is proportional to $L(T_p)$. Energy losses in the target, air and ΔE strips have been accounted for using parameterisations obtained from energy loss tables as described in Appendix C. Calculated proton energy assuming deuterium kinematics, corrected for energy losses, were thus plotted against $\sqrt{Q_1 Q_2}$ as shown in Figure 3.5 giving a very clear deuterium ridge from which straight line calibrations have been obtained. The gradient of the ridge varied by less than 3% over the whole data set obtained during the experimental period. The observed energy resolution of the E detectors in this experiment was 2.6 MeV FWHM at 60 MeV .

Nonuniform light collection near the ends of the E-blocks arises due to the lack of lightguides. To investigate this, a Monte Carlo code PHOTON has been written at Kelvin Laboratory [80] which tracks a scintillation photon through the volume of scintillator, calculating its probability of reaching one of the photomultipliers. Input parameters include the dimensions of the scintillator, the dimensions of the light guides, the starting coordinates of the photon, the material's attenuation length, its refractive index and the reflectivity of the surfaces. The probability that a photon will reach each photomultiplier for a given initial coordinate is calculated. This has been carried out for successive points along the central axis normal to the end faces and is compared in Figure 3.6 with the calculations for points along a line parallel to this but displaced by 5 cm in each of the other orthogonal axes. This

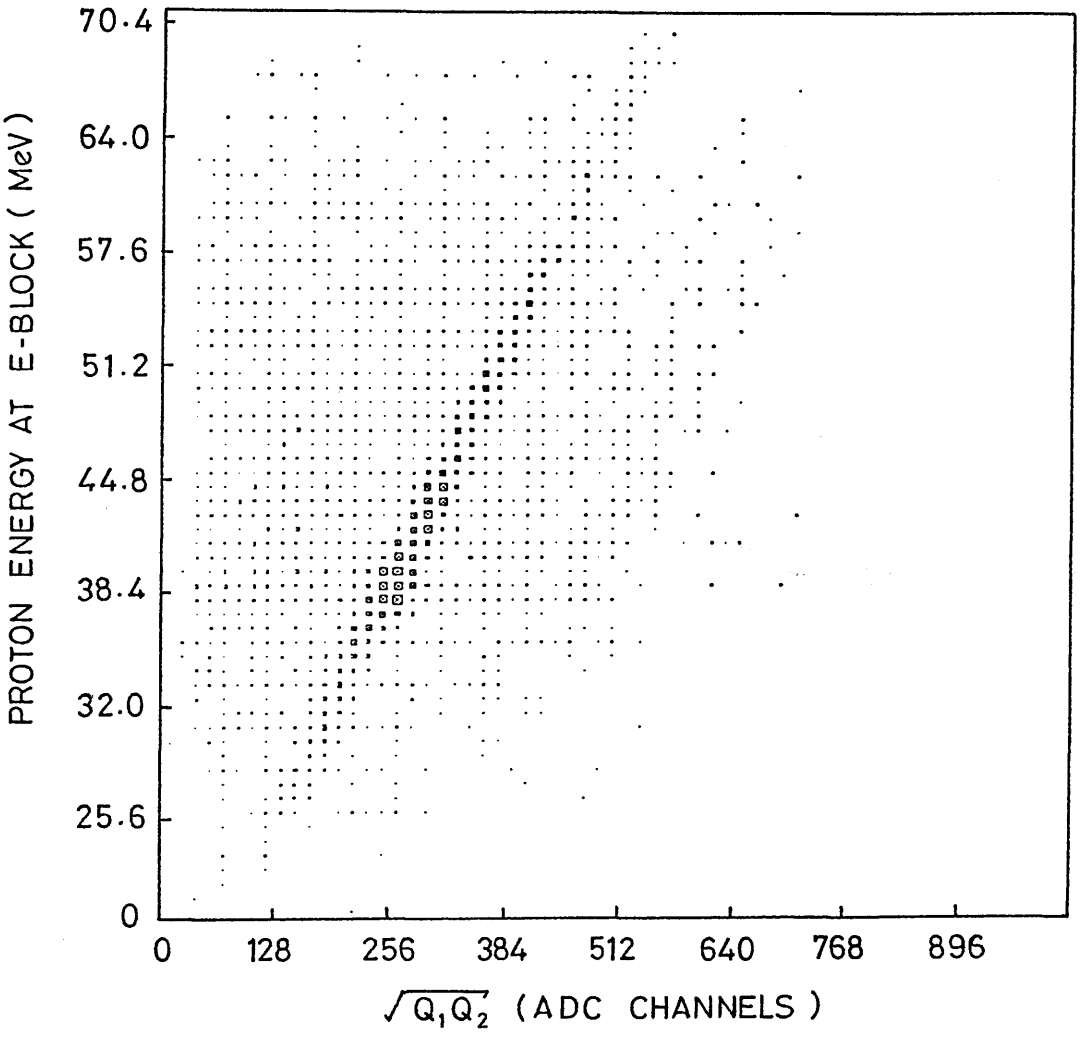

Figure 3.5: Calculated proton energy (assuming two-body breakup kinematics), corrected for energy losses, vs. $\sqrt{Q_1 Q_2}$, showing a ridge of D(γ,p)n events used for the energy calibration.

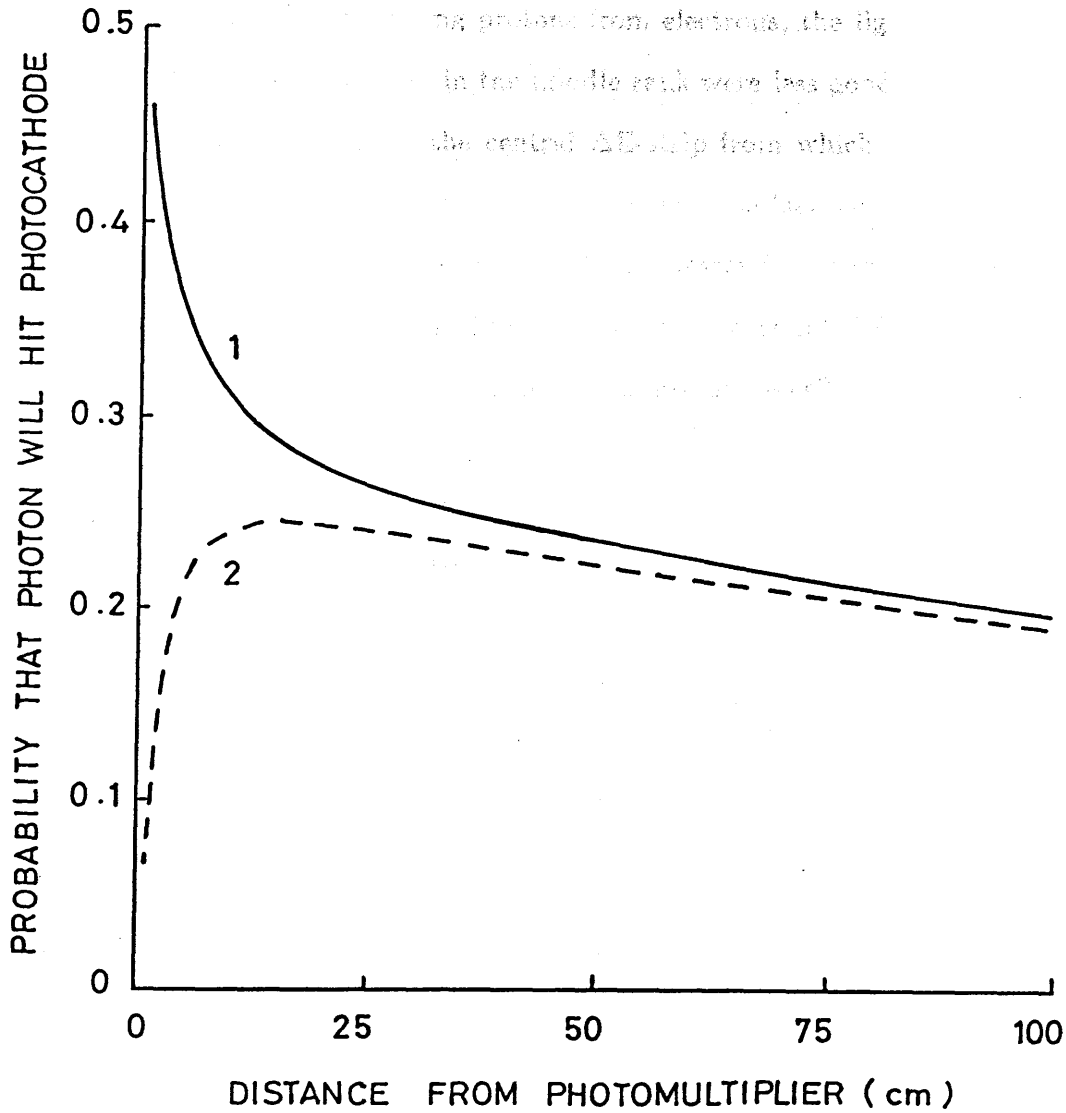

Figure 3.6: Monte Carlo calculation of the scintillator response as explained in the text. The full line (1) is the response function for photons originating from points on the central axis of the scintillator; the dashed line (2) is the result for an axis which is displaced from the central one.

line does not intersect the photomultiplier photocathode. The marked difference at the end nearest the photomultiplier is evidence of poor light collection in this region. Including the effect at both ends, the central 80 cm gives a reasonably reproducible signal regardless of where in the scintillator a particle should arrive.

Although sufficient for separating protons from electrons, the light collection and resolution of the ΔE detectors in the middle rank were less good. Figure 3.4 shows $\ln k$ as a function of y for the central ΔE-strip from which the effective attenuation length was determined to be 71.9$\pm$3.6 cm. The fact that it is a third of that calculated for the E elements indicates higher losses due to multiple reflections. Consequently, energy losses in these elements were accounted for using well established tabulations instead of the analogue signals, as described in Appendix C.

3.3.2 The Neutron Detectors

Position Calibrations

Position data from the detectors can be obtained in a similar way to that of the proton detector elements from time difference methods. Since the proton vertical position resolution is 4.2 cm FWHM at a distance of $\sim$55 cm, the 1-dimensional (2-dimensional) neutron detectors need only have a position resolution of 30 cm FWHM (22 cm FWHM) to match that of the proton detector. The calibration, then, need not be so accurately defined. To match the proton detector in the horizontal direction, the resolution of a 1-dimensional (2-dimensional) detector needs to be 17 cm FWHM (12 cm FWHM). Since the physical dimension of a 1-dimensional detector is greater than this, its resolution is slightly poorer.

In the case of the 1-dimensional detectors, the time difference to position relationship was assumed to be linear throughout the whole length of each one. Time difference spectra were accumulated for each detector, one of which is shown in

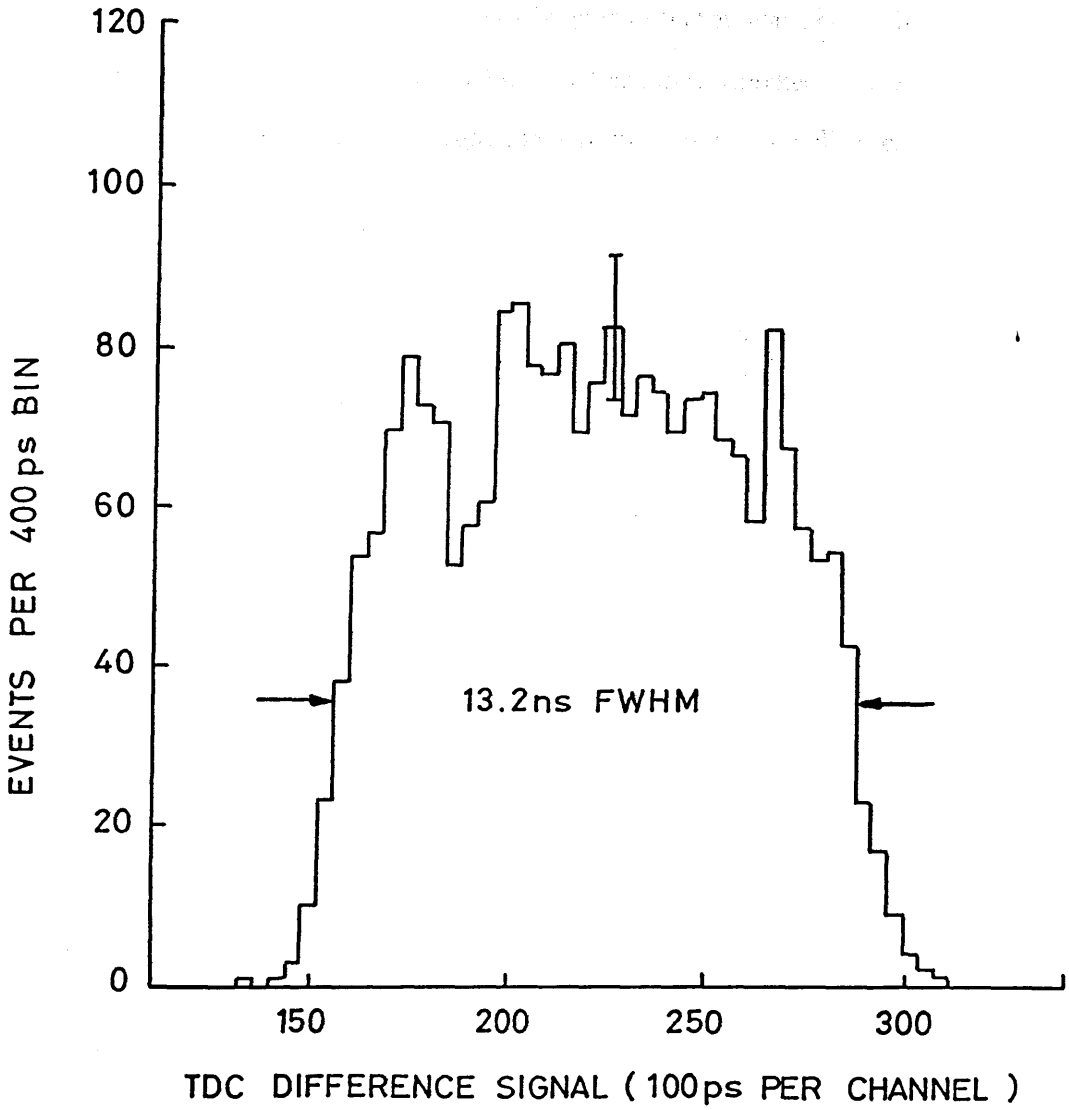

Figure 3.7: Neutron time difference spectrum for one detector. The arrows indicate assumed physical ends of the detector. 13.2 ns is the time taken by the photons to travel through 2 m of scintillator. This gives an effective speed 0.51c of light.

Figure 3.7. In that figure the arrows indicated at each end of the spectrum are assumed to correspond to the physical ends of the detector. The two points allow the linear position calibration to be established.

The square detector position calibration was determined during bench tests of the detector using cosmic rays. A small trigger detector was set up in coincidence with it and placed at points on a 10 cm×10 cm grid marked out on the surface of the detector wrapping. Accumulating timing spectra for different points and measuring the peak positions, a contour plot was built up as shown in Figure 3.8. The contours are approximately concentric about the photomultiplier with no significant variation in separation between them, except at very far distances from the photomultiplier. The average effective speed of light through the scintillator was deduced to be $0.43c$. This differs from the expected value of $0.63c$ because of multiple reflections of the light on the way to the photomultiplier.

A simple algorithm to determine position was tried. Time difference from signals at opposite ends of the two diagonals were first established and then the frame of reference was rotated 45° to a frame where the axes were parallel to the edges of the detector. Hence, position was obtained from the expressions

$$\begin{aligned} x &= \tfrac{1}{\sqrt{2}}(r_1 + r_2 - r_3 - r_4) \\ y &= \tfrac{1}{\sqrt{2}}(r_1 - r_2 - r_3 + r_4) \\ r_i &= v\tau_i(T_i - T_i^0) \quad (i = 1,2,3,4) \end{aligned} \tag{3.3}$$

where v is the effective velocity of light mentioned above, τ_i is the TDC channel to time conversion factor, T_i is the TDC channel, and T_i^0 is the time zero channel. The T_i^0 were accounted for empirically by accumulating the diagonal time difference spectra and calculating the shifts required to centre the spectra about zero.

Figure 3.9 shows the comparison between the real positions and those obtained from the algorithm during bench tests. The algorithm is seen to be very successful everywhere except at points near the edges of the scintillator and not too near

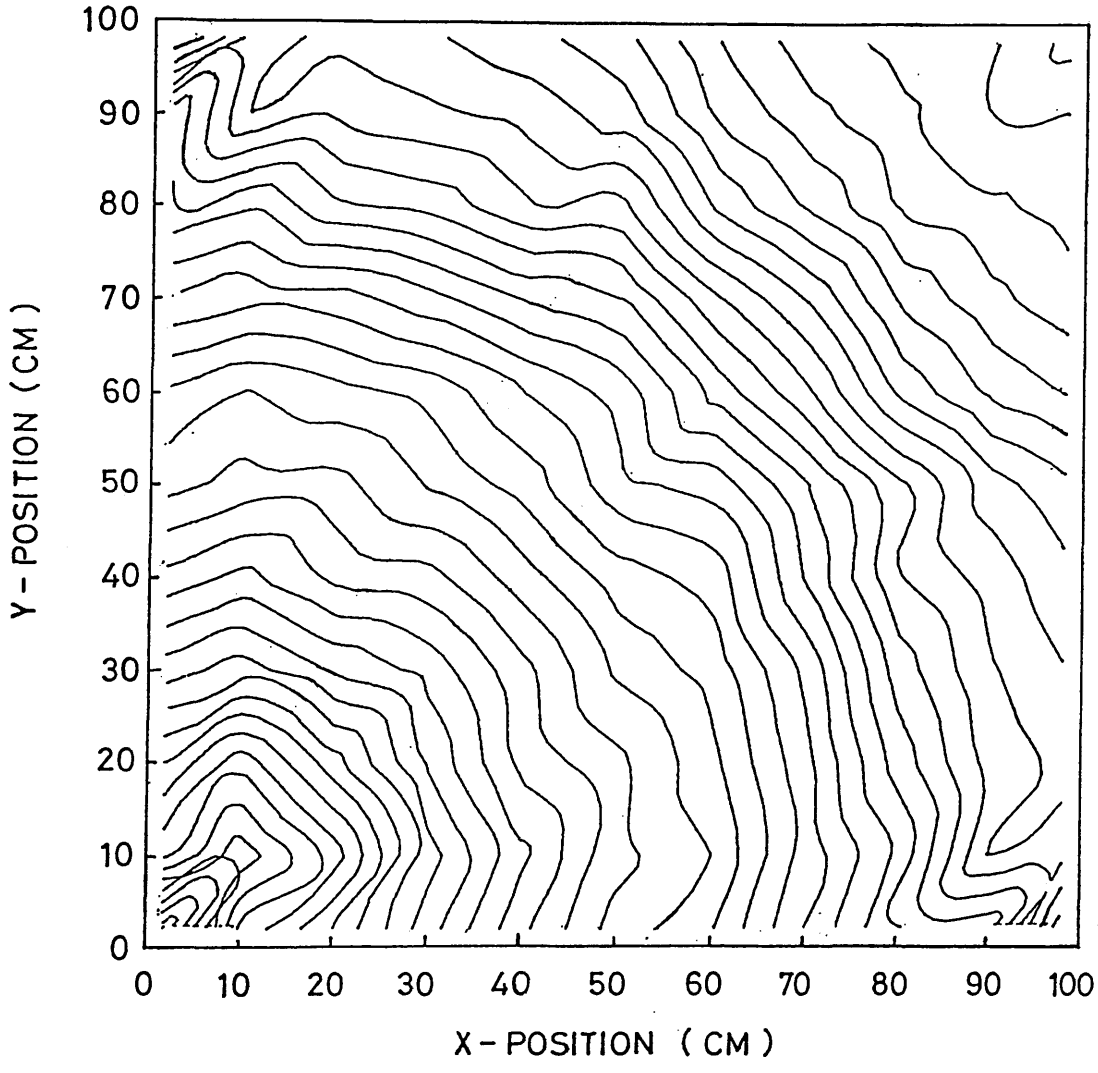

Figure 3.8: Neutron detector time contours seen by one photomultiplier situated at the bottom left corner for points over the whole detector. Each contour represents 0.5ns.

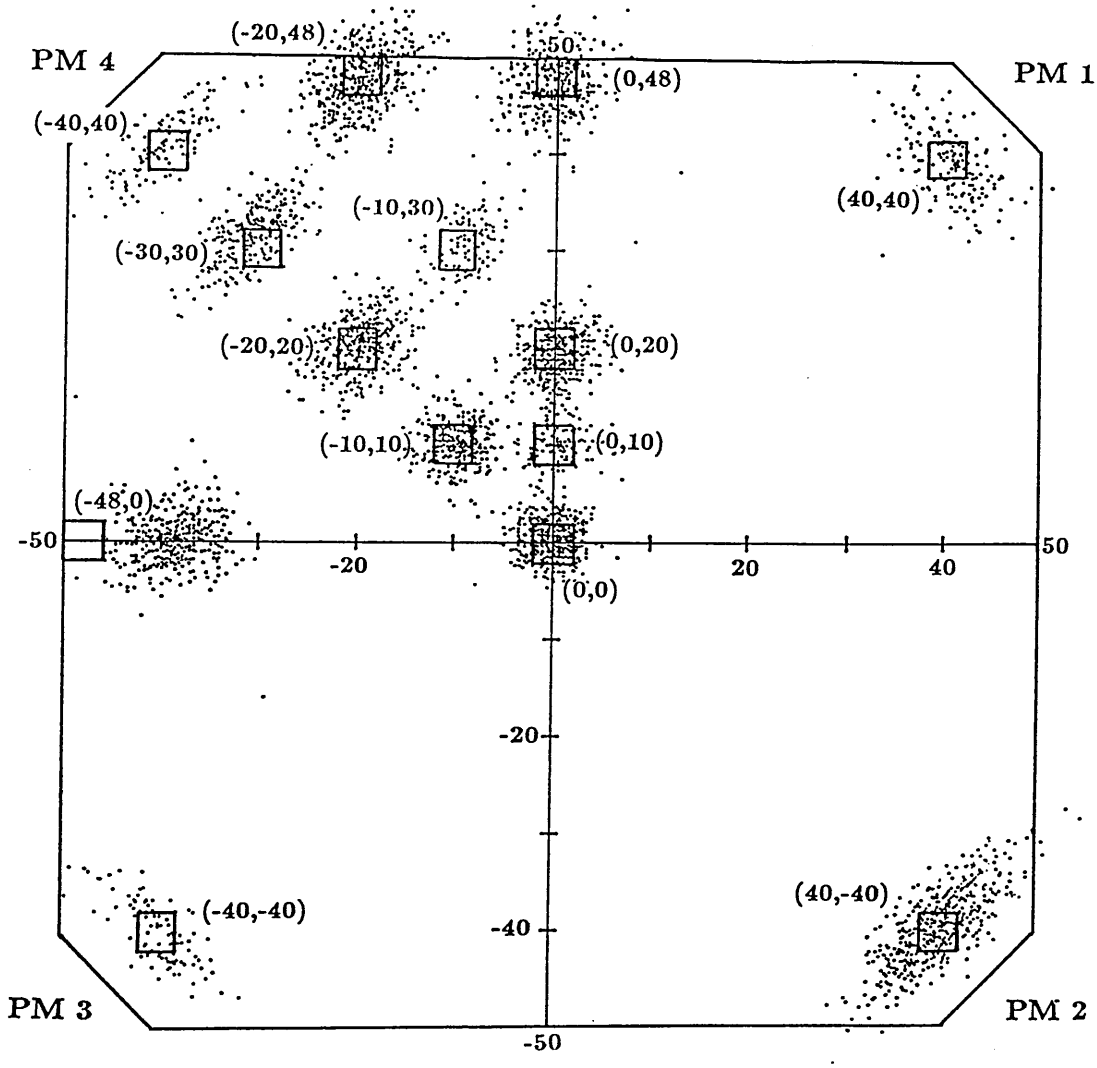

Figure 3.9: Comparison of actual detection points (indicated by squares) with those obtained from the algorithm (dots). Cosmic rays were used and the position was determined by a small trigger detector in coincidence. PM–photomultiplier tube.

any one photomultiplier. For the point shown at the left hand edge, the algorithm places it 11 cm too far towards the centre. It was found that at positions > 13 cm in from the edge the effect was negligible. Despite ambiguities in position determination in this region the algorithm was sufficiently good to match the position resolution of the proton detector.

Energy Calibration

TDCs were used to measure the time of flight of neutrons from the target, from which the neutron energy was calculated. These were set to a full range of 200 ns with each TDC channel nominally spanning 100 ps. A check using cables of known length showed that the gradient was in fact 98 ps per channel. As shown in Figures 2.10 and 2.11, each neutron TDC was started by the first signal arriving from the FPD and stopped by the signal from the corresponding neutron detector photomultiplier.

Owing to a low efficiency-solid angle product compared with that of the proton detector, insufficient statistics prohibited the use of the D(γ,n)p reaction as a means of calibrating the energy response of the neutron detectors. Therefore, to determine t_0 i.e. the TDC channel corresponding to the time when the neutron was ejected from the nucleus, each detector was wheeled directly into the photon beam at a known distance upstream of the target and used itself as an active target. A low flux beam was chosen to reduce random coincidences between the proton detector and the FPD. In this way the neutron detector start times were unambiguously defined. Discrimination thresholds on the proton detector were set to a minimum in order that atomic electrons from the neutron detector would produce X-triggers enabling events to be recorded. The times measured were made by a tagging electron in the FPD and the photon in the neutron detector. Since the cables from the FPD to the CAMAC crate are approximately time-matched

and both particles travel at the speed of light, there ought to be a constant time difference between them which is independent of where the recoil electron hits the FPD. As expected, a clear peak was obtained (see Figure 3.10).

The shape of the spectrum in Figure 3.10 however, is seen to be slightly asymmetrical. This arises because each TDC can be started by any one of the channels on the FPD and no account has yet been taken of slight variations in their cable lengths. Consequently, Figure 3.10 is a superposition of contributions from the 91 FPD elements, each of which must be time-shifted to reveal the true peak. The method of evaluating these shifts is described later in Section 3.4. These were applied event by event to the data. A further correction was necessary arising from a logical FIFO unit which fanned the pattern unit OR signals together. The unit provided the stop signal for the electron-proton TDCs and also the start signal for the neutron TDCs. The relative times that the two signals emerged from the FIFO depended on which part of the FPD the input signal originated from. The necessary corrections were evaluated and applied event by event to the data. An example of a resulting spectrum after all the corrections were made is shown in Figure 3.11 showing clearly the t_0.

Each corrected neutron TDC time signal is a sum of essentially three terms:

- t_f, the neutron flight time,
- $t_c^i \quad (i = 1, 2)$, the time for the signals to pass along the cables to the TDCs, which is constant, and
- t_s^i, the time taken by the scintillation light to travel from the interaction position to the photomultiplier.

To eliminate t_s^i, in the case of the 1-dimensional detectors, the two time signals were added. Thus $t_s^1 + t_s^2$ is constant since it is the time for the photons to travel through the whole length of the scintillator. The t_0 measurement included this as

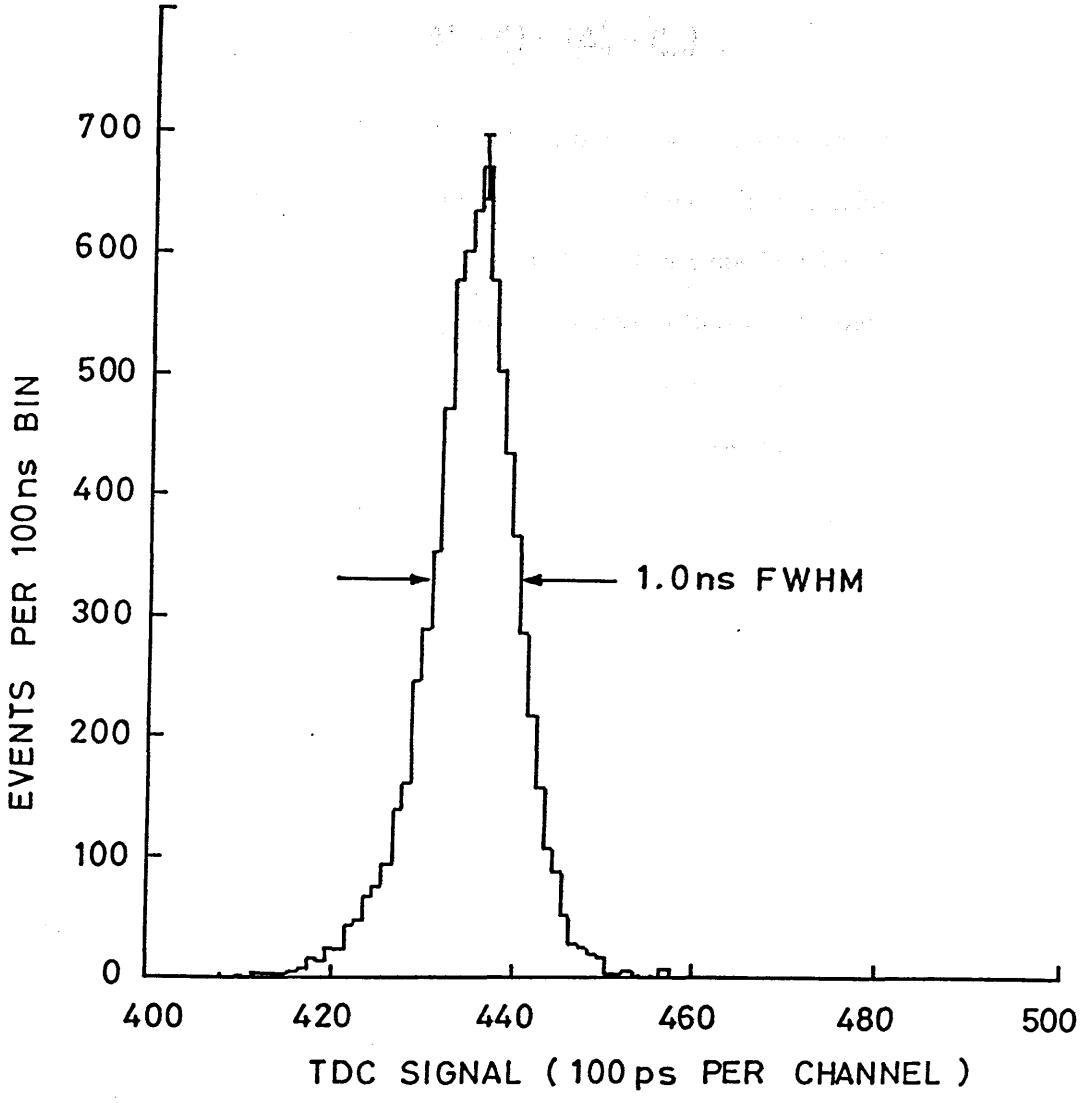

Figure 3.11: t_0 measurement: A corrected neutron TDC spectrum.

well as the effect of the cables and so subtraction of the sum of the two t_0 values from the measured sum yields the flight time of the neutron.

In the case of the square, the terms t_s^i $(i = 1,2,3,4)$ could be calculated explicity from the expression

$$t_f = (\Delta^i - t_s^i) - (\Delta_0^i - t_{s,0}^i)$$

where Δ^i is the contents of TDC i, t_s^i is as above, calculated from the interaction position in the detector and the effective speed of light in the scintillator, Δ_0^i is the measured time zero of the TDC, and $t_{s,0}^i$ is the time for the photons to get to photomultiplier i from the the position of interaction of the beam during the time zero measurement. In fact, the average value of those obtained from the four photomultipliers was used to reduce the effect of variations in the accuracy of position determination in the detector.

3.4 Selections on Raw Data

Selecting "(γ,pn)-like" Events

Since only a coincidence between the proton detector and the FPD is required to generate an interrupt, a large number of events recorded were such that no neutron detector fired[2] at all. These events are clearly useless for present purposes and consequently must be selected out and discarded. To do this, the TDCs for each neutron detector (either two in the case of the 1-dimensional detectors or four in the case of the square) were examined to test whether it fired or not. If exactly one detector of the array met this requirement the event was kept. "Exactly one fired" was chosen rather than "one or more fired" as an acceptable criterion since ambiguity as to which detector fired would remain if the latter had been chosen.

[2]A neutron detector is said to have "fired" if all of its corresponding TDCs record a signal within their full ranges.

Fraction of events which do not fire a neutron detector	=	$86.88 \pm 0.07\%$
Fraction which fire at least one detector	=	$13.12 \pm 0.02\%$
Of those which fire at least one, fraction which fire exactly one	=	$94.73 \pm 0.20\%$
Of those which fire at least one, fraction which fire more than one	=	$5.265 \pm 0.035\%$

Table 3.2: Population of event categories after a coincidence with the neutron detector array is required.

The distribution of event types is shown in Table 3.2. Corrections for the numbers of "multiples" were made to the final yields at a later stage.

Separating Protons from Other Particles

The electron reject circuit described in Chapter 2 was successful in excluding nearly all atomic electrons which entered the proton detector. Figure 3.12 shows an E-ΔE scatter plot of the hardware-summed signals seen by the electron reject circuit. The electron-reject discrimination threshold is indicated. Further software techniques were used to remove a ridge of deuterons which lie on a locus above the protons, as becomes clearer on further analysis.

The configuration of the detector elements allows the array to be considered as 15 distinct pixels (five ΔE strips $\times$ three E blocks) where each is treated as a distinct detector. Instead of considering the hardware–summed analogue signals, the E signal is taken from the two ADCs on the E-block which fired and the ΔE signals from the corresponding ΔE ADCs. As described in Section 3.3.1, the geometric mean of the two signals gives a better measure of energy deposited in the scintillator than the arithmetic mean. Figure 3.13 shows the resulting E-ΔE plot for the central pixel where protons are easily distinguished. A region is defined within which protons lie for each pixel. If the event lies within at least one of the 15 regions then the event is accepted, thereby separating proton events from other events.

It is recognised that there are some cases where an event may pass, say, from one E block into the neighbouring block and deposit a reduced amount of energy in both elements. If a good signal is left in a ΔE element then the event will have a high probability of being outside all selected regions and will thus be lost. The percentage of such events is estimated to be $5 \pm 2\%$. The final yield is corrected for this effect at a later stage.

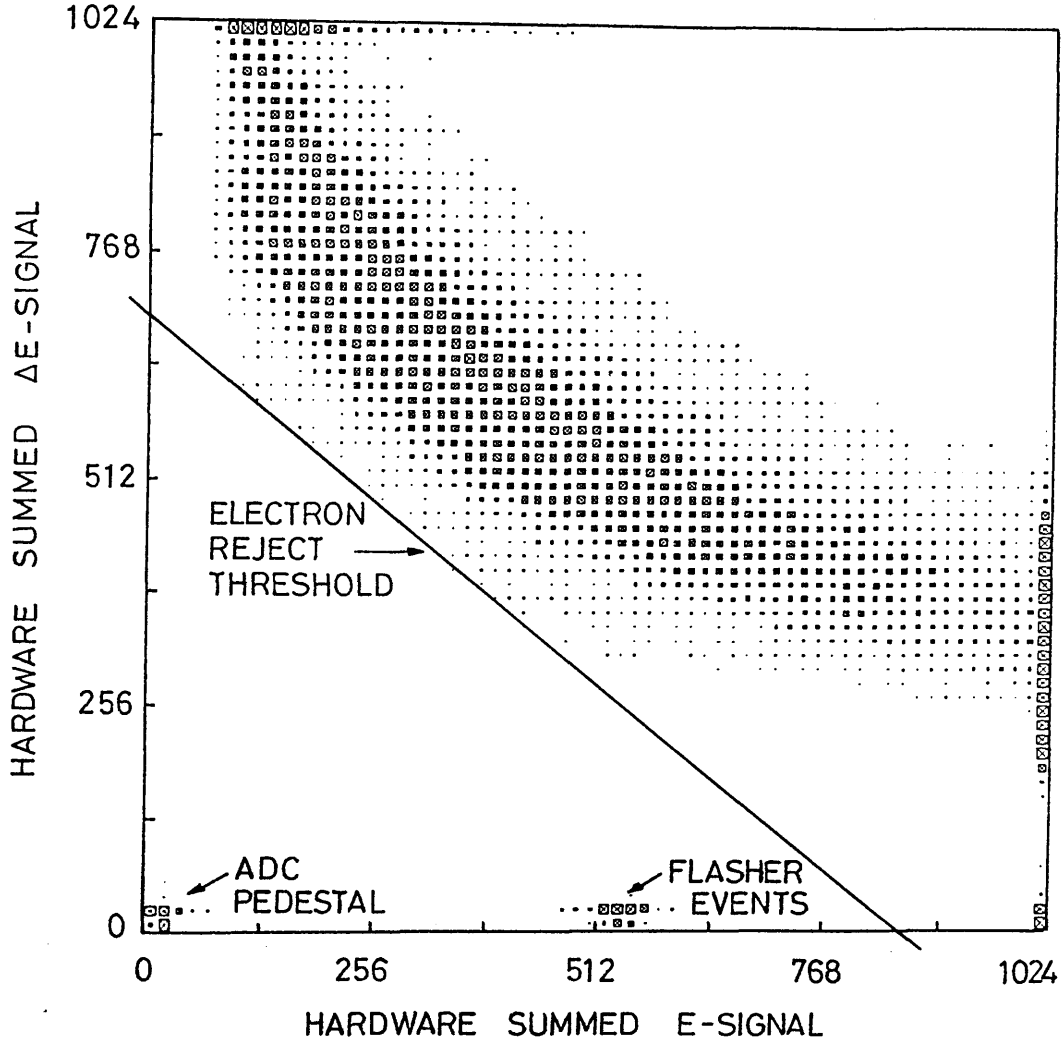

Figure 3.12: E-ΔE plot. The E and ΔE signals are fanned together in hardware. Flasher events are produced by an online stabilised LED used to monitor gain drifts in the photomultipliers. The z-scale is linear.

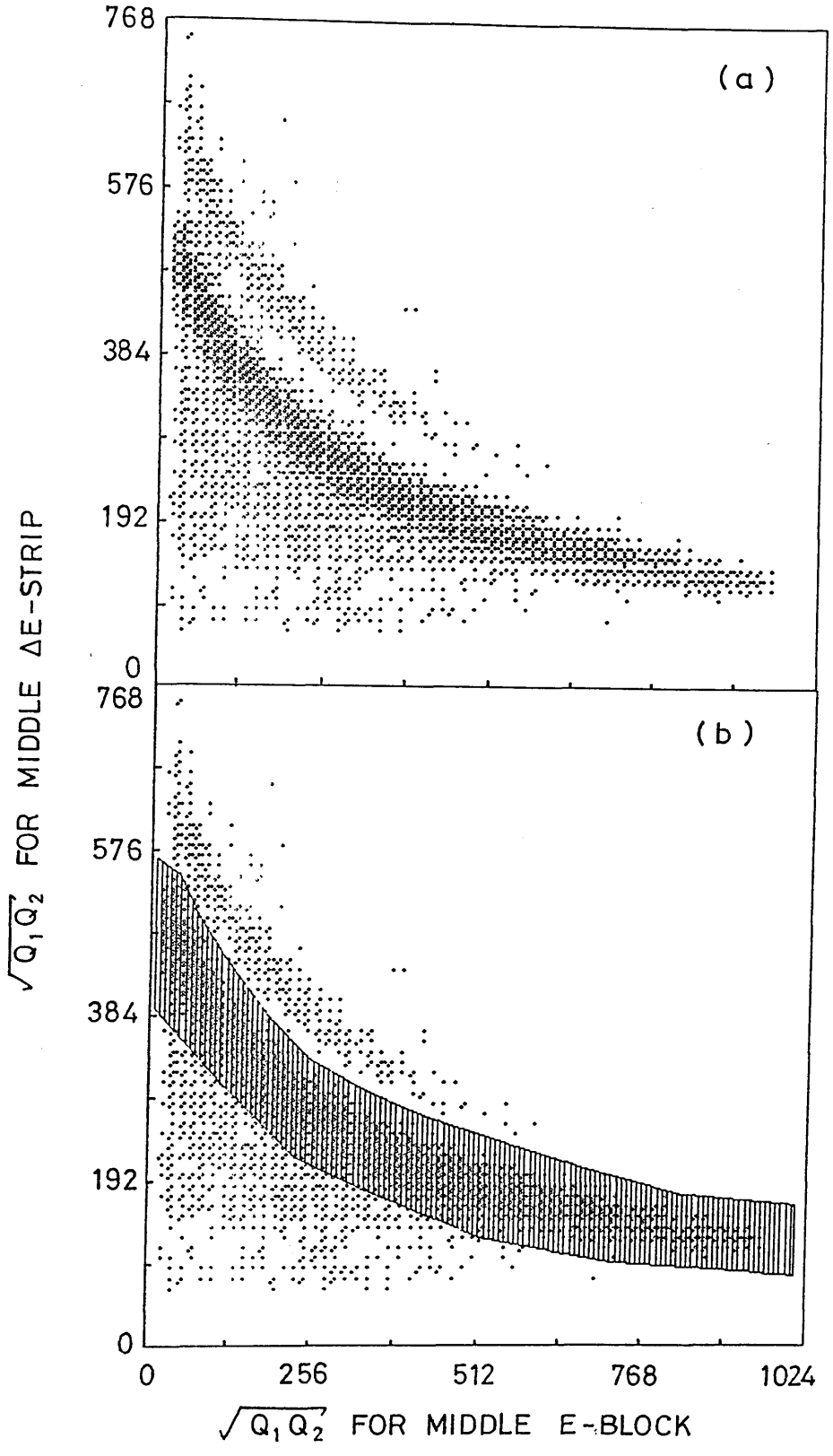

Figure 3.13: (a) E-ΔE plot for central pixel. (b) Defined region used in separating protons from other particles. The z-scale is logarithmic.

Real and Random Coincidences

Figure 3.14 shows a spectrum from the TDC measuring the time between the X-trigger pulse and the first signal received from the FPD. The spectrum has been accumulated after the above selections have been made. The finite width of the spectrum indicates the width of the enabling gate pulse sent to the PUs. The leftmost peak is a spurious effect caused by a pulse from the ladder straddling the leading edge of the gate pulse. In this case the TDC is both started and stopped by the X-trigger, giving rise to a peak. The central peak is the coincidence peak of "prompt" protons which sits on a background of random coincidences.

The spectrum is in fact a superposition of 91 similar spectra, one for each FPD element. Owing to slight differences in the cable lengths from each element of the FPD to the electronics, the coincidence peaks from each element do not appear in the same TDC channel, as illustrated in Figure 3.15. The peak in Figure 3.14 can be sharpened if all the contributory peaks are lined up.

The technique employed to measure the tagging efficiency (see Section 2.9) is ideal for measuring the shifts required for each element. Here, the X-trigger is produced by a photon, and the FPD pulse is produced by a highly relativistic electron ($v_e > 0.99995c$). Thus the relative positions of peaks free of spreading due to variable flight times can be measured. The resultant shifted TDC spectrum is shown in Figure 3.16.

Further improvements are possible before the data selection is made. It will be noticed that the coincidence peak in Figure 3.14 sits on a sloping random background. It can be shown (see Appendix B) that the random region to the left of the peak consists of two contributions:

1. Protons produced by untagged photons, that is, where the recoil electron is not detected in the FPD at all but the timing is determined by a random coincident electron, and

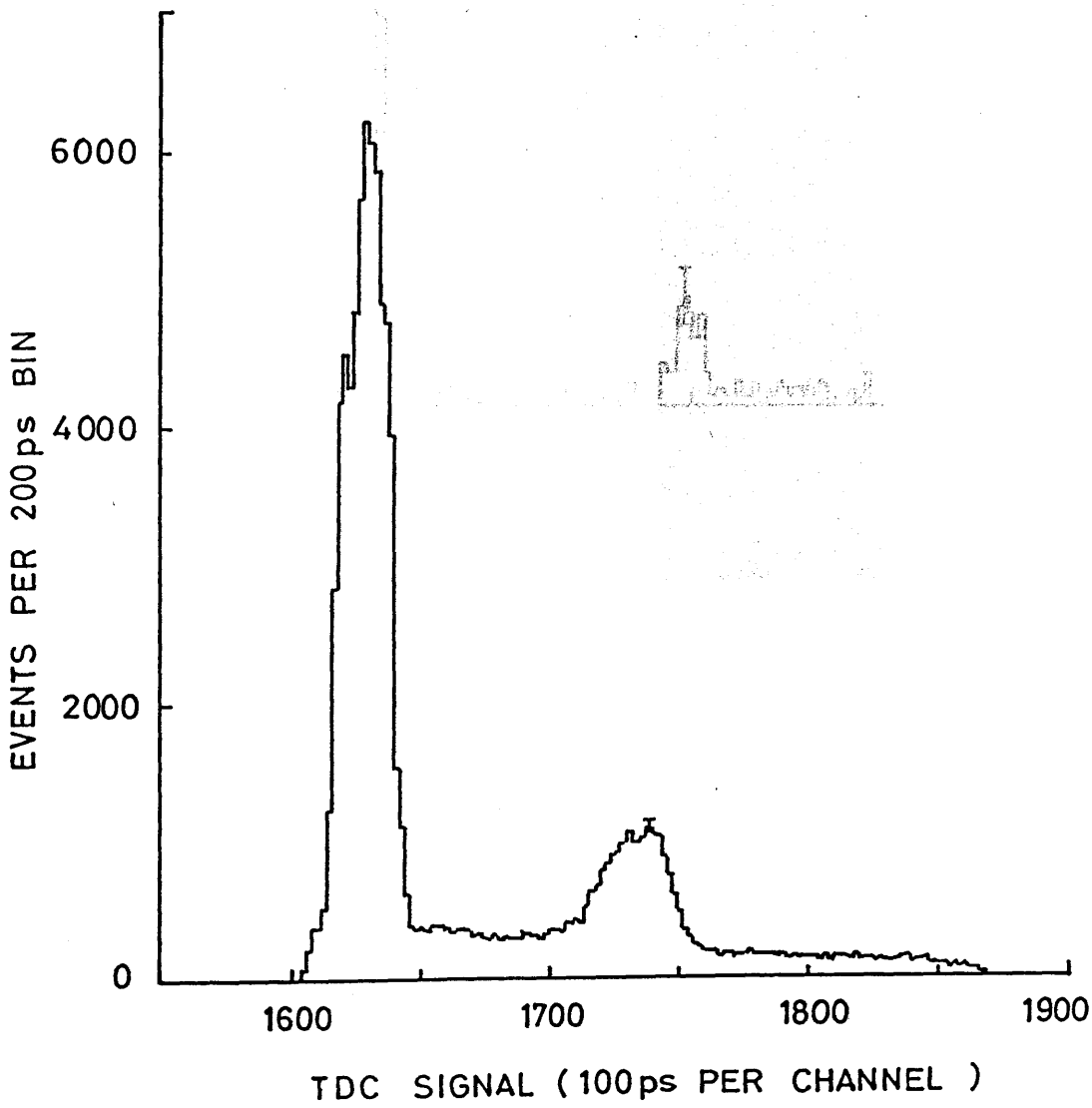

Figure 3.14: A raw TDC spectrum for whole FPD after proton selection.

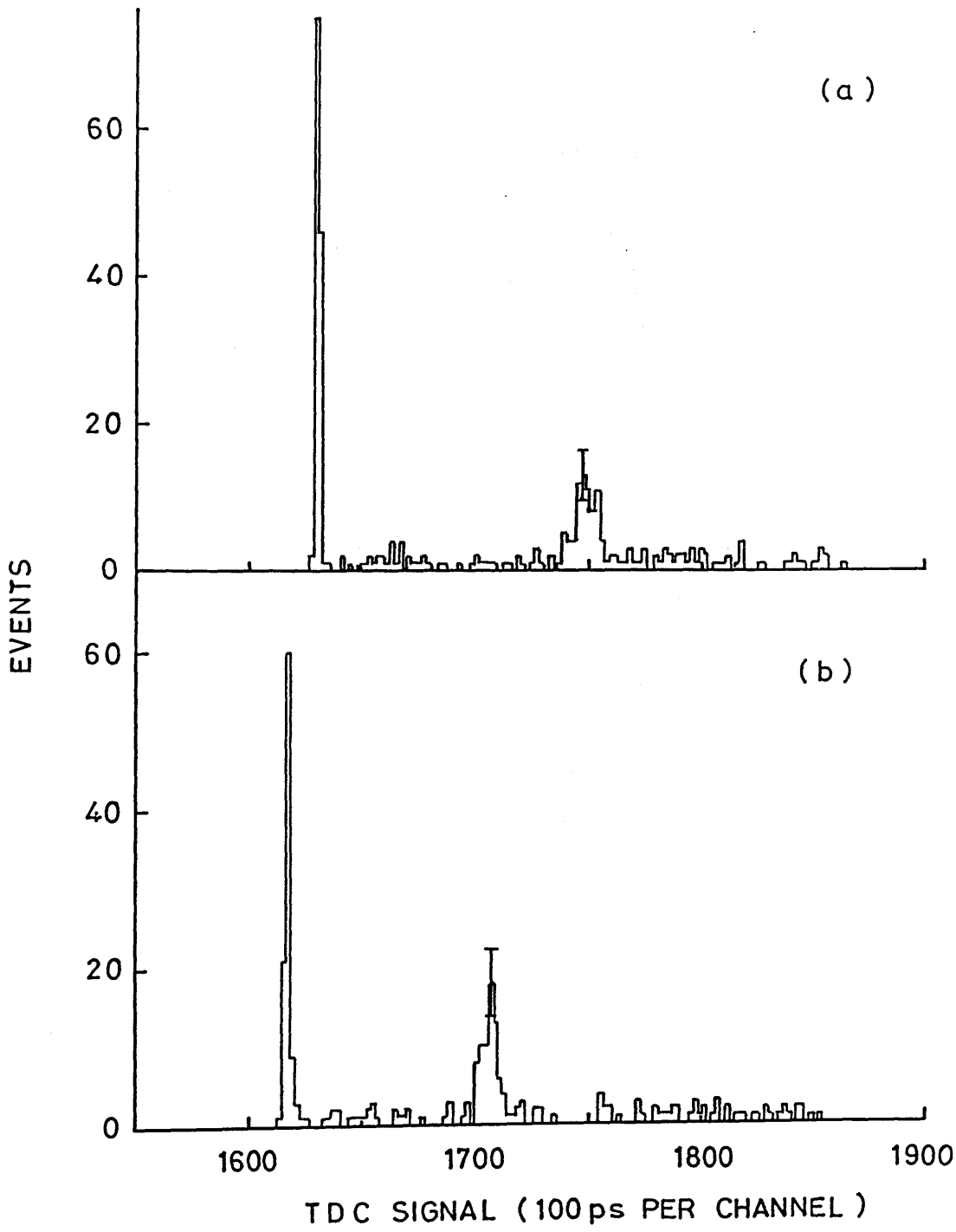

Figure 3.15: (a) Contribution to the overall TDC from channel 47. (b) Contribution from channel 63. Events which fire only one FPD channel are shown.

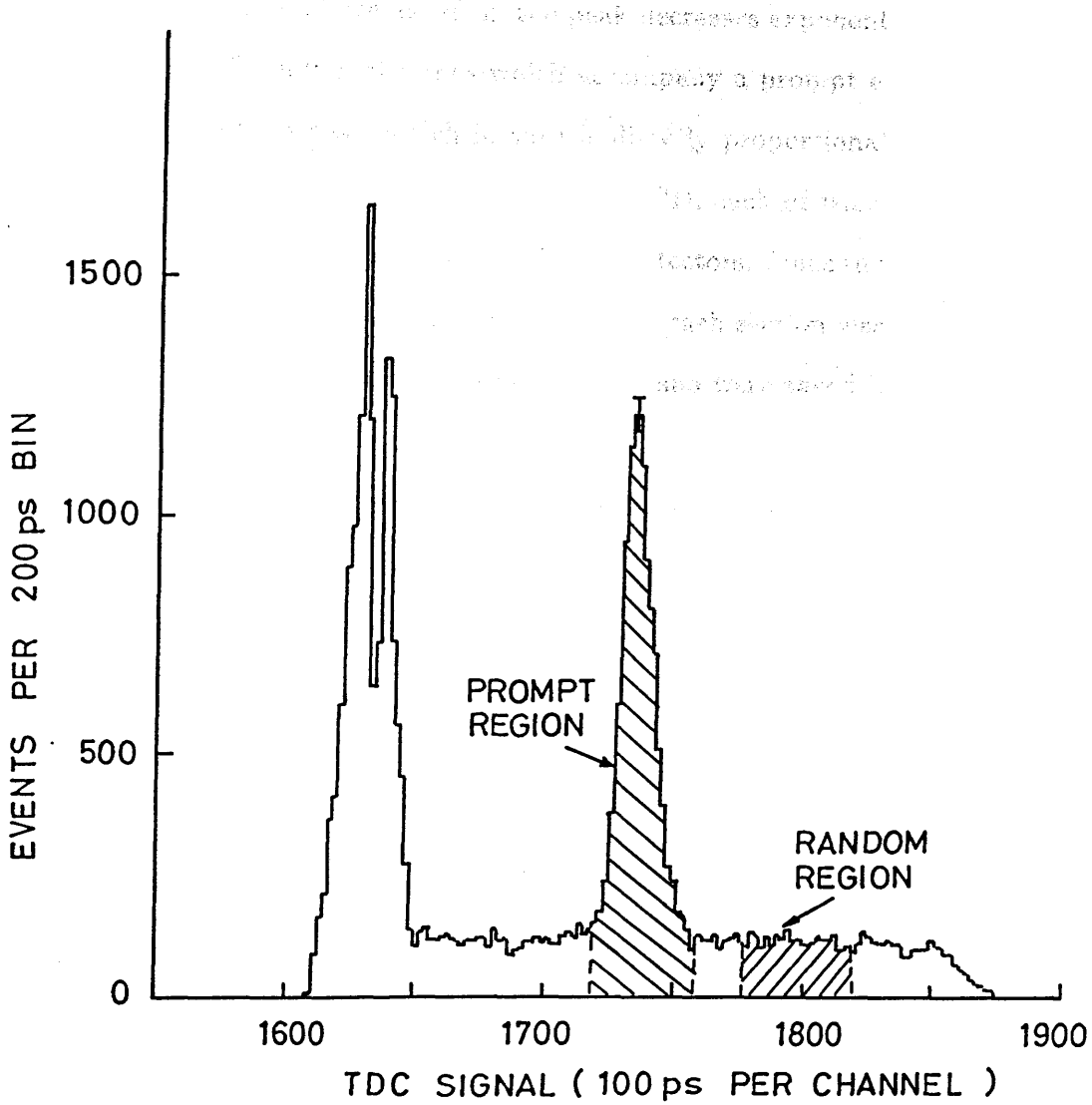

Figure 3.16: Time-Shifted TDC spectrum for whole FPD after proton selection, showing examples of prompt and random regions.

2. Events produced by tagged photons but where a random electron hits the FPD first and makes the timing.

In the latter case *bona fide* events are taken out of the coincidence peak by random electrons. The number of events left in the peak decreases exponentially with the average number of random electrons which accompany a prompt electron to the ladder within the time gate, which in turn is directly proportional to the beam intensity. To reduce this effect, sections of the FPD, each of which was had an associated TDC, were considered as independent detectors. Since the sections were each $\sim \frac{1}{6}$th of the whole, the random count rate in each section was $\sim \frac{1}{6}$th of the total. Consequently, a greater number of good events were saved by considering the TDC of each section separately.

In order to apply the correct cable corrections to a section TDC, it is necessary to know which channel of the FPD fired. Hence, in accumulating the corrected spectrum, only events where one channel in the section fired were accepted. Limits were set above and below the peaks of each corrected TDC and an event was accepted if exactly one of its TDC signals arrived within these limits. Again, "exactly one" was chosen as an acceptable criterion to avoid ambiguity.

Random coincidences included in the above selections needed to be corrected for. Since all randoms have on average the same properties, it is acceptable to account for these by selecting randoms from a similar region outside the peak. Limits were set for five such "random" regions to improve statistical accuracy (two from the left of the peak and three from the right) and data were selected in exactly the same way as for "prompts". If at a later stage a particular spectrum was required, it was accumulated from the prompt data set and then from the random data set and the latter was subtracted from the former.

After the subtraction is performed, only true coincidences remain. However, these constitute only a fraction of the original number, since some must be dis-

carded to avoid ambiguity. This fraction of events is photon energy dependent and is calculated in Appendix B. On average approximately 75% of events are accepted.

3.5 Selections on Calibrated Data

Selecting Events with Prompt and Random Neutrons

As with the electron-proton TDCs, the neutron TDCs also record signals which are random in time arising from, for example, room background, or atomic electrons from the target, or neutrons correlated with protons where the pair is produced by an untagged photon. If a prompt coincidence region can be identified then selections can be made.

Having applied the corrections event by event to the data as described in the determination of t_0 for the neutron detectors, one further correction, which applies only to the data-taking runs with high count rates, can also be applied to those events where a random coincidence in the FPD starts the neutron TDC. Such events can be corrected if the electron-proton TDC on each FPD section is compared with the overall electron-proton TDC.

Figure 3.17 illustrates such a comparison. The dark line at 45° to the axes is due events where the same electron stops both TDCs. The region above the line corresponds to events where an electron stops the section TDC but another electron elsewhere in the FPD arrives first and stops the overall TDC. Clearly, if the electron in the section TDC is prompt (in other words, it is the "true" electron), the resulting neutron time can be corrected by the amount by which the FPD section TDC signal is shifted vertically from the 45° line in Figure 3.17.

Figure 3.18 shows an example of a summed neutron TDC spectrum for one detector after the corrections described above and in Section 3.3.2 were applied. The peak is interpreted as "prompt" neutrons from the target sitting on a random

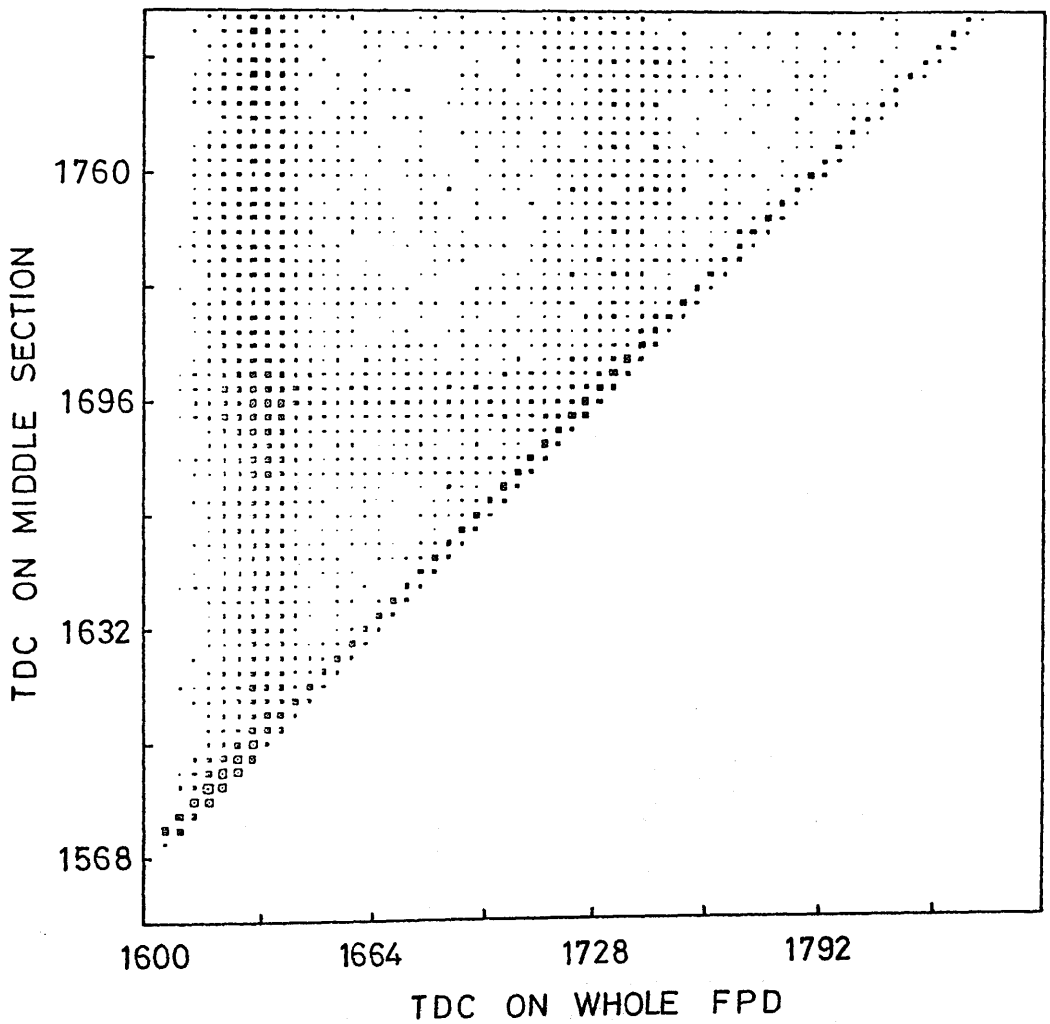

Figure 3.17: FPD TDC timing channels 49 to 64 versus TDC timing whole FPD.

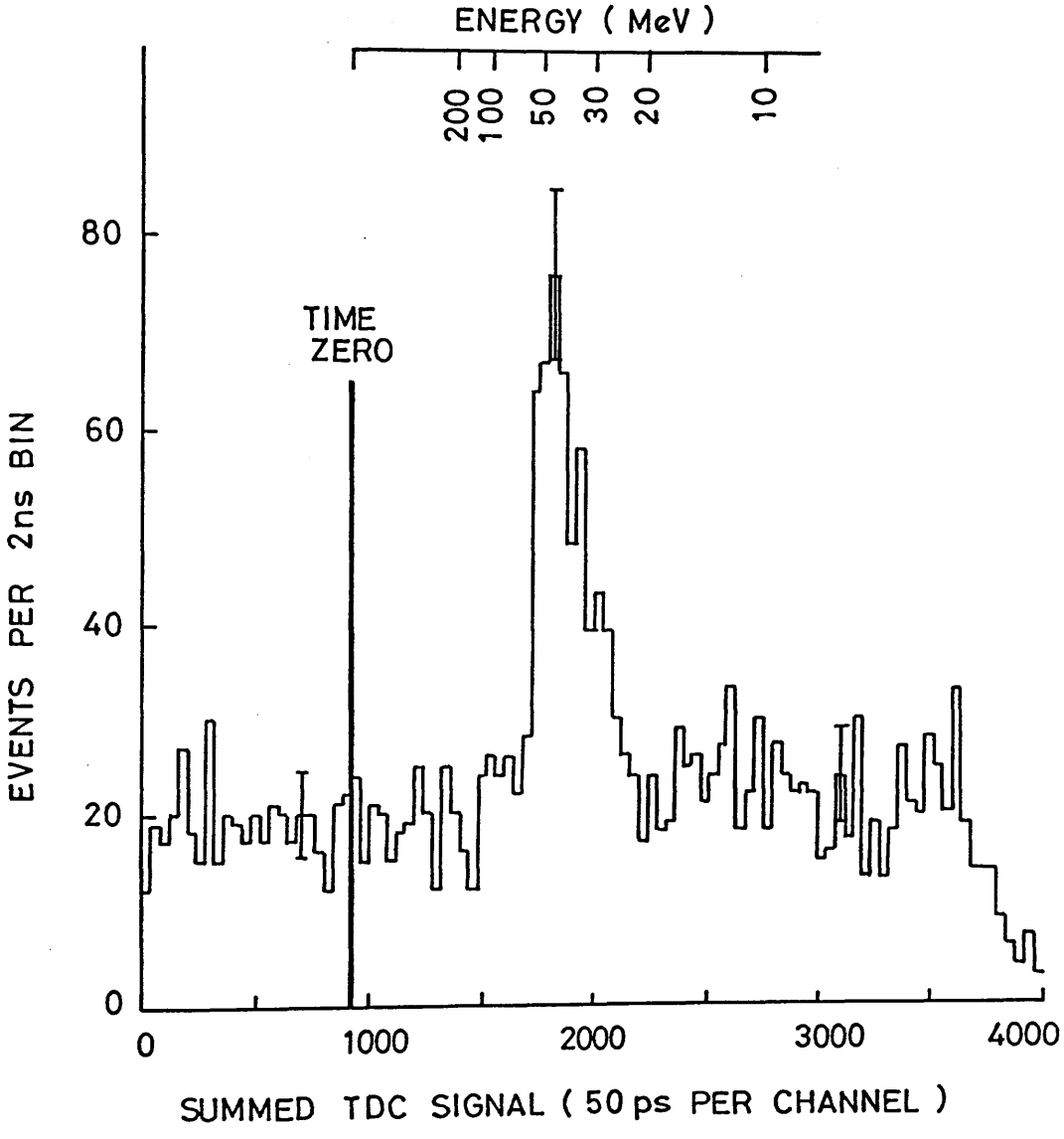

Figure 3.18: Sum of the TDCs (with all corrections included) for a 1-dimensional neutron detector.

background. For the same reasons as for the electron-proton TDCs, the shape of the background is exponential. However, after the selections which have been described up to now have been made, the number of random counts is low enough to assume that the background is flat. Such spectra were examined for each detector to determine the prompt region and a random region of the same time width.

Exactly the same procedure was carried out for the electron-proton random data sets previously selected as described in Section 3.4 i.e. selections were made from the neutron time of flight spectra over the same time bins as for the electron-proton prompt data sets.

Setting the Neutron Detector ADC Thresholds

It was found advantageous to make a further selection from the data by setting a software threshold on the geometric mean of the analogue output signals from the neutron detectors. Figure 3.19 is a scatter plot of $\sqrt{Q_1 Q_2}$ versus the summed TDC signal (with corrections included) for one of the 1-dimensional detectors. It shows clearly a band of events of low pulse height randomly distributed in time. These are the random events in Figure 3.18. The locus of events of higher pulse height near the centre are interpreted as prompt neutrons. Clearly, putting a higher software threshold on $\sqrt{Q_1 Q_2}$ will reduce the randoms quite markedly, while retaining most of the neutrons. The reduction in the latter events can be accounted for in the neutron detector efficiency if the software threshold is well known.

Figure 3.19 is replotted in Figure 3.20 with the x-axis converted to energy. The solid line corresponds to neutrons which transfer all their energy to a proton in the scintillator which then loses that energy in the usual way. Since $\sqrt{Q_1 Q_2}$ is approximately proportional to light output, the limit is fitted by the light out-

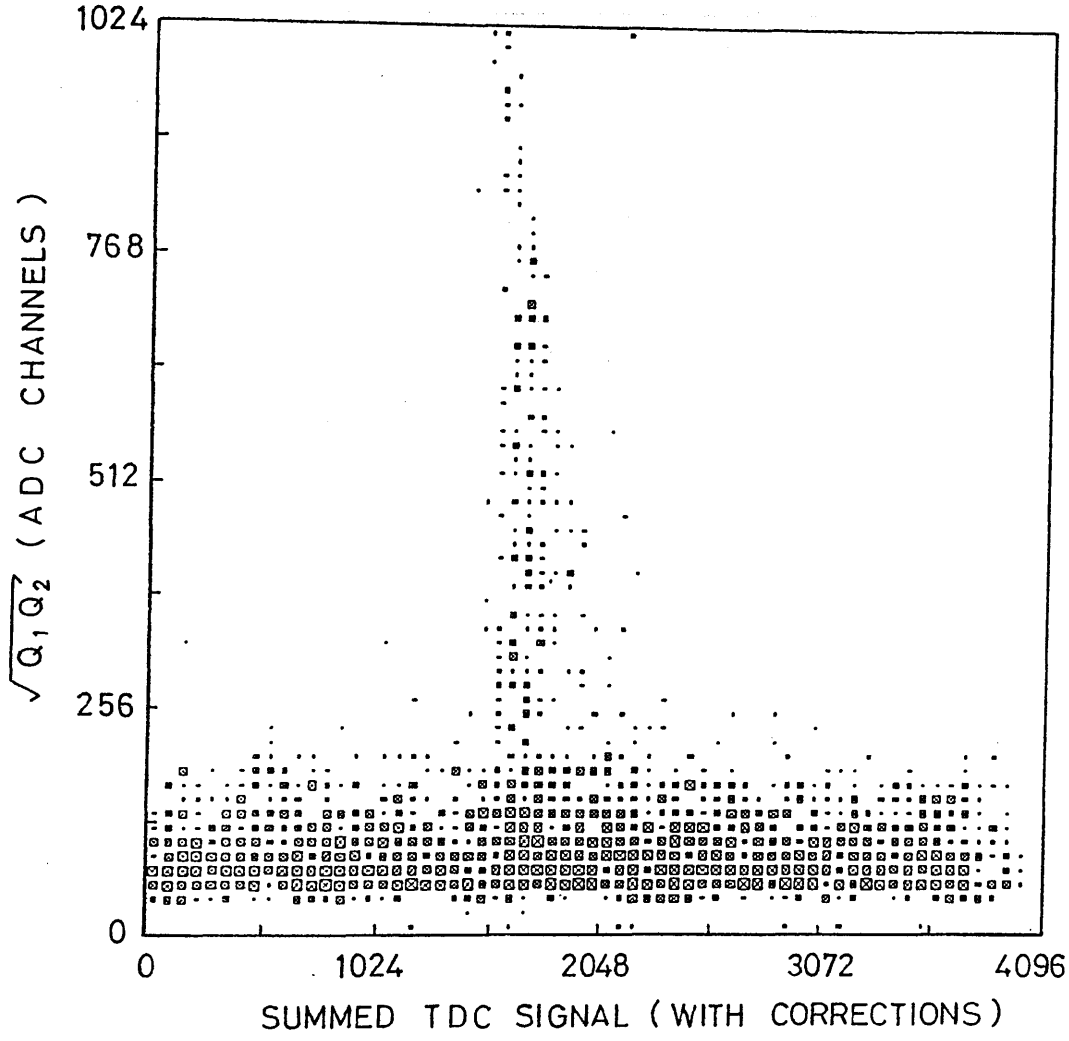

Figure 3.19: $\sqrt{Q_1 Q_2}$ vs. $t_f + t_0$ for one 1-dimensional neutron detector.

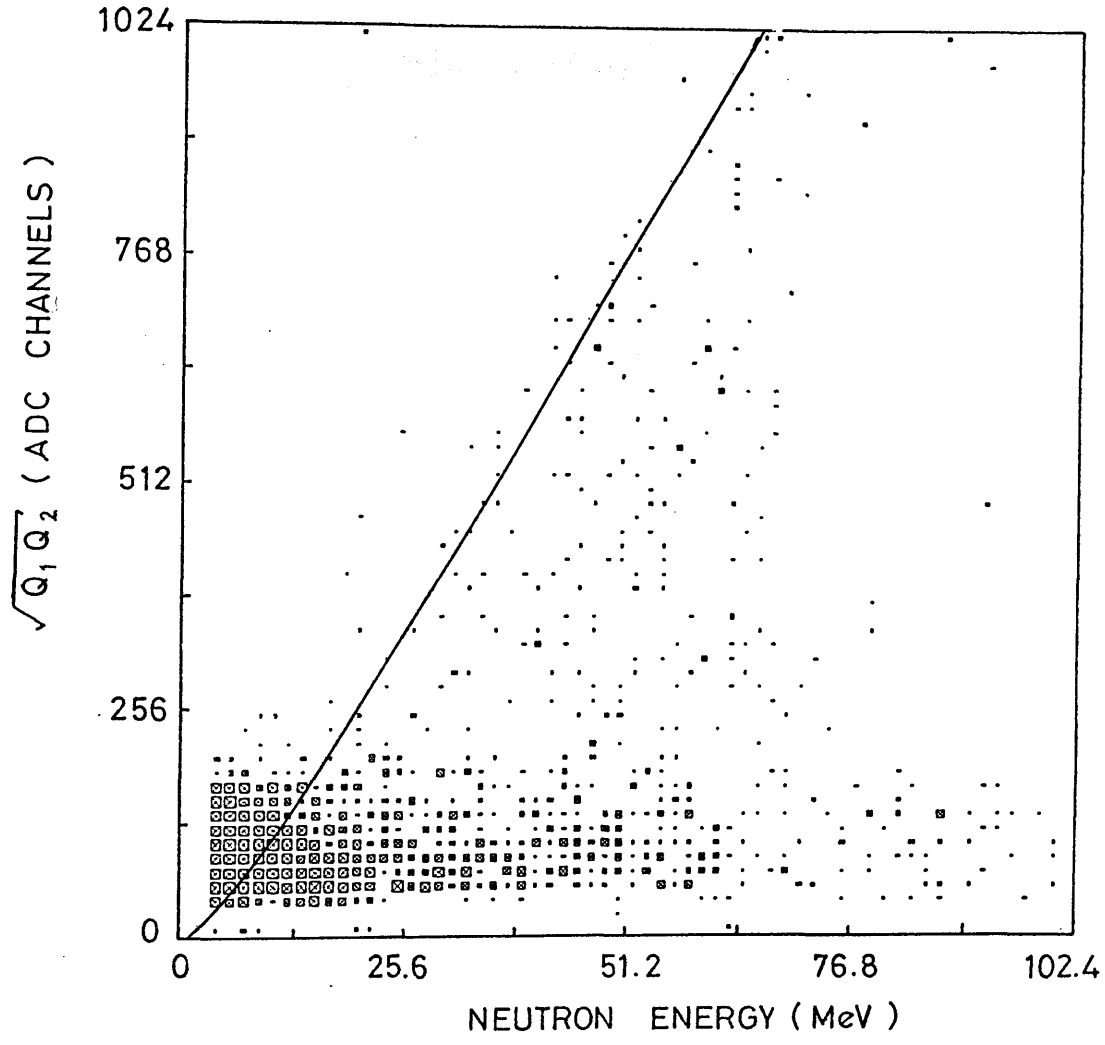

Figure 3.20: $\sqrt{Q_1 Q_2}$ vs. kinetic energy for one 1-dimensional neutron detector. The line is explained in the text.

put function obtained from Gooding and Pugh [86]. The line provides a way of quantifying for each detector the level of threshold set. A level of 10 MeV neutron energy was chosen as a suitable value for the threshold which was then applied to the data.

3.6 Monte Carlo Simulation Programs

The kinematics of deuteron photodisintegration are such that for a given photon energy E_γ and neutron angle θ_n (or any other pair of variables) all other variables are fixed. In particular the angle θ_p of the proton is fixed. In the case of a quasideuteron moving inside a complex nucleus and a known E_γ and θ_n, θ_p would be expected to lie within a cone of possible angles, the precise angle determined by the initial momentum **P** of the quasideuteron. The half angle of the cone is determined by the Fermi momentum of the quasideuteron. In evaluating the cross section $\frac{d\sigma}{d\Omega_n}$ for proton-neutron coincidences, an integration over all proton angles and nucleon energies should be performed. This would be experimentally possible if the proton detector was large enough to intercept all of the cone and both detector arrays had zero thresholds. A position sensitive detector which intercepted only a fraction of the cone would be equivalent to performing the integration over a limited range of the variables. Two Monte Carlo programs have been written to examine the way in which the experimental system selects the data. In both programs two assumptions are made:

1. The tagging efficiency is assumed constant over the photon energy range considered.

2. The neutron detector efficiency as a function of energy is approximated by a step function with the step occurring at the detector threshold.

The second assumption is the poorer of the two but the errors introduced are much

smaller than the errors incurred in correcting the real data for neutron detector efficiencies. The assumptions are considered acceptable for present purposes.

The first program has been written on the basis of Gottfried's quasideuteron model. The program has exactly the same structure as the data analysis program described in Section 3.2. However, the pseudo-data are randomly generated in the first instance. The generated data can be subjected to conditions and the resulting events can be stored for later analysis, in exactly the same way as real data.

Weighted choices of six variables are made:

1. The laboratory photon energy.
2. The quasideuteron momentum (P) and direction (θ_P,ϕ_P).
3. Both neutron direction in the centre of mass of the quasideuteron and the photon (θ_n,ϕ_n).

The probability distributions of the four variables in 1. and 2. are independent and these are chosen first. The distributions of the variables in 3. are, however, dependent on those in 1. and 2. and are chosen last. The photon energy is chosen, weighted by the bremsstrahlung spectrum, the shape of which is estimated from the count rate in the scalers of the FPD, folded in with the ^{2}H(γ,pn) total cross section in the laboratory, obtained from the parameterisations in [112]. The quasideuteron momentum vector is isotropic while its magnitude is chosen from the harmonic oscillator calculations of Gottfried [17] and Smith *et al.* [27] using a root mean square radius of 2.455 fm [111] to fix the oscillator parameters.

The next step is to transform the vectors to the centre of mass of the photon-quasideuteron system, where the total quasideuteron energy is given by

$$E_{qd} = M_p + M_n - E_s - E_x - T_{recoil} \tag{3.4}$$

where M_p and M_n are the proton and neutron masses respectively, E_s is the separation energy for a neutron and proton (27.4 MeV for ^{12}C), T_{recoil} is the residual

nucleus kinetic energy (evaluated through the approximation that $\mathbf{P}_{recoil} = -\mathbf{P}$) and E_x is the residual nucleus excitation energy. To match the data selection procedure, E_x has been chosen to be 0 MeV for two 1p-shell nucleons and 25 MeV for 1s- and 1p-shell nucleons. The neutron direction is chosen according to the ^{2}H(γ,p)n differential cross sections parameterised in [112]. Enough information is now known to determine all other variables.

The second program is based on a phase space decay of the ^{12}C nucleus into a proton, a neutron and a recoil particle in the centre of mass of the whole system. The kinematics of the process are described in Appendix D. When the kinetic energy available to the particles is known the distribution of recoil energy is fixed from which a value is chosen. The angular distribution of the recoil particle is isotropic in the centre of mass frame. The choice of P_{recoil} (and hence T_{recoil}) determines the limits of the variable $T_D = T_p - T_n$, which is uniformly distributed between these limits. The final variable chosen is the azimuthal angle of the neutron about the recoil particle vector in the centre of mass frame.

To simulate the experimental system, four conditions are applied to the pseudo-events generated in both programs:

1. The neutron must be intercepted by the neutron detector array.

2. The neutron must have more than 10 MeV kinetic energy

3. The proton must be intercepted by the proton detector.

4. The proton must have more than 28 MeV kinetic energy

If required, further conditions can be applied to match more detailed selections applied to the real data. The flexibility available for applying conditions has the advantage of allowing the user to apply the program to any experimental system. The cost is, however, reduced efficiency in generating events which the user wishes to examine. For the present system, 0.17 % of all events generated

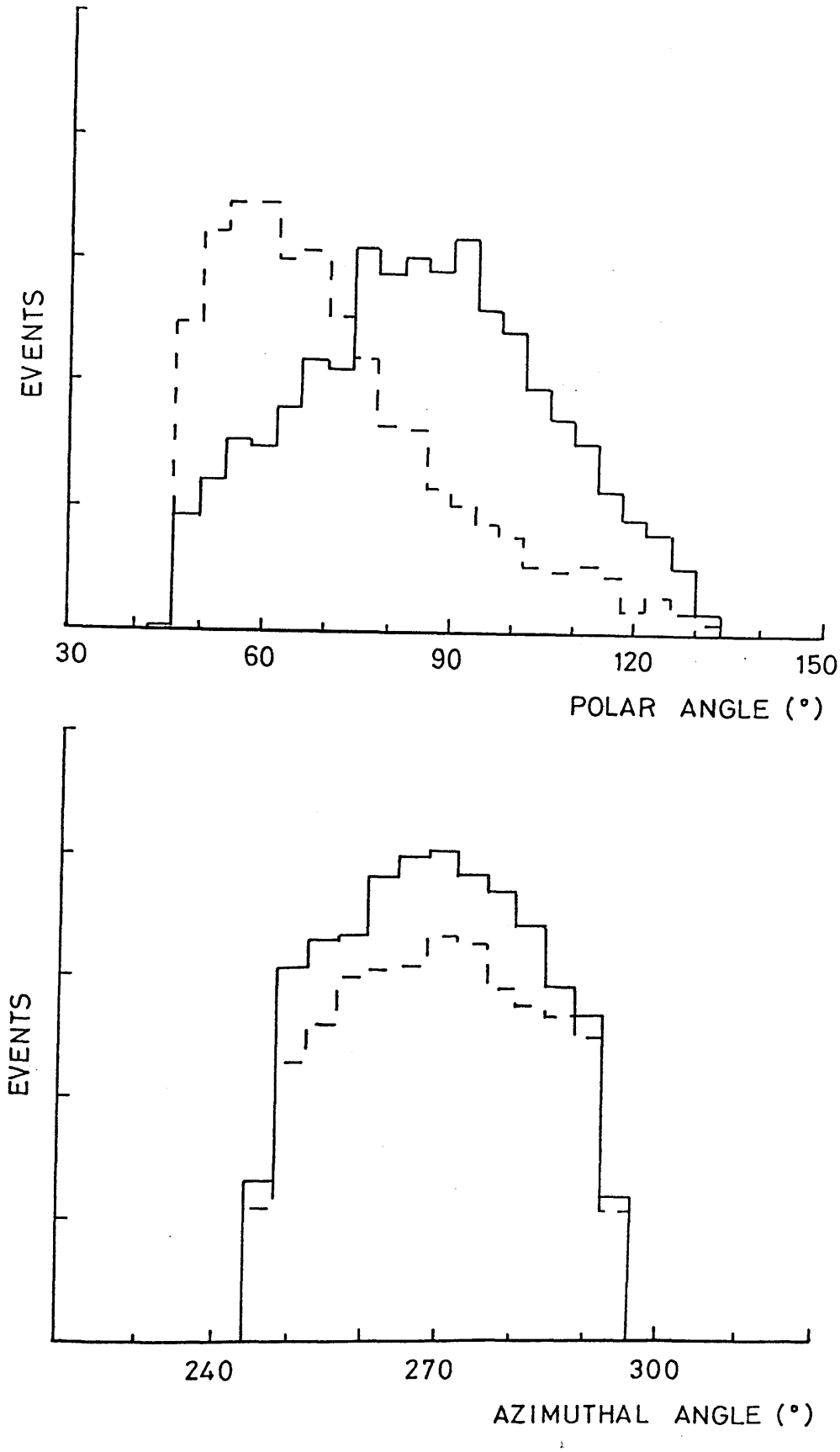

Figure 3.21: Polar and azimuthal proton angular distributions predicted by the Monte Carlo program. The calculation includes the effects of the solid angle of the proton detector and the detector thresholds. Solid histogram : $\theta_n = 67.5°$; dashed histogram : $\theta_n = 105°$.

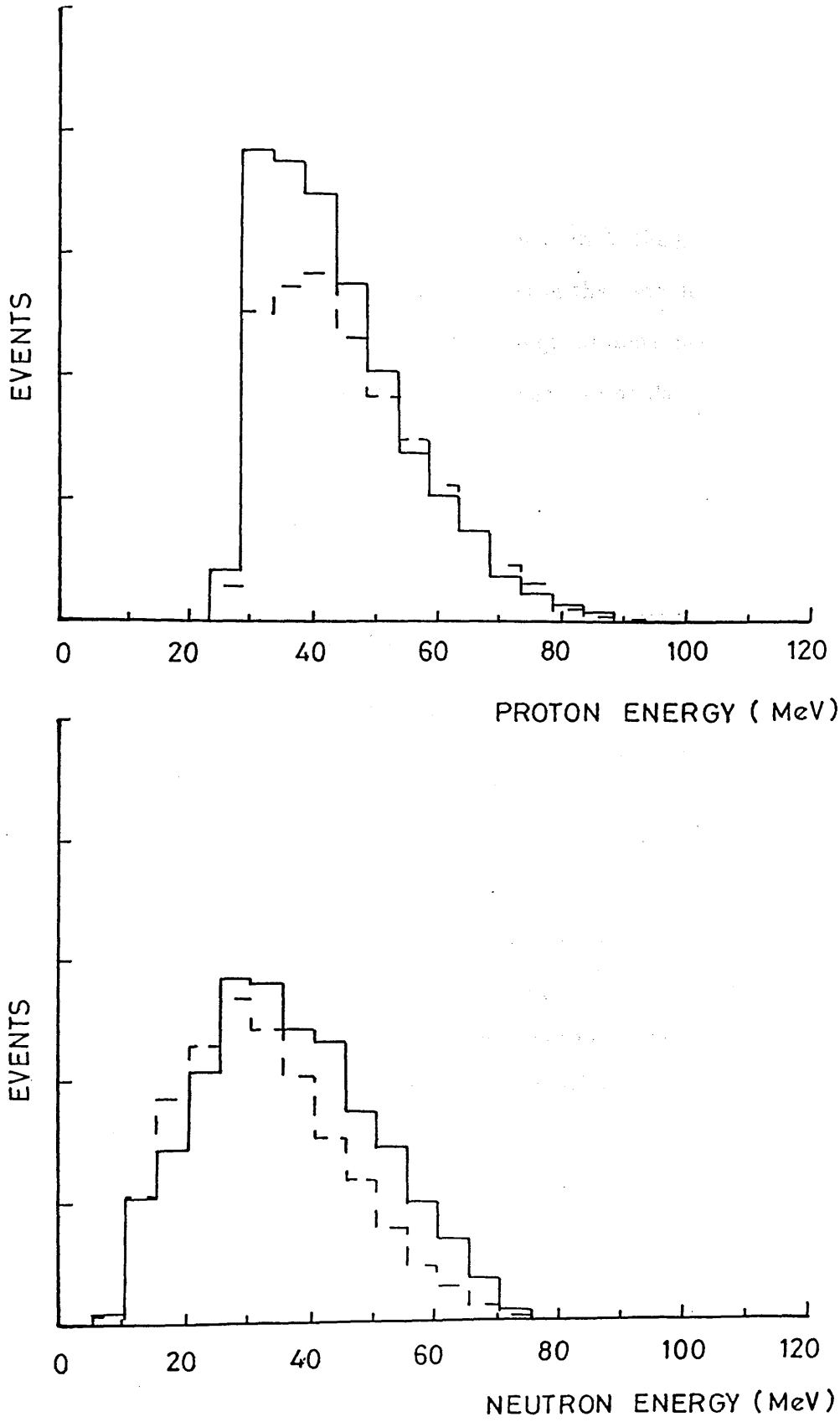

Figure 3.22: Proton and neutron energy spectra predicted by the Monte Carlo program. The calculation includes the effects of the solid angle of the proton detector and the detector thresholds. The lines are as defined in Figure 3.21.

by the quasideuteron program satisfied the above conditions. 0.062 % of events generated by the phase space calculation satisfied the same conditions.

Figure 3.21 shows how the Fermi cone of proton angles is intercepted by the proton detector set at the 90° position. For neutrons at 67.5° the horizontal extent of the proton detector is sufficient to intercept most of the cone in that direction. As the neutron angle increases, the more forward angle protons miss the detector. In the azimuthal direction it is clear that the wings of the angular distribution are cut off. The effect of the detector thresholds on the nucleon energy distributions is illustrated in Figure 3.22. The distributions of other kinematical variables are shown as the experimental data are presented.

3.7 Cross Section Calculations

When the yield of events has been determined from the data reduction process, and the correction factors evaluated, the differential cross section with respect to neutron angle can be calculated from

$$\frac{d\sigma}{d\Omega_n} = \frac{Y_{np}}{n_t \Phi_\gamma \epsilon_n \epsilon_p \Delta\Omega_n} f \tag{3.5}$$

where Y_{np} = the measured yield of n-p events over run period, within the selected kinematic region,

n_t = the number of target nuclei per unit area,

Φ_γ = the number of tagged photons which hit the target over the run period,

ϵ_n = neutron detector efficiency,

ϵ_p = proton detector efficiency,

$\Delta\Omega_n$ = solid angle of the neutron detector,

and f = the corrections to account for effects such as dead time, losses in the data reduction process and integration over part of the proton angular range and part of the nucleon energy ranges.

Since ϵ_n and ϵ_p are dependent on the respective nucleon energies, the product $\epsilon_n\epsilon_p$ was evaluated for each event and $1/\epsilon_n\epsilon_p$ was used as a weighting factor for that event. Accumulating a spectrum of weighted events thus gives $\frac{Y_{np}}{\epsilon_n\epsilon_p}$. Although it is possible in principle to measure neutron detection efficiency from the ^{2}H(γ,pn) reaction in the CD_2 target, insufficient statistics were obtained, after a necessary ^{12}C subtraction, to provide useful results. Instead it was necessary to resort to the Monte Carlo calculations of Cecil *et al.* [83]. In that paper, comparisons of the results of the Monte Carlo code with data from various kinds of plastic scintillator, including NE102, have been made. Agreement to within 10% has been found, with better agreement for data with high thresholds (>4 MeV_{ee}) and at neutron energies away from the detection thresholds.

Φ_γ is the product of $\epsilon_t N_e$, where N_e is the number of recoil electrons recorded in the FPD and ϵ_t is the tagging efficiency. N_e is the sum of the contents of twelve scalers, each of which counts signals from a group of eight neighbouring channels. This arrangement allows the calculation of fluxes of photons over several photon energy ranges.

The correction factor f is a product of the three quantities mentioned above. The dead time correction f_d was evaluated from the ratio of the total number of X-triggers supplied by the proton detector to the number of X-triggers accepted by the computer and found to be 1.0662 ± 0.0007. The correction for estimated losses due to ambiguous events during the data reduction process f_l consists of three contributions: losses due to the neutron selection (correction factor 1.056 ± 0.003); those due to the proton selection (correction factor 1.05 ± 0.02); and those due to the selection of prompt events (for which the details are described in Appendix B). The corrections for the integration over the proton angles and nucleon energies f_Ω are shown in Tables 3.3 and 3.4. Thus f is expressed as $f = f_d f_l f_\Omega$.

When evaluating the ratio of the carbon and deuterium differential cross sec-

Photon Energy	(1p1p) Correction Factor	(1p1s) Correction Factor
86.1	7.2±1.9	—
94.8	5.4±1.0	86 ±50
103.6	4.5±0.6	24.8±7.8
112.4	3.9±0.4	15.0±2.7
121.3	3.5±0.4	10.3±1.4
129.4	3.2±0.3	7.5±0.9

Table 3.3: Photon energy dependence of the integration correction f_Ω.

Neutron Angle	(1p1p) Correction Factor	(1p1s) Correction Factor
67.5	3.40	9.15
75.0	3.45	9.30
82.5	3.00	9.05
90.0	3.35	8.60
97.5	3.35	9.20
105.0	3.55	8.15
112.5	4.00	7.75
127.5	5.50	8.25

Table 3.4: Neutron angle dependence of f_Ω,the integration correction factor. ±10% and ±13% are estimated for the (1p1p) and (1p1s) correction factors respectively.

tions, ϵ_t, N_e, $\Delta\Omega_n$, f_d and f_l are the same for both nuclei. There are twice as many deuterium nuclei as there are of carbon, while the correction factor f_Ω applies only to complex nuclei since deuterium neither produces a Fermi cone of protons nor a range of nucleon energies. Thus the ratio is given by

$$\frac{d\sigma_C}{d\sigma_D}(\theta_n) = 2f_\Omega \left(\frac{Y_{np}}{\epsilon_n\epsilon_p}(\theta_n)\right)_C \Big/ \left(\frac{Y_{np}}{\epsilon_n\epsilon_p}(\theta_n)\right)_D . \tag{3.6}$$

The total cross section is related to the differential cross section by the integral equation,

$$\sigma = \int_{4\pi} \frac{d\sigma}{d\Omega_n} d\Omega_n. \tag{3.7}$$

Defining the average differential cross section as

$$\overline{\frac{d\sigma}{d\Omega_n}} = \frac{\int_{4\pi} \frac{d\sigma}{d\Omega_n} d\Omega_n}{\int_{4\pi} d\Omega_n.} = \frac{1}{4\pi}\int_{4\pi} \frac{d\sigma}{d\Omega_n} d\Omega_n \tag{3.8}$$

the total cross section can be written as

$$\sigma = 4\pi \overline{\frac{d\sigma}{d\Omega_n}}. \tag{3.9}$$

From the data $\overline{\frac{d\sigma}{d\Omega_n}}$ can be estimated from the expression

$$\overline{\frac{d\sigma}{d\Omega_n}} = \frac{f}{n_t \phi_\gamma \Delta\Omega_n} \frac{1}{k} \sum_{i=1}^{k} \left[\frac{Y_{np}}{\epsilon_p\epsilon_n}(\theta_i)\right] = \frac{f}{n_t \Phi_\gamma \Delta\Omega_n k} \frac{Y_{np}}{\epsilon_p\epsilon_n}(E_\gamma) \tag{3.10}$$

where θ_i represents the nominal detector polar angles, and k is the number of detectors, and $\sum_{i=1}^{k} \left[\frac{Y_{np}}{\epsilon_p\epsilon_n}(\theta_i)\right]$ is written as $\frac{Y_{np}}{\epsilon_p\epsilon_n}(E_\gamma)$.

The ratio of the carbon cross section to that of deuterium is then obtained by the expression

$$\frac{\sigma_C}{\sigma_D}(E_\gamma) = 2f_\Omega \left(\frac{Y_{np}}{\epsilon_n\epsilon_p}(E_\gamma)\right)_C \Big/ \left(\frac{Y_{np}}{\epsilon_n\epsilon_p}(E_\gamma)\right)_D \tag{3.11}$$

It should be noted that the cross sections are evaluated in the laboratory frame of reference.

Chapter 4

Results

4.1 Introduction

The results presented in this chapter are the fruit of ~27 hours run time with a CD_2 target and ~12 hours target out. The data shown in some of the figures are tabulated in Appendix E. The parameters of the experiment mentioned in Chapter 2 are summarised in Table 4.1. Table 4.2 summarises the number of useful events obtained over the running period under four classifications: prompt protons with prompt neutrons, prompt protons with random neutrons, random protons with prompt neutrons, and random protons with random neutrons.

4.2 Errors

The largest systematic error arises from the determination of the neutron detection efficiency. As mentioned in the previous chapter, the Monte Carlo code of Cecil [83] agrees with data obtained from scintillators of various shapes to within 10% over a wide range of neutron energies. In this experiment, the electron-equivalent threshold energy has been determined as 5.0±0.7 MeV_{ee}. This in turn gives rise to an average error in the detection efficiency of ~ ±13%. Combining these two sources of error, the total error is taken as ±16%.

Two measurements of the tagging efficiency were made during the run. The first was carried out half way through the run, the second at the end. Although they were consistent to within ±1.5%, slight drifts of the beam may have occurred between the measurements giving rise to changes in the efficiency. An ion chamber, employed as a photon beam flux monitor in the photon beam dump, indicated that only very minor changes occurred during the course of the run. If, in the worst case, the fluctuations are attributed entirely to slight changes in beam position at the bremsstrahlung radiator, rather than to fluctuations in primary beam current, it is estimated that the tagging efficiency will deviate by at worst by ±2%.

Errors in N_k arise from the determination of the area and weight of the target

Spectrometer:	photon energy range	83–133 MeV
	average photon energy bite per FPD element	0.5 MeV
	tagged photon rate	$\sim 3.8 \times 10^7$ s^{-1}
	tagging efficiency	0.68 ± 0.02
Proton detector:	solid angle	0.8 sr
	scattering angle range	45° to 135°
	azimuthal angle range	250° to 290°
	energy range	> 28 MeV
	energy resolution	2.6 MeV at 60 MeV
Neutron detector:	solid angle	$8 \times (0.0124 \pm 0.0004)$ sr
	scattering angles	52.5°,67.5°,75°,82.5°,90°, 97.5°,105°,112.5°,127.5°
	azimuthal angular range	83° to 97°
	energy range	> 10 MeV
	energy resolution	~ 6 MeV at 60 MeV
Target:	material	Deuterated polythene
	carbon:hydrogen ratio	1:2
	fraction of ^{2}H in hydrogen	100%
	thickness in beam direction	0.315 ± 0.009 mgcm^{-2}

Table 4.1: Summary of the experimental parameters.

# of events prompt in proton detector and prompt in neutron detector	=	21180±146
# of events prompt in proton detector and random in neutron detector	=	11636±108
# of events random in proton detector and prompt in neutron detector (average over five regions)	=	6003± 35
# of events random in proton detector and random in neutron detector (average over five regions)	=	3369± 26
Net # of useful events	=	6910±187

Table 4.2: Population of event categories after complete data reduction process.

as well as its angle to the beam. N_k was determined to within $\pm 2.9\%$. Imprecision in the solid angle of each neutron detector amounted to $\pm 3.2\%$. ϵ_p introduces an error only for protons which possess energy near the proton detector threshold. The number of events involved is $< 1\%$. The error is estimated to be of this order of magnitude. The error arising from the factors f_l and f_d amounts to $\pm 5.4\%$

The above errors are of a general systematic nature and apply to all the data regardless of how it is binned. Summed in quadrature they represent a total error of $\pm 17.6\%$. Not included is the error in f_Ω which, in contrast, depends quite sensitively on the binning of the data. This has been estimated by varying the input parameters of the Monte Carlo program within the tolerance of each and observing the changes in the resulting correction factors. The results for correction factors which are evaluated

1. by dividing the data into photon energy bins and integrating the yield over the six most forward neutron detectors, and

2. by choosing the neutron angle and integrating over the 113–133 MeV photon energy range

are shown in Tables 3.3 and 3.4 with their estimated errors.

Y_{pn} and N_e introduce statistical errors. That due to N_e is $\pm 0.025\%$ and is ignored. The error in the yields are displayed in the remaining diagrams in this chapter.

4.3 Missing Energy

As has already been stated, one of the objectives of the experiment was to measure enough parameters to completely determine the kinematics of the (γ,pn) reaction and to do so with sufficient energy resolution to determine the shells from which the nucleons were ejected. The resolution of the Glasgow-Edinburgh-Mainz

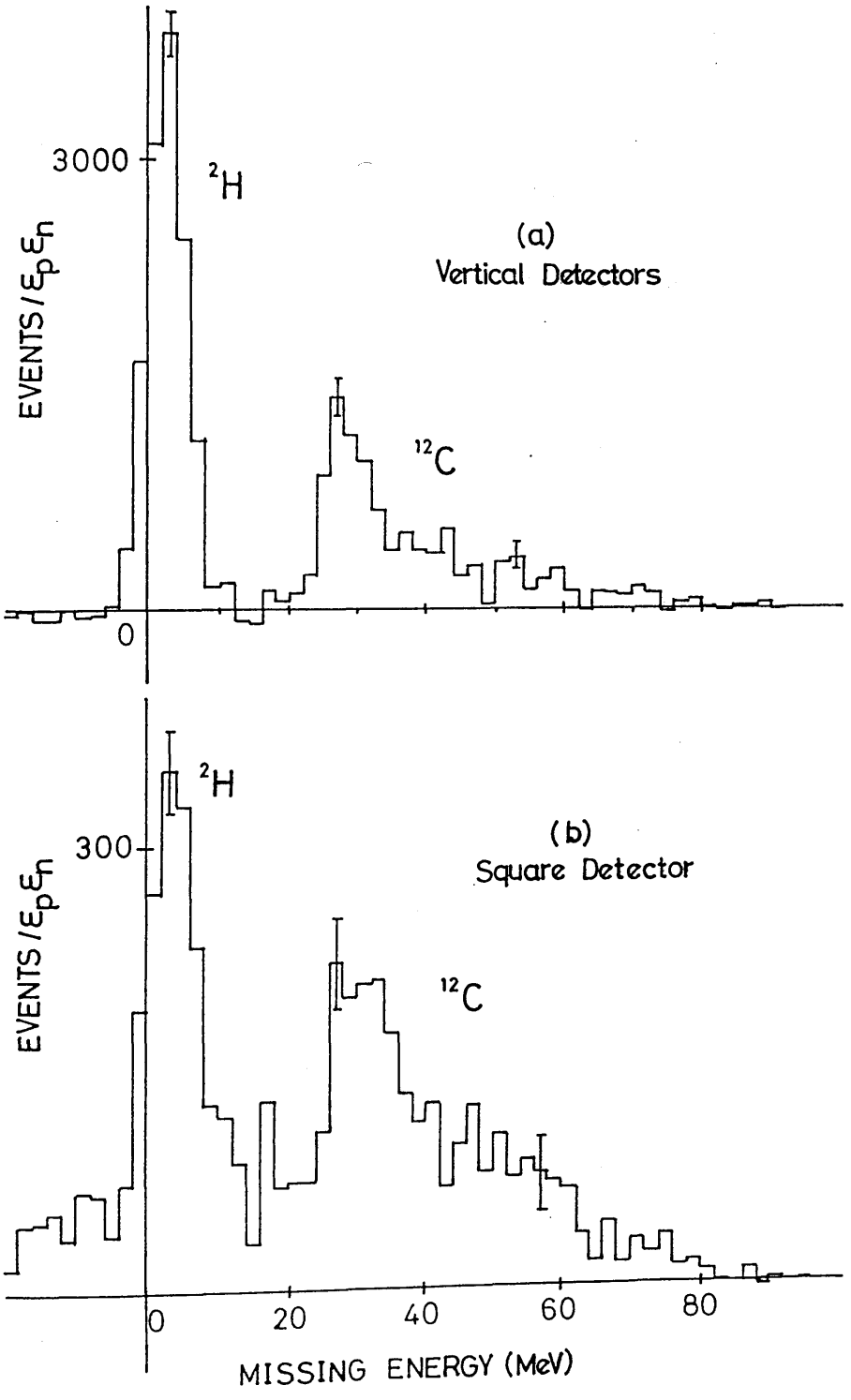

Figure 4.1: Missing energy spectra for all photon energies. (a) sum of the spectra from the vertical detectors at angles between 67.5° and 105° inclusive. (b) spectrum from the square detector.

system is displayed in Figure 4.1 which shows spectra of missing energy. The missing energy is defined as the difference between the total final and total initial masses of the particles involved,

$$E_m = m_p + m_n + M_R - M_T$$

where m_p, m_n, M_R and M_T are the rest masses of the proton, neutron, recoil nucleus, and target nucleus respectively. By conservation of mass-energy this may be rewritten as,

$$E_m = \omega - T_p - T_n - T_R$$

where ω, T_p, T_n and T_R are the kinetic energies of the photon, proton, neutron and recoil nucleus respectively. Since the momentum vectors of the photon, neutron and proton are measured, T_R is easily computed.

Figure 4.1(a) is the sum of all data obtained from the six most forward angle 1-dimensional detectors (67.5° to 105° inclusive) over all measured nucleon energies and photon energies. Figure 4.1(b) is the spectrum of all events obtained from the 2-dimensional square detector. Both figures illustrate separation of the ^{2}H data from the ^{12}C data although the square detector displays considerable smearing out of the distributions. The peak centred at ~3 MeV arises from the break up of deuterium nuclei which has a Q-value of 2.2 MeV . The energy resolution of the system, excluding the contribution from the square detector, is demonstrated by the width of the peak in Figure 4.1(a). This is measured to be ~ 7 MeV FWHM and derives mainly from the poorer neutron energy resolution. The second peak at ~ 29 MeV arises from from the photoemission of two nucleons from the 1p-shell of ^{12}C leaving the residual ^{10}B nucleus in or near its ground state. This process is known to have a Q-value of 27.4 MeV . At higher energies it would be expected that events in which one nucleon is ejected from the 1s-shell and the other from the 1p-shell would become visible. However, the effect of the nucleon detector thresholds

becomes more important with increasing E_m such that only a decreasing tail is observed.

4.4 Correlations and Momentum Distributions

The data presented in Figures 4.2, 4.3, and 4.5 to 4.9 are from events in the 83–133 MeV photon energy range integrated over all measured nucleon energies and the six most forward detector angles.

Since there are only two bodies in the final state of the deuteron photodisintegration reaction, the nucleons emerge from target at 180° to each other in the centre of mass frame of the photon-deuteron system. Figure 4.2(a) illustrates a spectrum of $\cos\theta_{pn}$, where θ_{pn} is the opening angle between nucleons in the centre of mass for all events in the missing energy range -10 to $+15$ MeV . The width of the peak indicates the the angular resolution of the system. A region, centred at $E_m = 27.5$ MeV, of width 25 MeV has been chosen to select data from the ground state peak of the ^{12}C data. Similarly, a region of the same width, centred at 52.5 MeV, has been used to select events ejected from deeper shells. For these regions distributions of the opening angles are shown in Figures 4.2(b) and 4.2(c). In these cases the calculation of θ_{pn} for each event assumes that the $A-2$ nucleons are spectators, that the total energy of the neutron-proton pair may be written as in Equation 3.4, and that the net momentum of the neutron-proton pair is zero in the ^{12}C nucleus. The last assumption allows a direct comparison of the effect of the non-zero momentum of the pair in the ^{12}C nucleus with that of the stationary deuteron. The histograms in Figure 4.2 are the results of the two Monte Carlo calculations described in Section 3.6 where excitation energies of 0 MeV and 25 MeV are assumed in Figures 4.2(b) and 4.2(c) respectively. A correlation is clear in both these figures. In both cases the phase space calculation predicts no events at $\theta_{pn} = \pi$, which contradicts both the data and the quasideuteron calculation,

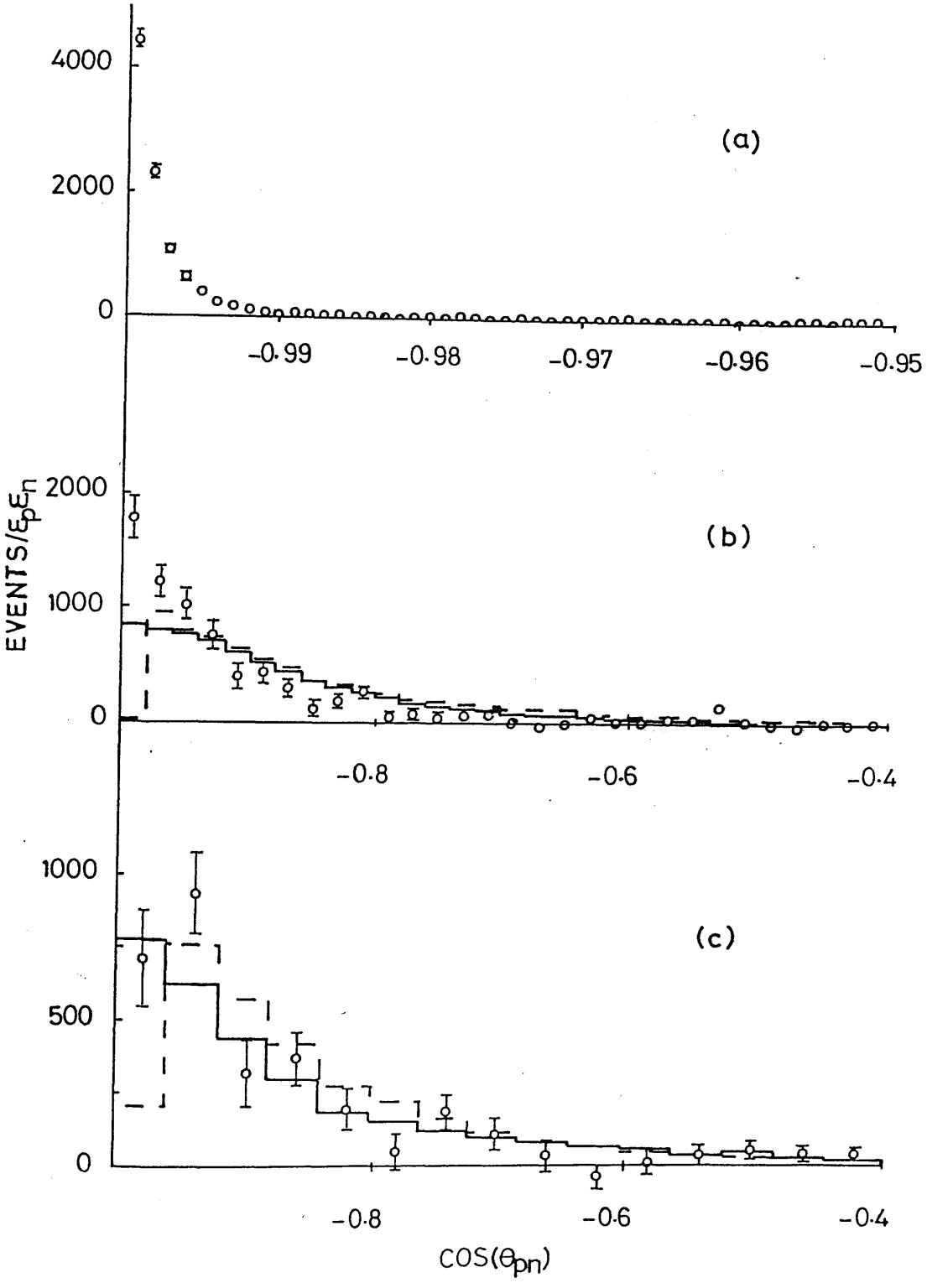

Figure 4.2: Distribution of events in the opening angle between the neutron and the proton evaluated in the frame of reference described in the text. (a) Deuterium data, (b) carbon (1p1p) data, and (c) carbon (1p1s) data. The solid histogram shows the expected distribution from a Monte Carlo calculation, based on the a quasideuteron model, which corrects for biasing owing to the detector sizes and thresholds. The dashed histogram is a similar calculation based on a 3-particle phase space decay (see Appendix E). The data and calculations are normalised to the same integral.

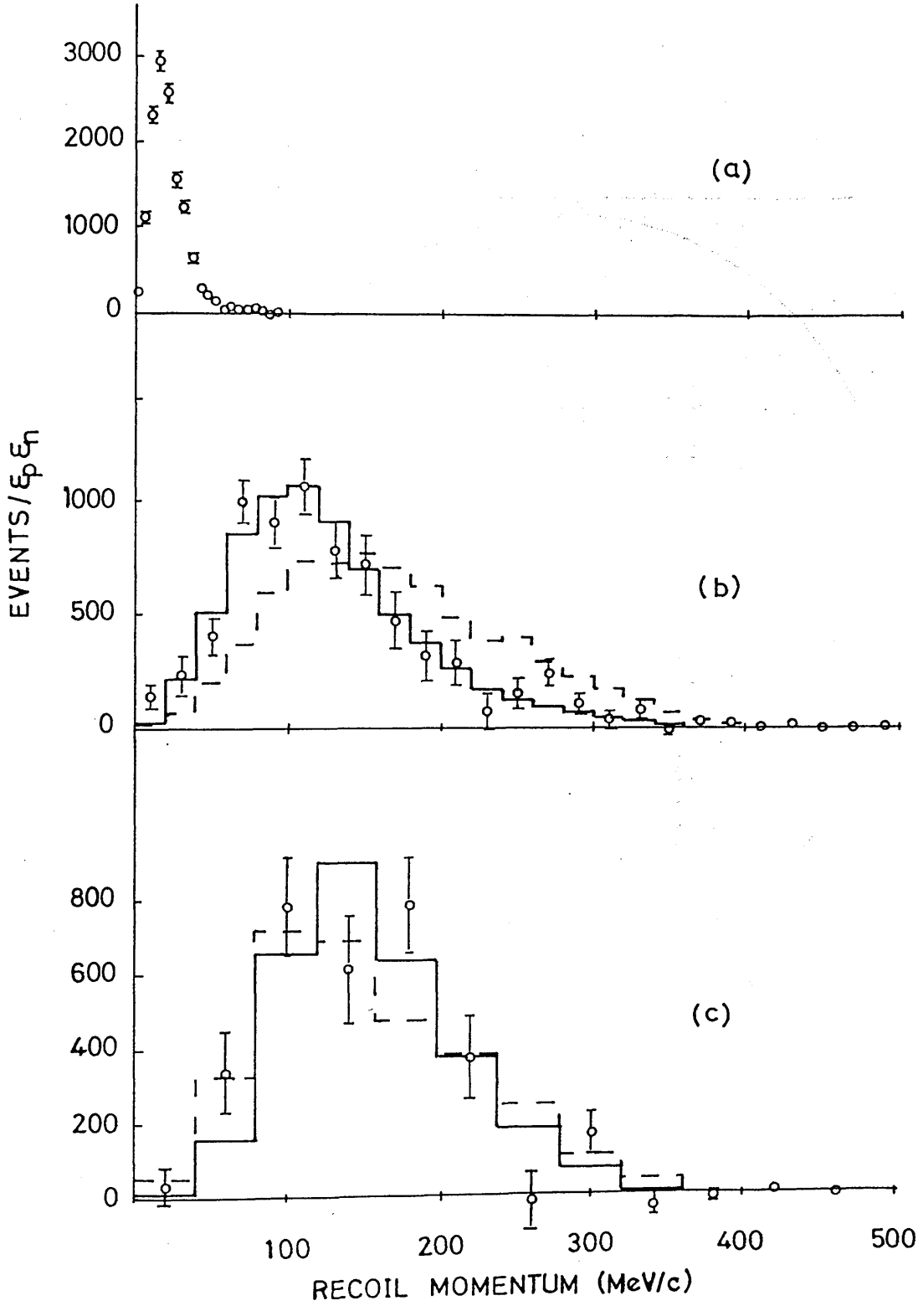

Figure 4.3: Distribution of events in the laboratory recoil nucleus momentum. (a) Deuterium data, (b) carbon (1p1p) data, and (c) carbon (1p1s) data. The histograms are as those in Figure 4.2.

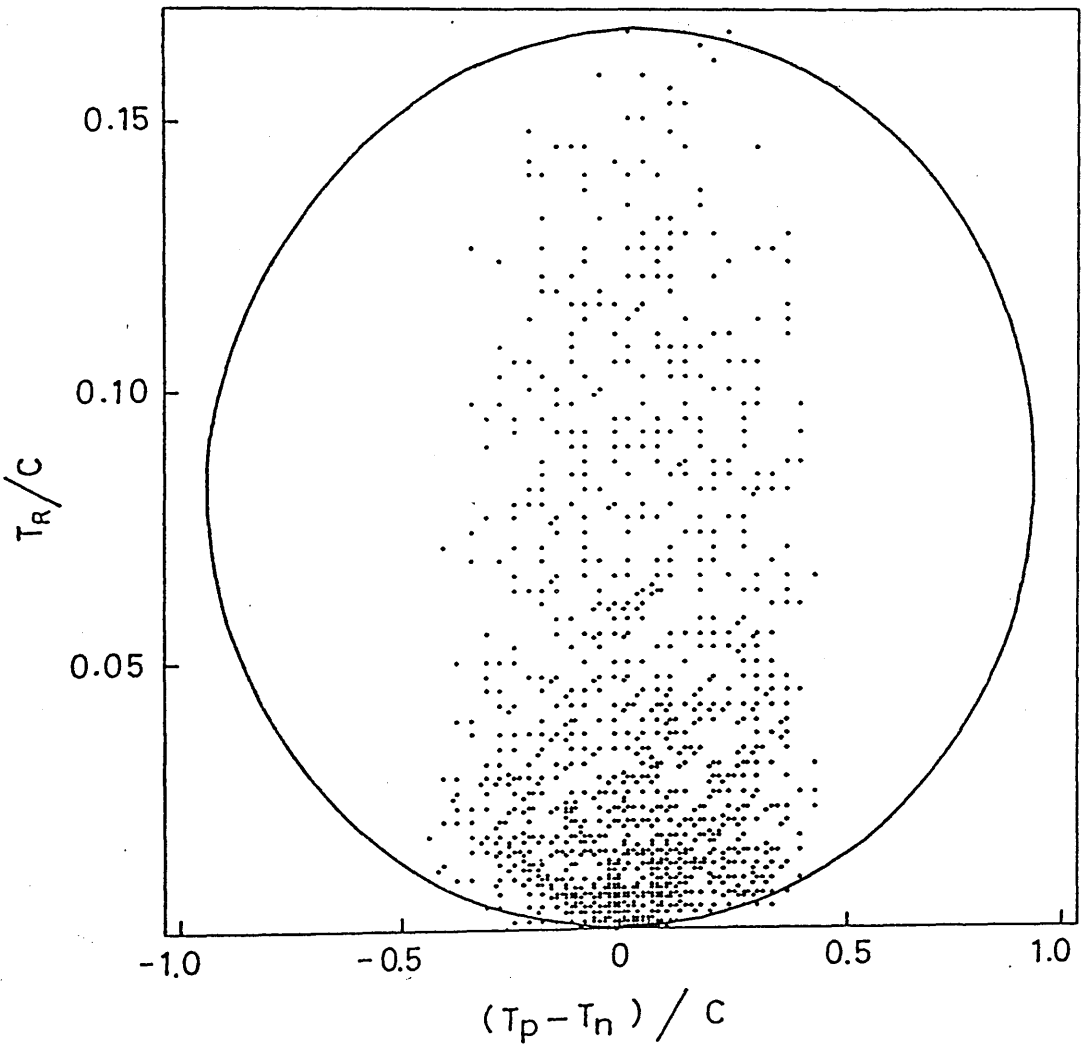

Figure 4.4: Dalitz plot of the ^{12}C(γ,pn) data for 80 MeV $< E_\gamma <$ 133 MeV, 15 MeV $< E_m <$ 40 MeV and $T_p, T_n >$ 30 MeV. T_p, T_n and T_R are the proton, neutron and residual ^{10}B kinetic energies in the centre of mass frame and $C = T_p + T_n + T_R$.

although both calculations show qualitatively similar results elsewhere. Also at $\theta_{pn} = \pi$, the peak observed in the (1p1p) data appears to be tighter than that predicted by the quasideuteron model.

The momentum of the recoil nucleus can be reconstructed easily from the momenta of the detected nucleons and the photon momentum. If the recoil nucleus is purely a spectator then the magnitude of the recoil nucleus momentum is the same as that of the initial neutron-proton pair but in the opposite direction. The distributions for events in the same missing energy regions as those in Figure 4.2 are plotted in Figure 4.3. The width of the data in the top figure indicates the recoil momentum resolution of the system which is found to be ~32 MeV/c. The solid histograms shown in the middle and bottom figures are derived from the angle integrated momentum distribution which is proportional to $P^2F(P)$ (where P is the pair momentum) obtained from Gottfried's formalism [17] using harmonic oscillator wavefunctions. 1p-wavefunctions are used to fit the data from the lower missing energy region while a 1p- and a 1s-wavefunction are used to fit the data from the higher missing energy region. The solid curves have been corrected for the detector biasing using the quasideuteron Monte Carlo calculation. The dashed histograms show the biased momentum distributions which would be obtained if the energy was shared according to the available phase space.

A Dalitz plot of the (1p1p) data in the variables T_R (recoil nucleus kinetic energy in the centre of mass frame) and T_D ($= T_p - T_n$, the difference between the nucleon centre of mass kinetic energies) is shown in Figure 4.4. As described in Appendix D, if the particles share the initial energy according to the available phase space the distribution of events within the allowed kinematic region would be expected to show a uniform density. This is not observed. Instead, the data are clustered at low values of T_R showing that the neutron-proton pair carries off most of the available kinetic energy.

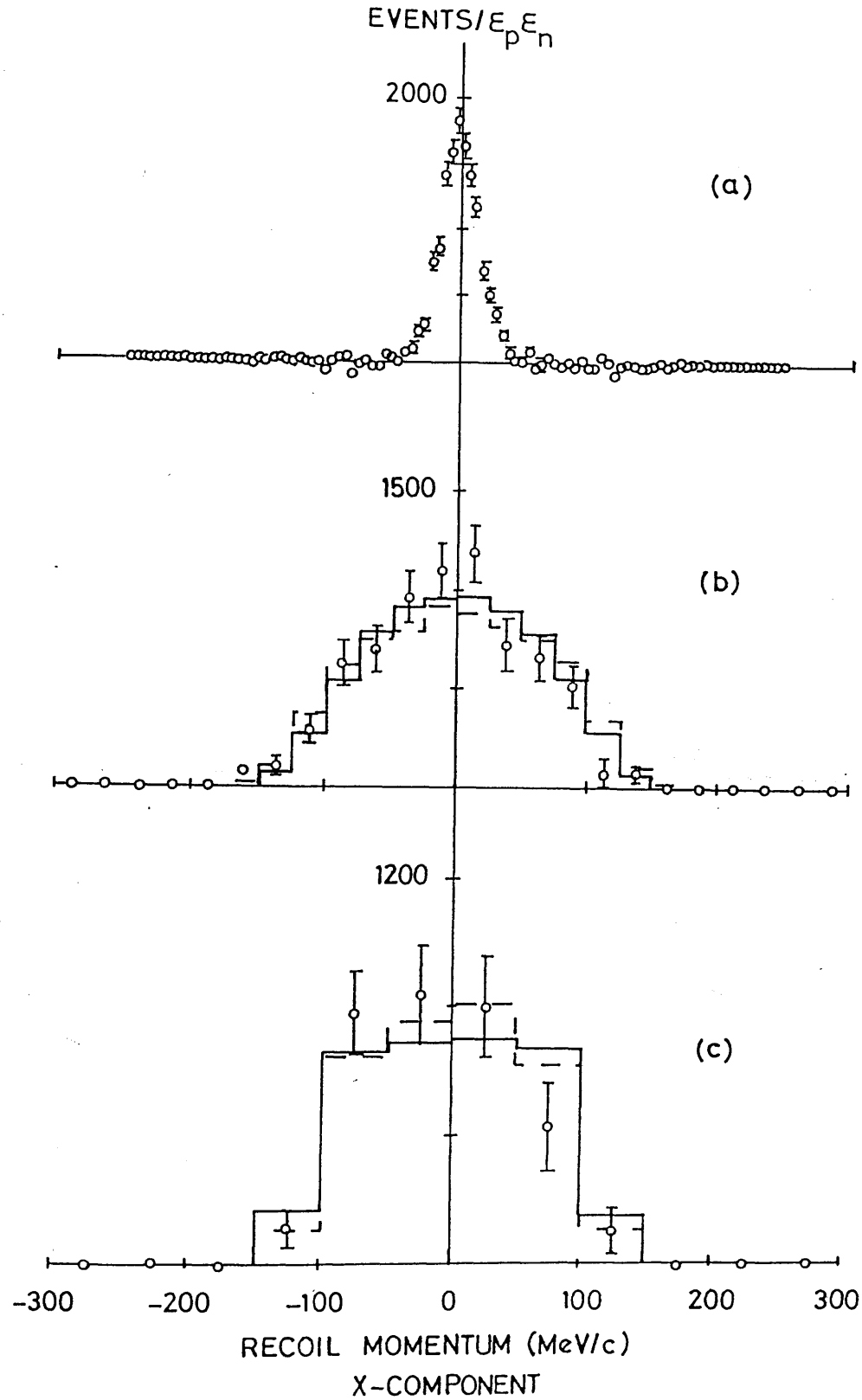

Figure 4.5: Distribution of events in the x-component of the laboratory recoil nucleus momentum. (The direction is defined in the text.) (a) Deuterium data, (b) carbon (1p1p) data, and (c) carbon (1p1s) data. The histograms are as those in Figure 4.2.

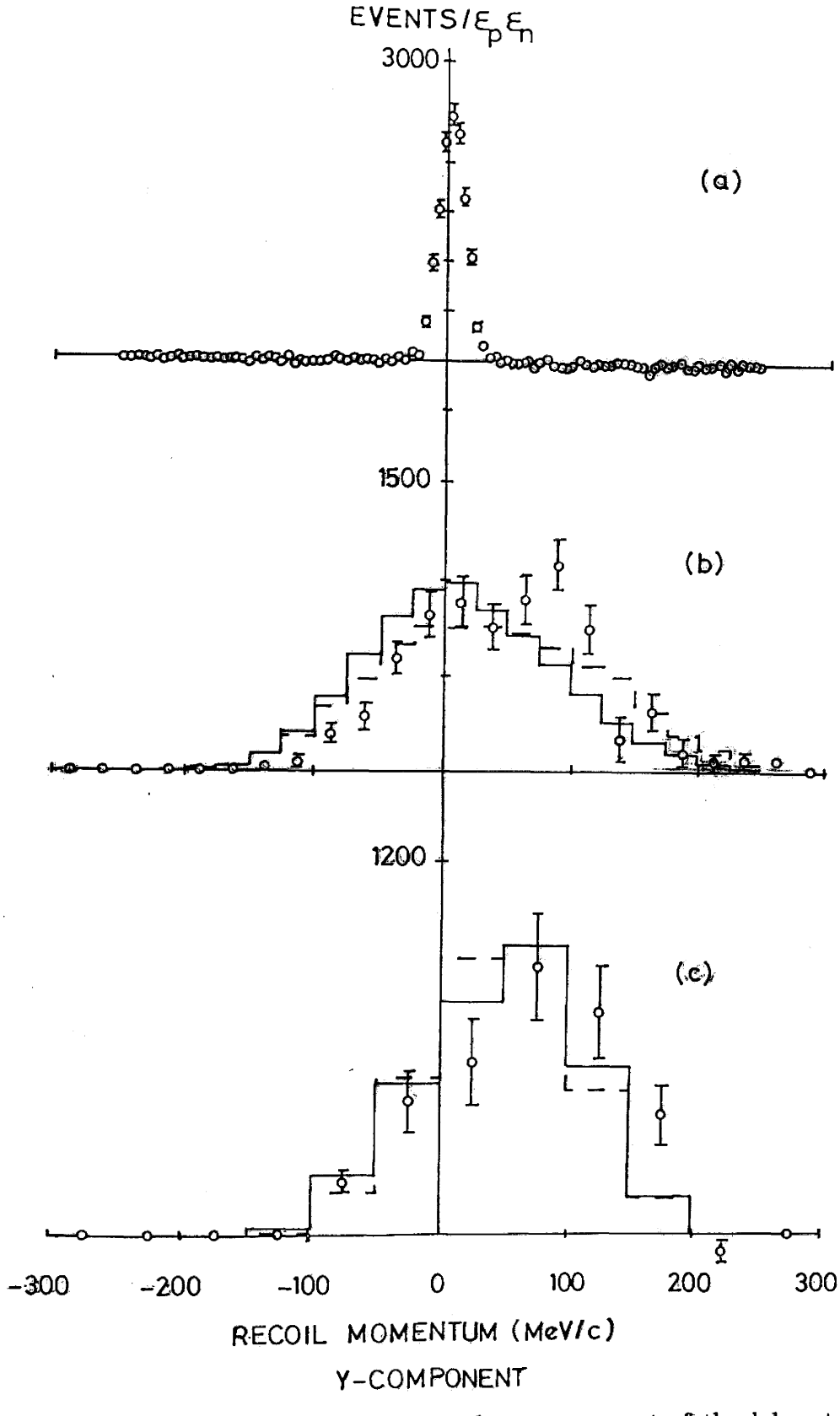

Figure 4.6: Distribution of events in the y-component of the laboratory recoil nucleus momentum. (The direction is defined in the text.) (a) Deuterium data, (b) carbon (1p1p) data, and (c) carbon (1p1s) data. The histograms are as those in Figure 4.2.

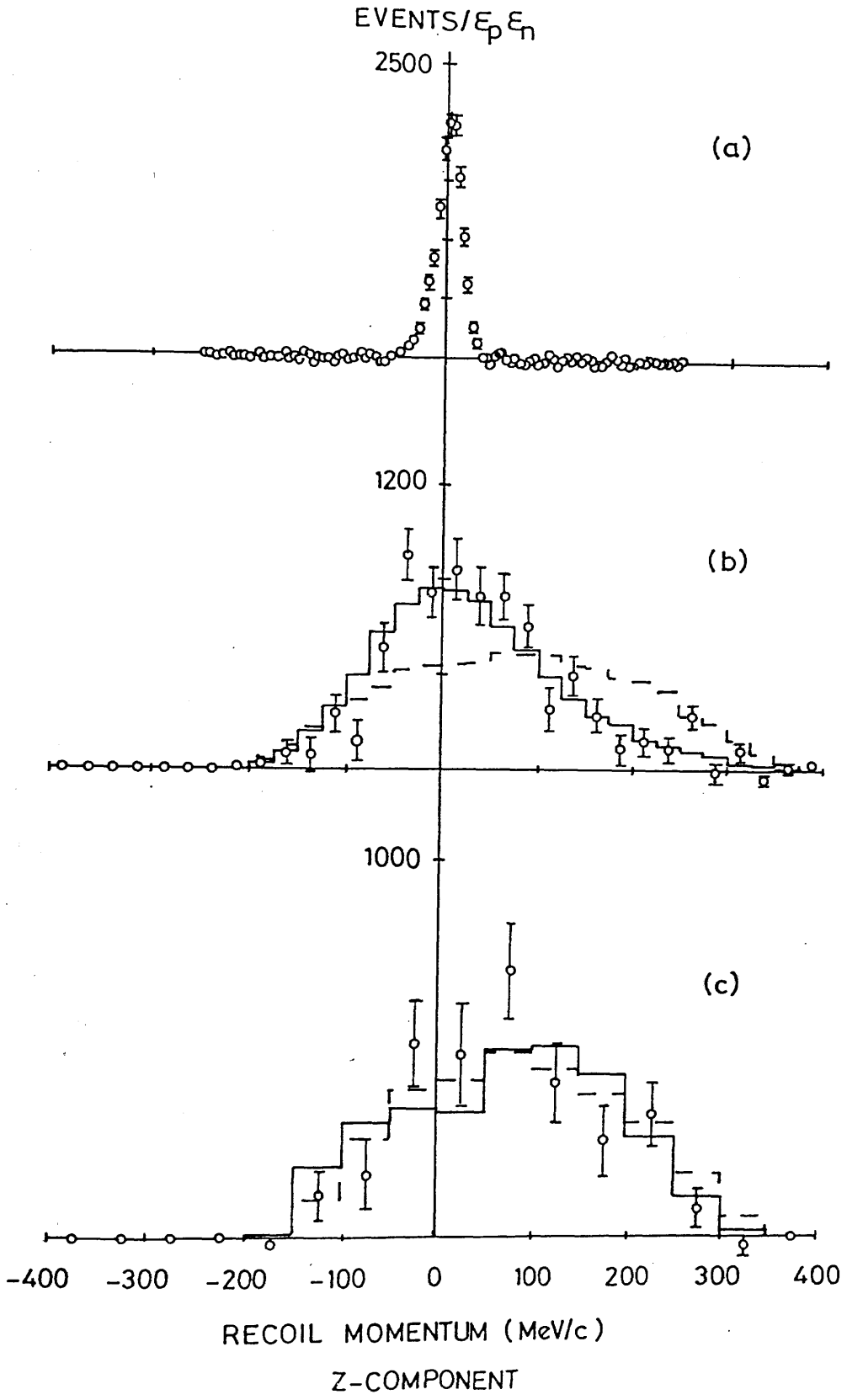

Figure 4.7: Distribution of events in the z-component of the laboratory recoil nucleus momentum. (The direction is defined in the text.) (a) Deuterium data, (b) carbon (1p1p) data, and (c) carbon (1p1s) data. The histograms are as those in Figure 4.2.

The distributions in the components of the momentum vector **P** are also shown. Figures 4.5, 4.6 and 4.7 show the distributions of the cartesian components while Figures 4.8 and 4.9 show the angular polar components. The x-, y- and z-directions are defined as:

x: Vertically upwards,

y: Horizontally from the target to the 90° neutron detector,

z: The direction of the photon beam.

From the deuterium data the momentum resolution in the three directions are found to be 38 MeV/c, 25 MeV/c, and 30 MeV/c the x-, y- and z-directions respectively. The poor value in the x-direction is attributable to the vertical position resolution of the of both the proton and neutron detectors. The y-component is best since it depends almost entirely on the energy resolution of the two detector arrays. The middle and bottom distributions in each of Figures 4.5 to 4.7 show the results for the data in the two missing energy regions already mentioned. The x-component data are centred about zero as expected while distributions in the y- and z-directions indicate peaks which are off centre. The Monte Carlo calculations aid the interpretation of the data as they show that the limited solid angle of the proton detector and the detector thresholds bias the data.

Biasing of the data is more evident when the angular polar components (Figures 4.8 and 4.9) are examined. The dependence of the function $F(P)$ on only the magnitude of the vector **P** shows that the angular distributions are expected to be isotropic. The data, however, are clearly anisotropic. Recoil nuclei which finally end up travelling in the direction of the neutron detectors (from the broad peak in Figure 4.9) but which are predominantly in the downstream direction (from Figure 4.8) are preferred. Although the quasideuteron Monte Carlo calculation provides good fits to other spectra it fails to explain the results of Figure 4.9(b).

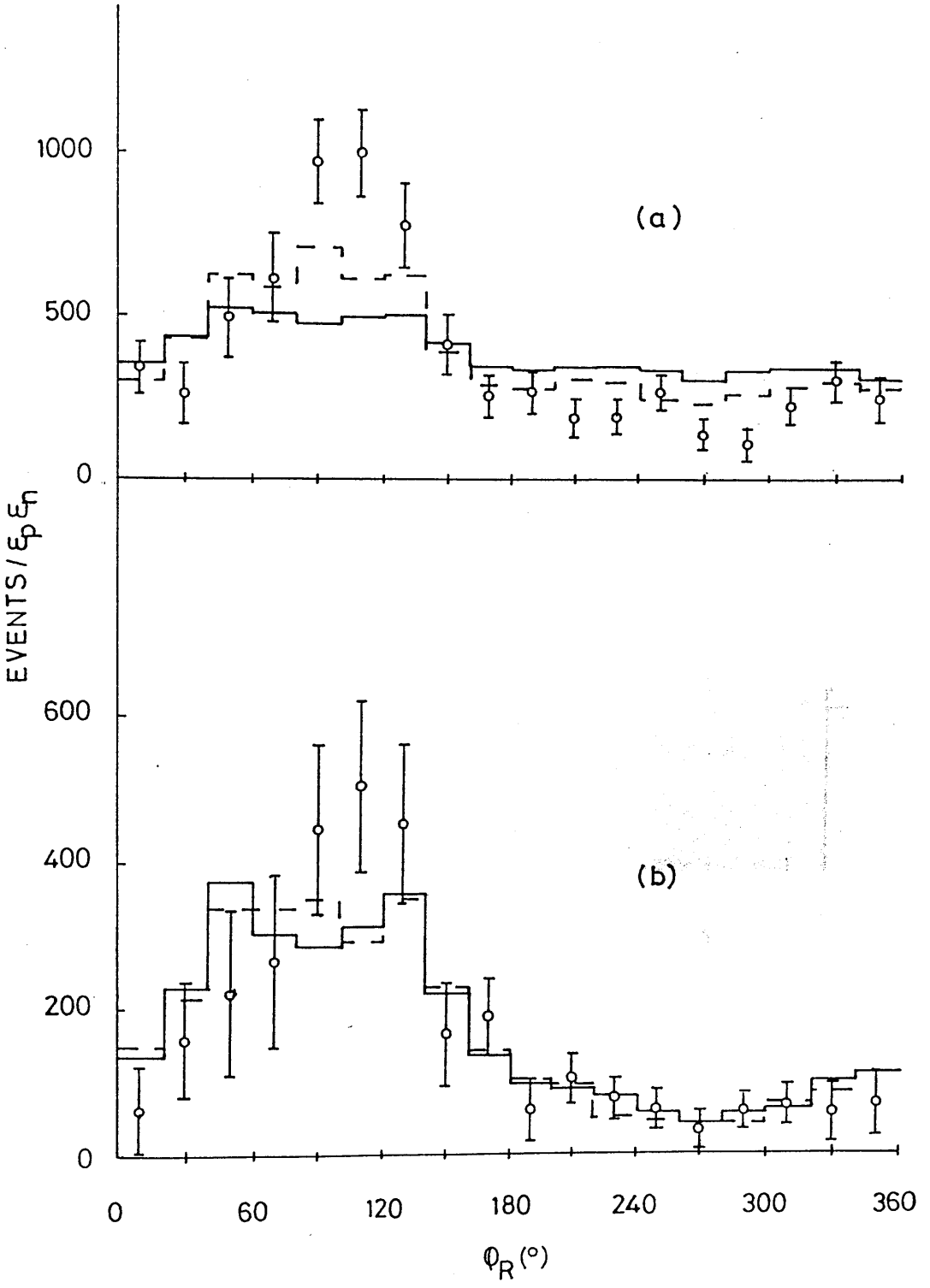

Figure 4.8: Distribution of events in the azimuthal angle of the laboratory recoil nucleus momentum. (The z-direction is defined in the text.) (a) carbon (1p1p) data, and (b) carbon (1p1s) data. The histograms are as those in Figure 4.2.

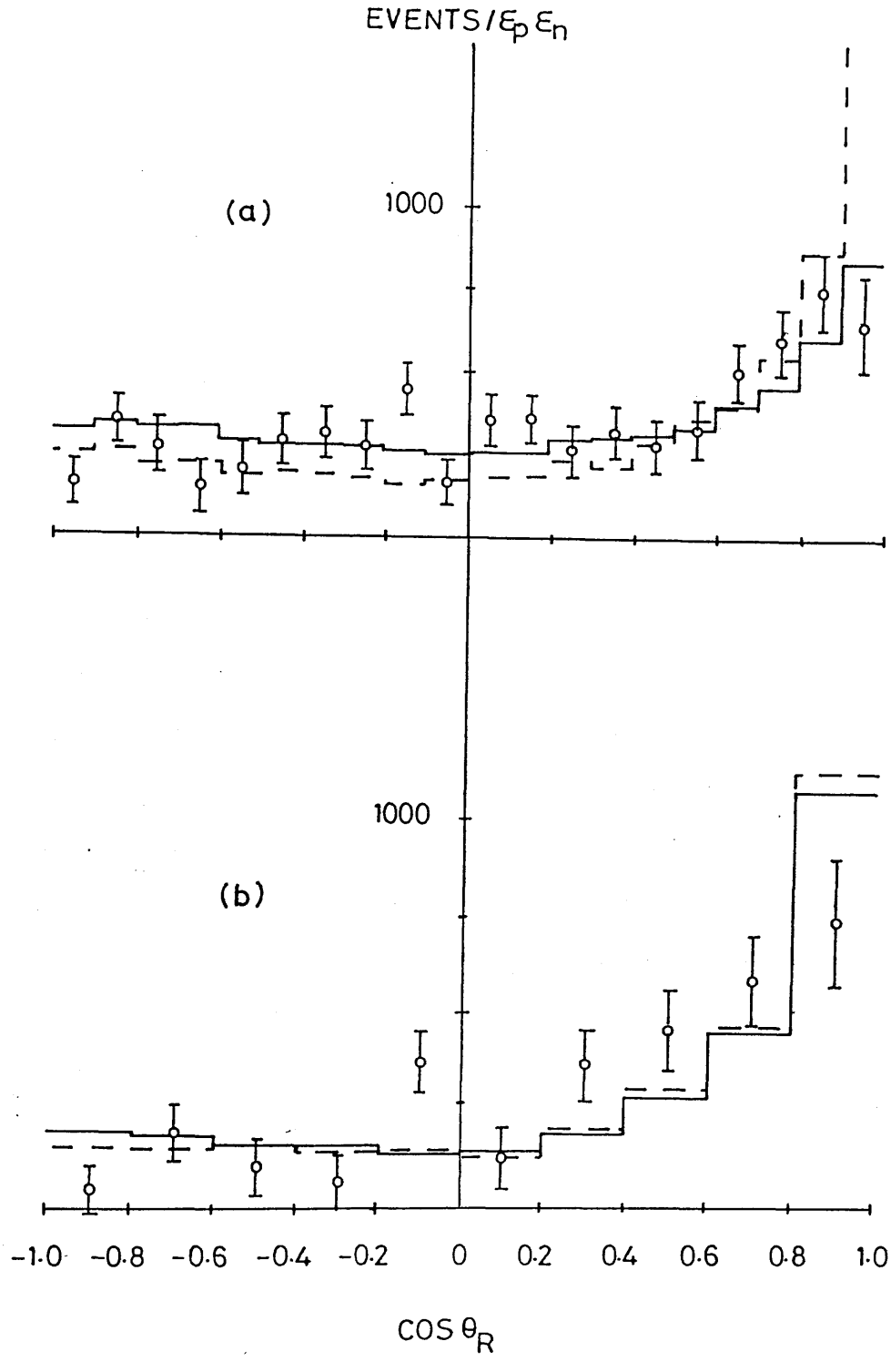

Figure 4.9: Distribution of events in the polar angle of the laboratory recoil nucleus momentum. (The z-direction is defined in the text.) (a) carbon (1p1p) data, and (b) carbon (1p1s) data. The lines are as in Figure 4.2.

4.5 Cross Sections

4.5.1 Photon Energy Dependence

The data have been divided into six approximately equal photon energy bins over the 83–133 MeV photon energy range since there are twelve scalars each of which counts the number of electrons which hit one group of eight FPD channels. Yields from the six most forward 1-dimensional neutron detectors were calculated by integrating over the appropriate regions of the missing energy spectra. Deuterium data were chosen over the -10 MeV to 15 MeV range. (1p1p) pairs from ^{12}C were taken from the 15 MeV to 40 MeV range. Data from the 40 MeV to 65 MeV range were also integrated and interpreted tentatively as (1s1p) pairs.

The energy dependence of the cross section, without the integration correction f_Ω, is shown in Figure 4.10. As expected the deuterium data show a steady decrease with photon energy. In contrast the (1p1p) data appear to slowly increase with energy. The same effect is present for the (1s1p) data but is more pronounced. Consequently, the ratio of the carbon cross section to that of deuterium (Figure 4.11 (a) and (b)) has a pronounced energy dependence. Further investigation using the quasideuteron Monte Carlo code shows that events predominantly from the low energy photons are lost because of the nucleon detector thresholds. The number of losses due to to this effect have been estimated from the code and used to correct the data. Figures 4.12((a) and (b)) and 4.13 ((a) and (b)) show the corrected carbon cross sections and their ratios with those of deuterium. The correction almost removes the energy dependence of the cross section ratios although both data sets would suggest a peak in the cross section in the 100–120 MeV photon energy region. The ratio averages out at 4.97 ± 0.30 in the (1p1p) case and 8.9 ± 1.0 in the (1s1p) case.

Also of interest is the ratio of the cross section from the (1p1p) region to that from the (1s1p) region. The uncorrected data (Figure 4.11(c)) are largely flat

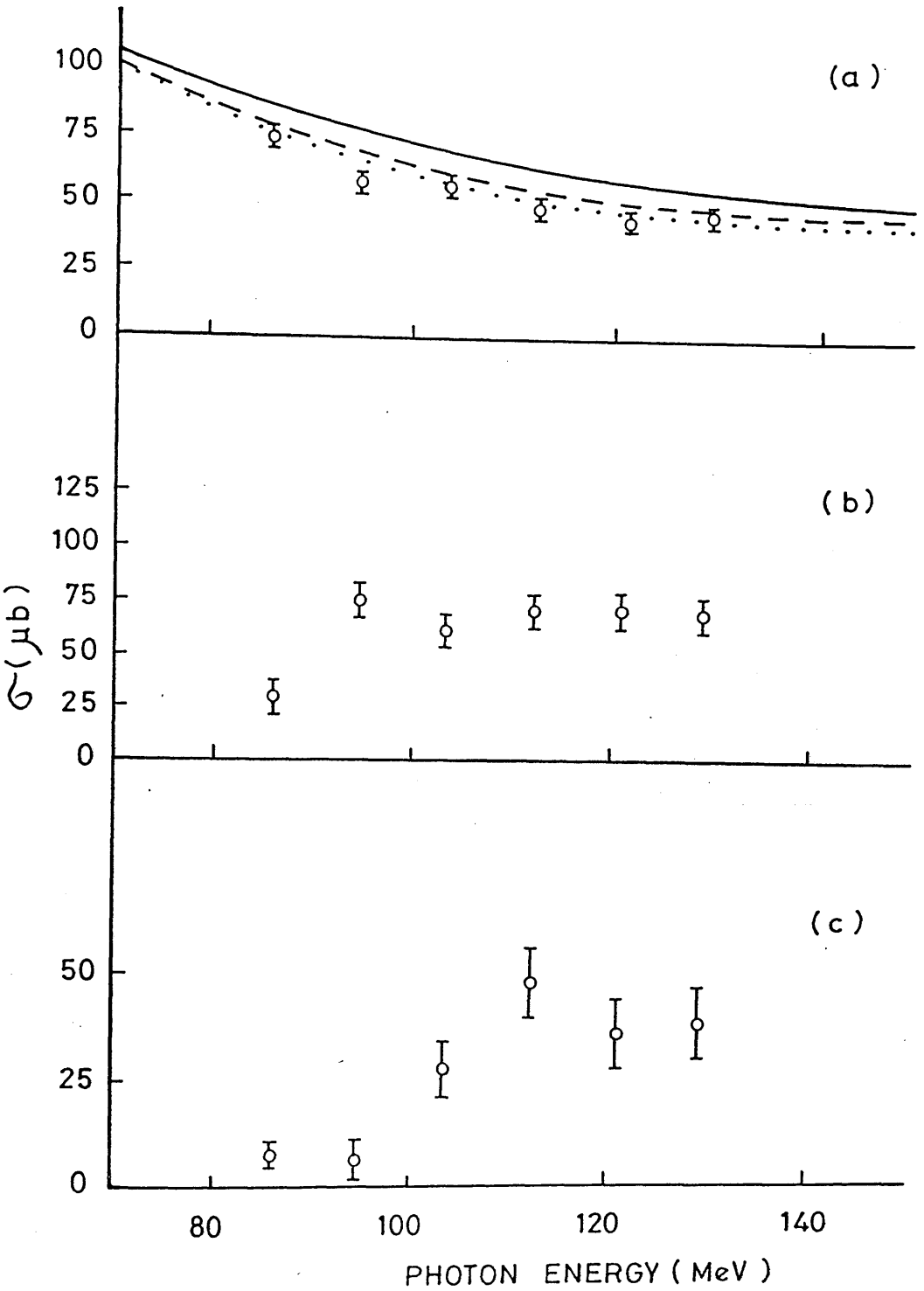

Figure 4.10: The (γ,pn) cross section as a function of photon energy, integrated over neutron angles from 67.5° to 105.0°. (a) Deuterium data (b) carbon (1p1p) data, and (c) carbon (1p1s) data. The curves in (a) are fits to three sets of recent data which are parameterised in ref. [112]. The carbon data do not include the integration correction f_Ω.

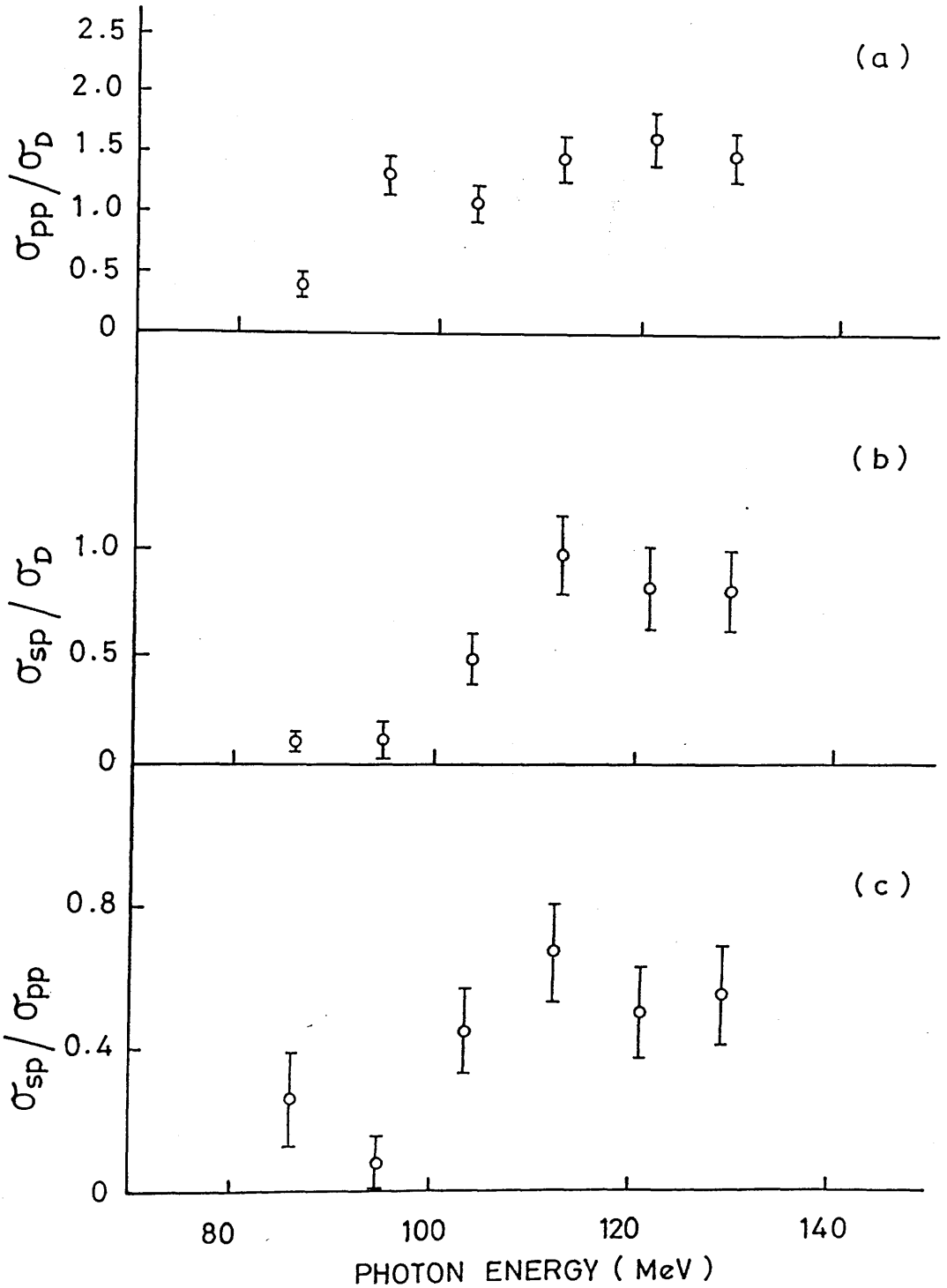

Figure 4.11: Ratios of the (γ,pn) cross section as a function of photon energy. (a) The carbon (1p1p):deuterium ratio, (b) carbon (1p1s):deuterium ratio, and (c) carbon (1p1s):carbon (1p1p) ratio. The carbon data do not include the integration correction f_Ω.

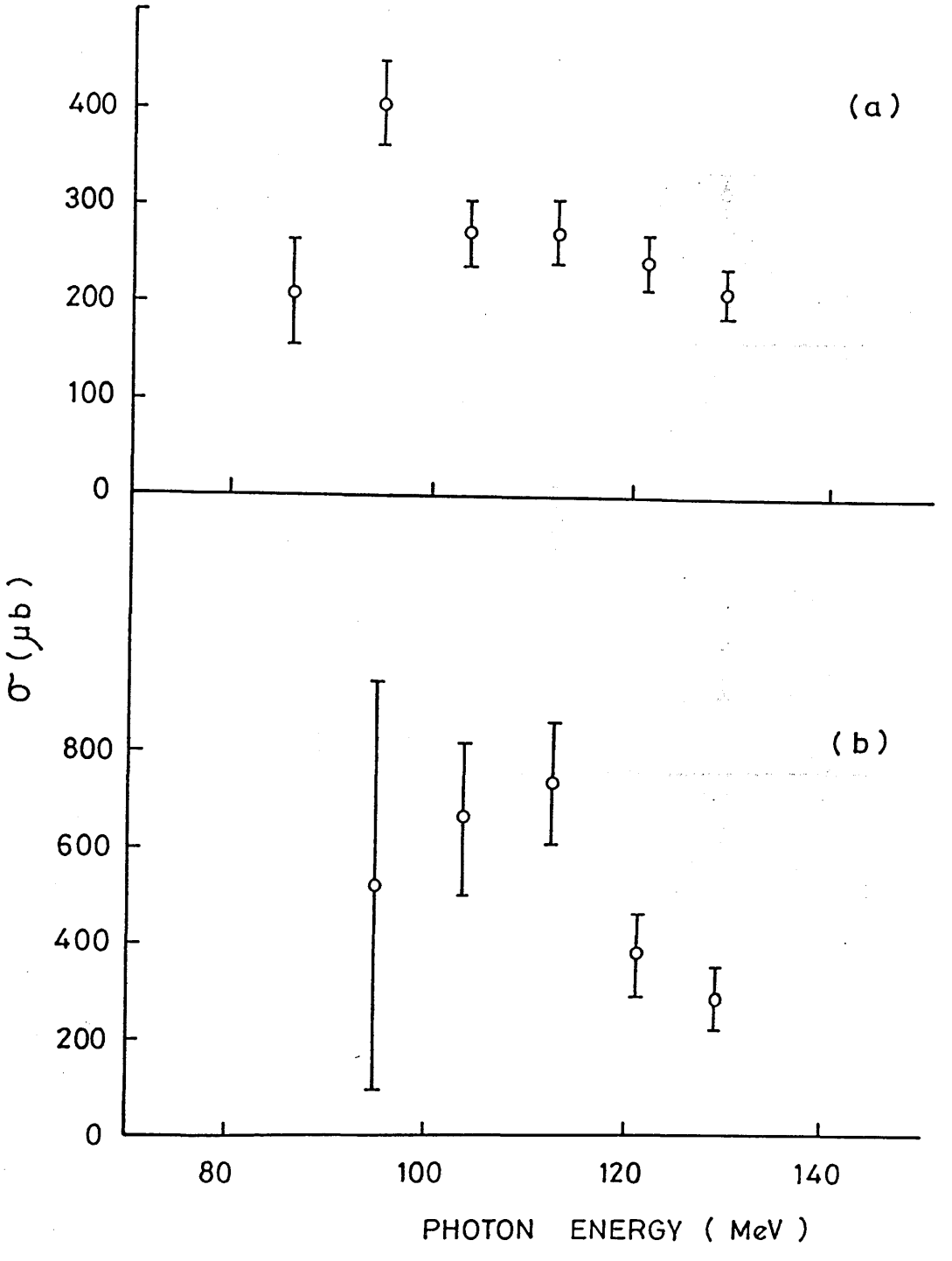

Figure 4.12: The (γ,pn) cross section as a function of photon energy, integrated over neutron angles from 67.5° to 105.0°, with the integration correction f_Ω included. (a) Carbon (1p1p) data, and (b) carbon (1p1s) data.

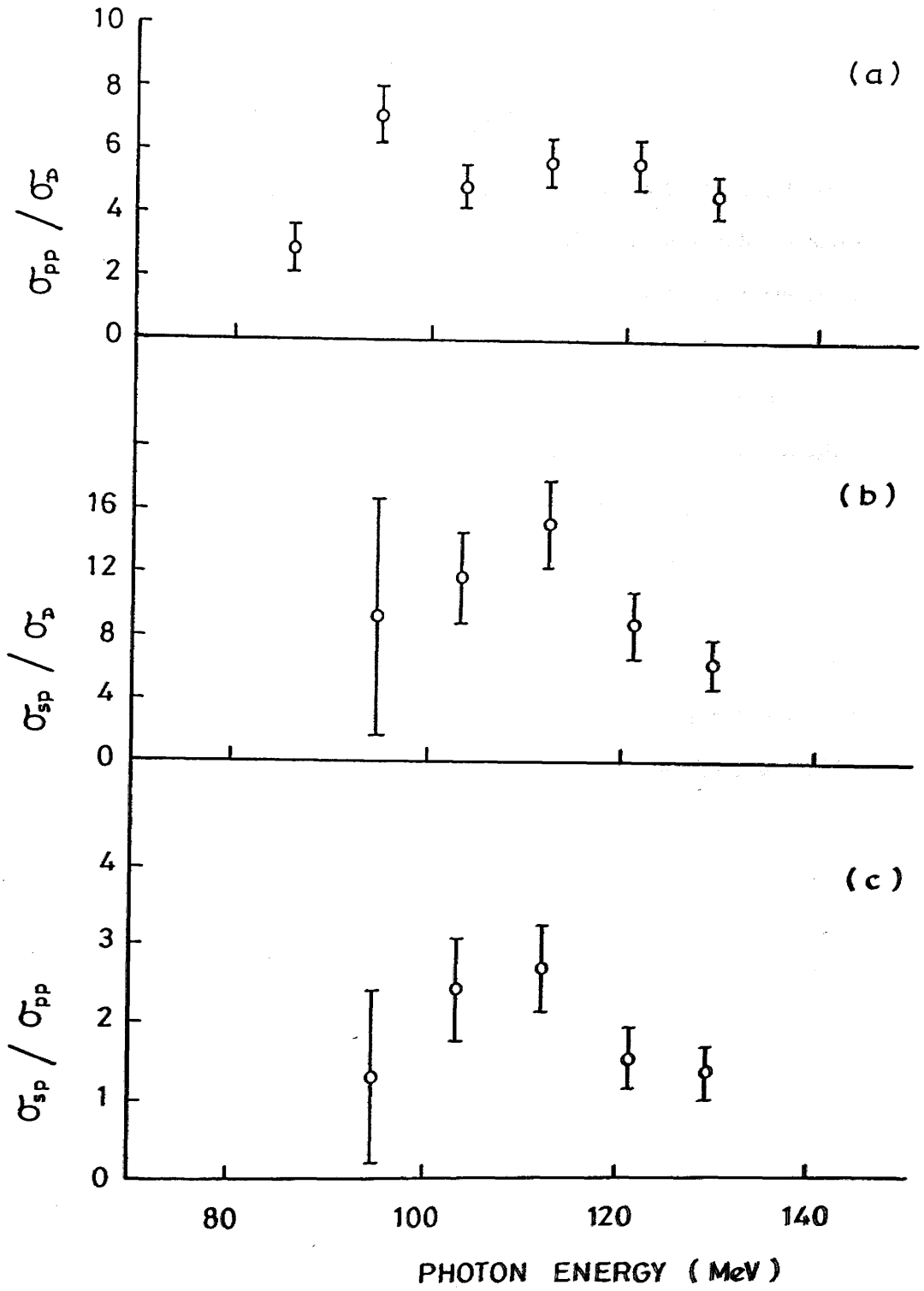

Figure 4.13: Ratios of the (γ,pn) cross section as a function of photon energy, with the integration correction f_Ω included. (a) The carbon (1p1p):deuterium ratio, (b) carbon (1p1s):deuterium ratio, and (c) carbon (1p1s):carbon (1p1p) ratio.

above 100 MeV. Introducing loss corrections introduces a negative slope to the data above 100 MeV (Figure 4.13(c)).

4.5.2 Neutron Angle Dependence

The data used to examine the angular dependence were selected from the top 20 MeV of the photon energy range i.e. 113–133 MeV. The measured values, without the integration correction, are shown in Figure 4.14 and the corresponding carbon to deuterium ratios are shown in Figure 4.15((a) and (b)). The latter shows a slight decrease in ratio with increasing angle. The corrections for detector biasing, the results of which are shown in Figure 4.16, increase with angle in the (1p1p) case but remain constant in the (1p1s) case. Thus, in the 67.5°–105.0° region both ratios with the deuterium cross section are seen to be isotropic (Figure 4.17). Figure 4.17(c) shows the cross section ratio for the two missing energy regions in the carbon data. The trend suggests that the relative frequency of emission of (1p1p) and (1p1s) pairs does not vary with angle. The average ratio would suggest that (1p1s) pairs are emitted more often. This surprising feature will be discussed further in Chapter 5.

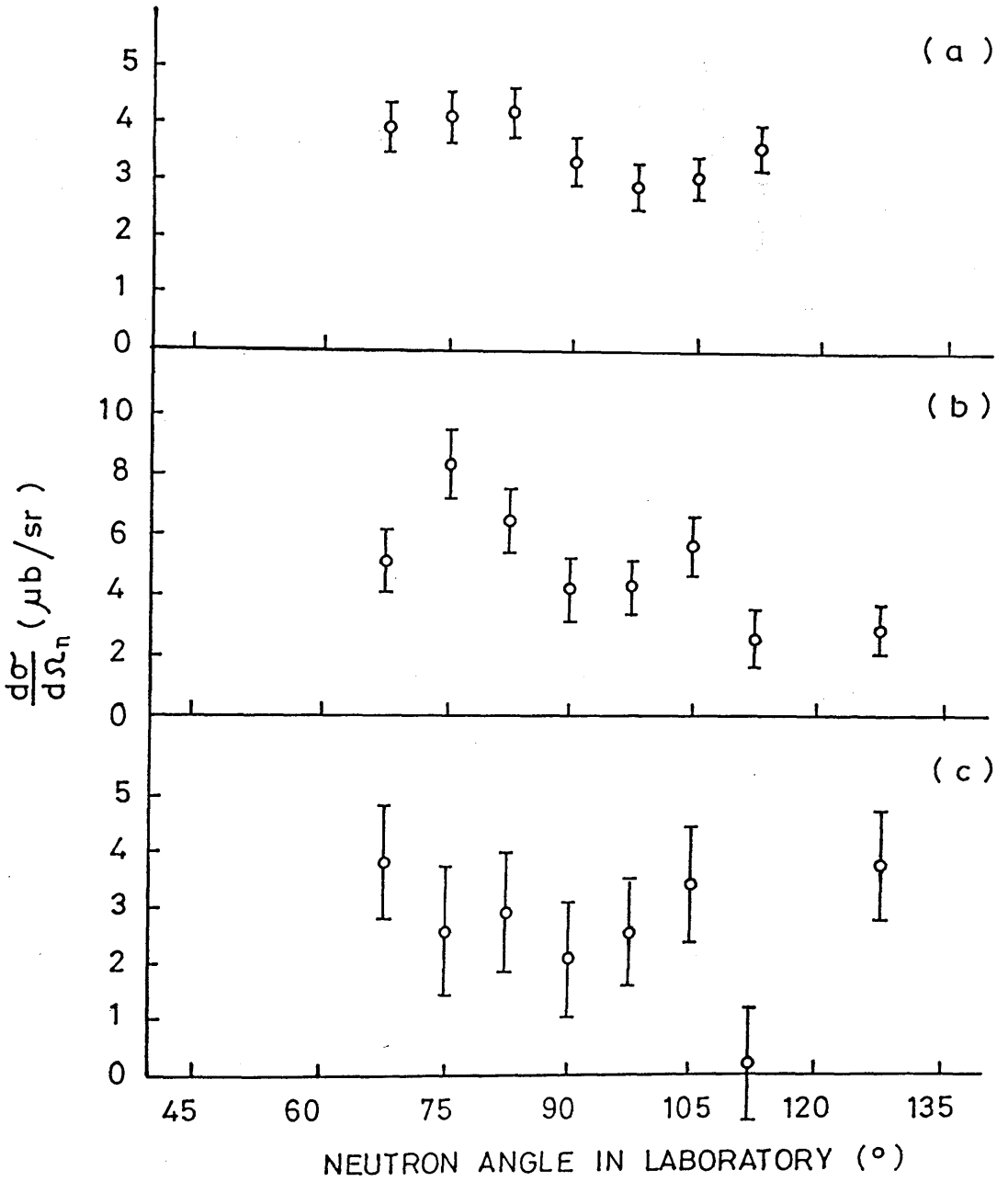

Figure 4.14: The (γ,pn) differential cross section as a function of neutron angle, integrated over all measured proton angles, and averaged over the 113 to 133 MeV photon energy range. (a) Deuterium data (b) carbon (1p1p) data, and (c) carbon (1p1s) data. The carbon data do not include the integration correction f_n.

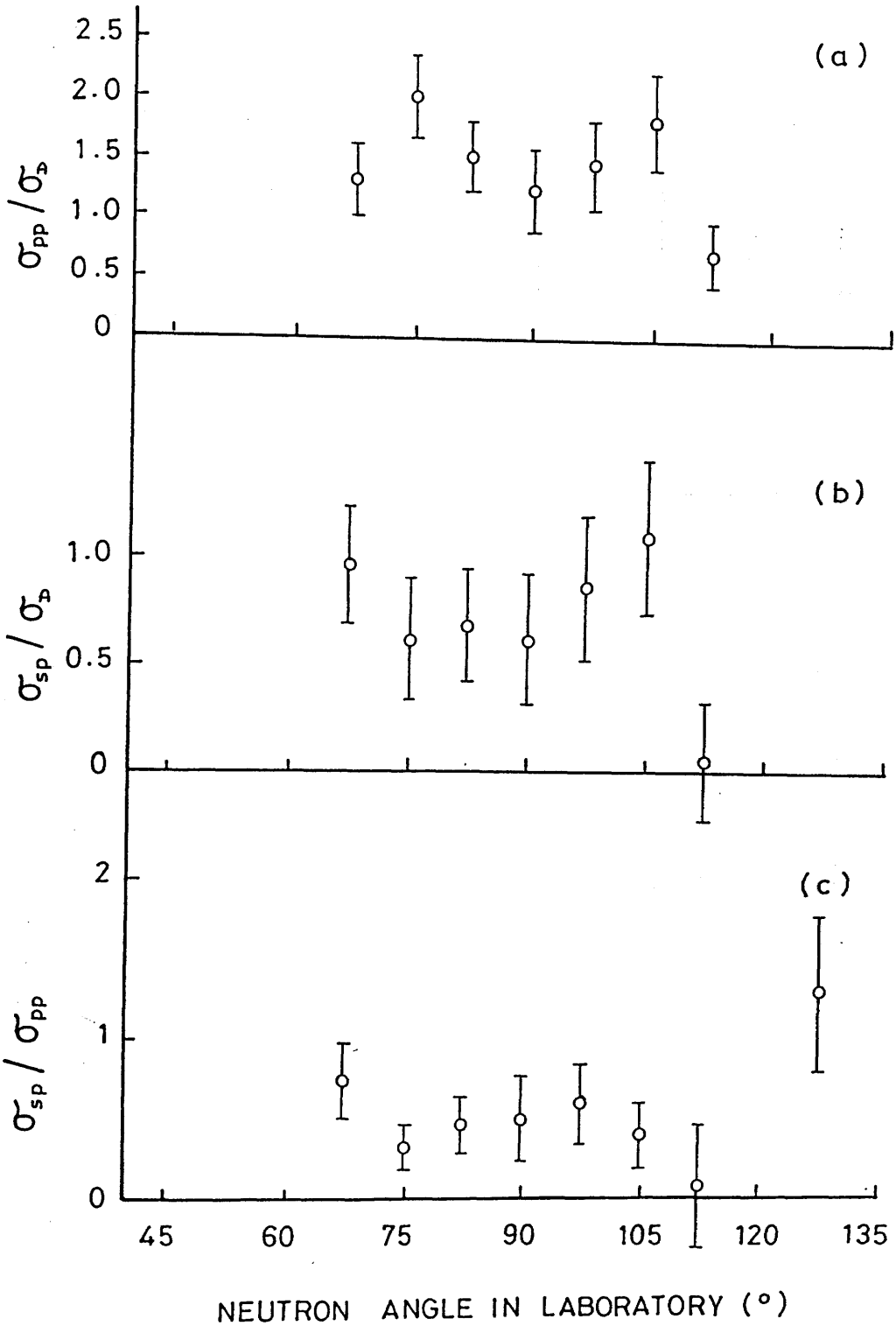

Figure 4.15: Ratios of the (γ,pn) differential cross section as a function of neutron angle, and averaged over the 113 to 133 MeV photon energy range. (a) The carbon (1p1p):deuterium ratio, (b) carbon (1p1s):deuterium ratio, and (c) carbon (1p1s):carbon (1p1p) ratio. The carbon data do not include the integration correction f_Ω.

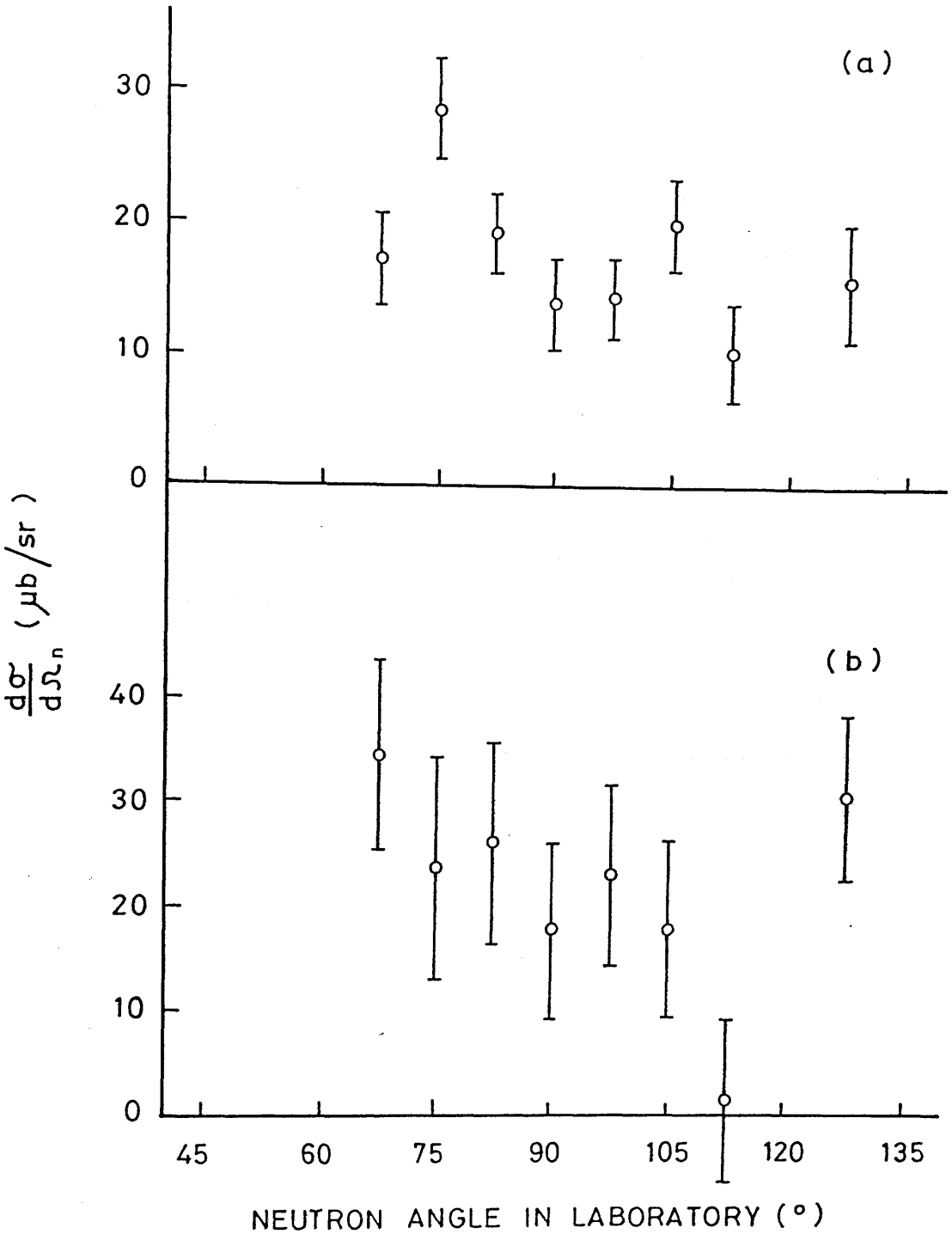

Figure 4.16: The (γ,pn) differential cross section as a function of neutron angle, integrated over all measured proton angles, and averaged over the 113 to 133 MeV photon energy range, with the integration correction f_n included. (a) Carbon (1p1p) data, and (b) carbon (1p1s) data.

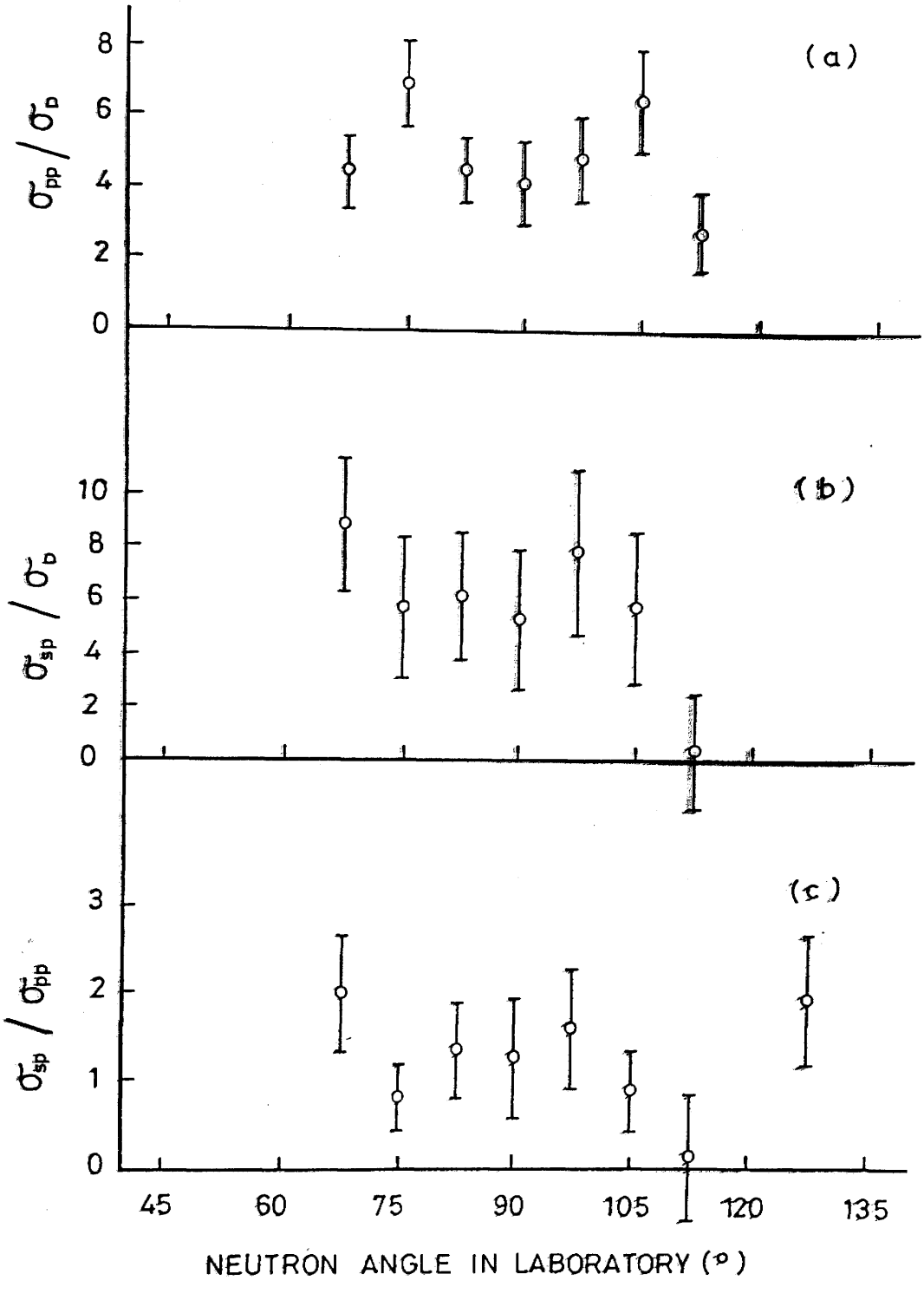

Figure 4.17: Ratios of the (γ,pn) differential cross section as a function of neutron angle, and averaged over the 113 to 133 MeV photon energy range, with the integration correction f_Ω included. (a) The carbon (1p1p):deuterium ratio, (b) carbon (1p1s):deuterium ratio, and (c) carbon (1p1s):carbon (1p1p) ratio.

Chapter 5

Discussion

5.1 The Low Missing Energy Region

5.1.1 The Reaction Mechanism

The data in this region show clear angular correlations, in agreement with the observations of previous authors. Such correlations are shown in Figure 4.2(b). The half width at half maximum corresponds to 20°. However, this in itself should not be taken as conclusive evidence of a quasideuteron mechanism since both the phase space and the quasideuteron calculations show similar correlations even though different mechanisms are assumed.

The Dalitz plot illustrated in Figure 4.4 shows that the recoil nucleus does not participate in the sharing of the available kinetic energy and acts more like a spectator in the absorption process. Again, however, caution is required since the effect may arise from the way the data are selected by the experimental system. Clear effects are observed in the comparison of the calculations with the recoil momentum distribution of Figure 4.3. The pure phase space prediction peaks at a higher momentum than does the distribution of experimental data points and so does not describe the data well. The agreement of the quasideuteron calculation is remarkable since no account has been taken of final state refraction or detector resolution effects.

The quasideuteron model also reproduces the distribution of the x- and z-components of the recoil momentum vector (Figures 4.5 and 4.7 respectively) and the distribution of its polar angle. Distributions in the y-component and the azimuthal angle of the vector do not agree in detail but show the correct qualitative features. In contrast, the phase space calculation fails everywhere except in the description of the x-component distribution and perhaps the azimuthal angular distribution.

The difference in the efficiency of the detection system for the two mechanisms has an important effect on the measured cross sections. The values, corrected

using the quasideuteron calculation, as a function of photon energy in Figure 4.13 reveal an average cross section of ~250 μb. Since the phase space calculation is a factor three less efficient, the resulting cross sections would be of the order of 700–800 μb. This would account for 70–80% of the total photon absorption cross section of Ahrens *et al.* [98], which show an average total cross section of ~1 mb in this range, and is considered unreasonable . This, and the preceding evidence, leads to the conclusion that, in this region, the reaction proceeds via a direct interaction of the photon with a correlated neutron-proton pair.

5.1.2 The Levinger Parameter

In the Levinger model the ratio of the nuclear cross section to that of deuterium is equated to the quantity LNZ/A (see Equation 1.1). The parameter L is dependent on the radius parameter r_0 and in his original calculation Levinger obtained $L = 6.4$ using $r_0 = 1.4$ fm. He later revised this to $L = 8$ [93] with $r_0 = 1.2$ fm. In fact r_0 is A-dependent and, from electron scattering data, has been parameterised by Elton [94] into the form

$$r_0 = 1.12 + 2.35A^{-\frac{2}{3}} - 2.07A^{-\frac{4}{3}} \text{ fm.}$$

Such variation (for example $r_0(A = 12) = 1.49$ fm, $r_0(A = 100) = 1.22$ fm) has led Tavares *et al.* [95], to parameterise L as a function of A. They arrived at

$$L = \frac{0.67}{NZ}A^{2.28} \tag{5.1}$$

so that for the ^{12}C nucleus a value of 5.4 is expected.

The product NZ represents the number of possible neutron-proton pairs, and in an experiment such as the present one, where cross sections from different shells can be measured, the contribution from these shells to the product NZ should be used in the model. In the 1p-shell $N_{1p} = Z_{1p} = 4$ so that for (1p1p) pairs the relevant number is $N_{1p}Z_{1p} = 16$. The same figure applies to (1p1s) pairs. However,

Nucleus	Group	Year	E_γ (MeV)	Final Value of L	Escape Factor Used	L without Escape Factor
^{4}He	Illinois	1958	150–280	6.3 ± 1.0	0.72	4.5 ± 0.7
	Tokyo	1985	190–430	4.2	1.00	4.2
^{6}Li	Illinois	1984	30	0.54 ± 0.03	1.00	0.54 ± 0.03
			40	1.02 ± 0.05	1.00	1.02 ± 0.05
			50	1.86 ± 0.12	1.00	1.86 ± 0.12
			60	2.61 ± 0.27	1.00	2.61 ± 0.27
	G.E.M.	1987	82–108	3.42 ± 0.30	1.00	3.42 ± 0.30
			108–133	4.14 ± 0.42	1.00	4.14 ± 0.42
			133–158	5.16 ± 0.36	1.00	5.16 ± 0.36
	Illinois	1958	150–280	4.1 ± 0.6	0.52	2.1 ± 0.3
	Glasgow	1967	~250	9.6 ± 2.3	0.37	3.6 ± 0.9
^{9}Be	Tokyo	1985	190–430	4.9	1.00	4.9
^{12}C	Sendai	1987	85	—	0.25	—
	G.E.M	1987	90.5	3.76 ± 0.44	1.00	3.76 ± 0.44
		1987	108.0	3.98 ± 0.38	1.00	3.98 ± 0.38
		1987	125.4	3.87 ± 0.38	1.00	3.87 ± 0.38
	Illinois	1958	150–280	—	0.42	—
	Glasgow	1967	~250	12.4 ± 3.0	0.31	3.8 ± 0.9
	M.I.T.	1960	~260	3.0	0.31	0.9
	Tokyo	1985	190–430	4.5	1.00	4.5
^{16}O	Glasgow	1965	~250	10.3 ± 2.6	0.30	3.1 ± 0.8
	Tokyo	1985	190–430	4.1	1.00	4.1
^{40}Ca	Glasgow	1967	~250	8.7 ± 2.1	0.18	1.57 ± 0.38

Table 5.1: L-values and probability-of-escape factors from (γ,pn) experiments. Data are found in refs. [23,24,25,26,27,42,78,100,102] and this thesis.

before the result of this experiment is presented the results of other authors are examined.

Photon Absorption Measurements

The total photon absorption cross section measurements of Leprêtre *et al.* [96] and Ahrens *et al.* [98] have proved useful in evaluating L. Levinger's theory fits the data well in the region above the Δ-resonance. However, in measurements of some heavy nuclei it overestimates the cross section at low energies near $E_\gamma = 40$ MeV. Levinger [99] explained this as arising from damping of the cross section due to Pauli blocking and introduced a factor e^{-D/E_γ} into his equation to account for it. Tavares further analysed the data of refs.[96,98] and found that for those nuclei considered, for which $A \leq 40$, D was approximately zero. In the case of lead he found a value of $D \approx 60$ MeV. From the data he parameterised L as

$$L = \frac{A^{2.147}}{NZ} \tag{5.2}$$

which agrees reasonably well with Equation 5.1 in the $A = 10$ to $A = 40$ region. It yields a value of 5.8 for ^{12}C.

Comparison with Other (γ,pn) Data

The (γ,pn) reaction was recognised early on as a valuable tool for investigating short range correlations via the parameter L. The analysis of the data has been hindered by confusion as to the importance of final state interactions, in particular absorption in the final state. Table 5.1 shows a list of the various L-values measured over the years for these experiments. It is evident that there are wide discrepancies between the measurements. Some of the discrepancies may be removed when the corrections to the data made by the various authors are removed as shown in the final column of that table. Figure 5.1 shows these results in graphical form. The ^{12}C data of the M.I.T. group is only displayed for interest and

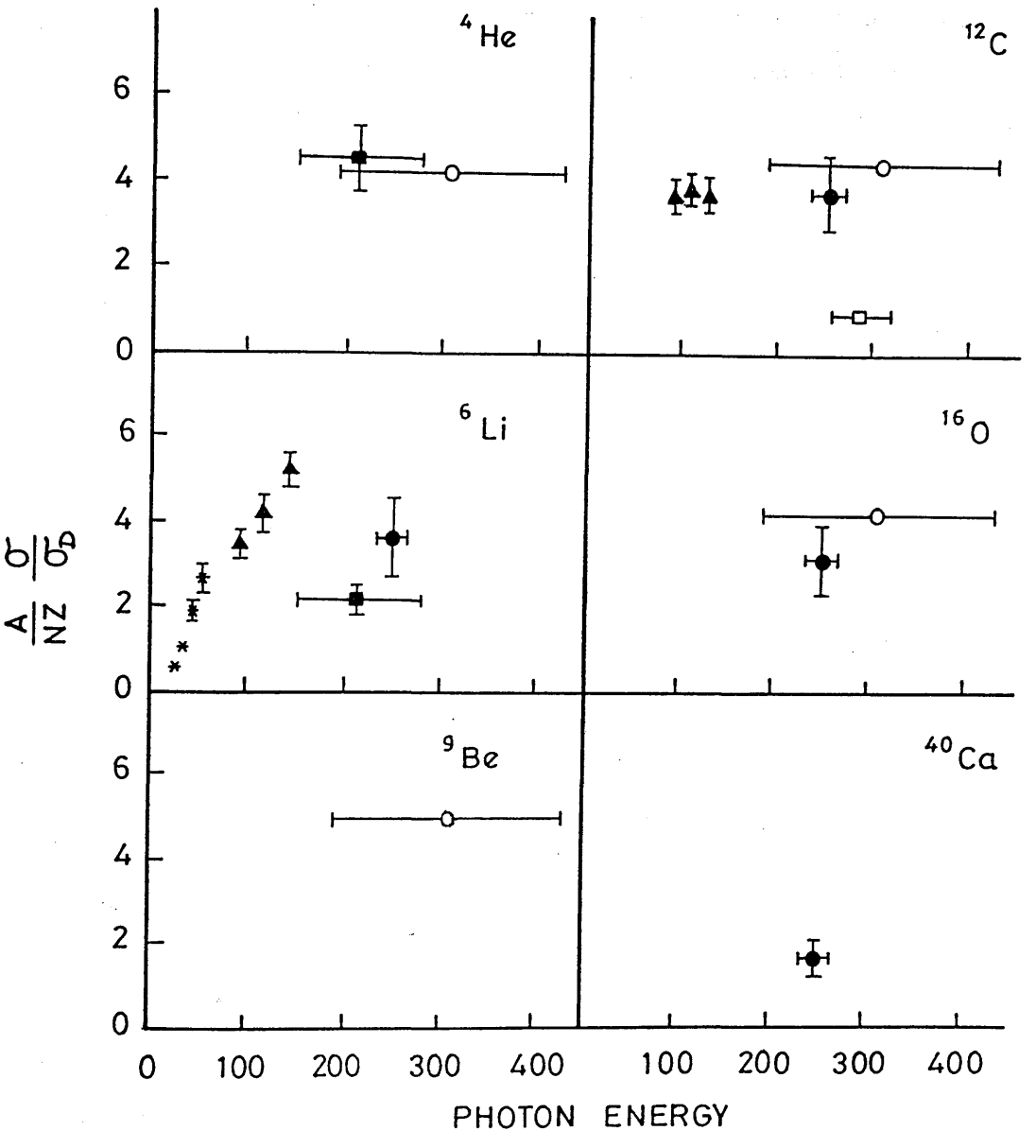

Figure 5.1: Values of $\frac{A}{NZ}\frac{\sigma}{\sigma_D}$ measured by various authors for various light nuclei. Correction factors to account for final state absorption have been removed. Solid squares–refs. [24,25]; open squares–ref. [23]; solid circles–refs. [26,27]; open circles–ref. [100]; stars–ref. [102]; triangles–ref. [78] and this thesis.

should not be treated equally with the other data (see the discussion of the M.I.T. data and the Glasgow data in Chapter 1). With this exception there is reasonably good agreement among other authors.

The most extensive measurements have been carried out on ^{6}Li by Vogt *et al.*. [78] and Wade *et al.* [102]. When comparing this data with the older data of Barton and Smith, taken at higher photon energies, a steadily increasing ratio $\frac{A}{NZ}\frac{\sigma_{QD}}{\sigma_D}$ with E_γ is observed. It is, perhaps, not surprising that the early results of Barton and Smith do not meet the data of Vogt since their experiment measured the cross section to all possible final states whereas the data of Wade and of Vogt measured the cross section to the state where there is an α-particle in its ground state. The data from the Barton and Smith experiment are more likely to be affected by final state absorption of the outgoing correlated neutron-proton pair since a nucleon from the deeper s-shell will have less kinetic energy and so be less able to escape.

The steep rise of Vogt's ^{6}Li data is not reproduced in the present ^{12}C data in Figure 5.1, which are separated into three photon energy bins for clarity. They yield an average Levinger parameter of 3.78 ± 0.23. The data show a constant cross section which agrees with the results of Tokyo and of Glasgow.

Pauli Blocking

The effect of Pauli blocking, as proposed by Levinger, would deplete the cross section at lower energies. The findings of Tavares, however, suggest that the effect is very small for light nuclei. Wade *et al.* fit their data, taken in the 30–60 MeV photon enery range, by appeal to a damping factor. However, to ascribe a Pauli blocking effect to the data of Wade would seem unreasonable since only pairs of 1p-shell nucleons are analysed which have a separation energy of 3.7 MeV, and are on the surface of the Fermi sea of nucleons. It would seem unlikely, considering the

photon energies used, that these nucleons are "blocked". Those authors themselves do not take their fit too seriously. Similarly, the present (1p1p) data from ^{12}C is unlikely to be affected by Pauli blocking although the (1p1s) data may be more susceptible to the effect. In the light of the findings of Tavares *et al.* and in the absence of a detailed theoretical treatment of Pauli blocking, the effect will be ignored.

Final State Interactions (FSI)

The variety of factors employed in the past to account for the probability of escape reveals considerable uncertainty as to their importance. Some authors [100,101] have ignored FSI altogether. A mean free path (mfp) approach to FSI has been followed by both M.I.T. and Glasgow to account for their high energy data. It is clear that the mfp of a nucleon in nuclear matter is dependent on the photon energy and nucleon emission angle. The effect will depend on exactly how the experiment is carried out. For lower nucleon energies the mfp is shorter since the reaction cross section of nucleons with residual nuclei is larger. (See the parameterisation of the absorption cross section in [97].) Figure 5.2 shows the effect of the mfp on the probability of escape factor as calculated by Stein *et al.* [23]. The FSI corrections are expected to decrease with increasing photon energy.

In the light of the good agreement of the total photon absorption cross section data in the high energy region with Levinger's model it is reasonable to assume that it will describe the (γ,pn) reaction. The discrepancy, however, between the present data and the expected value of $L = 5.8$ (in so far as this number can be applied to particular shells) from Equation 5.2 would require the inclusion of an escape probability factor of 0.65 to "make the data fit" the model in the (1p1p) case.

The importance of the contributory reaction channels to the photodisintegra-

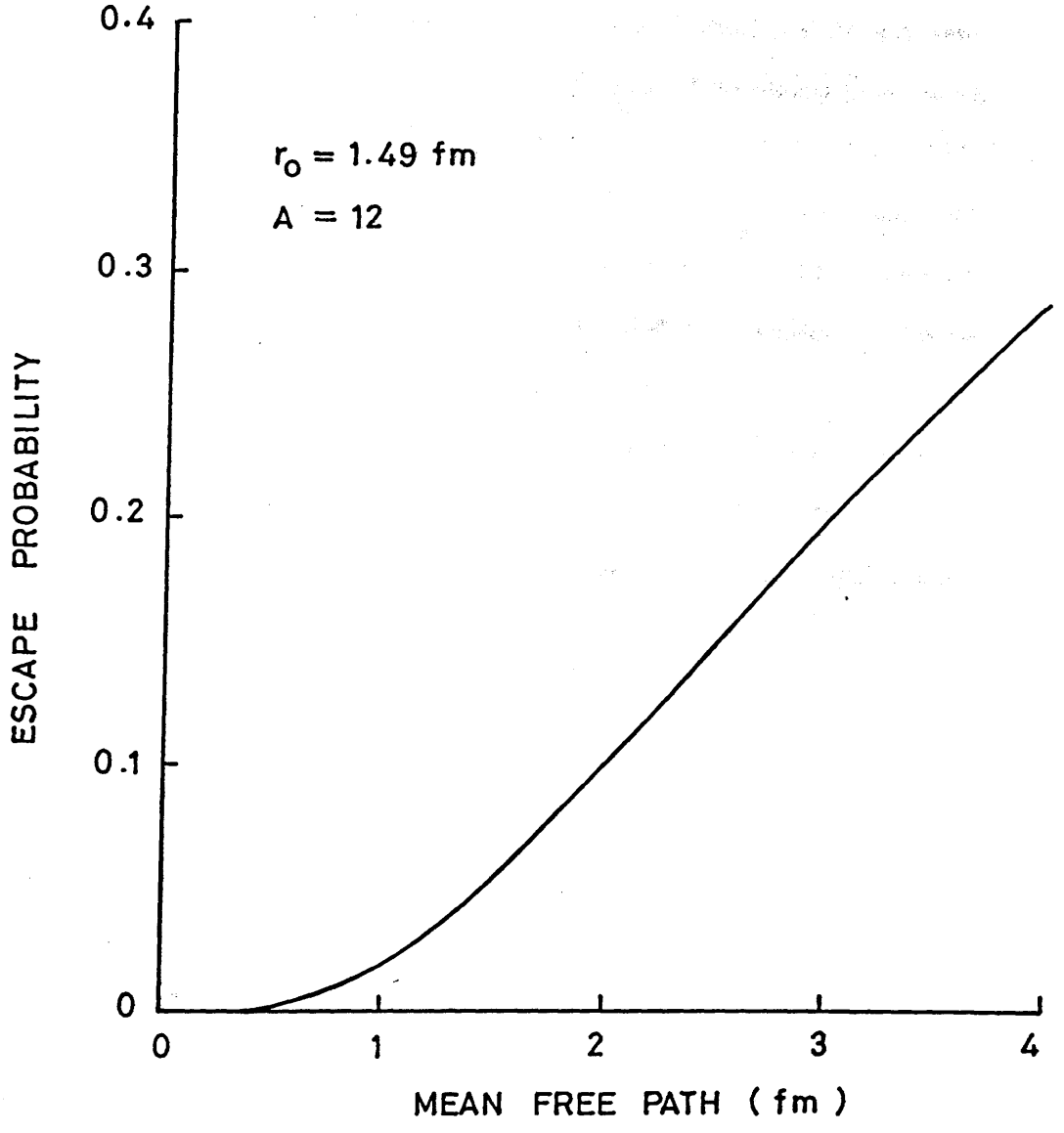

Figure 5.2: The probability that a proton-neutron pair will escape from a nucleus of mass $A = 12$ as a function of the mean free path.

tion of ^{16}O gives clues to the importance of FSI. An experiment performed by Carlos *et al.*[106] measured total photoneutron cross sections from ^{16}O from 30 to 140 MeV. It was shown that $\sigma(\gamma, 1\mathrm{n}\ldots)$[1] contributes ~85% to $\sigma^{(1)}(E_\gamma)$[2]. From the data of Gorbunov *et al.*[107,108] Carlos concluded that in the 30 to 170 MeV region only the (γ,pn), exclusive (γ,n), (γ,αn), (γ,αpn) and (γ,ppn) reactions contribute significantly to σ(γ,1n...). Gorbunov's data shows that, in this photon energy range, the integrated cross sections of the (γ,pn) reaction is 50% of that of (γ,1n...). Now Carlos also observed that $\sigma^{(1)}(E_\gamma)$ contributes nearly all of the total cross section in the 70 to 110 MeV range. Thus the (γ,pn) channel contributes at least 40% ($\sim 0.85 \times 0.5 \times 100\%$) to the total cross section in this region. The fraction will be similar over the 83 to 133 MeV range of this experiment. The radius of the ^{12}C nucleus is $\sim$ 10% less than that of ^{16}O and so the fraction of nucleon pairs which escape from ^{12}C will be greater. So in this energy region 0.40 marks a lower bound for the probability of escape of neutron-proton pairs. A value of 0.5 would yield a Levinger parameter of 7.5 ± 0.5 for the present data.

Angular Distribution

It should be borne in mind that the angular distributions (Figure 4.14) are sensitive to the accuracy of the neutron detection efficiency calculation obtained from the program STANTON which is estimated as $\pm$16%. Variation within this tolerance is not surprising, and the resulting distributions may show unusual effects. The cross section ratios, however, should be independent of this effect.

Except for a slight increase at the ends of the range, the efficiency correction f_n from the quasideuteron calculation shows little variation over the range of angles considered. Thus the shape of the distribution in Figures 4.14(b) remains largely the same as in 4.16(a). The cross section is forward peaked, presumably due to

[1] $\sigma(\gamma, i\mathrm{n}\ldots)$ is defined as $\sigma\,[(\gamma, in) + (\gamma, i\mathrm{np}) + (\gamma, in\alpha) + (\gamma, i\mathrm{n2p}) + \ldots]$ where $i = 1, 2, 3, \ldots$.

[2] $\sigma^{(j)}(E_\gamma)$ is defined as $\sum_{i=j}^{i_{max}} \sigma(\gamma, i\mathrm{n}\ldots)$ where $j = 1, 2, 3, \ldots$.

the centre of mass motion.

The cross section ratio of Figures 4.15(b) and 4.17(b) show no evidence of significant variation with angle, in agreement with the findings of Dogyust *et al.* [31], and with the more recent findings of Vogt *et al.* [78]. This is in accord with the quasideuteron model predictions.

5.2 The High Missing Energy Region

As in the case of the data at low missing energy, the quasideuteron model reproduces the shapes of the distributions shown in Figures 4.2, 4.3, and 4.5 to 4.9 for the high missing energy data quite well, within the statistical accuracy of the data points. The data would appear then to support the idea of absorption on a proton-neutron pair. It will be observed, however, that the phase space model also gives a reasonably good fit to the data thus rendering the results less conclusive.

Again, the efficiency of detection for the two processes helps clarify the situation, although not completely. As before the efficiency for the quasideuteron process is a factor 2–3 better than that for a phase space decay. Evaluating a correction factor for the former process yields an average total cross section of $\sim$500 μb whereas a phase space correction factor would yield a value of $\sim$1.0–1.5 mb. As before, this exceeds the total absorption measurement of Ahrens, and is therefore unrealistic.

There are still difficulties, however, since the quasideuteron efficiency correction renders cross sections for the (1p1s) data which are almost a factor two greater than those for the (1p1p) data(Figure 4.13(c)). The number of possible neutron-proton pairs available is 16 in each combination of shells and, to first order, it would be expected that each would yield a similar cross section. Further, the single particle wavefunctions for the two shells are completely different in character (the radial part of the 1s wavefunction is non-zero at zero radius, in contrast to the

1p wavefunction) so that the probability of finding two nucleons "close together" is less in the (1p1s) case than for the (1p1p) case thus reducing the (1p1s) cross section. The effect of FSI on an outgoing s-shell nucleon would be greater than the effect on a p-shell nucleon since it will have a shorter mean free path in the nucleus, thus further reducing the cross section.

The problem may lie in the fact that it is assumed in the Monte Carlo calculation that all the correlated pairs which absorb a photon will escape without experiencing any inelastic FSI. Suppose the cross section for absorption on a (1p1p) and a (1p1s) pair is σ^{1p1p} and σ^{1p1s} respectively. Because of FSI, the cross section for the emission of correlated neutrons and protons is depleted, written as $f_1\sigma^{1p1p}$ and $f_2\sigma^{1p1s}$ where f_1 and f_2 are depletion factors. Further, because of the limited solid angles and non-zero thresholds of the detectors only a fraction of the correlated pairs will be detected, written as $\frac{f_1}{f_\Omega^{1p1p}}\sigma^{1p1p}$ and $\frac{f_2}{f_\Omega^{1p1s}}\sigma^{1p1s}$, where the f_Ω's are defined in Section 3.6. It is assumed that the contribution to the absorption cross section $(1-f_1)\sigma^{1p1p}$, lost from the low missing energy region because of FSI, will still result in the emission of a neutron-proton pair. Such events will have a higher missing energy and will enhance the measured number of events there. These events behave in a manner more appropriate to phase space decay of the ^{12}C nucleus because of the liberal sharing of the available energy. Consequently the enhancement of the (1p1s) cross section is $\frac{1}{f_\Omega^{phase}}(1-f_1)\sigma^{1p1p}$. In the data analysis procedure the results are corrected for the detector limitations so that the corrected results give the dependence of

$$\Sigma_{1p1p} = f_1\sigma^{1p1p}$$

and

$$\Sigma_{1p1s} = f_2\sigma^{1p1s} + \frac{f_\Omega^{1p1s}}{f_\Omega^{phase}}(1-f_1)\sigma^{1p1p}.$$

Figure 4.13(c) shows that

$$\Sigma_{1p1s} = n\Sigma_{1p1p}$$

where $n = 1.7 \pm 0.2$. Defining $m = \sigma^{1p1p}/\sigma^{1p1s}$ and assuming $f_1 = f_2 = f$ it can be shown that

$$m = \frac{f}{fn - C(1-f)}$$

where $C = f_\Omega^{1p1s}/f_\Omega^{phase}$. The two Monte Carlo codes described in Section 3.6 indicate that C has a value of 0.3 to 0.5 over the photon energy range. From previous measurements $f \sim 0.5 \pm 0.1$. These figures give a value of

$$m = 0.8 \pm 0.3. \tag{5.3}$$

The average value of $C \sim 0.4$ is taken in the extreme case where the initial correlation is completely lost. The other extreme is where there is no loss of correlation and $C = 1$. A more realistic picture would be somewhere between the two. Since m increases with C the value quoted in Equation 5.3 may be taken as a lower limit of m.

The result suggests that between 10% to 40% of the events measured in the high missing energy region may arise from the absorption of a photon on a (1p1p) pair. The final state interaction will result in an excited ^{10}B nucleus which will decay through a variety of channels usually involving an α-particle. Measurement of these other channels is beyond the scope of this experiment since the heavier ions have a relatively short range in air compared with protons and are not detectable with the present system. Further detailed analysis of this region is thus difficult to carry out.

5.3 Meson Exchange Currents and Correlations

The success of the quasideuteron model at high energies points to a significant contribution from the interaction with meson exchange currents (MEC) in the nucleus since they contribute a substantial fraction to the deuteron photodisintegration cross section [105]. A phenomenological model such as Levinger's

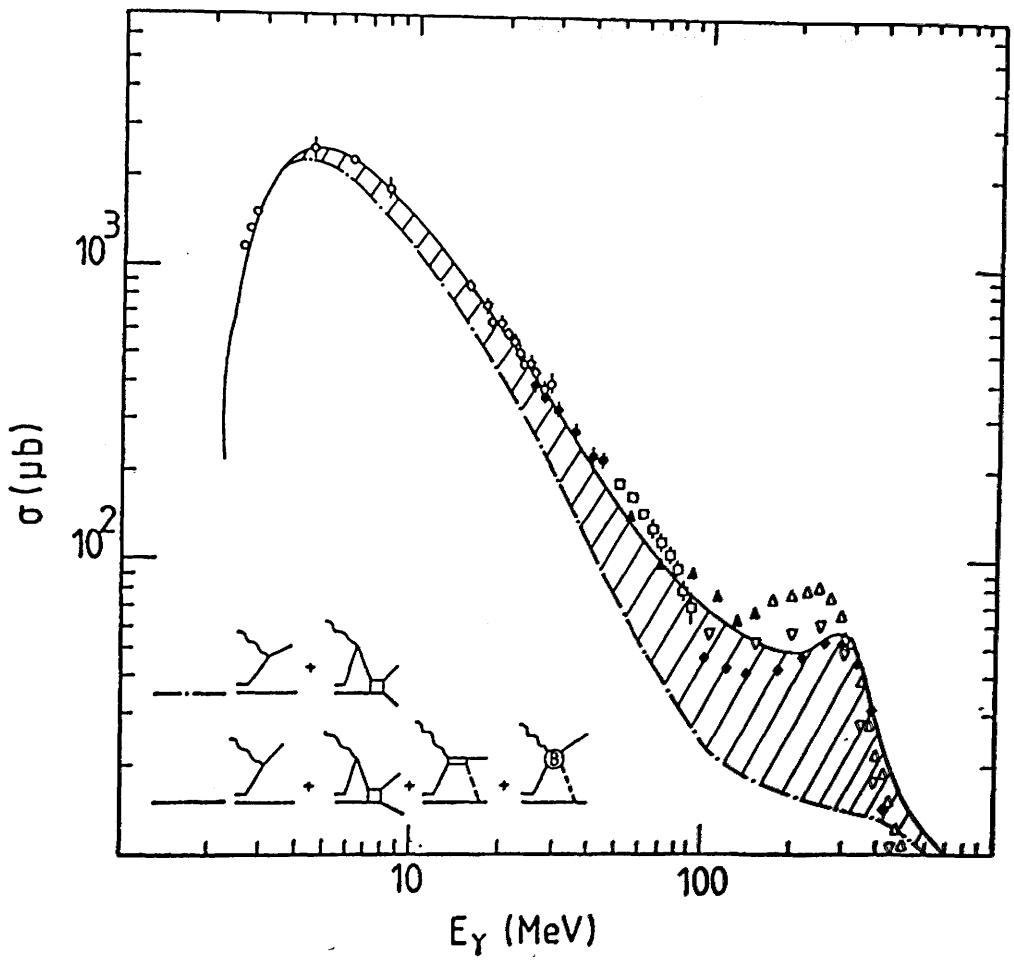

Figure 5.3: Laget's calculation of $\sigma_D(E_\gamma)$. The hatched area shows the contribution made by meson exchange currents over and above the simple direct plus rescattering contributions. The data points are described in [105].

contributes much to a general picture but provides little detail. Other authors have attempted to provide a detailed microscopic description.

Laget's Modified Model

It has been proposed by Laget [105] that the absorption of a 40–140 MeV photon ought to be associated with only the MEC contribution to the deuteron photodisintegration cross section,

$$\sigma_{QD} = L' \frac{NZ}{A} \sigma_D^{exch}. \tag{5.4}$$

The fraction of σ_D which is attributed to σ_D^{exch} is shown in Figure 5.3. The cross section contribution removed is that arising from the direct knockout and rescattering amplitudes. The rationale behind removing the former would be that the deuteron photodisintegration cross section already contains a contribution due to a direct interaction of a photon with the charge on the proton. This part of the cross section contributes mainly at low photon energies and depends on the momentum wavefunction of the proton in much the same way as the nuclear direct knockout cross section in Equation 1.8 does. It decreases rapidly with increasing photon energy as higher momentum parts of the wavefunction are probed. Retention of this part of the deuteron cross section in that of the quasideuteron, while treating the nuclear direct knockout process separately, introduces an element of "double counting" of parts of the cross section and should therefore be excluded. Meanwhile the excess cross section above the direct part arising from exchange current contributions becomes more important with increasing photon energy.

The function $L' \frac{\sigma_D^{exch}}{\sigma_D}$ is shown in Figure 5.4 with $L' = 11$ and is, in line with Equation 5.4, to be equated to $\frac{A}{NZ} \frac{\sigma_{QD}}{\sigma_D}$. Laget chose $L' = 11$ to fit the total photon absorption data of Leprêtre *et al.* taken from nuclei from Sn up to Pb. A value of $L' = 10$ provided a better fit to the photoneutron cross section data of Carlos *et al.* [106] from ^{16}O. Figure 5.4 also shows Levinger's modified model (which

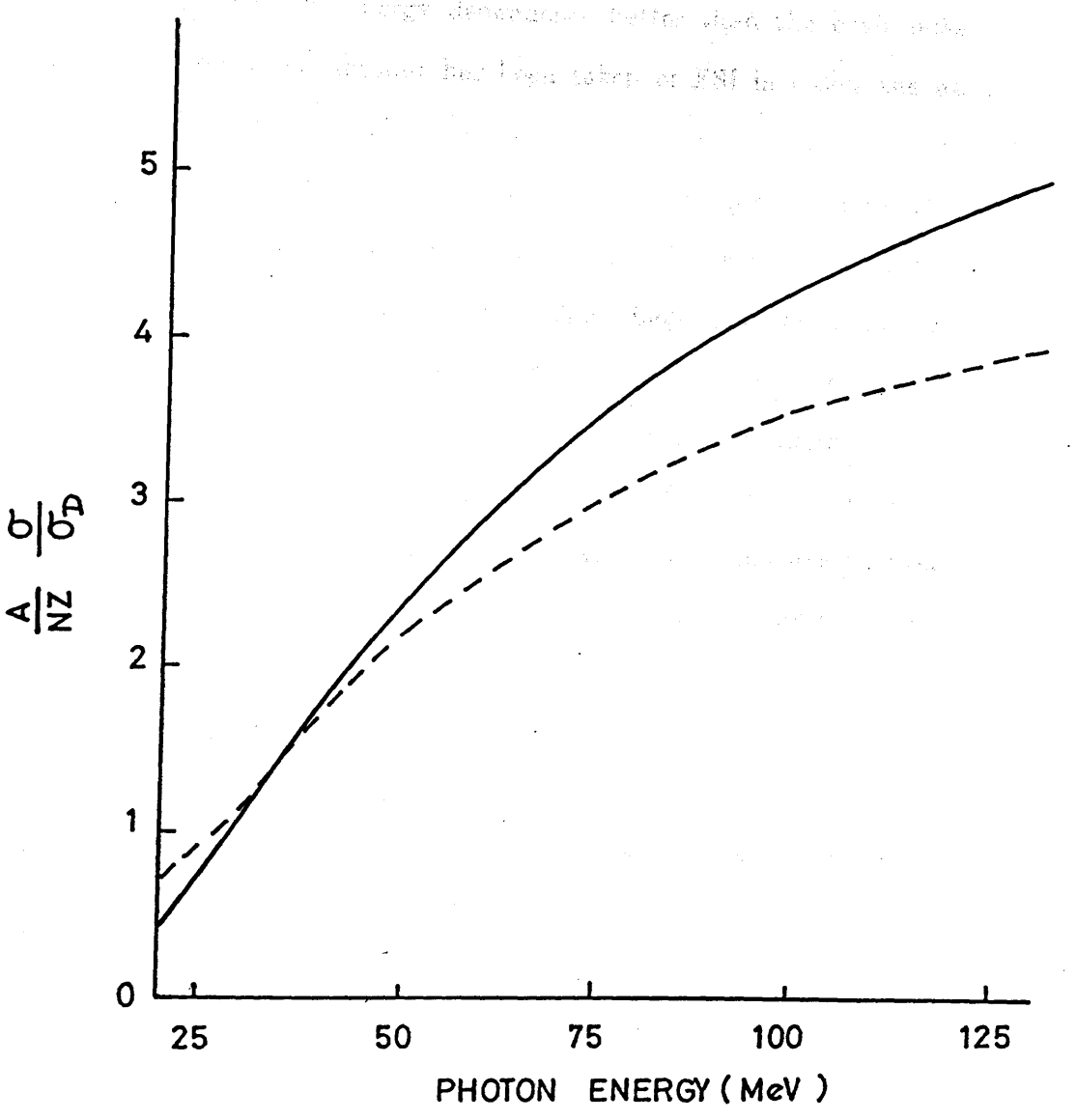

Figure 5.4: Dashed line : Laget's calculation of $L'\sigma_D^{exch}/\sigma_D$ with $L' = 11$. Solid line: Levinger's calculation of Le^{-D/E_γ} with $L = 8$ and $D = 60$ MeV.

includes the effect of Pauli Blocking) with parameters $L = 8$ and $D = 60$ MeV, the parameters appropriate for a heavy nucleus. Both models display the same qualitative effect of a gradually increasing function with photon energy.

The present data can be fitted with $L' = 10$ as shown in Figure 5.5. The theory reproduces the energy dependence better than the basic quasideuteron model. However, no account has been taken of FSI in either the data or the theory so that Laget's model may underestimate the cross section by up to 50%. It may be argued that the efficiency correction factor used to acquire the final data points is dependent on Gottfried's model. In particular it would be dependent on the ^{2}H(γ,n) reaction cross section. Since Laget's model is one for the total absorption cross section only, one can do no more than assume that his exchange contribution has the same angular dependence as the full differential cross section. The kinematics for deuteron breakup are fixed for a given photon energy and neutron angle so that the assumption will give the same correction factor. Until a more detailed model is available no further conclusions can be drawn.

A Microscopic Description with MEC

Gari and Hebach [44] have calculated the total (γ,pn) cross section for ^{16}O when the photon interacts with the MEC only. The contribution which arises from the interaction of the photon with the charge on the nucleon is ignored since in their calculation it contributes little. The calculation does not include the effect of final state interactions.

Considering the success of the quasideuteron model, it is assumed that,

$$\frac{A_C \sigma_C}{(NZ)_C} = \frac{A_O \sigma_O}{(NZ)_O} \tag{5.5}$$

in order to estimate the cross section for ^{12}C. The contribution to the total cross

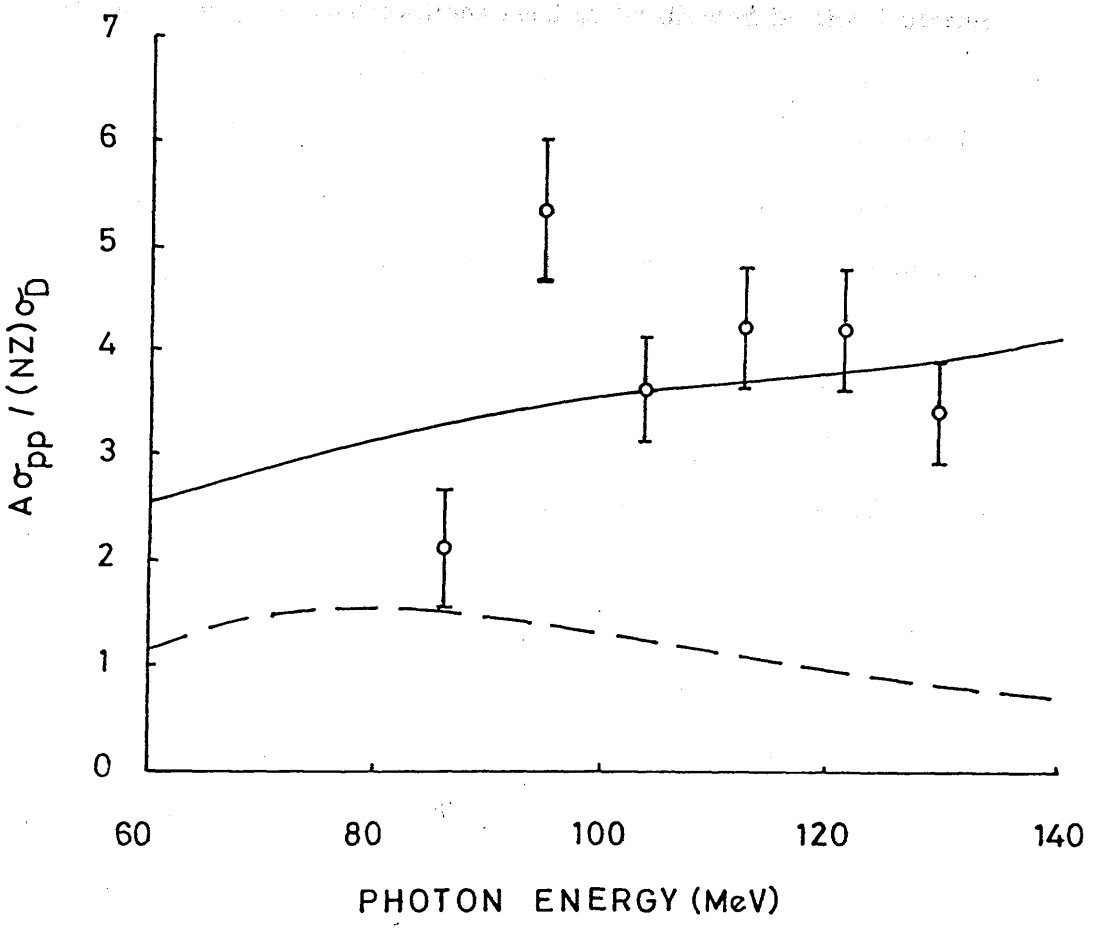

Figure 5.5: Comparison of the present $^{12}C(\gamma,pn)$ low missing energy data with the calculations of Laget (solid lines) and of Gari and Hebach (dashed lines).

section from each shell combination is estimated by further assuming

$$\sigma_C^i = \frac{(NZ)_C^i}{(NZ)_C}\sigma_C \tag{5.6}$$

where the superscript i indicates the particular shell combination ((1p1p), (1p1s) or (1s1s)). To compare the data with the cross section ratios as for the Laget treatment above, the contributions need to be divided by the deuterium photodisintegration cross section and multiplied by $A_C/(NZ)_C^i$. Thus the measured quantity $A_C\sigma_C^i/(NZ)_C^i\sigma_D$ should be compared with $\frac{1}{4}\sigma_O/\sigma_D^{th}$ for each shell, where σ_O is the cross section of Gari and Hebach and σ_D^{th} is some theoretical calculation. For consistency, the calculation of the total two body photodisintegration cross section by Laget [104] has been used.

The results for ^{12}C are shown in Figure 5.5. The calculation is, at best, a factor two lower at 60 MeV, and a factor five lower at 140 MeV. Unlike the Laget curve, that of Gari and Hebach has a maximum at ~80 MeV and falls off with increasing energy. Again FSI will be an important effect unaccounted for here. Qualitatively, the data appear to reach a maximum at higher photon energy. Strictly speaking the calculation is an average over all possible shell combinations and so the details of the cross section may differ slightly from those represented in the figure.

Jastrow-type Correlations

Weise, Huber and Danos (WHD) have presented evaluations of the cross sections for photoemission of (1p1p) and (1s1s) pairs, and the total cross section, for ^{16}O [19]. From these the author has synthesised the (1p1s) cross section (which comprises of that for a 1s-shell neutron and a 1p-shell proton and *vice versa*). WHD did not evaluate the corresponding cross sections for ^{12}C. However, assuming Equations 5.5 and 5.6, the cross section for (1p1p) pairs from ^{12}C is

$$\sigma_C^{(1p1p)} = \frac{16}{27}\sigma_O^{(1p1p)}.$$

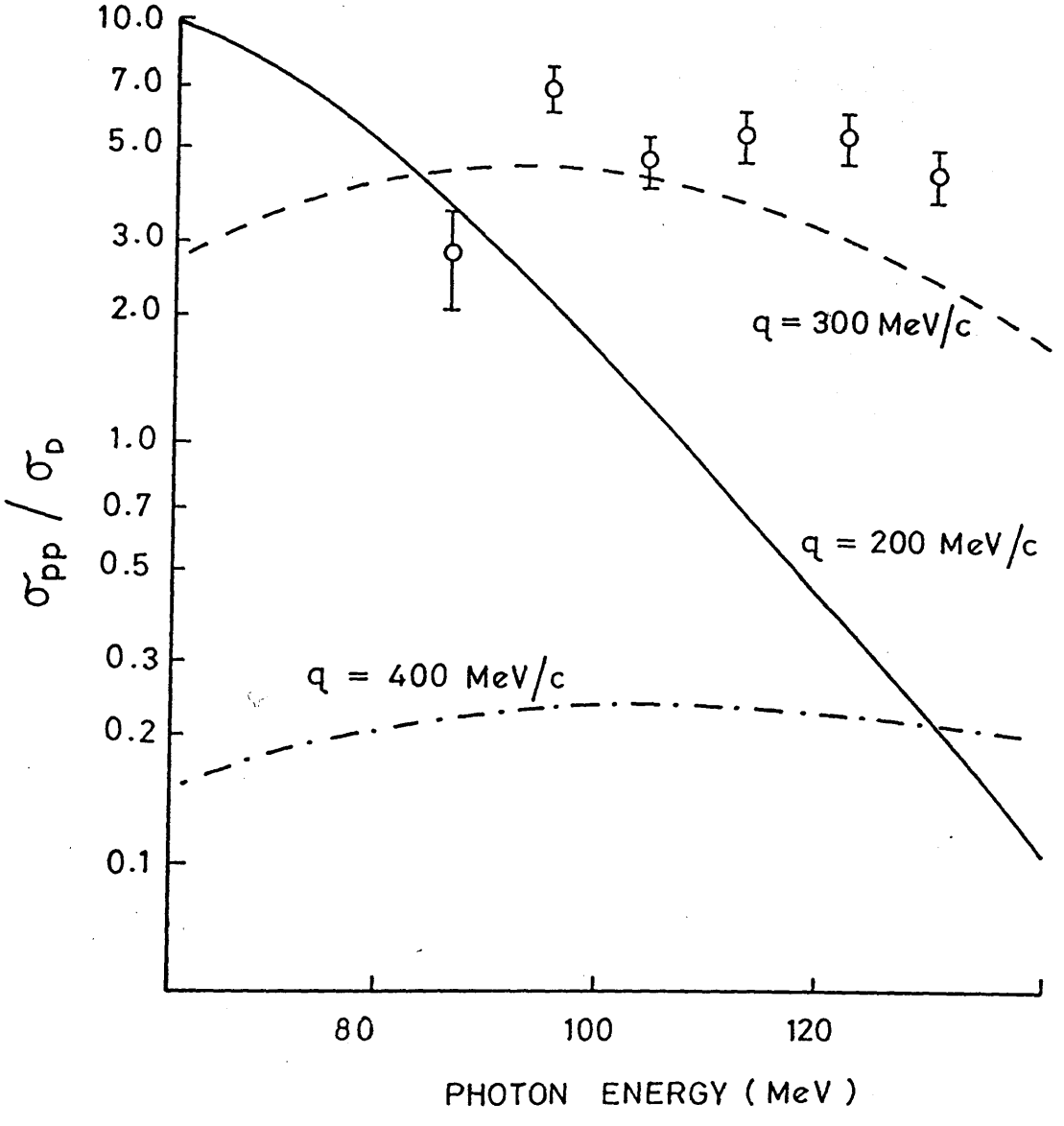

Figure 5.6: Comparison of the ratio σ/σ_D of the present (1p1p) data with the calculations of WHD for various values of q, the exchanged momentum.

The dependence of $\sigma_C^{(1p1p)}/\sigma_D$ (with σ_D given by Laget) is shown in Figure 5.6 for various values of the parameter q, the momentum exchanged between the nucleons during the absorption process. The results are qualitatively different from the calculations of Laget which predict a steadily increasing function $L'\frac{\sigma_D^{exch}}{\sigma_D}$ in this region. All the curves of WHD are either decreasing between $E_\gamma = 80$ MeV and $E_\gamma = 130$ MeV or reach a maximum in the region. It appears that for higher q, the rate of decrease with photon energy is less.

It will be observed that for the ratios shown in Figure 5.6 the data lie near the $q = 300$ MeV/c curve. This agrees with the results obtained by WHD in their analysis of (γ,p) data. Qualitatively, the (1p1p) data rises over its range while the $q = 300$ MeV curve is turning over.

Summary and Comments

It would appear that the attempt by Laget to parameterise the energy dependence of the the total photon absorption cross section by one parameter has been, according to other papers, succesful. Applied to the present (γ,pn) data the result is not so succesful. The energy dependence is reproduced but the magnitude is wrong. It may be that the assumption implicit in the data points, that each shell combination contributes exactly according to the number of pairs it contains, may be at fault. The treatment of Gari and Hebach is of a more fundamental nature and has a more correct form. Its failure to reproduce the correct magnitude of cross section may be due to inaccurate input parameters such as the unrealistically deep shell model potential used and the long range Yukawa-type form of the residual interaction.

It should be stressed that the WHD approach should only be considered as a rough outline of a calculation which needs much improvement. The principle of the WHD calculation should not contradict the work of Gari and Hebach and

others since the modifications to the wavefunctions introduced by the Jastrow formalism necessarily modify the two-body current (MEC) distribution, through the continuity equation. The problem is to find the modifications which give rise to the correct two-body current required to preserve guage invariance. Some possible directions are mentioned in the concluding section.

Chapter 6

Conclusions

At the experimental level, it has been shown that a working system has been developed which can accurately measure all the kinematic variables required to establish unambiguously the kinematics of the $^{12}C(\gamma,pn)^{10}B$ reaction. The importance of this cannot be understated in view of the consequences of some erroneous assumptions (made for example by Stein *et al.*) about the excitation energy of the residual nucleus.

The present data are more detailed than those taken in previous (γ,pn) measurements and, indeed, are the first kinematically complete measurements on ^{12}C attempted in this energy region. It has been possible, in principle, to distinguish the shells from which the nucleons have emerged, although in practice there is insufficient structure in the high missing energy region to substantiate this. For the present experiment it has been possible to reconstruct the recoil momentum of the residual nucleus and thus to establish that, in the low missing energy region, the reaction mechanism is a direct one with a correlated neutron proton pair. The high missing energy data suggest that there is some comtamination from the inelastically scattered (1p1p) pairs, although the uncertainties are considerable.

The basic quasideuteron theory of Levinger has survived long, owing, in the main, to inadequate experimental facilities and techniques. With a reasonable factor included for FSI it is still able to account for the present data. Models which try to associate the photoabsorption process with MEC give valuable insights into the details but, in that they can only account for fraction of the measured cross section, meet with only limited success. To compare the measured data with the contributions from MEC between nucleons in different angular momentum shells, more detailed calculations are required. The more exact calculations of Gari and Hebach need to be improved with more realistic parameters and assumptions.

Further work is required along the lines of Weise *et al.* before the worth of their calculations can be completely assessed. The present data best fit cross sections

calculated with $q = 300$ MeV/c, in broad agreement with earlier (γ,p) measurements. Shapes more realistic than a simple δ-function need to be tried for the exchanged momentum packet. Even the use of a Gaussian function is too restrictive. An additional modification would be to introduce momentum packets which have more than one parameter. For example, the function $\delta(q - q_0)$, in which the parameter q_0 is varied, says nothing about the likelihood that such a momentum is exchanged. Additional parameters, such as a "strength" parameter could be included. Such questions are being examined by Owens [110] in an attempt to explain (γ,p_0) reactions, and will also be applied to (γ,pn) reactions. Realistic wavefunctions and potential parameters are required and correct normalisations have to be evaluated. Detailed calculations of the expected angular distributions would be of value.

On the experimental side there is much work to be done. The present data need to be extended over wider ranges and new data taken with improved statistics to observe trends more clearly. In particular, lower photon energy data could be acquired. In this region the cross section from a complex nucleus is expected have a markedly different photon energy dependence compared to that of deuterium because of the Pauli blocking effect. The suggestion by some that Levinger's blocking parameter D is small for light nuclei would imply that the effect varies rapidly at lower photon energies. Such experiments should stimulate further theoretical efforts to investigate it. Data taken at higher photon energies would be less susceptible to detector threshold effects and final state interactions and would allow clearer observation of (1p1s)-pairs and also (1s1s)-pairs. If contamination from other secondary processes can be accounted for, the interactions of nucleons in different shells could be investigated.

Experiments on other nuclei are required. The most important of these are the lightest nuclei, especially ^{2}H and ^{3}He for which the wavefunctions can be calculated.

The $^2H(\gamma,p)n$ reaction needs to be accurately studied since the details of meson exchange currents can then be extracted. Previous measurements have lacked the precision required to do this. ^4He is likely to produce valuable information since it is the most dense of all nuclei and should reveal data on correlations at a very short range. With such prospects it is hoped that such experiments will greatly enhance our understanding of nucleon-nucleon interations within nuclear matter.

Appendix A

Photomultiplier Tubes

To determine which photomultiplier tube to use for the rear rank of the proton detector two kinds—Thorn EMI 9823B and Mullard XP2041 photomultipliers—were compared, testing each for

- the uniformity of response over the photocathode area, and
- the pulse height resolution.

The uniformity was considered important since any nonuniformity may introduce a degradation of resolution for events near the ends of the scintillator. There are two main factors which affect the uniformity of response,

- the variation in thickness of the photocathode coating, and
- how well the photoelectrons can be collected at the first dynode d_1 (see Figures A.2 and A.3).

The photomultiplier manufacturing process determines the thickness of the photocathode layer and the results vary from tube to tube. This, in turn, determines the probability that an incident photon will produce a photoelectron. This physical variation can be compensated for to some extent by the use of a focusing grid between the photocathode and d_1. The potential of the grid (V_g) is variable and is used to optimise the flight path of the photoelectrons so that as many as possible

are collected at d_1. The variation of V_g improves the collection of electrons from the thinly coated areas and reduces collection from thickly coated parts. The potential at d_2, the second dynode, also has a small, second order effect on electron collection at d_1.

Uniformity tests of the photocathode response showed that, after optimisation of the base chain, the output signal from a typical EMI tube dropped as much as 41% from the maximum along the worst diameter compared with a drop of more than 75% for that of a typical Mullard tube. Figure A.1 shows the deviation from uniformity of the whole cathode plotted against V_g. V_{d_2}, in its optimum setting, improves uniformity by ~10% on that of its worst setting. Comparisons of resolution of the two types of tube showed that EMI tube also gives slightly better resolution. One further factor which favoured the choice of the EMI tube over the Mullard tube was that the Mullard tube had a dome shaped photocathode and was supplied with an attaching plano-concave light guide. This would have necessitated a further optical join in the final detector assembly which was undesirable.

The base chain used for the test is shown in Figure A.2. A large potential between the photocathode and d_1 sweeps photoelectrons away towards the first dynode and through the focusing grid. From d_2 to d_7 the inter-dynode potential is constant, but from d_7 to d_{14} it increases steadily to reduce space charge effects caused by the large numbers of electrons being produced in the latter dynode stages. The effect would result in tube saturation for large scintillations, but this is further avoided by reducing the multiplication factor at d_8. Consequently, V_{d_8} is variable, the multiplication factor being dependent on this. Large amounts of charge incident on the later dynodes also cause fluctuations in the base chain current, causing instability in the inter-dynode potentials. This effect is greatly reduced by the use of decoupling capacitors. The optimum settings for the grid voltage and d_2 voltage were determined for each of the six photomultipliers used.

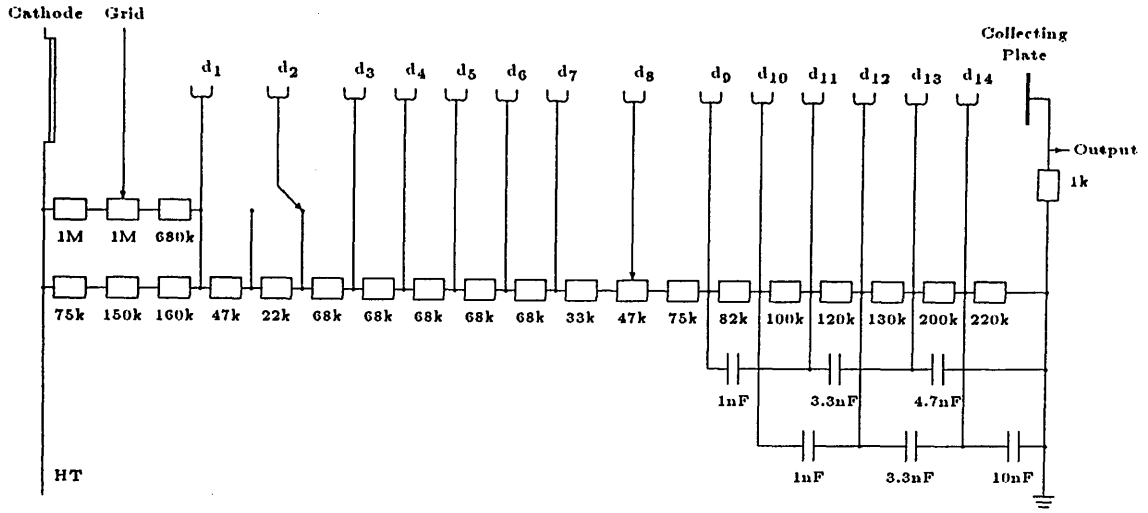

Figure A.2: Circuit diagram of base chain used in photomultiplier tests.

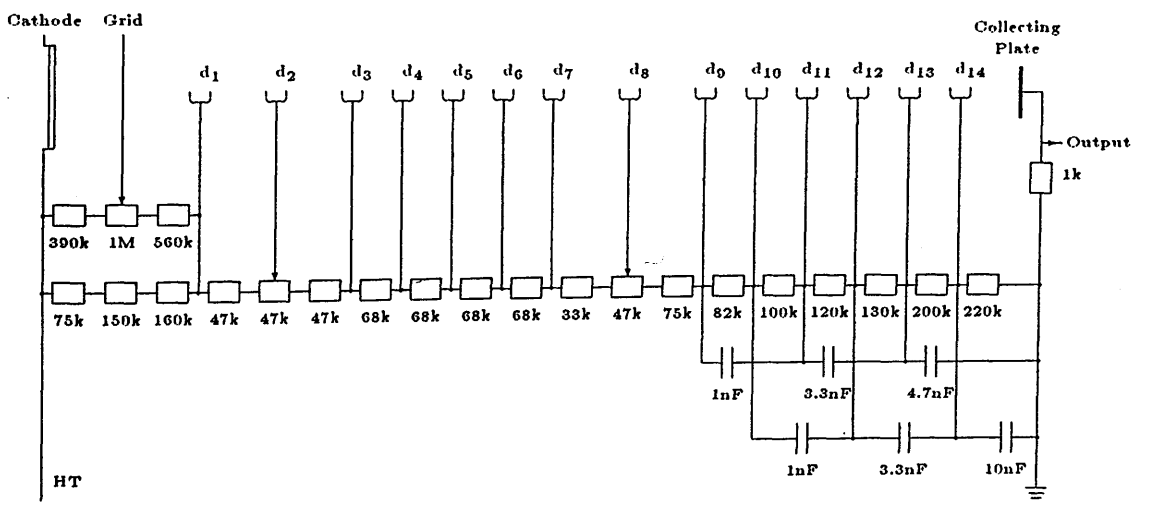

Figure A.3: Circuit diagram of final design of base chain used in the experiment.

The final design of the voltage divider was based on these results and is shown in Figure A.3.

When measuring the resolution of both tubes it was found that the voltage parameters obtained for best uniformity coincided very closely with those for optimum resolution. When optimised a typical EMI tube had slightly better resolution.

As for the 52 mm photomultiplier tubes used on the rest of the detector, uniformity of the photocathode layer thickness is less important owing to the smaller dimensions of the tubes and as light guides are used they have the effect of spreading the light more evenly over the photocathode surface. The resolution obtained from the middle rank of ΔE detectors is dominated by the light transmission of the twisted-strip light guides which are unusually shaped. Hence the grid voltages and d_8 voltages were adjusted to give maximum output with the cathode voltage set low enough to avoid saturation. Detailed setting up of the small front ΔE was less important as it was only used to indicate that a particle had come from the target.

Appendix B

The FPD-X-trigger TDC Spectrum Shape

In order to calculate the corrections necessary to allow for losses in the selection of prompt events it is necessary to know the shape of the electron-proton TDC spectrum. The shape can be calculated on the assumption that the random electrons are truly random in time.

B.1 The Whole FPD

In this section the the whole focal plane detector is considered. In the next section the principles are applied to the more complicated consideration of a part of the detector.

B.1.1 The Multiplicity Distribution of Random Electrons

In this appendix the detection of random electrons which come within the logic gate produced by an X-trigger is assumed to be a Poisson process. That is, the probability of detecting k random, uncorrelated electrons within the X-Trigger gate is $e^{-\alpha}\alpha^k/k!$. α depends on the flux of electrons and on the gate width and it can be shown that α is the mean value of the parameter k.

The FPD is made up of six sections each of which can be treated as an independent detector. Let k_i be the number of random electrons which hit section

i ($i = 1,\ldots,6$ and $k_i = 0,1,2,\ldots$). An event is characterised by the 6-tuple $(k_1,\ldots,k_6)$. The events recorded by the experiment in which all the electrons are random are denoted by the set $R = \left\{(k_1,\ldots,k_6) : \sum_{i=1}^{6} k_i > 0\right\}$. The condition $k = \sum_{i=1}^{6} k_i > 0$ is necessary since events are recorded only when an electron hits the FPD. Thus the probability of an event in the set R is

$$P(R) = \sum_{k=1}^{\infty} \frac{e^{-\alpha}\alpha^k}{k!} = 1 - e^{-\alpha} \qquad (B.1)$$

where α is the Poisson parameter for the whole detector. In the situation where l electrons hit the whole detector the set of events of interest is

$$R^l = \left\{(k_1,\ldots,k_6) : \sum_{i=1}^{6} k_i = l \text{ with } l \geq 0\right\}.$$

The probability of R^l occurring given that R also occurs is written $P(R^l|R)$ and is given by

$$P(R^l|R) = \frac{P(R^l \bigcap R)}{P(R)}. \qquad (B.2)$$

Now, $R^0 \bigcap R = \emptyset$ so $P(R^0 \bigcap R) = P(R^0|R) = 0$. If $l > 0$ then $P(R^l \bigcap R) = e^{-\alpha}\alpha^l/l!$. So, combining these with Equations B.1 and B.2, the probability distribution of interest is

$$P(R^l|R) = \begin{cases} 0 & \text{if } l = 0 \\ \frac{e^{-\alpha}\alpha^l}{l!(1-e^{-\alpha})} & \text{if } l > 0 \end{cases} \qquad (B.3)$$

B.1.2 The Time Distribution of Signals from Randoms

Now the distribution of timing pulses obtained from random electrons within the gate is calculated. To start with, a problem involving boxes and objects is examined.

Consider n boxes arranged in a line and numbered $1,2,\ldots,n$. The total number of ways of putting l objects ($l \geq 1$) in n different boxes is $\binom{n}{l}$, disregarding the order in which they were inserted. Suppose one object goes into box m ($1 \leq m \leq n$) an the remaining $l-1$ go into boxes $m+1,\ldots,n$. (Assume for the moment that $n - m + 1 \geq l$. This assumption becomes unnecessary later.) The number of ways

of putting $l-1$ objects in $n-m$ boxes is $\binom{n-m}{l-1}$. Thus the probability of this happening for a given m is

$$\binom{n-m}{l-1} / \binom{n}{l}. \qquad (B.4)$$

Now suppose that the boxes are time bins in a TDC measuring the time between signals from the proton detector (which start the TDC) and signals from the FPD (which stop the TDC). Let the bin width be Δt and let a time gate open at time T and close at time $T + t_g$. Let the first electron within the gate come at time $T + t_e$. Then the number of channels in the gate is $t_g/\Delta t$ and the electron arrives in channel $t_e/\Delta t$. So in Equation B.4 n is replaced by $t_g/\Delta t$ and m is replaced by $t_e/\Delta t$. If the first electron stops the TDC then the time probability distribution for l electrons incident on the detector within the time gate is

$$P^l_{t_e} = \binom{(t_g - t_e)/\Delta t}{l-1} / \binom{t_g/\Delta t}{l}.$$

This expands to

$$P^l_{t_e} = l\Delta t \frac{(t_g - t_e)\,(t_g - t_e - \Delta t)\ldots(t_g - t_e - (l-2)\,\Delta t)}{t_g\,(t_g - \Delta t)\ldots(t_g - (l-1)\,\Delta t)}.$$

Now, dividing by Δt, the probability density can be written as

$$p_l\,(t_e) = l \frac{(t_g - t_e)\,(t_g - t_e - \Delta t)\ldots(t_g - t_e - (l-2)\,\Delta t)}{t_g\,(t_g - \Delta t)\ldots(t_g - (l-1)\,\Delta t)}$$

Now suppose the TDC has infinite resolution or, equivalently, $\Delta t \longrightarrow 0$. Then the probability density becomes

$$p_l\,(t_e) = \frac{l}{t_g}\left(1 - \frac{t_e}{t_g}\right)^{l-1} \quad (l > 0) \qquad (B.5)$$

To obtain the time distribution for random electrons detected in the whole detector, Equation B.5 is summed over all nonzero values of l where each term is weighted by the distribution of Equation B.3. This gives

$$p\,(t_e) = \frac{\alpha}{t_g(1 - e^{-\alpha})} e^{-\alpha t_e/t_g} \qquad (B.6)$$

B.1.3 Multiplicity Distribution for Events with a Correlated Electron

Since all events considered here have one correlated or "prompt" electron, only events with $l > 0$ should be considered. The prompt electron comes at a known fixed time and the $l-1$ remaining electrons are random. Thus for such events $P(R) = 1$. The probability of obtaining l electrons is the same as the probability of obtaining $l-1$ randoms, so that the probability distribution for the FPD is given by

$$P_l = \frac{e^{-\alpha}\alpha^{l-1}}{(l-1)!} \quad (l > 0) \tag{B.7}$$

B.1.4 The Time Distribution of Signals from Events with a Prompt Electron

Again, consider n boxes in a line numbered sequentially and l objects, one of which always goes into the box labelled p $(1 \leq p \leq n)$. The problem splits into two cases: *(a)* The remaining $l-1$ objects can go into boxes $p+1, \ldots, n$ only (assuming for the moment that $n-p$ is sufficiently large), or *(b)* at least one of the $l-1$ objects goes into one of boxes $1, \ldots, p-1$. By similar arguments already given the respective probabilities of *(a)* and *(b)* occurring are

$$\binom{n-p}{l-1} \Big/ \binom{n-1}{l-1}$$

and

$$\binom{n-m-1}{l-2} \Big/ \binom{n-1}{l-1}.$$

As before m, n and p are replaced by $t_e/\Delta t$, $t_g/\Delta t$ and $t_p/\Delta t$ respectively, where t_p is the time of arrival of the prompt electron, and the limit $\Delta t \longrightarrow 0$ is taken. The probability densities derived from the above expressions are respectively

$$p_l(t_e) = \left(1 - \frac{t_e}{t_g}\right)^{l-1} \delta(t_e - t_p) \quad (0 \leq t_e \leq t_g, l \geq 1) \tag{B.8}$$

and

$$p_l(t_e) = \frac{l-1}{t_g}\left(1-\frac{t_e}{t_g}\right)^{l-2} \quad (0 \le t_e \le t_p, l \ge 2). \tag{B.9}$$

Hence the time distribution for l electrons can be written as

$$p_l(t_e) = \begin{cases} \delta(t_e - t_p) & \text{for } l = 1 \text{ and } 0 \le t_e \le t_g \\ \left(1-\frac{t_e}{t_g}\right)^{l-1}\delta(t_e - t_p) & \\ \quad +\frac{l-1}{t_g}\left(1-\frac{t_e}{t_g}\right)^{l-2} & \text{for } l > 1 \text{ and } 0 \le t_e \le t_p \\ 0 & \text{for } l > 1 \text{ and } t_p < t_e \le t_g. \end{cases} \tag{B.10}$$

A sum over all values of l, making use of Equation B.7, yields the net time distribution for the FPD:

$$p(t_e) = \begin{cases} e^{-\alpha t_e/t_g}\left\{\delta(t_e - t_p) + \frac{\alpha}{t_g}\right\} & (0 \le t_e \le t_p) \\ 0 & (t_p < t_e \le t_g) \end{cases}. \tag{B.11}$$

B.2 One section of the FPD

B.2.1 The Multiplicity Distribution of Random Events

Let R_j^l be the set of events where exactly l electrons ($l \ge 0$)) hit section j of the FPD, written as $R_j^l = \{(k_1, \ldots, k_6) : k_j = l\}$. To find the probability over l, $P(R_j^l|R)$ should be evaluated. Now,

$$\begin{aligned} R_j^l \bigcap R &= \left\{(k_1, \ldots, k_6) : \textstyle\sum_{i=1}^6 k_i > 0 \text{ and } k_j = l\right\} \\ &= \left\{(k_1, \ldots, k_6) : \textstyle\sum_{i=1, i\neq j}^6 k_i > -l \text{ and } k_j = l\right\}. \end{aligned} \tag{B.12}$$

If $l = 0$ then

$$R_j^0 \bigcap R = \left\{(k_1, \ldots, k_6) : \textstyle\sum_{i=1, i\neq j}^6 k_i > 0 \text{ and } k_j = 0\right\}$$

so that

$$P(R_j^0 \bigcap R) = e^{-\alpha_j}\sum_{k=1}^{\infty}\frac{e^{-\beta_j}\beta_j^k}{k!} = e^{-\alpha_j}(1 - e^{-\beta_j})$$

where α_j is the Poisson parameter for section j, β_j is the Poisson parameter for all sections except j, and $k = \sum_{i=1, i\neq j}^6 k_i$. In a similar way, for $l > 0$, it can be shown that

$$P(R_j^l \bigcap R) = \frac{e^{-\alpha_j}\alpha_j^l}{l!}$$

Thus the probability distribution is given by

$$P(R_j^l|R) = \begin{cases} e^{-\alpha_j}(1-e^{-\beta_j})(1-e^{-\alpha})^{-1} & \text{if } l=0 \\ e^{-\alpha_j}\alpha_j^l\,[l!(1-e^{-\alpha})]^{-1} & \text{if } l>0 \end{cases} \qquad (B.13)$$

It can be shown that $\sum_{l=0}^{\infty} P(R_j^l|R) = 1$ if and only if $\alpha = \alpha_j + \beta_j$.

B.2.2 The Time Distribution of Random Events

The arguments of Section B.1.4 apply here also, so that the time distribution for l electrons hitting the section in question is given by Equation B.5. Thus by summing over all possible values of l, the time distribution for random electrons, using Equation B.13, is

$$p^j(t_e) = \frac{\alpha_j}{t_g(1-e^{-\alpha})} e^{-\alpha_j t_e/t_g} \qquad (B.14)$$

Again the random background in a TDC spectrum is exponential with time.

B.2.3 The Multiplicity Distribution of Prompt Events

In dealing with a section of the FPD for events which include a prompt electron somewhere in the FPD there are two classes of event:

1. Those in which the prompt electron hits the section in question

2. Those in which the prompt electron hits the FPD somewhere other than in the section in question.

$R_j^l \bigcap R$ is as defined in Equation B.12.

In the first case $l = 0$ is impossible since the prompt electron hits this section. For $l > 0$ the probability that $k_j = l$ is $e^{-\alpha_j}\alpha_j^{l-1}/(l-1)!$. The probability that $\sum_{i=1,i\neq j}^{6} k_i > -l$ is simply 1. Thus the probability distribution is

$$P(R_j^l|R) = \begin{cases} 0 & \text{if } l=0 \\ \frac{e^{-\alpha_j}\alpha_j^{l-1}}{(l-1)!} & \text{if } l>0 \end{cases} \qquad (B.15)$$

In the second case, the probability that $\sum_{i=1,i\neq j}^{6} k_i > -l$ is again 1 and the probability distribution is

$$P(R_j^l|R) = \frac{e^{-\alpha_j}\alpha_j^l}{l!} \text{ for } l \geq 0. \qquad (B.16)$$

B.2.4 The Time Distribution of Prompt Events

The time distribution of Equation B.10 is appropriate here. Equation B.10 is subjected to a similar sum along with the distribution of Equation B.15 to obtain the same equation as that in B.11 but with α_j substituted for α. Lastly, the distribution for events in which the prompt electron goes elsewhere in the detector is obtained by summing Equation B.5, since all electrons which hit this section are random, using Equation B.16. A distribution identical to Equation B.14 is obtained but without the factor $(1-e^{-\alpha})^{-1}$.

B.3 Summary

To summarise, the important results for a section of the FPD are quoted for reference:

- The multiplicity distribution of randoms (Equation B.13) is

$$P(R_j^l|R) = \begin{cases} \frac{e^{-\alpha_j}(1-e^{-\beta_j})}{(1-e^{-\alpha})} & \text{if } l = 0 \\ \frac{e^{-\alpha_j}\alpha_j^l}{l!(1-e^{-\alpha})} & \text{if } l > 0 \end{cases}$$

- The time distribution of randoms (Equation B.5) is

$$p_l(t_e) = \frac{l}{t_g}\left(1 - \frac{t_e}{t_g}\right)^{l-1} \quad (l > 0)$$

- The multiplicity distribution of prompts is

$$P(R_j^l|R) = \begin{cases} 0 & \text{if } l = 0 \\ \frac{e^{-\alpha_j}\alpha_j^{l-1}}{(l-1)!} & \text{if } l > 0 \end{cases}$$

  if the prompt hits the section in question (Equation B.15), and

$$P(R_j^l|R) = \frac{e^{-\alpha_j}\alpha_j^l}{l!} \text{ for } l \geq 0.$$

if the prompt does not hit the section in question (Equation B.16)

- The time distribution of prompts is

$$p_l(t_e) = \begin{cases} \delta(t_e - t_p) & \text{for } l = 1 \text{ and } 0 \le t_e \le t_g \\ \left(1 - \frac{t_e}{t_g}\right)^{l-1} \delta(t_e - t_p) & \\ \quad + \frac{l-1}{t_g}\left(1 - \frac{t_e}{t_g}\right)^{l-2} & \text{for } l > 1 \text{ and } 0 \le t_e \le t_p \\ 0 & \text{for } l > 1 \text{ and } t_p < t_e \le t_g. \end{cases}$$

if the prompt hits the section in question (Equation B.10), and is, Equation B.5 if the prompt does not hit the section in question.

A complete, idealised distribution which would be expected for the section TDC can now be calculated. Let a be the probability that the event has a correlated electron or, in other words, that the event is from a tagged photon. The probability that the event is from an untagged photon is thus $(1 - a)$. The section must be treated carefully since of those events which have a prompt, there is a finite probability of the prompt hitting the detector section, written as b_j. The total probability for that type of event is ab_j, and $a(1 - b_j)$ is that for tagged events in which the prompt electron goes elsewhere. The net time distribution, summing over all possible values of l turns out to be

$$p(t_e) = \begin{cases} e^{-\alpha_j t_e/t_g}\left\{ab_j\delta(t_e - t_p) + \frac{\alpha_j(1-ae^{-\alpha})}{t_g(1-e^{-\alpha})}\right\} & (0 \le t_e \le t_p) \\ \frac{\alpha_j}{t_g}e^{-\alpha_j t_e/t_g}\left\{\frac{(1-ae^{-\alpha})}{(1-e^{-\alpha})-ab_j}\right\} & (t_p < t_e \le t_g) \end{cases}.$$

B.4 "Singles" in a Section TDC

The motivation for looking at singles (i.e. exactly one electron hitting the section in question per event) arises because of the difficulty in assigning a particular FPD channel to the timing signal from the FPD if more than one channel fires in an event. This is important in determining the photon energy. Only singles can be interpreted unambiguously. The probability density for singles events with a prompt in the section (from Equations B.15 and B.8) is

$$p_0(t_e) = ab_j e^{-\alpha_j}\delta(t_e - t_p) \qquad (B.17)$$

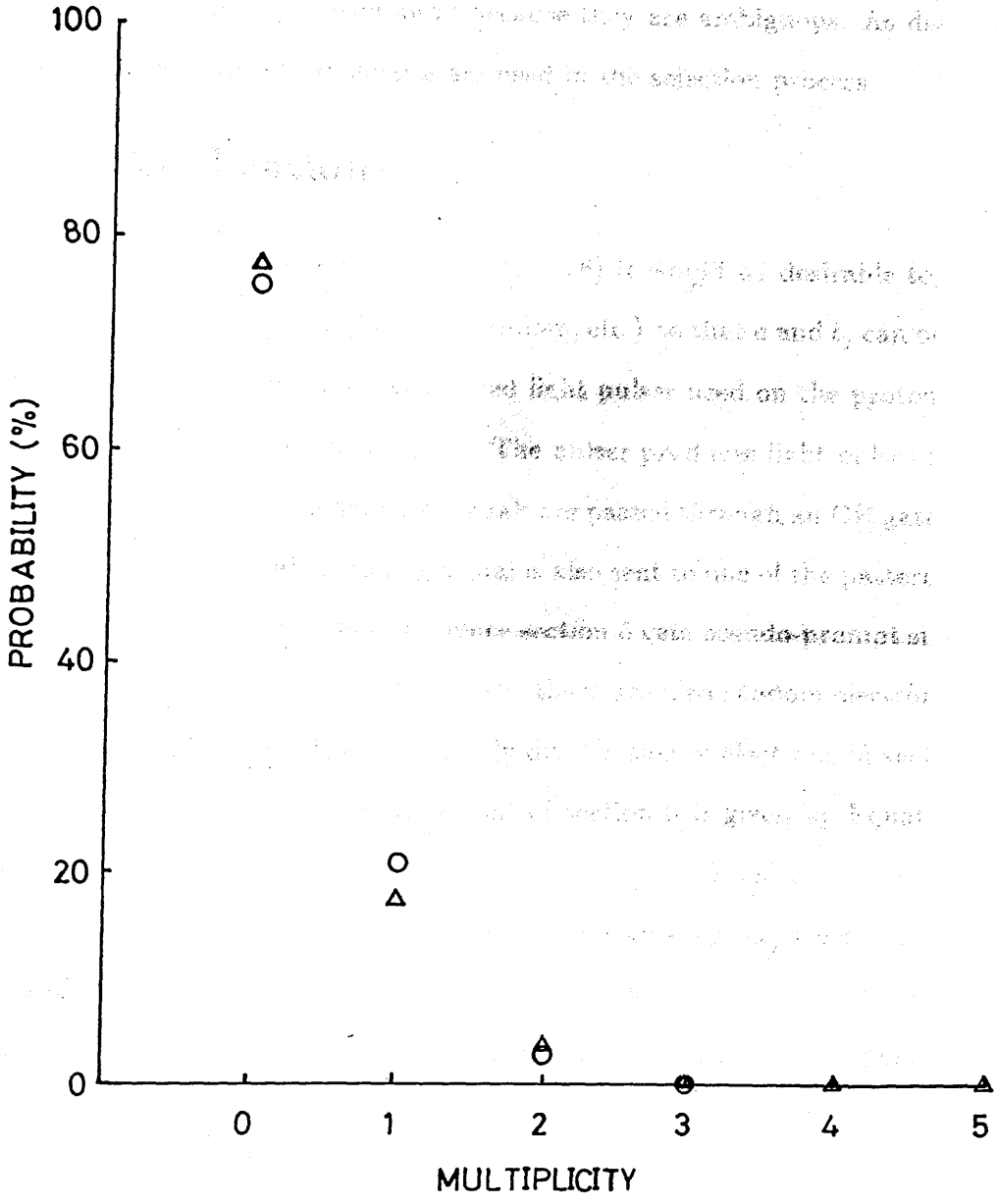

Figure B.1: Multiplicity distribution for TDC #3. Triangles: measured distribution which has an average multiplicity of 0.2774. Circles: theoretical distribution evaluated from Equation B.16 with the same average multiplicity.

On integrating over t_e the fraction of all the events which are in this category is $ab_j e^{-\alpha_j}$. $e^{-\alpha_j}$ then is simply the fraction of all events, in which a prompt hits the section, which are singles. This fraction is used to correct for the number of good events which must be thrown away because they are ambiguous. As described in Chapter 3, only spectra of singles are used in the selection process.

B.5 Application

To calculate the values of α_j $(j = 1, \ldots, 6)$ it would be desirable to limit the type of events accumulated (i.e. real, random, etc.) so that a and b_j can be ignored. Such data are supplied by the stabilised light pulser used on the proton detector to monitor the photomultiplier gains. The pulser produces light pulses at regular intervals and the resulting detector signals are passed through an OR gate with the normal X-Trigger signal. A timing signal is also sent to one of the pattern units on the FPD (in this case, number 6). Hence section 6 gets pseudo-prompt signals. As photons are being tagged simultaneously, there are also random electrons hitting each of the six sections. The multiplicity distribution of electrons in sections 1 to 5 are given by Equation B.16 while that of section 6 is given by Equation B.15. The average multiplicity in each case is α_j $(j = 1, \ldots, 5)$ and $\alpha_6 + 1$ respectively. The multiplicity distributions (see Figure B.1 for an example) from the data have been evaluated and values of α_j are shown in Table B.1 along with the correction factors e^{α_j}. These factors have been applied to the photon energy dependent cross sections in Chapter 4. The correction to the angle dependent data has been found by averaging over values for the top three FPD sections with the fifth and sixth sections being given a weight twice that of the fourth section. The factor was found to be 1.27 ± 0.08.

Photon Energy	TDC Number j	α_j	Correction Factor e^{α_j}
86.1	6	0.311	1.37
94.8	5	0.343	1.41
103.6	4	0.311	1.36
112.4	3	0.277	1.32
121.3	2	0.263	1.30
129.4	1	0.194	1.21

Table B.1: Photon energy dependence of the correction for losses during the selection of prompt data. An error of $\pm 5\%$ is estimated for the final correction factors.

Appendix C

Energy Loss Corrections to Proton Energy Calibrations

If a proton enters a material with initial energy E_1, then the proton has a finite range in that material and is denoted by R_1. Similarly, a proton with energy E_2 ($< E_1$) has a range R_2 ($< R_1$). Let

$$x = R_1 - R_2. \qquad (C.1)$$

Then the energy lost by a proton of initial energy E_1 while travelling through a thickness x of material is $E_1 - E_2$. Hence if the initial energy of the proton and the thickness of material are known the energy loss can be easily calculated from range tables.

In the present experiment, protons must travel through three types of material before entering an E block: target material (CD_2,^{12}C), air, and ΔE scintillator. Proton ranges as a function of energy are tabulated in [82]. Ranges for $C_{10}H_{14}$ ($CH_{0.7143}$), $C_{12}H_{14}$ ($CH_{0.8514}$), and CH_2 are also tabulated so that data for NE110 and NE102A ($CH_{1.104}$) have been obtained by interpolation. The data sets for target, air and ΔE are shown in Figure C.2 together parameters for fits.

From the parameterisations, R is expressed in the form $R = cE^k$ where c and k are parameters. On substitution into Equation C.1 the energy with which the

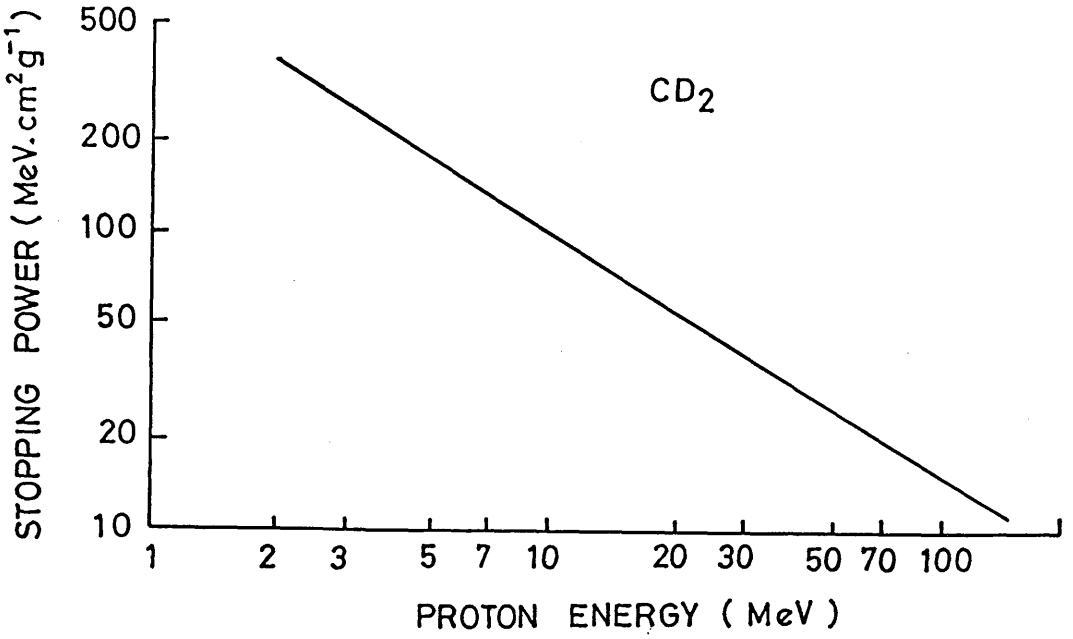

Figure C.1: The stopping power of CD_2 as a function of the incident proton energy. The parameterisation is $m_{CD_2} = 273.8E^{-0.8023}$ where E is in MeV.cm^{2}g^{-1}.

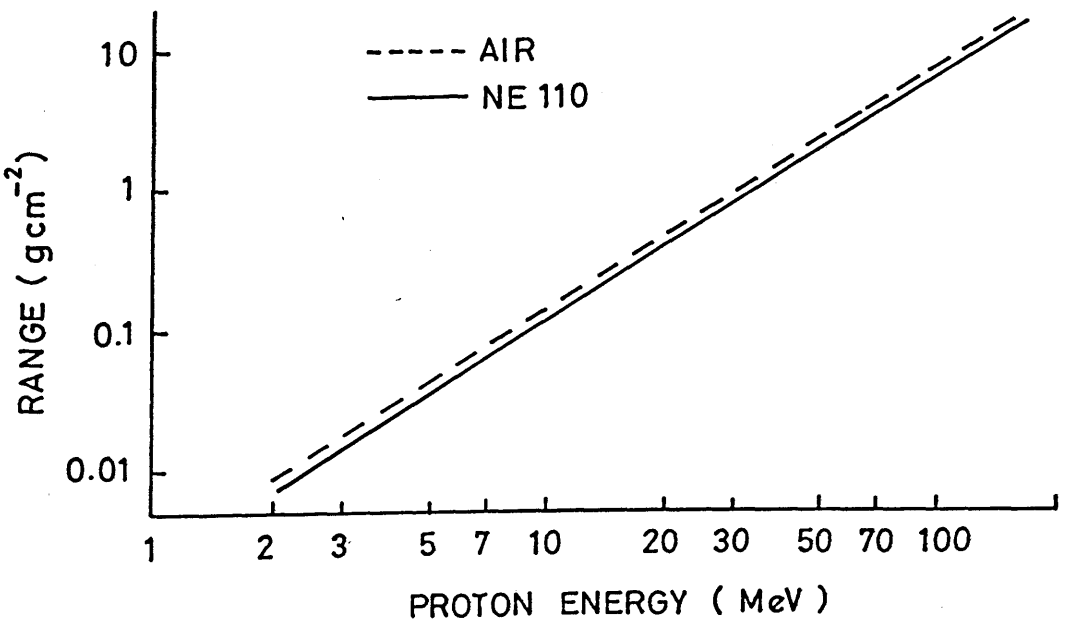

Figure C.2: The range of a proton in air and in the scintillator NE110 as a function of its incident energy. For air the parameterisation is $R = (2.3503 \times 10^{-3})E^{1.7844}$; for NE110, $R = (1.8917 \times 10^{-3})E^{1.8054}$ where E is in MeV and R is in gcm^{-2}.

proton emerges from the material can be expressed as

$$E_2 = \left[cE_1^k - \frac{x}{c} \right]^{1/k}$$

from which the energy loss can be easily obtained.

To find the energy loss in a composite material such as CD_2, for which range tables are not tabulated, the stopping powers of the material's constituents must be considered. $\frac{dE}{dx}$ for CD_2 is the sum of $\left(\frac{dE}{dx}\right)_{^{12}C}$ and $\left(\frac{dE}{dx}\right)_{^{2}H}$. Writing the stopping power as $m = \frac{1}{\rho}\frac{dE}{dx}$ then

$$m_{CD_2} = \frac{\rho_D}{\rho_{CD_2}} m_D + \frac{\rho_C}{\rho_{CD_2}} m_C.$$

Now $\frac{\rho_D}{\rho_{CD_2}} = \frac{1}{4}$ and $\frac{\rho_C}{\rho_{CD_2}} = \frac{3}{4}$, and since $m \propto \frac{Z}{A}$ for any medium [85] $m_D = \frac{1}{2} m_H$. So

$$m_{CD_2} = \frac{1}{8} m_H + \frac{3}{4} m_C.$$

m_{CD_2} has been evaluated and shown in Figure C.1. Having established these parameterisations of the stopping power, the range in CD_2 is obtained from

$$R = -\int_{E_0}^{0} \frac{1}{\left(\frac{dE}{dx}\right)} dE.$$

$\frac{dE}{dx}$ has been parameterised in the form aE^b from which the range is

$$R = \frac{E_0^{1-b}}{a(1-b)} = AE^B$$

with $B = 1 - b$ and $A = a^{-1}B^{-1}$.

Appendix D

Phase Space

In this appendix the kinematic boundary of allowed energies of the final state particles is calculated from the equations of motion in the centre of mass frame. From this boundary it is then possible to calculate the expected recoil momentum distribution when the sharing of energies in the final state is determined purely by the available phase space.

The Kinematic Boundary

For a proton, neutron and a recoil nucleus in a final state, the equations of motion in the centre of mass frame are

$$T_p + T_n + T_R = C \qquad (D.1)$$

for energy, where C denotes the total kinetic energy available to the final state particles, and

$$\mathbf{p}_p + \mathbf{p}_n + \mathbf{p}_R = 0 \qquad (D.2)$$

for momentum. The subscripts p, n and R indicate proton neutron and recoil nucleus respectively. From Equation D.2

$$p_R^2 = p_n^2 + p_p^2 + 2p_n p_p \cos\theta_{pn}. \qquad (D.3)$$

where θ_{pn} is the opening angle between the proton and neutron momentum vectors.

In the non-relativistic limit, writing $m_p = m_n = m$ for the nucleon rest masses,

$$\frac{m_R}{m}T_R = T_p + T_n + 2\sqrt{T_pT_n}\cos\theta_{pn}. \qquad (D.4)$$

The substitutions

$$C - T_R = T_p + T_n \qquad (D.5)$$

and

$$T_D = T_p - T_n \qquad (D.6)$$

into D.4 are made. Squaring both Equations D.5 and D.6 and subtracting D.6 from D.5 gives

$$2\sqrt{T_pT_n} = \left[(C - T_R)^2 - T_D^2\right]^{\frac{1}{2}}. \qquad (D.7)$$

Substituting D.5 and D.7 into D.4 gives

$$T_D^2 = (C - T_R)^2 - \sec^2\theta_{pn}\left[\frac{m_R}{m}T_R - (C - T_R)\right]^2. \qquad (D.8)$$

When $\theta_{pn} = 0$ or π, $\frac{d(T_D^2)}{d\theta_{pn}} = 0$ and T_D is a maximum. So the equation

$$T_D^2 = (C - T_R)^2 - \left[\frac{m_R}{m}T_R - (C - T_R)\right]^2 \qquad (D.9)$$

marks the boundary of the allowed values of T_D and T_R. Expressed more simply,

$$\frac{T_D^2}{a^2} + \frac{(T_R - b)^2}{b^2} = 1 \qquad (D.10)$$

which is the equation of an ellipse with semi-major axes $a = C\left[m_R/(m_R + 2m)\right]^{\frac{1}{2}}$ and $b = C\left[m/(m_R + 2m)\right]$.

Phase Space Recoil Momentum Distribution

It can be shown [109] that the density of final states is

$$\rho = (\text{const.})dT_pdT_n.$$

Thus phase space by itself, for which the matrix element of the interaction is constant, predicts that a 2-dimensional density plot of T_n against T_p would be of

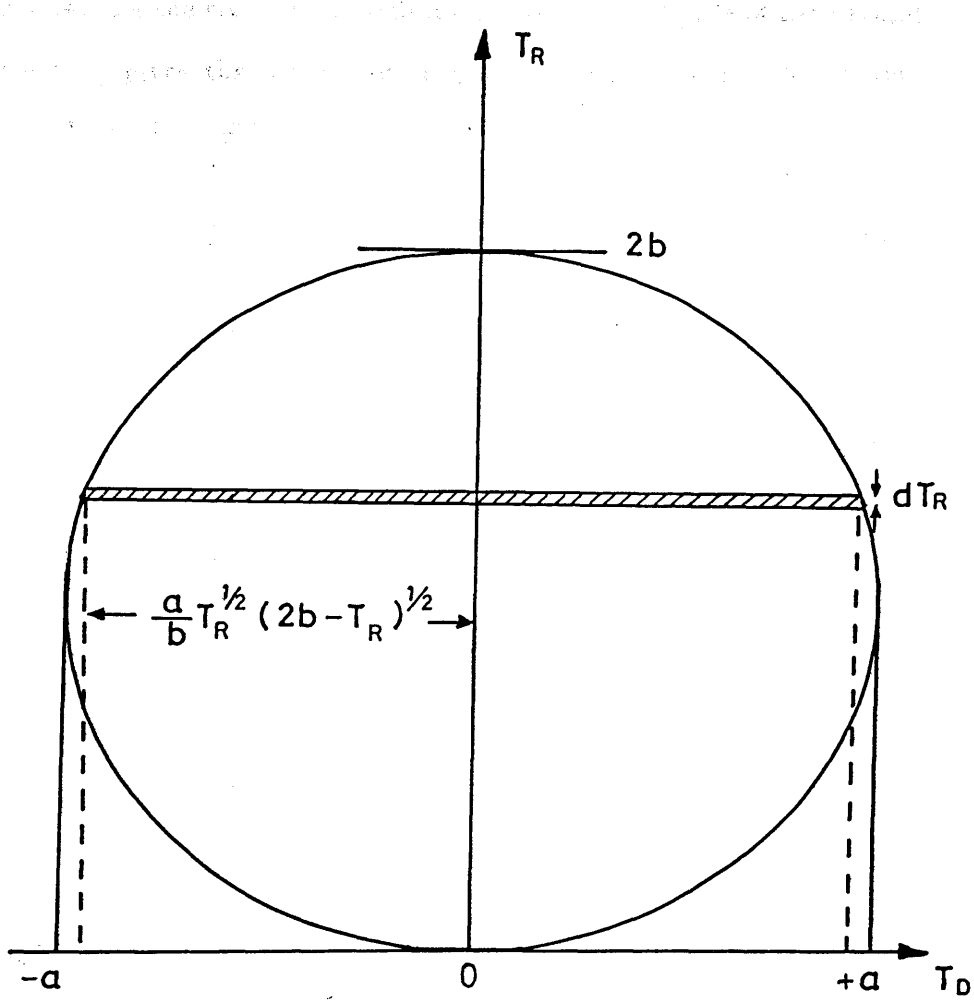

Figure D.1: Expected boundary shape of a plot of T_R versus $T_D = T_p - T_n$. The phase space distribution of T_R is obtained by integrating a uniform distribution over T_D.

uniform density within the allowed kinematical region. Since T_R and T_D are linear combinations of T_p and T_n with unit coefficients, a density plot of T_R against T_D would also result in a uniform distribution within the boundary defined by Equation D.10.

Integrating the constant distribution between the limits of the variable T_D (see Figure D.1) gives the density of states in T_R. So the number of states in the interval T_R to $T_R + dT_R$ is

$$(\text{const.}) \left(\int_{-T_D^{max}}^{T_D^{max}} dT_D \right) dT_R = (\text{const.}) \left(1 - \frac{(T_R - b)^2}{b^2} \right)^{\frac{1}{2}} dT_R$$

It is desirable to change from the variable T_R to the momentum p_R. The resulting distribution is then proportional to

$$p_R^2 \left(1 - p_R^2 \frac{m_R + 2m}{4Cmm_R} \right)^{\frac{1}{2}} dp_R.$$

Appendix E

Tables of Results

This appendix contains tabulations of some of the more important data acquired for this thesis and displayed graphically in Chapter 4. Included are tabulations of the recoil nucleus momentum distributions for the two missing energy regions considered. The angular and energy dependent cross sections for deuterium and carbon are also tabulated for data before and after the integration corrections f_0 from the quasideuteron Monte Carlo code (see Section 3.6) are applied.

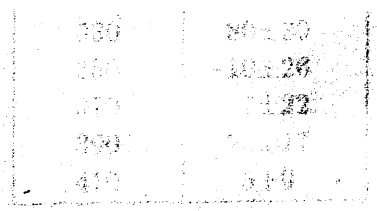

momentum distribution recoil ^{10}B nucleus for (1p1p) data
corrected for neutron detection efficiencies only.

Momentum (MeV/c)	# of events
10	141±50
30	231±86
50	399±80
70	994±94
90	902±112
110	1064±122
130	782±124
150	718±131
170	471±124
190	317±111
210	287±99
230	71±77
250	151±71
270	244±59
290	106±44
310	35±41
330	80±39
350	−10±26
370	27±22
390	20±17
410	5±9

Table E.1: Momentum distribution recoil ^{10}B nucleus for (1p1p) data. The numbers have been corrected for neutron detection efficiencies only.

Momentum (MeV/c)	# of events
20	34±50
60	338±108
100	784±133
140	613±146
180	784±130
220	371±111
260	−17±80
300	164±55
340	−31±28
380	−8±12
420	7±5

Table E.2: Momentum distribution recoil ^{10}B nucleus for (1p1s) data. The numbers have been corrected for neutron detection efficiencies only.

Photon Energy (MeV)	^{2}H	^{12}C ((1p1p) data)	^{12}C ((1p1s) data)
86.1±4.0	74.0±3.7	29.4±7.6	7.6±3.1
94.8±4.0	57.0±3.6	75.1±8.1	6.1±5.0
103.6±4.0	56.2±3.3	61.0±7.6	27.3±6.5
112.4±4.0	48.4±3.4	70.6±8.2	47.6±8.2
121.3±4.0	43.5±3.2	70.8±8.1	35.5±8.1
129.4±4.0	46.4±3.5	69.0±8.3	37.8±8.5

Table E.3: The (γ,pn) cross section as a function of photon energy (in microbarns), integrated over neutron angles from 67.5° to 105.0° and all measured proton angles. The carbon data do not include the integration correction factor f_Ω.

Photon Energy (MeV)	$\sigma_{(1p1p)}/\sigma_D$	$\sigma_{(1p1s)}/\sigma_D$	$\sigma_{(1p1s)}/\sigma_{(1p1p)}$
86.1±4.0	0.40±0.10	0.10±0.04	0.26±0.13
94.8±4.0	1.32±0.16	0.11±0.09	0.08±0.07
103.6±4.0	1.09±0.15	0.49±0.12	0.45±0.12
112.4±4.0	1.46±0.20	0.98±0.18	0.67±0.14
121.3±4.0	1.64±0.22	0.82±0.19	0.50±0.13
129.4±4.0	1.49±0.21	0.81±0.19	0.55±0.14

Table E.4: Ratios of the (γ,pn) cross section as a function of photon energy. The carbon data do not include the integration correction factor f_Ω.

Photon Energy (MeV)	(1p1p) data	(1p1s) data
86.1±4.0	211±55	—±—
94.8±4.0	409±44	520±430
103.6±4.0	275±34	660±160
112.4±4.0	276±32	740±130
121.3±4.0	247±28	382±87
129.4±4.0	215±26	290±65

Table E.5: The ^{12}C(γ,pn) cross section as a function of photon energy (in microbarns), integrated over neutron angles from 67.5° to 105.0°. All of the data include f_Ω, the integration correction. The Monte Carlo code predicted no events for the 86.1 MeV, (1p1s) data point and so a correction factor was not computed.

Photon Energy (MeV)	$\sigma_{(1p1p)}/\sigma_D$	$\sigma_{(1p1s)}/\sigma_D$	$\sigma_{(1p1s)}/\sigma_{(1p1p)}$
86.1±4.0	2.86±0.75	—±—	—±—
94.8±4.0	7.17±0.90	9.2±7.5	1.3±1.1
103.6±4.0	4.90±0.67	11.8±2.9	2.41±0.65
112.4±4.0	5.70±0.77	15.3±2.8	2.68±0.56
121.3±4.0	5.68±0.77	8.8±2.1	1.55±0.39
129.4±4.0	4.64±0.66	6.3±1.5	1.35±0.34

Table E.6: Ratios of the (γ,pn) cross section as a function of photon energy. The carbon data include the integration correction factor f_Ω.

Neutron Angle (°)	^{2}H	^{12}C ((1p1p) data)	^{12}C ((1p1s) data)
67.5	3.89±0.41	5.12±1.02	3.78±0.99
75.0	4.12±0.44	8.35±1.12	2.55±1.14
82.5	4.22±0.45	6.45±1.05	2.88±1.06
90.0	3.34±0.41	4.20±1.05	2.07±0.99
97.5	2.93±0.39	4.28±0.90	2.51±0.94
105.0	3.07±0.39	5.68±0.99	2.19±1.04
112.5	3.61±0.41	2.59±0.93	0.18±1.01
127.5	—±—	2.88±0.82	3.70±0.96

Table E.7: The (γ,pn) differential cross section (in μb/sr) as a function of neutron angle, integrated over all measured proton angles, and averaged over the 113 to 133 MeV photon energy range. The carbon data do not include the integration correction factor f_{Ω}.

Neutron Angle (°)	$\sigma_{(1p1p)}/\sigma_D$	$\sigma_{(1p1s)}/\sigma_D$	$\sigma_{(1p1s)}/\sigma_{(1p1p)}$
67.5	1.32±0.30	0.97±0.27	0.74±0.24
75.0	2.03±0.35	0.62±0.28	0.31±0.14
82.5	1.53±0.30	0.68±0.26	0.45±0.18
90.0	1.26±0.35	0.62±0.31	0.49±0.27
97.5	1.46±0.36	0.86±0.34	0.59±0.25
105.0	1.85±0.40	0.71±0.35	0.39±0.20
112.5	0.72±0.27	0.05±0.28	0.07±0.39
127.5	—±—	—±—	1.28±0.49

Table E.8: Ratios of the (γ,pn) differential cross section as a function of neutron angle, and averaged over the 113 to 133 MeV photon energy range. The carbon data do not include the integration correction f_{Ω}.

Neutron Angle (°)	(1p1p) data	(1p1s) data
67.5	17.3±3.5	34.6±9.1
75.0	28.8±3.9	23.7±10.6
82.5	19.3±3.1	26.1±9.6
90.0	14.0±3.5	17.8±8.5
97.5	14.4±3.0	23.1±8.6
105.0	20.2±3.5	17.9±8.5
112.5	10.4±3.7	1.4±7.8
127.5	15.8±4.5	30.6±7.9

Table E.9: The ^{12}C(γ,pn) differential cross section as a function of neutron angle (in μb/sr), integrated over all measured proton angles, and averaged over the 113 to 133 MeV photon energy range, with the integration correction f_Ω included.

Neutron Angle (°)	$\sigma_{(1p1p)}/\sigma_D$	$\sigma_{(1p1s)}/\sigma_D$	$\sigma_{(1p1s)}/\sigma_{(1p1p)}$
67.5	4.45±1.02	8.9±2.5	2.00±0.66
75.0	6.99±1.21	5.8±2.6	0.82±0.38
82.5	4.57±0.88	6.2±2.4	1.35±0.54
90.0	4.19±1.17	5.3±2.6	1.27±0.68
97.5	4.91±1.21	7.9±3.1	1.60±0.68
105.0	6.58±1.42	5.8±2.9	0.89±0.45
112.5	2.88±1.08	0.4±2.2	0.13±0.73
127.5	—±—	—±—	1.94±0.75

Table E.10: Ratios of the (γ,pn) differential cross section as a function of neutron angle, and averaged over the 113 to 133 MeV photon energy range, with the integration correction f_Ω included.

References

[1] B. Ziegler, "Proceedings of the International Conference on Nuclear Physics with Electromagnetic Interactions", edited by H. Arenhövel and D. Drechsel, in Lect. Notes Phys. **108**(1979)148.

[2] J. S. Levinger, Phys. Rev. **84**(1951)43.

[3] B. Schoch, Phys. Rev. Lett. **41**(1978)80.

[4] O. Hirzel and H. Wäffler, Helv. Phys. Acta **20**(1947)373.

[5] D. Walker, Phys. Rev. **81**(1951)634.

[6] C. Levinthal and A. Silverman, Phys. Rev. **82**(1951)822.

[7] J. C. Keck, Phys. Rev. **85**(1952)410.

[8] G. F. Chew and M. L. Goldberger, Phys. Rev. **77**(1950)470.

[9] J. W. Weil and B. D. McDaniel, Phys. Rev. **92**(1953)391.

[10] J. Heidmann, Phys. Rev. **80**(1950)171.

[11] L. I. Schiff, Phys. Rev. **78**(1950)733.

[12] J. F. Marshall and E. Guth, Phys. Rev. **78**(1950)738.

[13] J. W. Rosengren and J. M. Dudley, Phys. Rev. **89**(1953)603.

[14] B. T. Feld, R. D. Godbole, A. Odian, F. Scherb, P. C. Stein and A. Wattenberg, Phys. Rev. **94**(1954)1000.

[15] J. C. Keck and A. V. Tollestrup, Phys. Rev. **101**(1956)360.

[16] S. A. E. Johansson, Phys. Rev. **97**(1955)434.

[17] K. Gottfried, Nucl. Phys. **5**(1958)557.

[18] R. Jastrow, Phys. Rev. **98**(1955)1479.

[19] W. Weise, M. G. Huber and M. Danos, Zeit. Phys. **236**(1970)176.

[20] H. Myers, A. Odian, P. C. Stein, and A. Wattenberg, Phys. Rev. **95**(1954)576.

[21] A. C. Odian, P. C. Stein, A. Wattenberg and B. T. Feld, Phys. Rev. **102**(1956)837.

[22] A. Wattenberg, A. C. Odian, P. C. Stein, and H. Wilson, Phys. Rev. **104**(1956)1710.

[23] P. C. Stein, A. C. Odian, A. Wattenberg, and R. Weinstein, Phys. Rev. **119**(1960)348.

[24] M. Q. Barton and J. H. Smith, Phys. Rev. **95**(1954)573.

[25] M. Q. Barton and J. H. Smith, Phys. Rev. **110**(1958)1143.

[26] J. Garvey, B. H. Patrick, J. G. Rutherglen and I. L. Smith, Nucl. Phys. **70**(1965)241.

[27] I. L. Smith, J. Garvey, J. G. Rutherglen, and G. R. Brookes, Nucl. Phys. **B1**(1967)483.

[28] G. G. Taran, Sov. J. Nucl. Phys. **7**(1968)301.

[29] A. F. Khodyachikh, P. I. Vatset, I. V. Dogyust, V. A. Zolenko and V. V. Kirichenko, Sov. J. Nucl. Phys. **32**(1980)453.

[30] A. F. Khodyachikh, P. I. Vatset, V. N. Gur'ev, I. V. Dogyust and V. V. Kirichenko, Sov. J. Nucl. Phys. **34**(1981)789.

[31] I. V. Dogyust, P. I. Vatset, V. V. Kirichenko and A. F. Khodyachikh, Sov. J. Nucl. Phys. **35**(1982)471.

[32] I. V. Dogyust, V. I. Voloschuk, V. V. Kirichenko and A. F. Khodyachikh, Sov. J. Nucl. Phys. **40**(1984)878.

[33] F. Partovi, Ann. Phys. **27**(1964)79.

[34] F. Ajzenberg-Selove, Nucl. Phys. **A413**(1984)1.

[35] R. J. Cence and B. J. Moyer, Phys. Rev. **122**(1961)1634.

[36] J. Arends, J. Eyink, H. Hartmann, A. Hegarth, B. Mecking, G. Nöldeke and H. Rost, Zeit. Phys. **298**(1980)103.

[37] J. C. McGeorge, G. I. Crawford, R. O. Owens, M. R. Sené, D. Brandford, A. C. Shotter, B. Schoch, R. Beck, P. Jennewein, F. Klein, J. Vogt and F. Zettl, Phys. Lett. B **179**(1986)212.

[38] S. Homma, M. Kanazawa, K. Maruyama, Y. Murata, H. Okuno, A. Sasaki and T. Taniguchi, Phys. Rev. Lett. **45**(1980)706.

[39] S. Homma, M. Kanazawa, K. Maruyama, Y. Murata, H. Okuno, A. Sasaki and T. Taniguchi, Phys. Rev. C **27**(1983)31.

[40] S. Homma, M. Kanazawa, M. Koike, Y. Murata, H. Okuno, F. Soga, M. Sudo, M. Torikoshi, N. Yoshikawa, A. Sasaki and Y. Fujii, Phys. Rev. Lett. **45**(1980)706.

[41] S. Homma, M. Kanazawa, M. Koike, Y. Murata, H. Okuno, F. Soga, N. Yoshikawa, and A. Sasaki, Report, Institute for Nuclear Study, University of Tokyo, INS–Rep.–484, December 1983

[42] T. Suda, O. Konno, I. Nomura, T. Suzuki, T. Terasawa, Y. Torizuka, J. Yokokawa, K. Maeda, J. A. Eden, G. J. O'Keefe, R. Rassool, M. N. Thompson and J. G. Kim, Phys. Lett. , to be published.

[43] T. Terasawa, K. Mori, Y. Fujii, T. Suda, I. Nomura, O. Konno, T. Ichinohe, Y. Torizuka, K. Maeda, P. D. Harty, G. J. O'Keefe, M. N. Thompson, Nucl. Inst. Meth. **A248**(1986)429.

[44] M. Gari and H. Hebach, Phys. Rep. **72**(1981)1.

[45] J. L. Matthews, D. J. S. Findlay, S. N. Gardiner and R. O. Owens, Nucl. Phys. **A267**(1976)51.

[46] G. Manuzio, G. Ricco, M. Sanzone and L. Ferrero, Nucl. Phys. **A133**(1969)225.

[47] M. Sanzone, G. Ricco, S. Costa and L. Ferrero, Nucl. Phys. **A153**(1970)401.

[48] E. Mancini, G. Ricco, M. Sanzone, S. Costa and L. Ferrero, Nou. Cim. **15A**(1973)705.

[49] S. Fujii, Prog. Theor. Phys. **21**(1959)511.

[50] S. Fujii and O. Sugimoto, Nou. Cim. **12**(1959)513.

[51] S. Fujii, Prog. Theor. Phys. **29**(1963)374.

[52] J. Eichler and H. A. Weidenmüller, Zeit. Phys. **152**(1958)261.

[53] N. C. Francis, D. T. Goldman and E. Guth, Phys Rev. **120**(1960)2175.

[54] W. D. Heiss, Zeit. Phys. **179**(1964)256.

[55] M. Fink, H. Hebach and H. Kümmel, Nucl. Phys. **A186**(1972)353.

[56] D. J. S. Findlay and R. O. Owens, Phys. Rev. Lett. **37**(1976)674.

[57] D. J. S. Findlay and R. O. Owens, Nucl. Phys. **A292**(1977)53.

[58] L. R. B. Elton and A. Swift, Nucl. Phys. **A94**(1967)52.

[59] J. L. Matthews, W. Bertozzi, M. J. Leitch, C. A. Peridier, B. L. Roberts, C. P. Sargent, W. Turchinetz, D. J. S. Findlay and R. O. Owens, Phys. Rev. Lett. **38**(1977)8.

[60] D. J. S. Findlay, R. O. Owens, M. J. Leitch, J. L. Matthews, C. A. Peridier, B. L. Roberts and C. P. Sargent, Phys. Lett. **74B**(1978)305.

[61] H. Schier and B. Schoch, Nucl. Phys. **A229**(1974)93.

[62] H. Schier and B. Schoch, Nou. Cim. Lett. **12**(1975)334.

[63] H. Göringer and B. Schoch, Phys. Lett. **97B**(1980)41.

[64] H. Göringer, B. Schoch and G. Lührs, Nucl. Phys. **A384**(1982)414.

[65] M. R. Sené, Ph. D. Thesis, Glasgow University, 1982.

[66] M. R. Sené, I. Anthony, D. Brandford, A. G. Flowers, A. C. Schotter, C. H. Zimmerman, J. C. McGeorge, R. O. Owens and P. J. Thorley, Phys. Rev. Lett. **50**(1983)1831.

[67] W. Weise and M. G. Huber, Nucl. Phys. **A162**(1971)330.

[68] W. Weise, Phys. Lett. **38B**(1972)301.

[69] T. W. Donnelly and G. E. Walker, Phys. Rev. Lett. **22**(1969)1121.

[70] M. Gari and H. Hebach, Phys. Rev. C **10**(1974)1629.

[71] S. Boffi, C. Giusti and F. D. Pacati, Phys. Lett. **98B**(1981)11.

[72] E. D. Arthur, W. C. Lam, J. Amato, D. Axen, R. L. Burman, P. Fessenden, R. Macek, J. Oostens, W. Shlaer, S. Sobottka, M. Salomon and W. Swenson, Phys. Rev. C **11**(1975)332.

[73] B. Bassalleck, W. -D. Klotz, F. Takeutchi, H. Ullrich and M. Furić, Phys. Rev. C **16**(1977)1526.

[74] M. Dörr, W. Fetscher, D. Gotta, J. Reich, H. Ullrich, G. Backenstoss, W. Kowald and H. -J. Weyer, Nucl. Phys. **A445**(1985)557.

[75] R. Hartmann, H. P. Isaak, R. Engfer, E. A. Hermes, H. S. Pruys, W. Dey, H. J. Pfeiffer, U. Sennhauser, H. K. Walter and J. Morgenstern, Nucl. Phys. **A308**(1978)345.

[76] M. E. Nordberg Jr. , K. F. Kinsey and R. L. Burman, Phys. Rev. **165**(1968)1096.

[77] H. S. Pruys, R. Engfer, R. Hartmann, U. Sennhauser, H. J. Pfeiffer, H. K. Walter, J. Morgenstern, A. Wyttenbach, E. Gadioli and E. Gadioli-Erba, Nucl. Phys. **A316**(1979)365.

[78] J. M. Vogt, Ph. D. Thesis, Institut für Kernphysik, Universität Mainz, 1987.

[79] J. R. M. Annand *et al.*, Nucl. Inst. and Meth., to be published.

[80] J. R. M. Annand, private communication.

[81] I. Anthony, Internal Report 1987, Kelvin Laboratory, University of Glasgow.

[82] W. H. Barkas and M. J. Berger, *Tables of Energy Losses and Ranges of Heavy Charged Particles*, National Aeronautics and Space Administration, 1964.

[83] R. A. Cecil, B. D. Anderson and R. Madey, Nucl. Instr. and Meth. **161**(1979)439.

[84] S. Cierjacks, T. Petković, H. Ullrich, D. Gotta, S. Ljungfelt and N. Šimičevič, Nucl. Instr. and Meth. **A238**(1985)354.

[85] J. B. A. England, *Techniques in Nuclear Structure Physics pp. 466-478*, The MacMillan Press, 1974.

[86] T. J. Gooding and H. G. Pugh, Nucl. Instr. and Meth. **7**(1960)189.

[87] I. J. D. MacGregor, S. N. Dancer, J. R. M. Annand, P. A. Wallace, J. D. Kellie, S. J. Hall, J. C. McGeorge, S. V. Springham, M. R. Sené, D. Brandford, A. C. Shotter, J. M. Vogt and B. Schoch, Nucl. Inst. and Meth., to be published.

[88] H. Herminghaus, A. Feder, K. H. Kaiser, W. Manz and H. v. D. Schmitt, Nucl. Instr. and Meth. **138**(1976)1.

[89] H. Herminghaus, K. H. Kaiser and U. Ludwig, Nucl. Instr. and Meth. **187**(1981)103.

[90] J. D. Kellie, I. Anthony, S. J. Hall, I. J. D. MacGregor, A. McPherson, P. J. Thorley, S. L. Wan and F. Zettl, Nucl. Instr. and Meth. **A241**(1985)153.

[91] *Scintillators for the Physical Sciences*, Catalogue (Nuclear Enterprises, Sighthill, Edinburgh EH11 4BY, U.K.)

[92] P. L. Meyer, *Introductory Probability and Statistical Applications*, 2nd Edition, Addison-Wesley Publishing Company Inc. , 1970.

[93] J. S. Levinger, *Nuclear Photodisintegration*, Oxford University Press 1960.

[94] L. R. B. Elton, *Introductory Nuclear Theory*, London 1965.

[95] O. A. P. Tavares, J. D. Pinhiero Filho, V. di Napoli, J. B. Martins and M. L. Terranova, Nou. Cim. Lett. **27**(1980)358.

[96] A. Leprêtre, H. Beil, R. Bergère, P. Carlos, J. Fagot, A. Veyssière, J. Ahrens, P. Axel and U. Kneissl, Phys. Lett. B **79**(1978)43.

[97] S. Homma and H. Tezuka, J. Phys. Soc. Jap. **55**(1986)780.

[98] J. Ahrens, H. Blochert, K. H. Kzock, B. Eppler, H. Gimm, H. Gundrum, M. Krönig, P. Riehn, G. Sita Ram, A. Ziegler and B. Ziegler, Nucl. Phys. **A251**(1975)479.

[99] J. S. Levinger, Phys. Lett. B **82**(1979)181.

[100] S. Homma, Report, Institute for Nuclear Study, University of Tokyo, INS–Rep.–547, July 1985

[101] G. Ricco, "Workshop on Intermediate Energy Nuclear Physics with Polarised Photons", edited by S. Matone, Frascati 1980.

[102] M. W. Wade, M. K. Brussel, L. J. Koester, Jr. and J. H. Smith, Phys. Rev. Lett. **53**(1984)2540.

[103] A. Leprêtre, H. Beil, R. Bergère, P. Carlos, J. Fagot, A. de Miniac and A. Veyssière, Nucl. Phys. **A367**(1981)237.

[104] J. M. Laget, Nucl. Phys. **A312**(1978)265.

[105] J. M. Laget, "Workshop on Nuclear Physics with Real and Virtual Photons", Bologna, in Lect. Notes Phys. **137**(1980)148.

[106] P. Carlos, H. Beil, R. Bergère, B. L. Berman, A. Leprêtre, and A. Veyssière, Nucl. Phys. **A378**(1982)237.

[107] A. N. Gorbunov, V. A. Dubrovnia, V. A. Osipova, S. Silaeva and P. A. Cerenkov, Sov. Phys. J.E.T.P. **15**(1962)520.

[108] A. N. Gorbunov and V. A. Osipova , Sov. Phys. J.E.T.P. **16**(1963)27.

[109] D. H. Perkins, *Introduction to High Energy Physics, pp130-132*, Addison-Wesley Publishing Co. Inc, 1982.

[110] R. O. Owens, Annual Report 1987, Kelvin Laboratory, University of Glasgow.

[111] C. W. de Jager, H. de Vries and C. de Vries, Atomic Data and Nuclear Data Tables **14**(1974)479.

[112] A. E. Thorlacius and H. W. Fearing, Phys. Rev. C **33**(1986)1830.

[113] K. G. Dedrick, Phys. Rev. 100(1955)58